

Distribution Agreement

In presenting this thesis or dissertation as a partial fulfillment of the requirements for an advanced degree from Emory University, I hereby grant to Emory University and its agents the non-exclusive license to archive, make accessible, and display my thesis or dissertation in whole or in part in all forms of media, now or hereafter known, including display on the world wide web. I understand that I may select some access restrictions as part of the online submission of this thesis or dissertation. I retain all ownership rights to the copyright of the thesis or dissertation. I also retain the right to use in future works (such as articles or books) all or part of this thesis or dissertation.

Signature:

Sha Li

Date

ENGINEERING ASYMMETRIC PEPTIDE MEMBRANES

By

Sha Li
Doctor of Philosophy
Chemistry

Dr. David G. Lynn
Advisor

Dr. Fred M. Menger
Committee Member

Dr. Khalid S. Salaita
Committee Member

Accepted:

Lisa A. Tedesco, Ph.D.
Dean of the James T. Laney School of Graduate Studies

_____ Date

ENGINEERING ASYMMETRIC PEPTIDE MEMBRANES

By

Sha Li

B. S., Wuhan University, 2010

Advisor: David G. Lynn, PhD.

An abstract of

A dissertation submitted to the Faculty of the
James T. Laney School of Graduate Studies of Emory University
in partial fulfillment of the requirements for the degree of

Doctor of Philosophy

in Chemistry

2015

Abstract

Engineering asymmetric peptide membranes

By Sha Li

Peptide self-assembly offers rich opportunities for the controlled synthesis of supramolecular architectures with unique structural features and functions. Historically, this area has been inspired by the elaborate assemblies of biological systems. Despite this precedent, generating asymmetrical structures with optical and electrical functions has proven challenging. The nucleating core of the Alzheimer's disease peptide, A β (16-22) or KLVFFAE, has been heavily studied and characterized to the point where specific assembly codes are now emerging. In this dissertation, I expanded the molecular recognition codes from A β (16-22), a single-component system, to multi-component systems that enable us to build asymmetry into self-assembled networks. Strategies to engineer the peptide membrane surfaces were systematically investigated and novel biophysical methods including utilizing Electrostatic Force Microscopy and solid-state NMR to characterize complex co-assemblies were developed to define the unique asymmetric charged surfaces and segregated domains of the peptide membranes. Furthermore, I demonstrate the potential of these assemblies for donor-acceptor arrays transferring energy and electrons across the peptide membranes. Taken together, I argue that amyloid peptide membranes present robust and patterned surfaces capable of routinely controlling asymmetry and extending the capabilities of biological membranes. Developing these systems for light-harvesting and charge separation of artificial photosynthesis is now within reach.

ENGINEERING ASYMMETRIC PEPTIDE MEMBRANES

By

Sha Li

B. S., Wuhan University, 2010

Advisor: David G. Lynn, PhD

A dissertation submitted to the Faculty of the
James T. Laney School of Graduate Studies of Emory University
in partial fulfillment of the requirements for the degree of
Doctor of Philosophy
in Chemistry

2015

Acknowledgements

I would never have been able to finish my dissertation without the guidance of my committee members, help from colleagues and friends, and support from my family.

I would like to express my deepest gratitude to my advisor, Dr. David Lynn, who has been my teacher, guide and philosopher. I have been amazingly fortunate to have an advisor who gave me the freedom to explore on my own and at the same time the guidance to recover when my steps faltered. He taught me how to question thoughts and express ideas, and truly care for my personal development. I have benefited greatly from our scientific discussions. His enthusiasm and hard-working attitude is always an inspiration for me during my research and will forever influence my life. I appreciate the feedback given by my committee members, Dr. Fred Menger and Dr. Khalid Salaita. Their valuable comments drove me to have a deeper understanding of my work. They never hesitate to help me both in the lab and in life, encouraging me to learn and grow.

I would like to thank Dr. Anil Mehta for guidance and practical advices. He has been my mentor during my research and taught me countless knowledge and skills. I have enjoyed our working together to puzzle many problems. I will always be thankful to Dr. Savannah Johnson, Dr. Chenrui Chen, Tolu Omosun and Dr. Junjun Tan, who have been great lab mates and friends. They have taught me many lab techniques and cheered me up with their warm attitude. I was very fortunate to follow the footsteps and learn from Dr. Seth Childers, Dr. James Simmons and Dr. Rong Ni, their research discoveries created fascinating questions and helped me build foundation for my own studies. I'm grateful to Dr. Jill Smith, Dr. Dibyendu Das, Dr. Neil Anthony and Dr. Daniel Pierce from whom I have learned a great deal and received plenty of help in conducting experiments and writings. Many thanks to Li Zhang for his friendship; I have enjoyed sharing in our many adventures together. I have been very lucky to work with

Chen Liang, Rolando Rengifo, Ting Pan, Noel Li and Allisandra Mowles. I'm always impressed by their intellectual daring discoveries and enthusiasm. I would like to thank Dr. Jay Goodwin, Dr. Yi-Han Lin and Dr. Yue Liu for their valuable insights and suggestions to me. I would like to acknowledge Dr. Anton Sidorov, Dr. Thomas Orlando, Dr. Zheyuan Chen, Dr. Zhigang Jiang and Dr. Martha Grover for their collaborations on analysis of peptide assemblies and modeling. Thanks to Anthony Bisignano and Mitesh Bhalani, I have learned as much from them as they have from me. I am thankful to Dr. Vincent Conticello, Dr. Stefan Lutz and Dr. Brian Dyer for lectures and courses that have helped me improve my knowledge in chemistry. I thank Hong Yi and John Bacsa for their instructions to me on TEM and X-ray diffraction.

Finally, I could never thank my family enough for their love and support. I thank my parents for giving me the greatest gift of all, education and the freedom of choice. It was under their watchful eye that I gained so much drive and an ability to tackle challenges head on. Thanks to my dear husband, his optimism has brought me joy and his humor has kept me sane. His enduring love, support and encouragement underpins my persistence in the graduate career.

Table of Contents

Chapter 1 Exploiting Biomimetic Strategies to Expand the Horizons of Self-assembly	1
<i>From Supramolecular Chemistry to System Chemistry</i>	1
<i>Designing Asymmetry in Nonbiological Self-assembly Systems</i>	2
<i>Amyloid β Peptide Self-Assembles into Ordered Bilayer Architectures</i>	3
<i>Molecular Recognition Codes Direct Peptide Assembly</i>	5
<i>Nucleation and Seeded Growth in Amyloid Self-Assembly</i>	7
<i>Engineering Cross-β Peptide Surfaces for New Functions</i>	9
Chapter 2 Construction of Patterned Phosphorylated Peptide Membranes	15
INTRODUCTION	15
RESULTS	16
<i>Self-Assembly of Phosphorylated Peptide Membranes</i>	16
<i>Structural Characterization of Phosphorylated Peptide Assemblies</i>	20
<i>Diversifying Negatively-Charged Peptide Nanotube Surfaces</i>	25
<i>Solvent and Temperature Dependence of Phosphorylated Peptide Membranes</i>	29
<i>AuNPs Binding with Peptide Membranes</i>	31
<i>Salt-induced Macroscale Assembly of Peptide Nanotubes</i>	33
<i>Development of Electrostatic Force Microscopy</i>	35
<i>Analysis of Supramolecular Assemblies via Electrostatic Force Microscopy</i>	37
<i>Small Molecules Binding with Phosphorylated Peptide Nanotube Surfaces</i>	40
<i>Neurofibrillar Tangle Surrogates: Histone H1 Binding to Phosphotyrosine Peptide Nanotubes</i>	41
CONCLUSIONS	48
METHODS	49
Chapter 3 Generating Asymmetric Peptide Membranes	60
INTRODUCTION	60
RESULTS	60
<i>Model of Asymmetric Peptide Membranes</i>	60
<i>Preliminary Evaluation of Peptide Mixing</i>	61
<i>Structural Characterization of the Co-Assembly</i>	63
<i>Thermal Studies of the Co-Assembly</i>	67
<i>Surface Charge Evaluation via Salt Bundling</i>	71
<i>Surface Charge Evaluation via Electrostatic Force Microscopy</i>	72

<i>Peptide Registry Characterization via Solid-State REDOR NMR</i>	74
<i>Peptide Interfaces Analysis</i>	79
<i>Domain Segregation Built upon Cross-Seeding</i>	81
<i>Exploit Surface Charge Distribution and N-terminal Residue Sizes</i>	97
<i>Exploit Peptide Specificity in Co-Assembly</i>	100
CONCLUSIONS	103
METHODS.....	105
Chapter 4 Energy and Electron Transfer across Asymmetric Peptide Membranes.....	117
INTRODUCTION	117
RESULTS	118
<i>Covalent Coupling of Fluorophores to Peptide Membrane Surfaces</i>	118
<i>Noncovalent Association of Fluorophores to Peptide Membrane Surfaces</i>	122
<i>Energy Transfer across Asymmetric Cross-β Peptide Membranes</i>	126
<i>Electron Transfer across Asymmetric Cross- β Peptide Membranes</i>	132
CONCLUSIONS	146
METHODS.....	146
Chapter 5 Assembly of Lipid-Peptide Chimeras	153
INTRODUCTION	153
RESULTS	157
<i>Accommodating Unsaturated Lipid Chains within Aβ Peptide Membranes</i>	157
<i>Self-assembly and Structural Characterization of Lipid-Peptide Chimeras</i>	161
<i>Thermal Studies of Lipid-Peptide Chimeras</i>	165
<i>Modulating Conformation and Aggregation Capability of Peptides via Lipidation</i>	169
<i>Coassembly of Lipid-Peptide Chimeras</i>	180
<i>Cross-Seeding of Lipid-Peptide Chimeras</i>	185
CONCLUSIONS	195
METHODS.....	196
Chapter 6 Engineering Asymmetric Cross- β Peptide Membranes for Emergent Functions.....	202
<i>Surface Engineering of Peptide Membranes</i>	202
<i>Surface Characterization of Peptide Membranes</i>	204
<i>Design Asymmetry and Control Defects in Multicomponent Self-Assembly</i>	204
<i>Expand Molecular Codes for Supramolecular Self-Assembly</i>	205
<i>Toward Dynamic Functional Self-Assembly System</i>	206

List of Figures

Chapter 1

Figure 1-1 A simplified model of phospholipid membrane asymmetry.	3
Figure 1-2 Model of the KLVFFAE peptide bilayer and trapped TFA.	4
Figure 1-3 Amino acid complementary and self-pairings.	6
Figure 1-4 Nucleation mechanism of peptide self-assembly.	8
Figure 1-5 (A) Model of bound to Ac-KLVFFAL-NH ₂ nanotube surface with charged lysines (in blue) and hydrophobic leucines (in grey). B) Fluorescence imaging of Rh-LVFFAE-NH ₂ /Ac-KLVFFAE-NH ₂ ratios at 1:75. C) Molecular models of Rh-LVFFAE-NH ₂ and Alexa 555 binding with Ac-KLVFFAE-NH ₂ tube surfaces (D) Cartoon describing the observed FRET across the surface.	10

Chapter 2

Figure 2-1 Peptide bilayer model for Ac-KLVFFAL peptide nanotube.	16
Figure 2-2 Molecular structure of lysine (left) and phosphotyrosine (right).	17
Figure 2-3 Circular Dichroism of Ac-pYLFFAL assembled under different conditions. .	18
Figure 2-4 TEM micrographs of Ac-pYLFFAL-NH ₂	19
Figure 2-5 Width measurements from TEM images of A) (E22L) and B) (K16pY)(E22L) nanotube assemblies.	20
Figure 2-6 Circular dichroism of (E22L) (blue) assembled in 40% MeCN/H ₂ O with TFA and (K16pY)(E22L) (red) assembled in 40% MeCN/H ₂ O with TEAA, pH7.	21
Figure 2-7 X-ray powder diffraction of (E22L) (blue) assembled in 40% MeCN/H ₂ O with TFA and (K16pY)(E22L) (red) assembled in 40% MeCN/H ₂ O with TEAA.	21
Figure 2-8 FT-IR spectra of (E22L) (blue) assembled in 40% MeCN/H ₂ O with TFA and (K16pY)(E22L) (red) assembled in 40% MeCN/H ₂ O with TEAA.	22
Figure 2-9 Solid-state NMR ¹³ C{ ¹⁵ N}EDOR measurements of [1- ¹³ C]V18 [1 ¹⁵ N]A21 (K16pY)(E22L) peptides assembled as nanotubes.	23
Figure 2-10 Sample AFM measurements of top: (E22L) and bottom: (K16pY) (E22L). ..	25
Figure 2-11 Model for (K16pY)(E22L) bilayer nanotubes with each leaflet composed of antiparallel out-of-register β-sheets.	25
Figure 2-12 TEM micrographs of (A) Ac-ELVFFAL and (B) Ac-pSLVFFAL nanotubes. .	26
Figure 2-13 Width measurements from TEM images of A) Ac-ELVFFAL and B) Ac-pSLVFFAL nanotube assemblies.	26
Figure 2-14 Circular dichroism of (K16pS)(E22L) (red) and (K16E)(E22L) assembled in 40% MeCN/H ₂ O with TEAA, pH7.	27

Figure 2-15 FT-IR spectra of (K16pS)(E22L) (red) and (K16E)(E22L) (black) assembled in 40% MeCN/H ₂ O with TEAA, pH7.....	27
Figure 2-16 X-ray powder diffraction of (K16E)(E22L) assembled in 40% MeCN/H ₂ O with TEAA.	28
Figure 2-17 X-ray powder diffraction of (K16pS)(E22L) assembled in 40% MeCN/H ₂ O with TEAA.	29
Figure 2-18 TEM micrographs of mature Ac-pYLVFFAL-NH ₂ nanotubes formed 40%MeCN/TEAA and resuspend in water.....	30
Figure 2-19 TEM images of A) matured Ac-pYLVFFAL-NH ₂ nanotubes incubated under 4 °C and B) C) D) incubated under 75 °C for 4 hours and then cool back to RT.....	31
Figure 2-20 TEM micrographs of gold nanoparticles binding with Ac-KLVFFAL nanotubes with different experimental methods.....	32
Figure 2-21 Gold nanoparticle binding to (E22L) and (K16pY) (E22L) peptide nanotubes visualized by TEM without stain.....	33
Figure 2-22 (A-F) Transmission electron microscopy micrographs of salt-induced bundling of (E22L) (top) and (K16pY)(E22L) (bottom) nanotubes.....	34
Figure 2-23 (A-F) Transmission electron microscopy micrographs of salt-induced bundling of (K16E) (E22L) (top) and (K16pS)(E22L) (bottom) nanotubes.....	35
Figure 2-24 EFM maps locally charged domains on the sample surface.	36
Figure 2-25 The standard sample (left) and its magnified view (right).....	36
Figure 2-26 Topography (left) and EFM amplitude (middle) and EFM phase (right) signals of the standard sample.....	37
Figure 2-27 Atomic and electrostatic force micrographs of (A) (E22L) and (B) (K16pY)(E22L) nanotube assemblies.....	38
Figure 2-28 Topography (left) and EFM amplitude (right) micrographs of dried salt solutions of (A) NH ₄ Cl ₂ and (B) Na ₂ HPO ₄ , with a DC bias of +1 V..	39
Figure 2-29 3D electrostatic force micrographs of dried salt solutions of (A) NH ₄ Cl ₂ and (B) Na ₂ HPO ₄ with a DC bias of +1 V. In the EFM amplitude micrographs.....	39
Figure 2-30 Model of Ac-KLVFFAL and Ac-pYLVFFAL nanotubes.....	40
Figure 2-31 UV-Vis absorbance comparison of 16 μM CR (black), 16 μM CR + 160 μM (K16pY) (E22L) peptide nanotubes (red).....	41
Figure 2-32 Florescence spectra of 250 μM ThT (black), 250 μM ThT μM CR + 500 μM (K16pY) (E22L) peptide nanotubes (red).....	41

Figure 2-33 (A) TEM image of 500 μM (K16pY)(E22L) nanotube assemblies in the presence of 4.6 μM histone H1–Alexa 488 conjugate. (B–D) Single slices of the two-photon fluorescence image excited at 780 nm of 4.6 μM Alexa 488-labeled calf thymus histone H1 alone (B), in the presence of 500 μM E22L nanotube assemblies (C), and in the presence of 500 μM (K16pY)(E22L) nanotube assemblies (D).....	42
Figure 2-34 Atomic and electrostatic force microscopy images of (K16pY) (E22L) nanotube assemblies with surfaces coated by the Histone H1 protein.	43
Figure 2-35 Single slices of confocal fluorescence image of 4.6 μM Alexa 488-labeled calf thymus histone H1 in the presence of 500 μM (A) Ac-pYLVFFAL nanotubes, (B) Ac-pYLVFFAL nanotubes, (D) Ac-pSLVFFALnanotubes..	43
Figure 2-36 Typical ITC titration curve for the addition of Histone H1 to (E22L) nanotube solutions.....	45
Figure 2-37 Typical ITC titration for addition of Histone H1 to (K16pY) (E22L) nanotube solutions.....	46
Figure 2-38 Fluorescence polarization saturation data for Histone H1-Alexa 488 conjugate and (K16pY) (E22L) nanotubes	47
Chapter 3	
Figure 3-1 Model of asymmetric peptide membranes.....	61
Figure 3-2 Structural characterization for Ac-pYLVFFAK.....	62
Figure 3-3 Circular Dichroism of matured Ac-KLVFFAL (black) and Ac-pYLVFFAL (red) nanotubes. The two matured nanotubes assemblies were pelleted and suspended together in 40% MeCN/H ₂ O and monitored ellipticity at 1min, 5mins, 20 mins, 30 mins, 4hrs and 24 hrs.	63
Figure 3-4 Circular Dichroism of Ac-KLVFFAL assembled in 40% MeCN/H ₂ O with TFA (blue), Ac-pYLVFFAL in 40% MeCN/H ₂ O with TEAA (red) and coassemblies in 40% MeCN/H ₂ O (black) at 4°C.....	64
Figure 3-5 FT-IR spectra of Ac-KLVFFAL assembled in 40% MeCN/H ₂ O with TFA (blue), Ac-pYLVFFAL in 40% MeCN/H ₂ O with TEAA (red) and coassemblies in 40% MeCN/H ₂ O (black) at 4°C.	65
Figure 3-6 X-ray powder diffraction of coassemblies of Ac-KLVFFAL and Ac-pYLVFFAL peptides in 40% MeCN/H ₂ O at 4°C, showing reflections at d-spacings of 4.7 Å and 10.6 Å.	65
Figure 3-7 Atomic force microscopy height measurements of coassembled Ac-KLVFFAL and Ac-pYLVFFAL peptides as nanotubes in 40% MeCN/H ₂ O at 4°C.....	66

Figure 3-8 CD melting profiles for Ac-KLVFFAL peptide nanotubes formed in 40% MeCN/H ₂ O at 4 °C.....	67
Figure 3-9 CD melting profiles for Ac-pYL ¹⁶ VFFAL peptide nanotubes formed in 40% MeCN/H ₂ O at 4 °C and resuspended in 60% (black), 70% (red) and 80% (blue) MeCN/H ₂ O respectively.....	68
Figure 3-10 Melting temperature of Ac-pYL ¹⁶ VFFAL in 60%, 70% and 90% MeCN/H ₂ O plot vs hydrophobicity of the solvent.....	69
Figure 3-11 Melting temperature of Ac-pYL ¹⁶ VFFAL in 60%, 70% and 90% MeCN/H ₂ O plot vs dielectric constant of the solvent.....	69
Figure 3-12 CD melting profiles for Ac-KLVFFAL and Ac-pYL ¹⁶ VFFAL coassemblies formed in 40% MeCN/H ₂ O at 4 °C and resuspended in 90% MeCN/H ₂ O.....	70
Figure 3-13 Transmission electron microscopy micrographs of salt-induced bundling of (E22L) (top), (K16pY)(E22L) (middle) and mixed peptides (bottom) nanotubes.....	72
Figure 3-14 Topography (left) EFM amplitude (middle) and EFM phase micrographs (right) of Ac-KLVFFAL and Ac-pYL ¹⁶ VFFAL peptides co-assemblies in 40% MeCN/H ₂ O, DC bias +1 V.....	73
Figure 3-15 Topography (left) and EFM amplitude micrographs (right) of Ac-KLVFFAL and Ac-pYL ¹⁶ VFFAL peptides co-assemblies in 40% MeCN/H ₂ O over time.....	74
Figure 3-16 REDOR-NMR enrichment scheme for assessment of two models: homogeneous leaflets and heterogeneous leaflets.....	75
Figure 3-17 The ¹³ C{ ¹⁵ N}REDOR dephasing data points (blue) of co-assembled Ac-KLVFFAL and Ac-pYL ¹⁶ VFFAL, compared to ¹³ C{ ¹⁵ N}REDOR dephasing curve (black) of neat Ac-KL[¹⁵ N]VFF[¹³ C]AL.....	77
Figure 3-18 The ¹ - ¹³ C{ ¹⁵ N}REDOR dephasing fits to summation of 3-spin and 2-spin systems.....	78
Figure 3-19 The ³ - ¹³ C{ ¹⁵ N}REDOR dephasing fits to summation of 3-spin and 2-spin systems.....	79
Figure 3-20 Peptide leaflets analysis of Ac-KLVFFAL and Ac-pYL ¹⁶ VFFAL co-assemblies.....	80
Figure 3-21 Peptide domains analysis of Ac-KLVFFAL and Ac-pYL ¹⁶ VFFAL co-assemblies.....	81
Figure 3-22 TEM micrographs of domain observed on single tubes in the co-assemblies shown by the red arrow.....	82

Figure 3-23 Circular Dichroism on day1 (A), 4 (B), 7 (C) and 11 (D) of Ac-KLVFFAL nanotubes as seeds for Ac-KLVFFAL monomers (black), Ac-pYLFFAL nanotubes as seeds for Ac-KLVFFAL monomers (red), Ac-KLVFFAL and Ac-pYLFFAL coassembled into nanotubes as seeds for Ac-KLVFFAL monomers (blue).	83
Figure 3-24 Circular Dichroism on day1 (A), 4 (B), 7 (C) and 11 (D) of Ac-KLVFFAL nanotubes as seeds for Ac-pYLFFAL monomers (black), Ac-pYLFFAL nanotubes as seeds for Ac-pYLFFAL monomers (red), Ac-KLVFFAL and Ac-pYLFFAL coassembled into nanotubes as seeds for Ac-pYLFFAL monomers (blue).	84
Figure 3-25 TEM micrographs of (A) Ac-KLVFFAL nanotubes, (B) Ac-pYLFFAL nanotubes, (C) Ac-KLVFFAL and Ac-pYLFFAL nanotubes applied on a same grid sequentially..	85
Figure 3-26 TEM micrographs of (A) Ac-KLVFFAL nanotubes, (B) Ac-pYLFFAL nanotubes, (C) Ac-KLVFFAL and Ac-pYLFFAL nanotubes applied on a same grid sequentially..	86
Figure 3-27 TEM micrographs of (A) Ac-KLVFFAL nanotubes seed, (B) Ac-pYLFFAL nanotubes seed (C) Ac-KLVFFAL nanotubes seed Ac-KLVFFAL monomer, (D) Ac-pYLFFAL nanotubes seed Ac-pYLFFAL monomer, (E) Ac-KLVFFAL nanotubes seed Ac-pYLFFAL monomer, (F) Ac-pYLFFAL nanotubes seed Ac-KLVFFAL monomer..	88
Figure 3-28 TEM micrograph of Ac-KLVFFAL nanotubes seed Ac-pYLFFAL monomer + negatively-charged AuNPs. Peptide vs AuNPs concentration ratio is 1:12.	89
Figure 3-29 Concept illustration of cross-seeding mechanism.....	90
Figure 3-30 TEM micrograph of Ac-KLVFFAL peptides seeded with co-assembled peptide nanotubes.....	91
Figure 3-31 TEM micrograph of Ac-pYLFFAL peptides seeded with co-assembled peptide nanotubes.....	92
Figure 3-32 Circular Dichroism on day1 (A), 6 (B), 18 (C), 30 (D) and 45 (E) of Ac-KLVFFAL nanotubes as seeds for Ac-KLVFFAL and Ac-pYLFFAL mixed monomers (black), Ac-pYLFFAL nanotubes as seeds for Ac-KLVFFAL and Ac-pYLFFAL mixed monomers (red), Ac-KLVFFAL and Ac-pYLFFAL coassembled into nanotubes as seeds for Ac-KLVFFAL and Ac-pYLFFAL mixed monomers (blue),.	94
Figure 3-33 Circular Dichroism of (A) Ac-KLVFFAL and Ac-pYLFFAL mixed monomers, (B) Ac-KLVFFAL nanotubes as seeds for Ac-KLVFFAL and Ac-pYLFFAL mixed monomers, (C) Ac-pYLFFAL nanotubes as seeds for Ac-KLVFFAL and Ac-pYLFFAL mixed monomers, (D)Ac-KLVFFAL and Ac-pYLFFAL coassembled into nanotubes as	

seeds for Ac-KLVFFAL and Ac-pYLVFFAL mixed monomers Ac-KLVFFAL nanotubes as seeds for Ac-KLVFFAL and Ac-pYLVFFAL mixed monomers..	96
Figure 3-34 TEM micrograph for (A) Ac-KLVFFAL nanotubes as seed for mixed Ac-KLVFFAL and Ac-pYLVFFAL peptide monomers, (B) Ac-pYLVFFAL nanotubes as seed mixed Ac-KLVFFAL and Ac-pYLVFFAL peptide monomers, (C) Ac-KLVFFAL and Ac-pYLVFFAL mix peptides coassembled as nanotubes as seeds for Ac-pYLVFFAL peptide monomers..	97
Figure 3-35 TEM micrograph of (A) Ac-KLVFFAL in 40% MeCN/H ₂ O with TFA, (B) Ac-ELVFFAL in 40% MeCN/H ₂ O with TEAA, (C) mixed Ac-KLVFFAL and Ac-ELVFFAL assembled as nanotubes in 40% MeCN/H ₂ O.	98
Figure 3-36 Circular Dichroism of Ac-KLVFFAL, Ac-ELVFFAL and coassembled Ac-KLVFFAL and Ac-ELVFFAL as nanotubes in 40% MeCN/H ₂ O.	99
Figure 3-37 CD melting profiles for Ac-ELVFFAL peptide nanotubes formed in 40% MeCN/H ₂ O at 4 °C.	99
Figure 3-38 CD melting profiles for mixed Ac-KLVFFAL and Ac-ELVFFAL peptide nanotubes formed in 40% MeCN/H ₂ O at 4 °C and resuspended in 70% MeCN/H ₂ O.	100
Figure 3-39 Topography (left) EFM amplitude (middle) and EFM phase micrographs (right) of Ac-KLVFFAL and Ac-ELVFFAL peptides co-assemblies in 40% MeCN/H ₂ O.	100
Figure 3-40 Circular Dichroism of Ac-KLVFFAV and Ac-pYLVFFAL mature nanotubes pelleted and resuspended in 40% MeCN/H ₂ O.	101
Figure 3-41 Circular Dichroism of co-assembled Ac-KLVFFAV and Ac-pYLVFFAL peptides 1:1 ratio in 40% MeCN/H ₂ O.	102
Figure 3-42 TEM micrograph of (A) Ac-KLVFFAV nanotubes in 40% MeCN/H ₂ O	103
Figure 3-43 CD melting profiles for Ac-pYLVFFAL nanotubes in 40% MeCN/H ₂ O.	107
Figure 3-44 CD melting profiles for co-assembled Ac-KLVFFAL and Ac-pYLVFFAL nanotubes in 40% MeCN/H ₂ O.	108
Figure 3-45 CD melting profiles for co-assembled Ac-KLVFFAL and Ac-pYLVFFAL nanotubes formed in 40% MeCN/H ₂ O and resuspended in 70% and 80% MeCN/H ₂ O.	109
Figure 3-46 HPLC trace of Ac-KLVFF[1- ¹³ C]AL-NH ₂ stock solution and the Ac-pYL[¹⁵ N]VFFA[3- ¹³ C]L-NH ₂ stock solution in HFIP.	110
Figure 3-47 Ac-KLVFFAL and Ac-pYLVFFAL mass peak intensity ratio measured by MALDI plot vs peptides ratio.	111
Figure 3-48 NMR spectra of [1- ¹³ C]A (Ac-KLVFFAL) and [3- ¹³ C]A (Ac-pYLVFFAL).	112

Figure 3-49 Ideal $^{13}\text{C}\{^{15}\text{N}\}$ REDOR curves that vary the percent of ^{13}C near an ^{15}N from 25% to 100%..... 113

Figure 3-50 The $1^{-13}\text{C}\{^{15}\text{N}\}$ REDOR dephasing fits to 3-spin and 2-spin systems.. 114

Chapter 4

Figure 4-1 Surface charge models for Ac-KLVFFAL nanotubes, Ac-pYLFFAL nanotubes and mixed Ac-KLVFFAL and Ac-pYLFFAL coassembled as nanotubes ... 118

Figure 4-2 TEM micrographs of (A) Rho-KLVFFAL assemblies, (B) mixed Rho-KLVFFAL and Ac-pYLFFAL in 1:250 ratio coassembled as nanotubes, (C) mixed Rho-KLVFFAL and Ac-pYLFFAL in 1:250 ratio coassembled as nanotubes (D) : mixed Rho-KLVFFAL, Ac-KLVFFAL and Ac-pYLFFAL in 1:250:250 ratio coassembled as nanotubes. 119

Figure 4-3 Single slices of confocal fluorescence images of (A) mixed Rho-KLVFFAL and Ac-pYLFFAL in 1:250 ratio coassembled as nanotubes, (B) mixed Rho-KLVFFAL and Ac-pYLFFAL in 1:250 ratio coassembled as nanotubes (C) : mixed Rho-KLVFFAL, Ac-KLVFFAL and Ac-pYLFFAL in 1:250:250 ratio coassembled as nanotubes. 119

Figure 4-4 Fluorescence spectra for Rho labeled peptides assemblies.. 121

Figure 4-5 TEM micrographs of (A) Dried and flattened Ac-KLVFFAL nanotubes (bar=100 nm) bound with negatively charged AuNPs and (B) cross-sectioned, epoxy resin embedded assemblies oriented perpendicular to the tube long axis 122

Figure 4-6 Molecular structures of Congo Red (left) and Methylene blue (right). 123

Figure 4-7 (A) UV spectra of methylene blue with strong peaks at 292 and 661nm and a shoulder peak at 610nm; (B) Circular Dichroism of Ac-pYLFFAL nanotubes alone (black), Methylene Blue alone (red) and Methylene Blue in the presence of Ac-pYLFFAL nanotubes (blue). 123

Figure 4-8 Circular Dichroism of 0.05 mM 200 μL Methylene Blue with addition of 1, 2, 3, 4... 18, 19, 20 μL 2mM Ac-pYLFFAL peptides nanotubes. 124

Figure 4-9 Plot the ellipticity vs pY/MB ratio, the first to fourth refer to peaks at 291, 305, 654 and 675 nm respectively..... 124

Figure 4-10 TEM micrographs of (A) Ac-pYLFFAL in the presence of 1.1mM Methylene Blue, (B) Ac-pYLFFAL in the presence of 8.4mM Methylene Blue. 125

Figure 4-11 Cuvette flow LD of Ac-pYLFFAL nanotubes. Panels show (A) the nanotube amide transition and (B) 50 μM MB (red) with (blue) and without (black) 500 μM nanotubes. 126

Figure 4-12 Two-photon fluorescence imaging (Ex=780nm) of Rh110-A β (16-22) donor nanotubes (A) and bound Alexa555 acceptor (Em=565nm) (B)..... 127

Figure 4-13 Molecular structures of Acridine orange and Alexa 633 (top), absorption (dashed line) and emission spectra (solid line)of Acridine orange and Alexa 633 (bottom).	128
Figure 4-14 (A) UV spectra of Acridine orange 10 μ M in the absence (black) and presence (red) of 1mM Ac-pYLVFFAL peptide nanotubes. (B) Circular Dichroism of Acridine orange 10 μ M in the absence (black) and presence (red) of 1mM Ac-pYLVFFAL peptide nanotubes.	128
Figure 4-15 Single slices of confocal fluorescence image of (A) Alexa 633 in the presence of Ac-KLVFFAL nanotubes, (B) Alexa 633 in the presence of Ac-pYLVFFAL nanotubes, (C) Alexa 633 in the presence of mixed Ac-KLVFFAL and Ac-pYLVFFAL coassembled as nanotubes, (D) Acridine orange in the presence of Ac-KLVFFAL nanotubes, (E) Acridine orange in the presence of Ac-pYLVFFAL nanotubes, (F) Acridine orange in the presence of mixed Ac-KLVFFAL and Ac-pYLVFFAL coassembled as nanotubes.	129
Figure 4-16 Single slices of confocal fluorescence image (A) Alexa 633 in the presence of mixed Ac-KLVFFAL and Ac-pYLVFFAL coassembled as nanotubes, (B) Acridine orange in the presence of mixed Ac-KLVFFAL and Ac-pYLVFFAL coassembled as nanotubes, (C) overlay of image (A) and (B).	130
Figure 4-17 Single slices of confocal fluorescence image (A) overlay of image Alexa 633 and Acridine orange binding with the co-assemblies. (B) Zoom in on image.	130
Figure 4-18 Fluorescence spectra of peptide nanotubes with FRET pairs.	132
Figure 4-19 Conceptual figure of donor and acceptor binding on Ac-KLVFFAL (left), Ac-pYLVFFAL (middle) and mixed Ac-KLVFFAL and Ac-pYLVFFAL coassembled as nanotubes (right).	132
Figure 4-20 Molecular structure of Protoporphyrin IX (left) and methyl viologen (right).	134
Figure 4-21 Absorption spectra of 3.33 μ M PPIX and 0.4mM Methyl viologen in TEAA.	134
Figure 4-22 Fluorescence emission spectra of 3.33 μ M PPIX with emission at 624 and 688 nm (black) and 0.4mM Methyl viologen in TEAA (red). Excitation 397 nm.	135
Figure 4-23 Fluorescence emission spectras of PP IX, PP IX in the presence of Ac-KLVFFAL nanotubes, PP IX in the presence of Ac-pYLVFFAL nanotubes, PP IX in the presence of mixed Ac-KLVFFAL and Ac-pYLVFFAL coassembled as nanotubes.	136

Figure 4-24 Fluorescence spectras of Protoporphyrin IX with addition of varying concentration of methyl viologen.	138
Figure 4-25 Plots of Protoporphyrin IX fluorescence intensity I_0/I vs methyl viologen concentration. I_0 : in the absence of methyl viologen, I : in the presence of methyl viologen. (A) in the absence of peptide nanotubes, (B) in the presence of Ac-KLVFFAL nanotubes, (C) in the prescence of mixed Ac-KLVFFAL and Ac-pYLVFFAL coassembled as nanotubes..	140
Figure 4-26 Fluorescence spectras of Protoporphyrin IX with addition of varying concentration of methyl viologen	140
Figure 4-27 Plots of Protoporphyrin IX fluorescence intensity I_0/I vs methyl viologen concentration.....	141
Figure 4-28 Plots of Protoporphyrin IX fluorescence intensity I_0/I vs methyl viologen concentration.....	144
Figure 4-29 Electron transfer models between Protoporphyrin IX and Methyl viologen in the presence of Ac-KLVFFAL tubes (A) and in the presence of co-assembled Ac-KLVFFAL and Ac-pYLVFFAL peptides (B).	144
Figure 4-30 Fluorescence lifetime decay of Protoporphyrin IX, Protoporphyrin IX in the prescence of mixed Ac-KLVFFAL and Ac-pYLVFFAL coassembled as nanotubes, Protoporphyrin with the addition of methyl viologen, Protoporphyrin IX in the prescence of mixed Ac-KLVFFAL and Ac-pYLVFFAL coassembled as nanotubes with the addition of methyl viologen.	145
Figure 4-31 (A) UV spectra of Alexa 633 absorbance, (B) fluorecence spectra of Acridine orange emission.	148
Figure 4-32 Excitation spectra of Protoporphyrin IX.....	149
Chapter 5	
Figure 5-1 Structure of N-lauroyl-Ab(16-22) (top) and TEM, cryo-SEM (inset) (bottom) of 1.2 mm N-lauroyl-Ab(16-22) assembled in 40% acetonitrile/water with 0.1% trifluoroacetic acid for 1–2 weeks..	155
Figure 5-2 Powder and oriented electron diffraction of N-acyl-Ab(16-22) peptide assemblies.	155
Figure 5-3 Model of lauryl chain packing (red) within β -sheet laminates.....	156
Figure 5-4 Molecular structure of (A) C12-KLVFFAE, (B) C12:1 (cis-5)-KLVFFAE, (C) C12:1 (trans-5)-KLVFFAE, (D) C12:1 (cis-2)-KLVFFAE, (E) C12:1 (trans-2)-KLVFFAE and (F) C12:1 (11)-KLVFFAE.....	158

Figure 5-5 Family of structures within 19kJ/mol of lowest energy structure of macromodel conformational search using the MMFFs force field, for C12-KLVFFAE peptides.	159
Figure 5-6 Family of structures within 19kJ/mol of lowest energy structure of macromodel conformational search using the MMFFs force field, for C12:1 (cis-5)-KLVFFAE peptides.....	159
Figure 5-7 Family of structures within 19kJ/mol of lowest energy structure of macromodel conformational search using the MMFFs force field, for C12:1 (trans-5)-KLVFFAE peptides.....	160
Figure 5-8 Family of structures within 19kJ/mol of lowest energy structure of macromodel conformational search using the MMFFs force field, for C12:1 (cis-2)-KLVFFAE peptides.....	160
Figure 5-9 Family of structures within 19kJ/mol of lowest energy structure of macromodel conformational search using the MMFFs force field, for C12:1 (trans-2)-KLVFFAE peptides.....	160
Figure 5-10 Family of structures within 19kJ/mol of lowest energy structure of macromodel conformational search using the MMFFs force field, for C12:1 (11)-KLVFFAE peptides.....	161
Figure 5-11 Circular dichroism of 1mM C2-KLVFFAE (black), C12-KLVFFAE (red) and C12:1 (cis-5)-KLVFFAE (blue) assemblies in 40% MeCN/H ₂ O, 0.1% TFA, pH2.....	162
Figure 5-12 TEM micrographs of (A) C2-KLVFFAE, (B) C12-KLVFFAE and (C) C12:1 (cis-5)-KLVFFAE self-assembled as homogeneous nanotubes in 40%MeCN/H ₂ O, 0.1% TFA, pH2.....	162
Figure 5-13 Nanotube widths distribution of A) C2-KLVFFAE, B) C12-KLVFFAE and C) C12:1(cis-5)-KLVFFAE.....	163
Figure 5-14 Powder X-ray diffraction of C12:1 (cis-5)-KLVFFAE showing reflections at d-spacings of 4.7 Å and 10.6 Å.....	164
Figure 5-15 Cartoon model of C2-KLVFFAE (top) and C12-KLVFFAE, C12:1(cis-5)-KLVFFAE (bottom) nanotubes.	165
Figure 5-16 Melting profiles for (A) C2-KLVFFAE with T _m 48.6 °C; (B) C12-KLVFFAE with T _m 55.5 °C; (C) C12:1(cis-5)-KLVFFAE T _m 51.4 °C.....	166
Figure 5-17 Circular Dichroism of C2-KLVFFAE, C12-KLVFFAE and C12:1(cis-5)-KLVFFAE assembled from monomer under 4, 37 or 55 °C respectively for a week	168

Figure 5-18 TEM micrographs of (A) C2-KLVFFAE assembled as particles (B) C12-KLVFFAE assembled as nanotubes and (C) C12:1(cis-5)-KLVFFAE assembled as nanotubes at 37 °C	168
Figure 5-19 TEM micrographs of (A) C2-KLVFFAE assembled as particles, (B) C12-KLVFFAE with no ordered assemblies and (C) C12:1(cis-5)-KLVFFAE with no ordered assemblies at 55 °C	169
Figure 5-20 TEM micrographs of mature nanotubes formed at 4°C and reincubated at 37 °C: (A) C2-KLVFFAE transformed from nanotubes to spherical particles, (B) C12-KLVFFAE and (C) C12:1(cis-5)-KLVFFAE stayed as nanotubes.....	169
Figure 5-21 Circular dichroism of C2-KLVIIAE (black), C2-KLVYYAE (red) and C2-KLVWWAE (blue). C12-KLVIIAE (magenta), C12-KLVYYAE (green) and C12-KLVWWAE (orange).	171
Figure 5-22 TEM micrographs of (A) C2-KLVIIAE; (B) C12-KLVIIAE; (C) Ac-KLVYYAE; (D) C12-KLVYYAE, (E)Ac-KLVWWAE; (F) and (G) C12-KLVWWAE. All lipid-peptide chimeras and peptides were incubated in 40% MeCN/H ₂ O with 0.1% TFA (pH2) at 4°C	174
Figure 5-23 Width measurements from TEM images of C12-KLVIIAE.....	174
Figure 5-24 Width measurements of particles from TEM images of C12-KLVWWAE..	175
Figure 5-25 Powder X-ray diffraction of C12-KLVIIAE	176
Figure 5-26 Powder X-ray diffraction of C12-KLVYYAE	176
Figure 5-27 Circular dichroism of C2-EAFFVLK (black) and C2-ELVFFAK (red), C12-EAFFVLK (blue) and C12-ELVFFAK (magenta). All lipid-peptide chimeras and peptides were incubated in 40% MeCN/H ₂ O with 0.1% TFA (pH2) at 4°C.....	177
Figure 5-28 TEM micrograph of C12-EAFFVLK self-assembled as fibers in 40% MeCN/H ₂ O, pH2.	178
Figure 5-29 TEM micrograph of C12-ELVFFAK self-assembled as fibers in 40% MeCN/H ₂ O, pH2.	178
Figure 5-30 Powder X-ray diffraction of C12-EAFFVLK.....	179
Figure 5-31 Powder X-ray diffraction of C12-ELVFFAK.....	179
Figure 5-32 Circular dichroism and TEM micrograph of C12-ELVFFAK in 40%MeCN/H ₂ O, pH7	180
Figure 5-33 Circular Dichroism of C2-KLVFFAE 0.65mM alone (black), C12-KLVFFAE 0.65mM alone (red) and mixed peptides coassemblies in 1:1 ratio, 0.65mM each (blue).	181

Figure 5-34 Circular Dichroism of C2-KLVFFAE 1.17mM alone (black), C12-KLVFFAE 0.13mM alone (red) and mixed peptides coassemblies in 9:1 ratio,.....	182
Figure 5-35 Circular Dichroism of C2-KLVFFAE 1.287mM alone (black), C12-KLVFFAE 0.013mM alone (red) and mixed peptides coassemblies in 99:1 ratio,.....	183
Figure 5-36 TEM micrographs of (A) C2-KLVFFAE assembled as homogeneous nanotubes; (B) C12-KLVFFAE assembled as homogeneous nanotubes; (C) nanotubes (D) nanotubes (E) ribbons (E) ribbons (G) fibrils that are observed in coassemblies of C2-KLVFFAE and C12-KLVFFAE in all 1:1, 9:1 and 99:1 coassemblies	184
Figure 5-37 Powder X-ray diffraction of mixed C2-KLVFFAE and C12-KLVFFAE coassemblies in 1:1 ratio.....	185
Figure 5-38 Circular Dichroism of C2-KLVFFAE alone (black), C12-KLVFFAE alone (red) C2-KLVFFAE seeded by 1% C12-KLVFFAE (blue) and 10% C12-KLVFFAE (magenta).	186
Figure 5-39 TEM micrographs of (A) unseeded C2-KLVFFAE; (B) C12-KLVFFAE seed parent; (C) ribbons and (D) nanotubes that are observed in C2-KLVFFAE seeded by 1% or 10% C12-KLVFFAE	187
Figure 5-40 Circular Dichroism of C2-KLVFFAE 0.23mM alone (black), C12:1 (cis-5)-KLVFFAE 0.23 mM alone (red) and C2-KLVFFAE peptide monomers seeded by 50% C12:1 (cis-5)-KLVFFAE (blue).....	188
Figure 5-41 TEM micrographs of (A) unseeded C2-KLVFFAE; (B) C12:1 (cis-5)-KLVFFAE seed parent; (C) ribbons and (D) fibrils that are observed in C2-KLVFFAE seeded by 50% C12:1 (cis-5)-KLVFFAE assemblie	189
Figure 5-42 Circular Dichroism of C2-KLVFFAE 0.23mM alone (black), C12-KLVIIAE 0.23 mM alone (red) and C2-KLVFFAE peptide monomers seeded by C12-KLVIIAE (blue).....	190
Figure 5-43 TEM micrographs of (A) unseeded C2-KLVFFAE; (B) C12-KLVIIAE seed prarent; (C) and (D) C2-KLVFFAE seeded C12-KLVIIAE in 1:1 ratio.....	191
Figure 5-44 Circular Dichroism of C2-KLVFFAE 0.23mM alone (black), C12-KLVYYAE 0.23 mM alone (red) and C2-KLVFFAE peptide monomers seeded by C12-KLVYYAE (blue).....	192
Figure 5-45 TEM micrographs of (A) unseeded C2-KLVFFAE; (B) C12-KLVYYAE seed parent; (C) C12-KLVYYAE seeded by 50% C2-KLVFFAE.....	192

Figure 5-46 Circular Dichroism of C2-KLVFFAE 0.23mM alone (black), C12-EAFFVLK 0.23 mM alone (red) and C2-KLVFFAE peptide monomers seeded by C12- EAFFVLK (blue)..... 193

Figure 5-47 TEM micrographs of (A) C2-KLVFFAE; (B) C12-EAFFVLK; (C) C12-EAFFVLK seeded by 50% C2-KLVFFAE 193

Figure 5-48 Circular Dichroism of C2-KLVFFAE 0.23mM alone (black), C12-ELVFFAK 0.23 mM alone (red) and C2-KLVFFAE peptide monomers seeded by C12-ELVFFAK (blue)..... 194

Figure 5-49 TEM micrographs of (A) unseeded C2-KLVFFAE; (B) C12-ELVFFAK seed parent; (C) C12-ELVFFAK seeded by 50% C2-KLVFFAE 194

List of Tables

Table 3-1 Melting temperature of Ac-pYLVFFAL at different solvent conditions.	70
Table 3-2 Summary of melting temperature of Ac-KLVFFAL, Ac-pYLVFFAL and co-assemblies at different solvents conditions.....	71
Table 4-1 Lifetime measurements and electron transfer rate.....	145
Table 5-1 Summary of morphologies observed by TEM in seeding experiments. All assemblies were incubated in 40% MeCN/H ₂ O, pH2. C2-KLVFFAE monomers were seeded by the following peptides in 1:1 concentration ratio. C2-KLVFFAE self-assembles into homogeneous nanotubes with ~48nm diameter.....	195

Chapter 1 Exploiting Biomimetic Strategies to Expand the Horizons of Self-assembly

From Supramolecular Chemistry to System Chemistry

Molecular self-assembly¹ is defined as the spontaneous arrangement of molecules into highly-ordered, functional supramolecular architectures from single components of a system with defined environmental conditions. The study of supramolecular self-assembly is crucial to understand many biological processes: individual strands of DNA form double helices; lipid bilayers form spontaneously via self assembly; proteins fold and assemble into tertiary and quaternary structures. As a consequence, biological systems are often the inspiration for supramolecular research in designing functional objects. Self-assembly as a strategy for fabricating functional objects has the advantage of being flexible and adaptable to change. The past couple of decades have experienced great growth in supramolecular self-assembly²⁻⁴ with the continuous goal that chemists can control non-covalent interactions to craft the size, shape and structure of nanoscale objects with the same precision achieved by synthetic organic chemistry. Intermolecular non-covalent interactions^{1,5} such as electrostatic interactions, van der Waals forces⁶⁻⁸, hydrophobic effects^{9,10}, pi-pi interactions¹¹⁻¹⁴ and hydrogen bonding¹⁵⁻²⁰ act like the joints of Lego pieces to direct the monomeric building blocks to self-assemble into higher order supramolecular structures. Through the appropriate design of molecular composition and structural features, these interactions can be manipulated for well-defined patterns and specific functionalities.

Currently more researchers are looking into complex mixtures of interacting molecules, thanks to the rapid growth of modern analytical techniques. Inspired by systems biology²¹, which addresses how the function of a biological system is directed by the interactions between various biomolecular components, systems chemistry²² aims to control variables in chemical networks simultaneously and answer questions, including 1) how collections of different molecules self-assemble into complex structures, 2) how secondary interactions between molecules and competitions for molecular building blocks lead to complex behaviors, and 3) how these give rise to emergent properties--- properties a complex system exhibits that can't be predicted by considering its subcomponents in isolation.

Looking ahead, combining supramolecular chemistry and systems chemistry can make an impact on a number of areas. Self-assembly of complex chemical systems offers a very promising route for making nano- and microscale functional components. Model systems that can form feedback loops and have the capability of self-repair may contribute to an improved understanding of biological networks as well as ways to manipulate them. Systems chemistry of a multicomponent self-assembly system could also be an approach for unraveling the origin of life.

Designing Asymmetry in Nonbiological Self-assembly Systems

When attacking complex problems in the field of self-assembly, biology generously offers a variety of strategies. The cell exists as a result of processes that generate multicomponent, functional structures by self-assembly. Incorporating these biomimetic strategies into systems chemistry expands the horizons of self-assembly beyond static systems into dynamic self-assembly. Compared with biological self-assembly, there is a vital but still unanswered question in non-biological self-assembly: how can asymmetry be achieved in self-assembly systems? Typically the ordered aggregation of identical components drives the formation of structurally defined crystals, usually with high symmetries. However, to build functional materials, especially electrically or optically functional materials, asymmetrical elements must be incorporated in the self-assembly design.

When considering self-assembly of biological systems, a good first example is the phospholipid membrane. Biological phospholipid membranes consist of a bilayer of lipid molecules that are composed of a hydrophilic head and two hydrophobic hydrocarbon tails. When introduced into an aqueous environment, these amphiphilic molecules aggregate spontaneously into two symmetric mono-molecular layers held together by weak non-covalent hydrophobic forces. Then, introducing degrees of asymmetry into what is essentially a symmetrical structure provides for functionalities of the membrane that are far beyond its use as a cell barrier. For example, cells have thousands of different lipids and these lipids are distributed unevenly on the two leaflets of the lipid bilayer (Figure 1-1). Flip-flop of uncharged small lipids like cholesterol^{23,24} and diacylglycerol (DAG), the formation of lipid rafts composed of clusters of different lipids, and distinct membrane protein associations all build asymmetry. Lipid membranes use

these toolkits and energy to maintain asymmetry. The study of these biological strategies may suggest new and useful ideas for non-biological self-assembly systems.

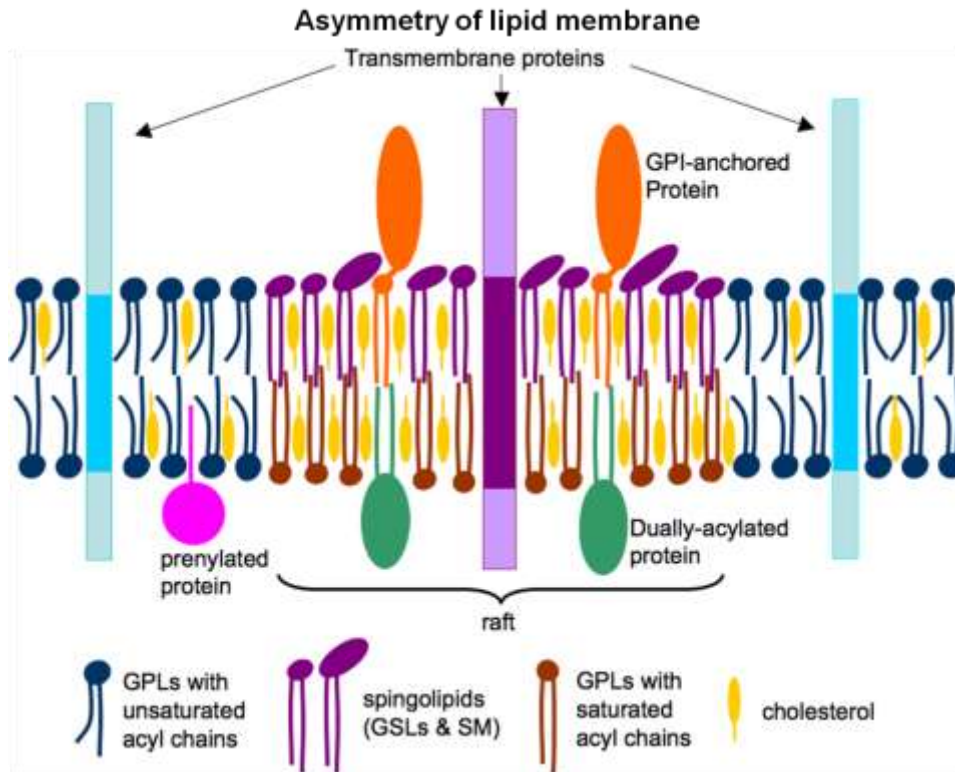


Figure 1-1 A simplified model of phospholipid membrane asymmetry. The phospholipids (blue and brown) and cholesterol (yellow) are distributed in both the leaflets, whereas sphingolipids (violet) are enriched in the outer leaflet of the bilayer. Saturated lipids (violet and brown) may form lipid rafts with those in non-raft domains containing singly or multiply unsaturated acyl chains (blue). Peripheral proteins including dually-acetylated (green), GPI-anchored (brown), renylated (green) and transmembrane (blue) proteins all contribute to lipid membrane asymmetry. Reprinted from Waheed, A. A.et, al. *Virus Res.* 2009 with permission from Elsevier.

Amyloid β Peptide Self-Assembles into Ordered Bilayer Architectures

When considering materials that could act as a biomimetic to the plasma membrane, peptides prove to be an excellent starting medium. Peptides produced in vitro have the advantages of user-designed flexibility sequence and, critically, the ability to associate spontaneously. Simple peptides in different environmental conditions have been used to construct numerous supramolecular architectures such as ribbons²⁵, fibrils²⁶⁻²⁸ and hollow tubes^{27,29,30} with nanoscale order, and rules governing peptide-peptide interactions are being actively investigated worldwide.

Peptide self-assembly was first examined not as used as the template for developing novel nanomaterials^{2,31}, but due to its central role in the formation of some neurodegenerative diseases³²⁻³⁴. In particular, it was discovered that the nucleating core of the Amyloid β peptide of the Alzheimer's disease, KLVFFAE and its E22L congener KLVFFAL can assemble into micrometer-long nanotubes under acidic conditions. A series of solid-state NMR and diffraction measurements revealed antiparallel one-residue out-of-register β -sheets with a sheet-sheet lamination distances of 9.9 Å. Further characterization highlights a (4.3 ± 1) nm wall thickness and a peptide bilayer leaflet interface. This bilayer contains maximally-extended peptides of about 2 nm, and end-to-end peptide termini stacking of the two amyloid sheets (Figure 1-2).

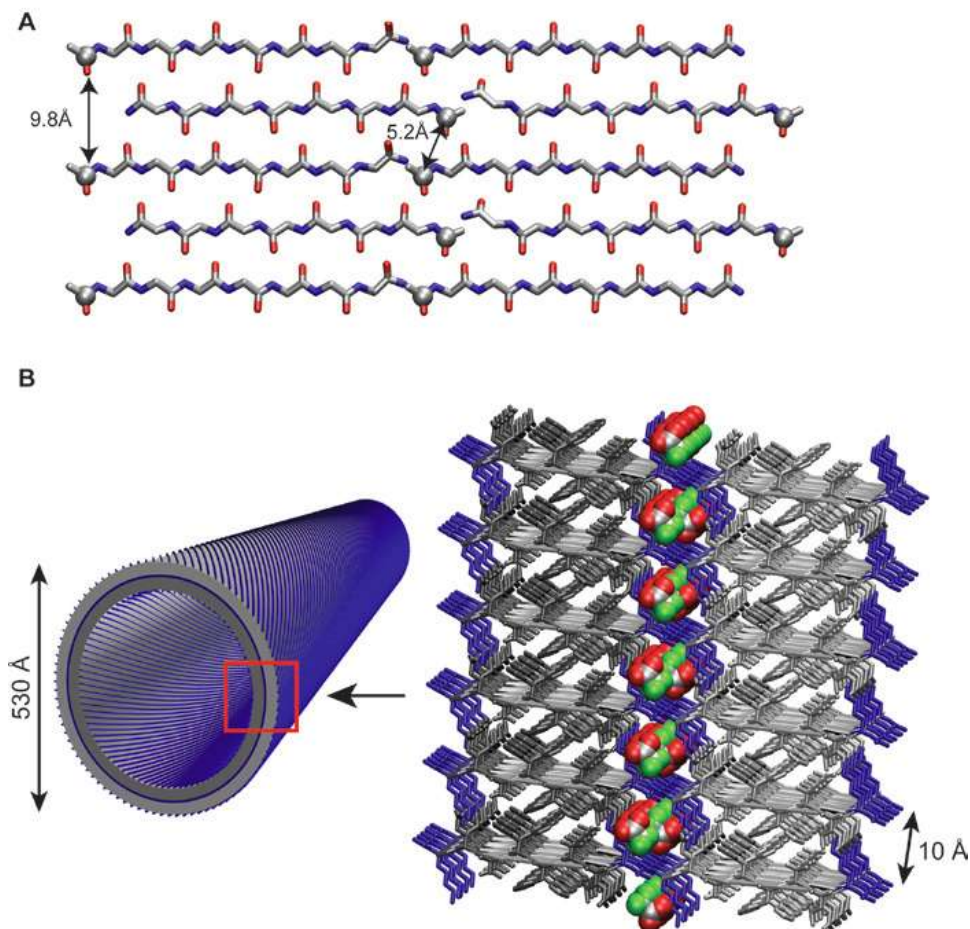


Figure 1-2 Model of the KLVFFAE peptide bilayer and trapped TFA. (A) Positions for the acetate carbonyl carbons are shown (gray spheres). The antiparallel out-of-register peptide configuration places the distance of the solvent-exposed acetates at 9.8 Å, the bilayer interface has a ^{13}CO - ^{13}CO distance of 5.2 Å to the bilayer interface. (B) Bilayer model of tube wall composed of anti-parallel out-of-register β -sheets. Lysine residues colored in blue and are located at the tube surface and the bilayer interface. TFA ions (space filling representation) are trapped within the bilayer interface³⁵.

The patterned surfaces created from the well-defined β -secondary protein structure displays dimensions that are remarkably similar to biological phospholipid membranes. However, unlike lipids, the driving force for assembly is more directional with a distinct local order while the peptide side chains can display more functionality than lipid tails. Using this peptide tube model, it is now possible to construct new patterned bilayer surfaces and functional scaffolds from these simple peptides for various applications.

Molecular Recognition Codes Direct Peptide Assembly

In order to construct patterned surfaces and functional scaffolds, it's critical to understand the rules and molecular recognition codes for peptide self-assembly. The term 'code' implies that a specific type of structure can be formed by design with diverse sets of molecules³⁶. Biology uses a spectacular set of codes to program structure and function: nucleic acids with specific base pair association rules and protein folding of primary peptide sequences with specific surface domains and hydrophobic pockets. In the self-propagating cross- β assemblies, where progress is being made elucidating peptide self-assembling pathways for disease, short self-templating cross- β peptides³⁷⁻³⁹ are being used to uncover the amino acid diversity and conformational flexibility that preferentially direct folding landscapes. For example, both computational models⁴⁰⁻⁴² and experimental studies⁴³⁻⁴⁵ support the importance of non-specific electrostatic interactions during the initial peptide aggregation and ordering stages. These interactions between charged amino acids, although nonspecific, underpin the dynamic code.

There are several examples of a predictable cross- β folding code that creates peptide assemblies, derived from the KLVFFAE peptide. This hepta-peptide, Ac-KLVFFAE-NH₂, at neutral pH where the E residue on the C-terminus is charged, forms complementary K-E salt-bridges to stabilize anti-parallel in-register β -sheet assemblies²⁷ (Figure 1-3A). At acidic pH, the salt bridge is weakened and complementary steric pairing between V-A dominate to give anti-parallel, out-of-register register β -sheet assemblies (Figure 1-3B).²⁷ Consistent with this proposal, E to leucine (L), Ac-KLVFFAL-NH₂, removes the salt bridge²⁷ and allows steric cross-strand pairing between the valine and the alanine to direct the out-of-register orientation independent of pH.²⁷ When the valine is substituted with nor-leucine (nL), the more sterically demanding t-butyl side chain in Ac-KLnLFFAE-NH₂ overwhelms the K/E salt bridge at neutral pH to give out-of-register nanotubes⁴⁶.

Hydrogen-bonded cross-strand pairing interactions offers directional control between strands, and the E22Q substitution mentioned above, Ac-KLVFFAQ-NH₂, assembles as parallel strands stabilized by H-bonded Q-tracks stretching along the sheet (Figure 1-3C)⁴⁷. Cross-sheet pairing interactions have been constructed with β -(cytosine-1-yl)-alanine to construct single-wall peptide nanotubes⁴⁸ (Figure 1-3D).

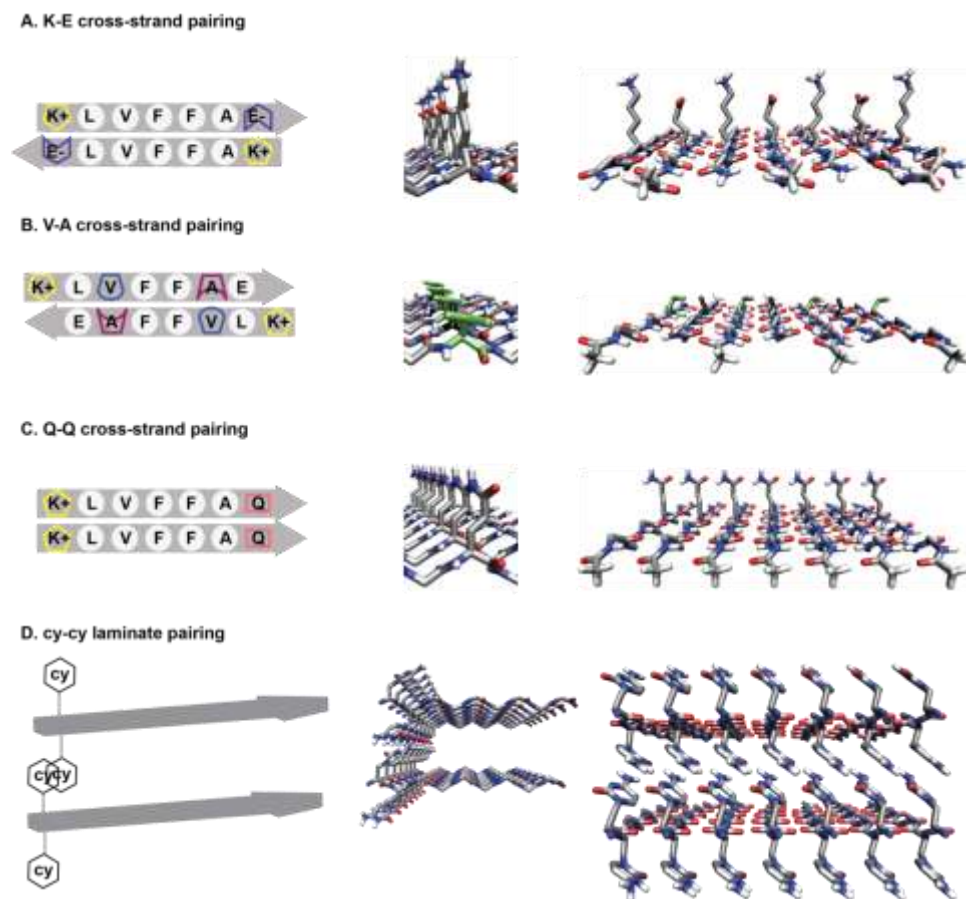


Figure 1-3 Amino acid complementary and self-pairings. (A) Salt bridge interactions between K-E. (B) Packing of bulky β -branched V against less bulky A. (C) Side-chain hydrogen bonding via Q as parallel in-register strands. (D) Cytosine-cytosine laminate pairing.

This growing tool kit for cross- β assemblies has been exploited for materials synthesis, including lipid/peptide⁴⁹, fluorophore/peptide⁵⁰, biotin/peptide⁵¹ chimeric materials, and the subtle information encoded in sequence space can now be used to access unique supramolecular assemblies. The knowledge of the assembly pathway can now be used to create the functional feedbacks for the progressive growth of higher supramolecular order.

Nucleation and Seeded Growth in Amyloid Self-Assembly

Prions and other amyloid-forming proteins devoid of nucleic acids are recognized as containing analog molecular information in the form of morphological diversity,^{38,52} and subject to mutation and amplification.⁵³ Prions form when the protein changes from its normal, soluble structure to an aggregated, amyloid-like structure rich in β -sheets^{54,55}. It's a highly ordered process that occurs via a nucleation-dependent pathway with the nucleation step being the rate-determining step.^{56,57} In vitro studies of prions formation have revealed crucial intermediates of structurally fluid oligomeric complexes in amyloid nucleus formation⁵⁸. Direct observation by fluorescence lifetime Imaging (FLIM)⁵⁹ and fluorescence correlation spectroscopy (FCS)⁶⁰ of amyloid peptide self-assembly also identified an initial globular phase, fluid particle-like aggregates and conclusively established that these intermediate disordered phases serve as nucleation centers for the transition to crystalline phases (Figure 1-4A). Other disordered oligomer assemblies and particle-like aggregates have been documented kinetically as on pathway⁶¹⁻⁶³. Propagation occurs when the peptide monomers are added to the ordered nuclei which serve as templates (Figure 1-4B). Furthermore, the discovery of kinetic intermediate of amyloid self-assembly suggests a progressive assembly pathway^{47,64} that is subject to mutation and propagation.

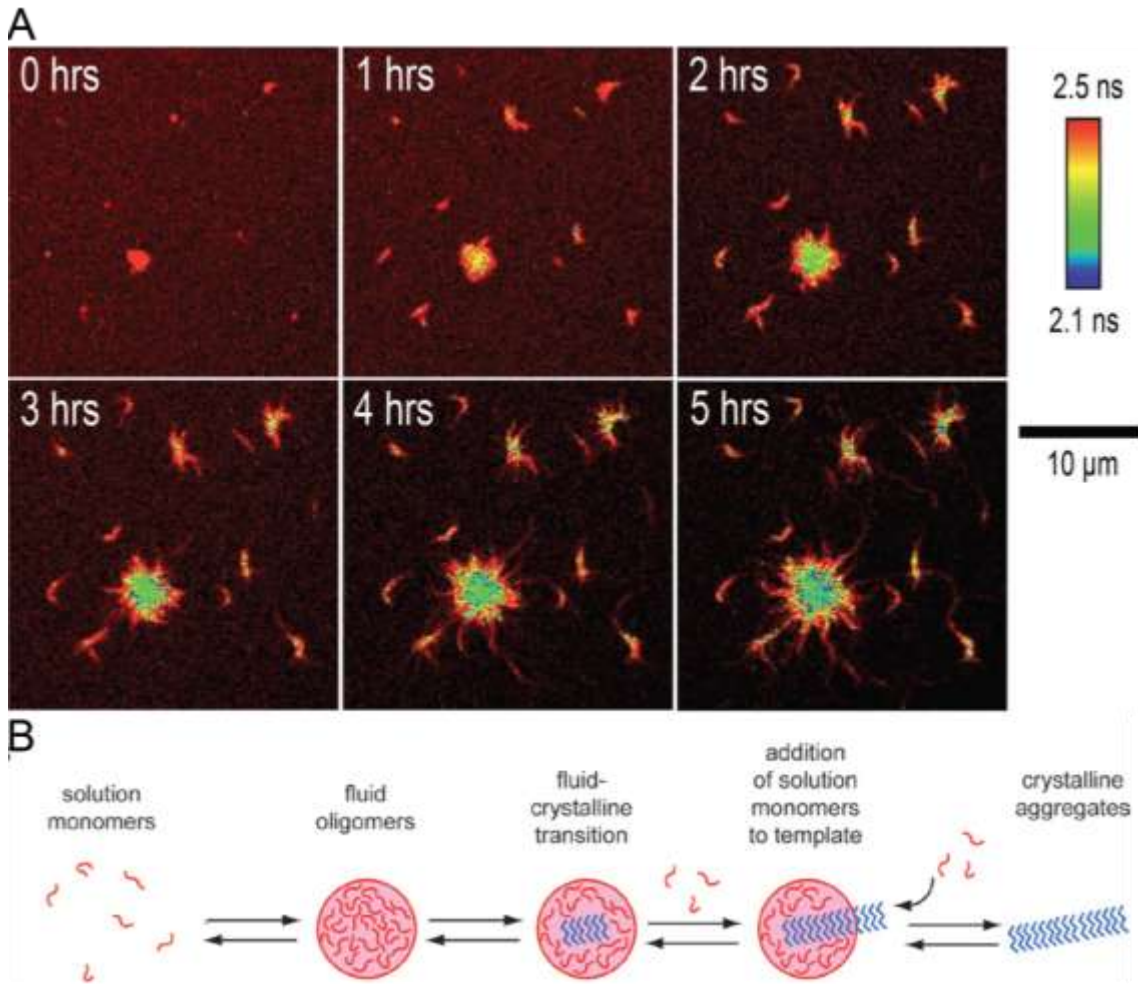


Figure 1-4 Nucleation mechanism of peptide self-assembly. (A) FLIM analysis of A β (16-22)/Rhodamine17-22 assembly and propagation of aggregate phases at the glass surface. Small aggregates adhered to the surface of the glass observed over time are seen to increase in size and serve as the epicentre of growing tubes. Adapted from Anthony, N. R. et, al. *Soft Matter* 2014 with permission from Royal Society of Chemistry. (B) Model of amyloid nucleation and propagation in which peptides collapse into a fluid oligomer that serves as amyloid nucleation sites. Propagation occurs by addition of solution monomers (red) onto the ordered β -sheet nuclei which serve as templates (blue).

It is widely recognized that in order to form an A β nuclei, a local supersaturation mechanism must occur.^{65,66} If seeds or a preformed nucleus are added to a kinetically supersaturated solution, immediate polymerization can be achieved.⁶⁷ Amyloid formation can be seeded *in vivo* and an ordered aggregate of infectious prion can act as a seed to induce interconversion from identical soluble protein molecules to the aggregated state, and thus lead to transmissible amyloidosis⁶⁸. Indeed, research has been done on

heterogeneous seeding events, and in spite of low sequence similarity, proteins can seed across the species barrier⁶⁹.

Emerging evidence suggests that protein molecules with the same amino acid sequence can still present structural heterogeneity that is observed in diseases. Antibody stained A β (1-40) and A β (1-42) reveal micro heterogeneity in the amyloid deposit distribution⁷⁰, demonstrated that both pure assembly and mixed assembly may occur within complex tissue environments. The relevance of pure versus mixed assembly can be illuminated by a case where homozygous carriers of an A β (1-42) A2V mutant are susceptible to familial Alzheimer's disease, while heterozygous carriers are unaffected⁷¹. Both A β (1-42) and A β (1-42) A2V have the capacity to form amyloid structures in vitro; however, equimolar peptide mixtures appear incapable of forming amyloid assemblies under the conditions studied⁷¹. The present data highlights the importance of studying both pure and mixed assembly for understanding amyloidogenesis.

An initial attempt in decoding the rules of specificity in seeding was performed by mixing two short peptides that are differed by a single methylene (Ac-KLVFFAL vs Ac-KLVFFAV)⁷². These peptides assemble into with nanotubes with different peptide arrangements and different diameters (38 nm vs 278 nm). These peptides do not mix in the assembly, but instead phase separate into each distinct assembly.⁷² This astonishing example demonstrated how subtle changes in peptide sequence can direct self-assembly nucleation and peptide behavior.

Engineering Cross- β Peptide Surfaces for New Functions

Surfaces formed from peptide-based patterns could be useful in molecular recognition events for biosensing or in recruitment of extrogenous molecules and even catalysts. For instance, biophysical characterization of cross- β peptide bilayer with 4 nm walls reveal lysine residues exposed on the surface of the tubes, as shown in Figure 1-5A. The leucine-lined hydrophobic groove has been shown to the amyloid histochemical dye Congo red (CR) between the cross- β sheets.⁷³ Electron diffraction and linear dichroism analyses place CR oriented parallel to the amyloid long axis and packed in both J- and H-aggregates along the laminate grooves as shown in Figure 6A,⁷³ illuminating the ability of the amyloid to organize molecules into extended arrays.

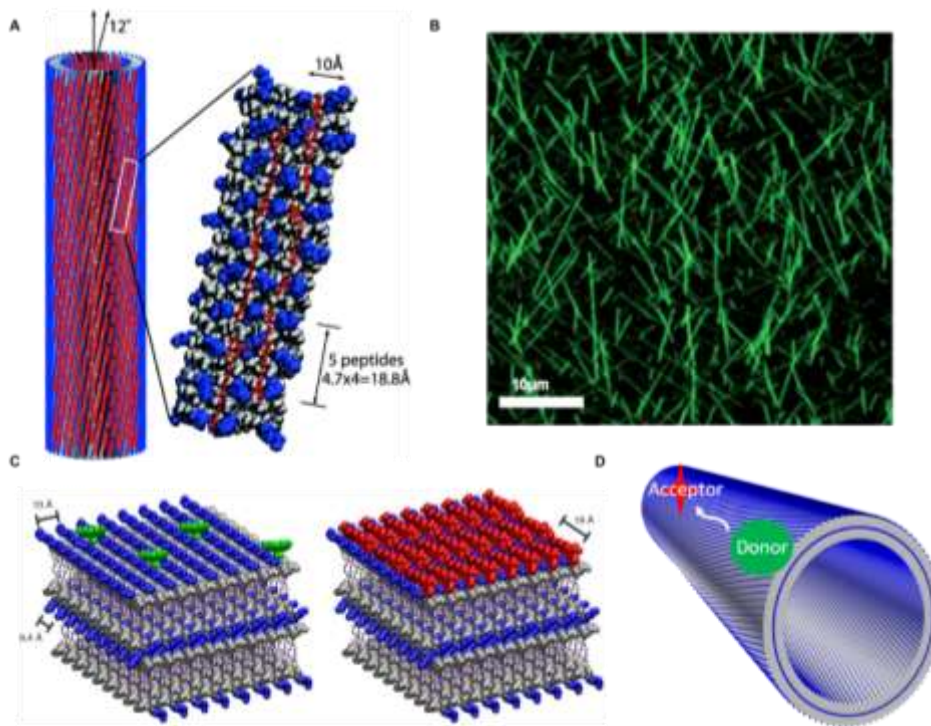


Figure 1-5 A) Model of bound to Ac-KLVFFAL-NH₂ nanotube surface with charged lysines (in blue) and hydrophobic leucines (in grey). Cross- β assemblies have 4.7Å in the H-bonding direction and 10Å in the β -sheet stacking direction, resulting in a ~1nm x 1nm lysine grid on the solvent exposed surface. B) Fluorescence imaging of Rh-LVFFAE-NH₂/Ac-KLVFFAE-NH₂ ratios at 1:75. C) Molecular models of Rh-LVFFAE-NH₂ and Alexa 555 binding with Ac-KLVFFAE-NH₂ tube surfaces (Adapted from Childers, W.S. et, al. *Curr. Opin. Chem. Biol* 2009 with permission from Elsevier). (D) Cartoon describing the observed FRET across the surface.

These extended surfaces have now been used to increase the functionality of the assemblies. For instance, the Rhodamine 110-containing probe peptide, Rh-LVFFAE-NH₂ allowed for the visualization of nanotube growth using fluorescence lifetime image microscopy (FLIM) (Figure 1-5B). Not only have these probes provided direct mechanistic insight into nanotube assembly,^{59,60,74} but also for the inter-conversion of physical and chemical energy. Based on the insights gained from CR binding, the fluorescent nanotubes were shown to readily bind the Alexa 555 dye (Figure 1-5C). Fluorescence resonance energy transfer (FRET) (Figure 1-5D) across the nanotube surfaces from Rhodamine and Alexa 555 demonstrates an early first step in functional light energy capture and transfer.⁵⁰ The surfaces can be further engineered with cofactors. Stoichiometric Zn(II) added to the extended cross- β segment Ac-HHQALVFFAE-NH₂ prior to assembly reduces the lag phase and propagates a morphological transition from fibers to ribbons and nanotubes.^{25,75} These peptides assemble as antiparallel β -strands with the HH-dyad bridging the β -sheets. Both Zn(II)

and Cu(II) alter assembly kinetics and morphology.⁷⁵ It may now be possible to extend such responsive networks synthetically, like a fluctuating metabolism, and use the network to select for new functional materials. Success in the creation of such dynamic networks will depend on an understanding of assembly energetics.

Peptide self-assembly has proven to be a rich field for the controlled synthesis of architectures with desired structural features and unique functions. The resulting nanostructures could be of great interest in many biomedical and biomaterial applications³¹, including tissue engineering, regenerative medicine, drug delivery, and light-harvesting applications. In the past, peptide self-assembly research has been inspired by nature's self-assembly of biopolymers. Although we are still a long way from duplicating the elaborate molecular assemblies, the intricate chemical strategies and the cooperative molecular networks that have emerged in living systems have provided lessons that propel us further. Surely we cannot assume that biology demonstrates all strategies for self assembly, but it offers a wonderful array of successful examples.

The nucleating core of the Alzheimer's disease peptide, KLVFFAE or A β (16-22), has been heavily studied and characterized using an array of biophysical techniques^{27,76-78}. In this dissertation, I will extend the self-assembly codes we learned from the A β (16-22) model system, systematically explore the strategies to engineer the peptide membrane surfaces, and employ novel biophysical techniques to characterize them. I will build from single components to multi-component systems that incorporate the asymmetry we see in biological self-assembly towards the creation of non-biological self-assembly networks for the purpose of constructing patterned nanotube surfaces and functional scaffolds.

References

- (1) Lehn, J.-M. *Supramolecular Chemistry, Concepts and Perspectives*; Wiley VCH, 1995.
- (2) Zhang, S. *Nat Biotech* **2003**, *21*, 1171.
- (3) Colfen, H.; Mann, S. *Angewandte Chemie-International Edition* **2003**, *42*, 2350.
- (4) Lehn, J. M. *Rep. Prog. Phys.* **2004**, *67*, 249.
- (5) Atwood J L, D. J. E. D., MacNicol D D, Vögtle F, Lehn J-M *Comprehensive Supramolecular Chemistry* Pergamon: Oxford, 1996.
- (6) Vericat, C.; Vela, M. E.; Benitez, G.; Carro, P.; Salvarezza, R. C. *Chem. Soc. Rev.* **2010**, *39*, 1805.
- (7) Jiang, J.; Lima, O. V.; Pei, Y.; Zeng, X. C.; Tan, L.; Forsythe, E. *J. Am. Chem. Soc.* **2009**, *131*, 900.
- (8) Dhotel, A.; Delbreilh, L.; Youssef, B.; Jiang, J.; Coquerel, G.; Saiter, J.-M.; Tan, L. *J. Therm. Anal. Calorim.* **2013**, *112*, 301.
- (9) Van Oss, C. J.; Good, R. J.; Chaudhury, M. K. *J. Colloid Interface Sci.* **1986**, *111*, 378.
- (10) Silverstein, T. P. *J. Chem. Educ.* **1998**, *75*, 116.
- (11) Beaujuge, P. M.; Fréchet, J. M. J. *J. Am. Chem. Soc.* **2011**, *133*, 20009.
- (12) Jiang, J.; Lima, O. V.; Pei, Y.; Jiang, Z.; Chen, Z.; Yu, C.; Wang, J.; Zeng, X. C.; Forsythe, E.; Tan, L. *ACS Nano* **2010**, *4*, 3773.
- (13) Pluth, M. D.; Raymond, K. N. *Chem. Soc. Rev.* **2007**, *36*, 161.
- (14) Ferri, T.; Frasca, D.; Arias de Fuentes, O.; Santucci, R.; Frasconi, M. *Angew. Chem. Int. Ed.* **2011**, *50*, 7074.
- (15) Rose, G. D.; Fleming, P. J.; Banavar, J. R.; Maritan, A. *Proceedings of the National Academy of Sciences* **2006**, *103*, 16623.
- (16) Deng, R.; Liu, S.; Li, J.; Liao, Y.; Tao, J.; Zhu, J. *Adv. Mater.* **2012**, *24*, 1889.
- (17) Deechongkit, S.; Nguyen, H.; Powers, E. T.; Dawson, P. E.; Gruebele, M.; Kelly, J. W. *Nature* **2004**, *430*, 101.
- (18) Mignon, P.; Loverix, S.; Steyaert, J.; Geerlings, P. *Nucleic Acids Res.* **2005**, *33*, 1779.
- (19) Yakovchuk, P.; Protozanova, E.; Frank-Kamenetskii, M. D. *Nucleic Acids Res.* **2006**, *34*, 564.
- (20) Kool, E. T. *Annu. Rev. Biophys. Biomol. Struct.* **2001**, *30*, 1.
- (21) O'Malley, M. A.; Dupre, J. *Bioessays* **2005**, *27*, 1270.
- (22) Ludlow, R. F.; Otto, S. *Chem. Soc. Rev.* **2008**, *37*, 101.
- (23) Lange, Y.; Dolde, J.; Steck, T. L. *J. Biol. Chem.* **1981**, *256*, 5321.
- (24) López-Montero, I.; Rodriguez, N.; Cribier, S.; Pohl, A.; Vélez, M.; Devaux, P. F. *J. Biol. Chem.* **2005**, *280*, 25811.
- (25) Dong, J. J.; Shokes, J. E.; Scott, R. A.; Lynn, D. G. *J. Am. Chem. Soc.* **2006**, *128*, 3540.
- (26) López de la Paz, M.; Serrano, L. *Proc. Natl. Acad. Sci. U.S.A.* **2004**, *101*, 87.
- (27) Mehta, A. K.; Lu, K.; Childers, W. S.; Liang, Y.; Dublin, S. N.; Dong, J.; Snyder, J. P.; Pingali, S. V.; Thiyagarajan, P.; Lynn, D. G. *J. Am. Chem. Soc.* **2008**, *130*, 9829.
- (28) Lu, K.; Jacob, J.; Thiyagarajan, P.; Conticello, V. P.; Lynn, D. G. *J. Am. Chem. Soc.* **2003**, *125*, 6391.
- (29) Reches, M.; Gazit, E. *Science* **2003**, *300*, 625.

- (30) Santoso, S.; Hwang, W.; Hartman, H.; Zhang, S. *Nano Lett.* **2002**, *2*, 687.
- (31) Ulijn, R. V.; Smith, A. M. *Chem. Soc. Rev.* **2008**, *37*, 664.
- (32) Chromy, B. A.; Nowak, R. J.; Lambert, M. P.; Viola, K. L.; Chang, L.; Velasco, P. T.; Jones, B. W.; Fernandez, S. J.; Lacor, P. N.; Horowitz, P.; Finch, C. E.; Krafft, G. A.; Klein, W. L. *Biochemistry* **2003**, *42*, 12749.
- (33) Hamley, I. W. *Angewandte Chemie-International Edition* **2007**, *46*, 8128.
- (34) von Bergen, M.; Friedhoff, P.; Biernat, J.; Heberle, J.; Mandelkow, E. M.; Mandelkow, E. *Proc. Natl. Acad. Sci. U.S.A.* **2000**, *97*, 5129.
- (35) Childers, W. S.; Mehta, A. K.; Bui, T. Q.; Liang, Y.; Lynn, D. G. *Toward Intelligent Materials*, 2013.
- (36) Palmer, L. C.; Velichko, Y. S.; Olvera de la Cruz, M.; Stupp, S. I. *Supramolecular self-assembly codes for functional structures*, 2007; Vol. 365.
- (37) Goodwin, J. T. W., S.I.; Amin, S.; Armbrust, G.; Burrows, C.J.; Lynn, D.G. Available online: <http://chemistry.emory.edu/home/assets/alternativechem.pdf> 2014.
- (38) Goodwin, J. T.; Mehta, A. K.; Lynn, D. G. *Acc. Chem. Res.* **2012**, *45*, 2189.
- (39) Childers, W. S.; Anthony, N. R.; Mehta, A. K.; Berland, K. M.; Lynn, D. G. *Langmuir* **2012**, *28*, 6386.
- (40) Yun, S. J.; Urbanc, B.; Cruz, L.; Bitan, G.; Teplow, D. B.; Stanley, H. E. *Biophys. J.* **2007**, *92*, 4064.
- (41) Buell, Alexander K.; Hung, P.; Salvatella, X.; Welland, Mark E.; Dobson, Christopher M.; Knowles, Tuomas P. *Biophys. J.* **2013**, *104*, 1116.
- (42) Tarus, B.; Straub, J. E.; Thirumalai, D. *J. Mol. Biol.* **2005**, *345*, 1141.
- (43) Konno, T. *Biochemistry* **2001**, *40*, 2148.
- (44) Raman, B.; Chatani, E.; Kihara, M.; Ban, T.; Sakai, M.; Hasegawa, K.; Naiki, H.; Rao, C. M.; Goto, Y. *Biochemistry* **2005**, *44*, 1288.
- (45) Shammas, S. L.; Knowles, T. P. J.; Baldwin, A. J.; MacPhee, C. E.; Welland, M. E.; Dobson, C. M.; Devlin, G. L. *Biophys. J.* **2011**, *100*, 2783.
- (46) Liang, Y.; Pingali, S. V.; Jogalekar, A. S.; Snyder, J. P.; Thiyagarajan, P.; Lynn, D. G. *Biochemistry* **2008**, *47*, 10018.
- (47) Liang, C.; Ni, R.; Smith, J. E.; Childers, W. S.; Mehta, A. K.; Lynn, D. G. *J. Am. Chem. Soc.* **2014**, *136*, 15146.
- (48) Liu, P.; Ni, R.; Mehta, A. K.; Childers, W. S.; Lakdawala, A.; Pingali, S. V.; Thiyagarajan, P.; Lynn, D. G. *J. Am. Chem. Soc.* **2008**, *130*, 16867.
- (49) Ni, R.; Childers, W. S.; Hardcastle, K. I.; Mehta, A. K.; Lynn, D. G. *Angewandte Chemie-International Edition* **2012**, *51*, 6635.
- (50) Liang, Y.; Guo, P.; Pingali, S. V.; Pabit, S.; Thiyagarajan, P.; Berland, K. M.; Lynn, D. G. *Chem. Commun.* **2008**, 6522.
- (51) Scarfi, S.; Gasparini, A.; Damonte, G.; Benatti, U. *Biochem. Biophys. Res. Commun.* **1997**, *236*, 323.
- (52) Prusiner, S. B. *Proceedings of the National Academy of Sciences* **1998**, *95*, 13363.
- (53) Li, J.; Browning, S.; Mahal, S. P.; Oelschlegel, A. M.; Weissmann, C. *Science* **2010**, *327*, 869.
- (54) Chien, P.; Weissman, J. S.; DePace, A. H. *Annu. Rev. Biochem* **2004**, *73*, 617.
- (55) Wickner, R. B.; Edskes, H. K.; Shewmaker, F.; Nakayashiki, T. *Nature reviews. Microbiology* **2007**, *5*, 611.
- (56) Xue, W.-F.; Homans, S. W.; Radford, S. E. *Proc. Natl. Acad. Sci. U.S.A.* **2008**, *105*, 8926.
- (57) Chiti, F.; Dobson, C. M. *Nat. Chem. Biol.* **2009**, *5*, 15.

- (58) Serio, T. R.; Cashikar, A. G.; Kowal, A. S.; Sawicki, G. J.; Moslehi, J. J.; Serpell, L.; Arnsdorf, M. F.; Lindquist, S. L. *Science* **2000**, *289*, 1317.
- (59) Anthony, N. R.; Mehta, A. K.; Lynn, D. G.; Berland, K. M. *Soft Matter* **2014**, *10*, 4162.
- (60) Liang, Y.; Lynn, D. G.; Berland, K. M. *J. Am. Chem. Soc.* **2010**, *132*, 6306.
- (61) Harper, J. D.; Lieber, C. M.; Lansbury, P. T., Jr. *Chem. Biol.*, *4*, 951.
- (62) Stine, W. B.; Dahlgren, K. N.; Krafft, G. A.; LaDu, M. J. *J. Biol. Chem.* **2003**, *278*, 11612.
- (63) Hellstrand, E.; Boland, B.; Walsh, D. M.; Linse, S. *ACS Chemical Neuroscience* **2010**, *1*, 13.
- (64) Smith, J. E.; Liang, C.; Tseng, M.; Li, N.; Li, S.; Mowles, A. K.; Mehta, A. K.; Lynn, D. G. *Isr. J. Chem.* **2015**, n/a.
- (65) Collins, S. R.; Douglass, A.; Vale, R. D.; Weissman, J. S. *PLoS Biol.* **2004**, *2*, 1582.
- (66) Jarrett, J. T.; Lansbury, P. T. *Cell* **1993**, *73*, 1055.
- (67) Harper, J. D.; Lansbury, P. T. *Annu. Rev. Biochem.* **1997**, *66*, 385.
- (68) Jarrett, J. T.; Lansbury, P. T., Jr. *Cell*, *73*, 1055.
- (69) Vishveshwara, N.; Liebman, S. W. *BMC Biol* **2009**, *7*, 26.
- (70) Walker, L. C.; Rosen, R. F.; Levine, H., III *Romanian Journal of Morphology and Embryology* **2008**, *49*, 5.
- (71) Di Fede, G.; Catania, M.; Morbin, M.; Rossi, G.; Suardi, S.; Mazzoleni, G.; Merlin, M.; Giovagnoli, A. R.; Prioni, S.; Erbetta, A.; Falcone, C.; Gobbi, M.; Colombo, L.; Bastone, A.; Beeg, M.; Manzoni, C.; Francescucci, B.; Spagnoli, A.; Cantù, L.; Del Favero, E.; Levy, E.; Salmona, M.; Tagliavini, F. *Science (New York, N.Y.)* **2009**, *323*, 1473.
- (72) Childers, S. W. T., Emory University, 2010.
- (73) Childers, W. S.; Mehta, A. K.; Lu, K.; Lynn, D. G. *J. Am. Chem. Soc.* **2009**, *131*, 10165.
- (74) Anthony, N. R.; Lynn, D. G.; Berland, K. *Biophys. J.* **2011**, *100*, 201.
- (75) Dong, J.; Canfield, J. M.; Mehta, A. K.; Shokes, J. E.; Tian, B.; Childers, W. S.; Simmons, J. A.; Mao, Z.; Scott, R. A.; Warncke, K.; Lynn, D. G. *Proc. Natl. Acad. Sci. U.S.A.* **2007**, *104*, 13313.
- (76) Childers, W. S.; Mehta, A. K.; Ni, R.; Taylor, J. V.; Lynn, D. G. *Angewandte Chemie-International Edition* **2010**, *49*, 4104.
- (77) Klimov, D. K.; Thirumalai, D. *Structure* **2003**, *11*, 295.
- (78) Petty, S. A.; Decatur, S. M. *J. Am. Chem. Soc.* **2005**, *127*, 13488.

Chapter 2 Construction of Patterned Phosphorylated Peptide Membranes

Introduction

Living cells contain a range of densely phosphorylated surfaces, including phospholipid membranes, ribonucleoproteins, and nucleic acid polymers. Hyperphosphorylated surfaces also accumulate in neurodegenerative diseases as neurofibrillar tangles of the microtubule-associated tau protein¹⁻³. Tauopathies, including Alzheimer's disease (AD) and Pick's disease, are characterized by the cytoplasmic accumulation of densely tau phosphorylated neurofibrillar tangles⁴. The recent identification of specific ribonucleoprotein colocalization with hyperphosphorylated tau aggregates implies co-aggregation or even cross-seeding events⁵ as etiologically significant in AD to RNA processing⁶.

The nucleating core of amyloid β peptide, A β (16–22), Ac-KLVFFAE-NH₂ and its congener, Ac-KLVFFAL-NH₂ (E22L), assemble as peptide bilayer nanotubes^{7,8} with diameters of 54 ± 3 nm⁷. The robust peptide bilayer membrane is morphologically similar to lipids but structurally quite distinct from the traditional lipid assemblies⁹. The peptides in each leaflet of the peptide bilayer are arrayed as β -sheets having antiparallel out-of-register strand arrangements, placing the N-terminal residues outside the H-bonded array⁷. The positively charged lysine side chains repeat every nanometer on each leaflet face as rows running the length of the tube⁸. This structure also places the lysine at high density with the leaflet interface. Considering the mostly seen phospholipids in cell membranes, placing phosphorylated residues at the same charge density on peptide membranes becomes our first biomimetic approach. This can be easily tested by replacing the N-terminal lysine with phosphorylated tyrosine or phosphorylated serine. In this chapter, I'll explore the self-assembly of the paracrystalline phase of the A β peptide with phosphorylated surfaces and its association with nucleic acid binding proteins histone H1.

1

¹ Results published as Li, S.; Sidorov, A. N.; Mehta, A. K.; Bisignano, A. J.; Das, D.; Childers, W. S.; Schuler, E.; Jiang, Z.; Orlando, T. M.; Berland, K.; Lynn, D. G. *Biochemistry* 2014, 53, 4225.

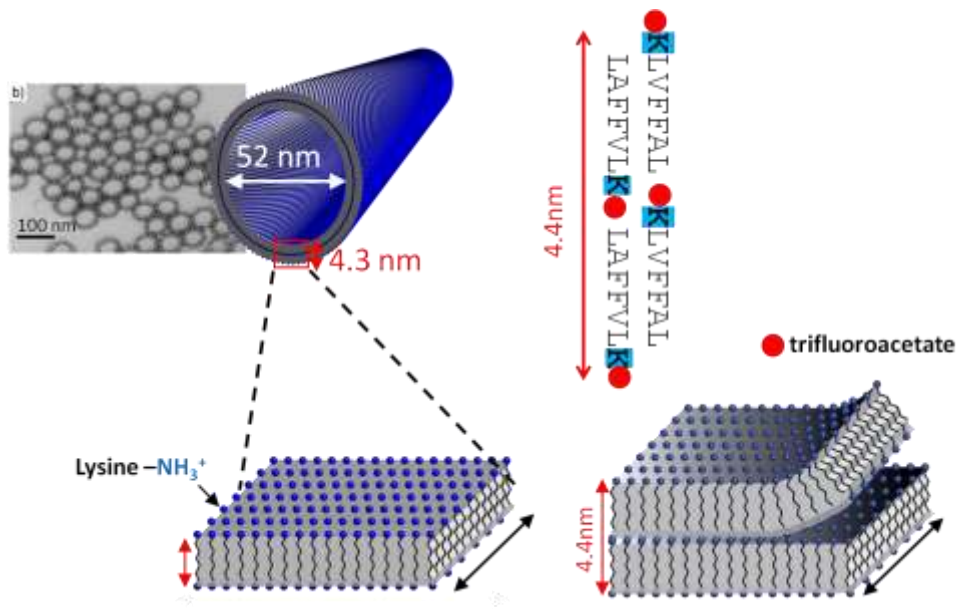


Figure 2-1 Peptide bilayer model for Ac-KLVFFAL peptide nanotube. The diameter of the nanotube is 52 nm with a ~4nm tube wall thickness as shown in the cross-section TEM on the top left. The nanotube wall is composed by two leaflet with lysine exposed on the surfaces of both sides of the leaflets. The blue dots represent positively-charged lysine residues; red dots represent negatively-charged counterion trifluoroacetate.

Results

Self-Assembly of Phosphorylated Peptide Membranes

Ac-KLVFFAL-NH₂ (E22L) peptide assembles as homogeneous nanotubes in 40% MeCN/H₂O at pH7 in the presence of trifluoroacetic acid (TFA) which exists in the solvents from HPLC purification process. Trifluoroacetate is critical for the peptide bilayer formation because it compensates the positive charge of lysine both within the bilayer interface as well as along the entire aqueous surface of the nanotubes as has been observe at pH2⁸. It is therefore hypothesized that a positively-charged counterion is needed to compensate the negatively-charged phosphate groups (Figure 2-2) under neutral condition.

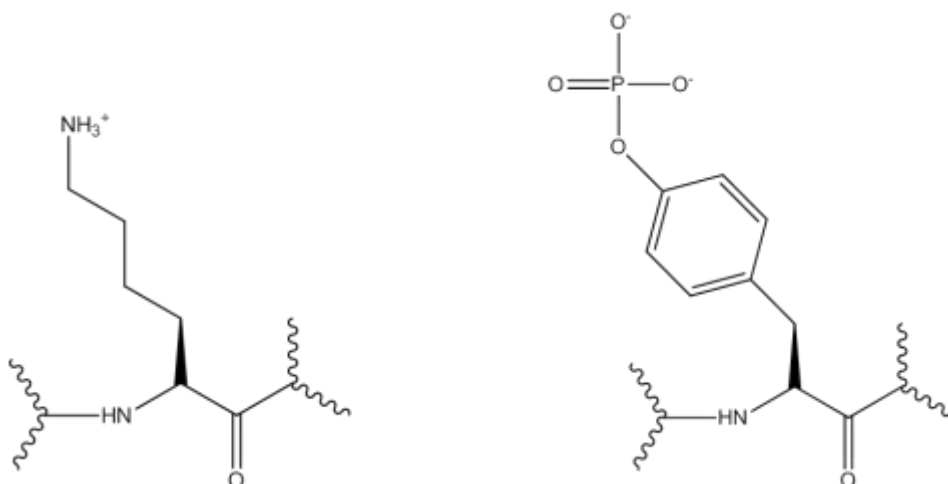


Figure 2-2 Molecular structure of lysine (left) and phosphotyrosine (right).

Phosphotyrosine Ac-pYLVFFAL-NH₂ peptide (K16pY)(E22L) was synthesized and assembled under different solvent conditions. Triethylammonium acetate (TEAA) and trimethylammonium acetate (TMAA) were selected as a buffer component in the self-assembly of (K16pY)(E22L) peptide. TEAA and TMAA are commonly used buffer at neutral pH. Also, the counterion triethylammonium and trimethylammonium sizes are comparable to that of trifluoroacetate. Assembly of (K16pY)(E22L) peptide in 10 mM to 50mM TEAA was tested from without obvious difference in results. Therefore, TEAA and TMAA concentration is selected as 15mM if not otherwise specified.

In order to test whether acetonitrile is needed for peptide nanotube formation, Ac-pYLVFFAL peptide was assembled in A) 40%MeCN/TEAA, pH7, B) TEAA, pH7 and E) H₂O, pH7 conditions and evaluated by Circular Dichroism (CD) and Transmission Electron Microscopy (TEM) (Figure 2-3 and Figure 2-4). In 40% MeCN/TEAA, Ac-pYLVFFAL peptide exhibits diagnostic β -sheet ellipticity with maximum at 202nm and minimum at 225nm and assembles as homogeneous nanotubes (nanotube is negatively stained tube structures with white edges) (Figure 2-3 and 2-4A). Without the presence of acetonitrile, Ac-pYLVFFAL peptide only assembled as fibrils with weak ellipticity at 202 nm (in TEAA) (Figure 2-3 and 2-4B) or no ellipticity (in H₂O) (Figure 2-3 and 2-4E), confirmed that acetonitrile is needed for hydrophobic collapse of peptide nanotube structure during self-assembly process. Condition A) 40%MeCN/TEAA, C) 40%MeCN/H₂O, pH7 and D) 40%MeCN/H₂O+0.1%TFA, pH2 were designed to test what counterion was necessary for peptide bilayer formation. In 40%MeCN/H₂O with (Figure

2-3 and 2-4C) or without TFA (Figure 2-3 and 2-4D), peptides only form amorphous aggregates without β -sheet ellipticity, verified the hypothesis that positively-charged counterions are needed for phosphate peptide bilayer formation.

A comparison of condition A and F showed that in 40%MeCN/TMAA (Figure 2-3 and 2-4F), Ac-pYL^VFFAL peptides still assembled as nanotubes with diagnostic β -sheet signature, suggested that both triethylammonium and trimethylammonium are able to compensate the charges of phosphate groups and facilitate the formation of peptide bilayer nanotubes. TEM tube width measurements (Figure 2-5) showed that Ac-KLVFFAL and Ac-pYL^VFFAL have identical diameters of 32 ± 5 and 32 ± 3 nm respectively.

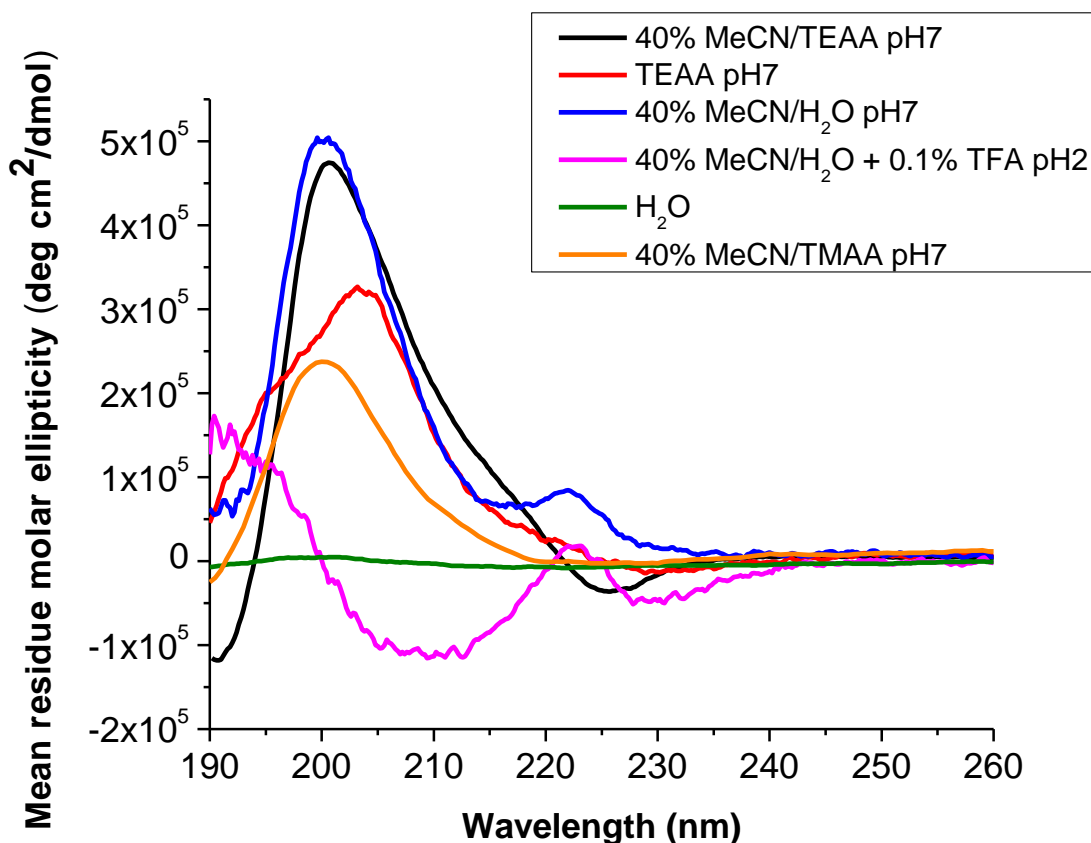


Figure 2-3 Circular Dichroism of Ac-pYL^VFFAL assembled under different conditions: A) 40%MeCN/TEAA, pH7 (black); B) TEAA, pH7 (red); C) 40%MeCN/H₂O, pH7 (blue); D) 40%MeCN/H₂O+0.1%TFA, pH2 (magenta); E) H₂O, pH7 (green) and F) 40%MeCN/TMAA pH7 (orange). All samples were assembled under 4 °C if not specified otherwise.

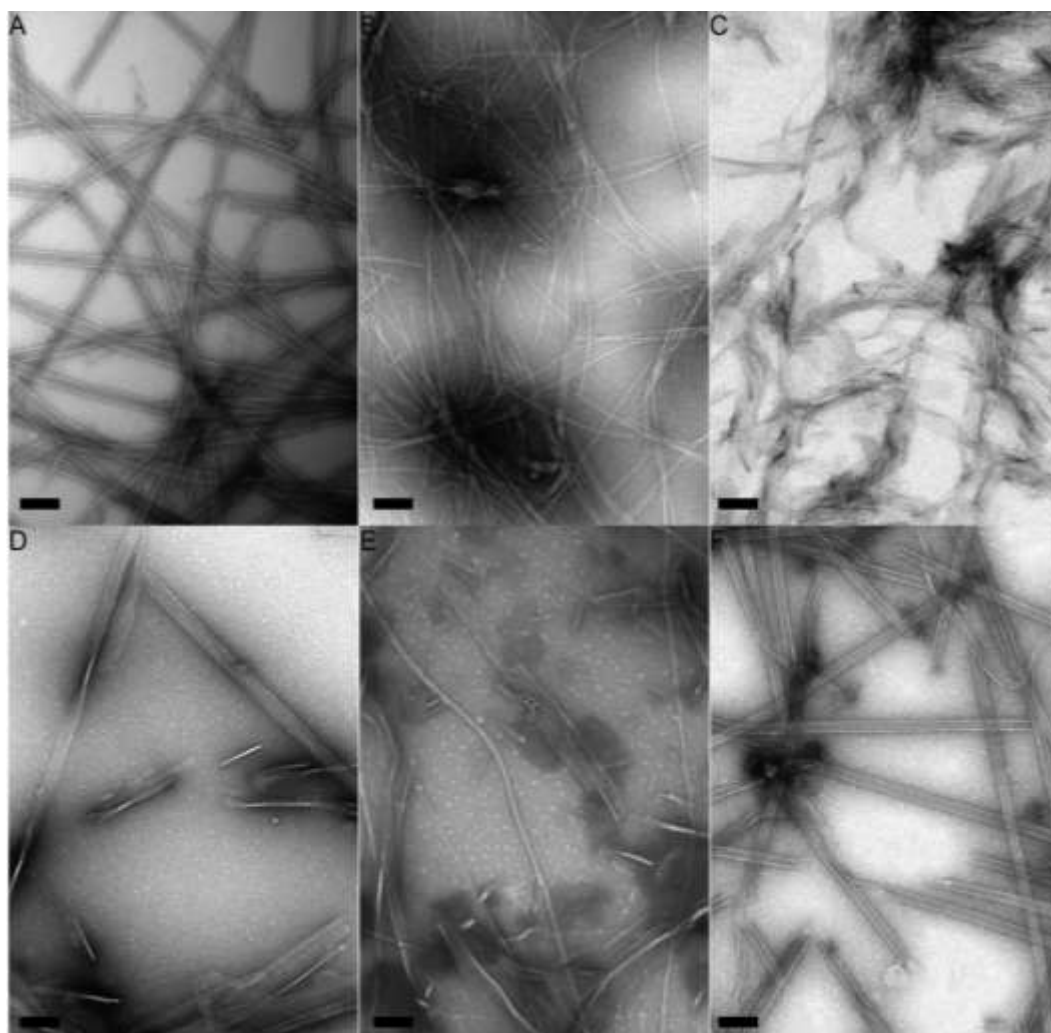


Figure 2-4 TEM micrographs of Ac-pYL VFFAL-NH₂ assembled under (A) 40%MeCN/TEAA, pH7, (B) TEAA, pH7, (C) 40%MeCN/H₂O, pH7; (D) 40%MeCN/H₂O+0.1%TFA, pH2, (E) H₂O, pH7, (F) 40%MeCN/TMAA pH7. Scale bar 200nm.

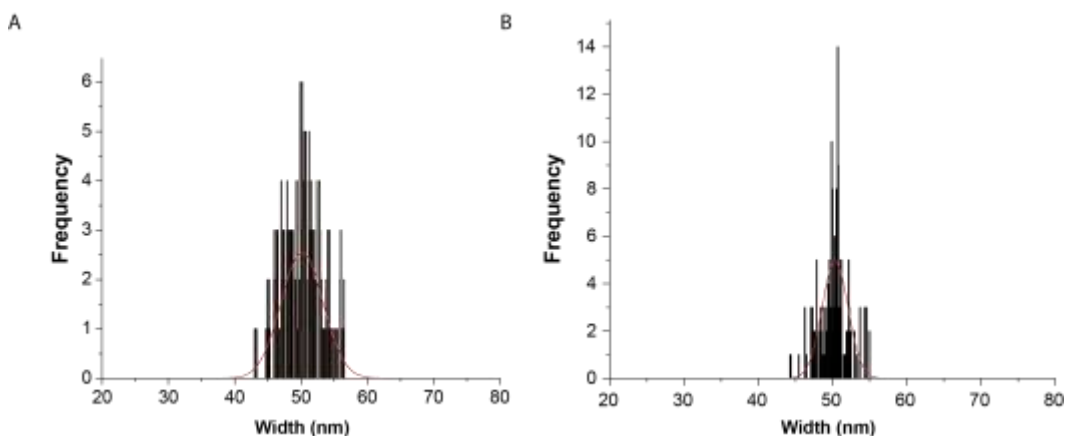


Figure 2-5 Width measurements from TEM images of A) (E22L) and B) (K16pY)(E22L) nanotube assemblies. 150-200 tube widths measurements were taken with an average of 3 measurements on each single tube at different positions. The frequency was plotted against widths and fit to Gaussian distributions with center \pm width of 50.2 ± 7.4 nm (E22L) and 50.4 ± 4.1 nm (K16pY)(E22L). Nanotube diameters can be estimated as diameter = width*2/ π to give 32 nm for both nanotubes.

Structural Characterization of Phosphorylated Peptide Assemblies

The (K16pY)(E22L) nanotubes exhibit ellipticity minima at 225 nm (Figure 2-6), most consistent with β -sheets¹⁰. Powder X-ray diffraction (XRD) reflections of d-spacing of 4.7 and 10.3 Å (Figure 2-7) can be assigned as β -strand and β -sheet, respectively, of a cross- β assembly.^{7,11-15} Fourier transform infrared spectra (Figure 2-8) shows a strong amide I absorption band at 1623 cm^{-1} , further supporting H-bonded β -sheet structures, and a weak band at 1693 cm^{-1} consistent with antiparallel strand arrangements. The out-of-register antiparallel organization is confirmed via solid-state nuclear magnetic resonance (NMR) $^{13}\text{C}\{^{15}\text{N}\}$ REDOR¹⁶ measurements on $[1-^{13}\text{C}]\text{V18}, [^{15}\text{N}]\text{A21}$ - (K16pY)(E22L) assemblies, assigning Val18 as H-bonded to Ala21 on adjacent strands with ^{13}C - ^{15}N distances of 4.2 ± 0.2 and 5.8 ± 0.2 Å and a ^{15}N - ^{13}C - ^{15}N angle of 156° (Figure 2-9), identical to $\text{A}\beta(16-22)$ and (E22L) tubes. As shown in Figure (Figure 2-10), atomic force microscopy (AFM) measurements are consistent with E22L and (K16pY)(E22L) tubes each maintaining the 4 nm thick wall of a cross- β peptide bilayer. The antiparallel β -sheet registry then places the phosphorylated residues on inner and outer tube surfaces and within the bilayer interface, establishing that this peptide bilayer is indeed capable of accommodating polar phosphates at the leaflet interface. The cross- β sheets laminate and coil up into ribbons to form nanotubes, resulting in individual H-bonded β -sheets running at an angle of with respect to the tube axis (Figure 2-11).

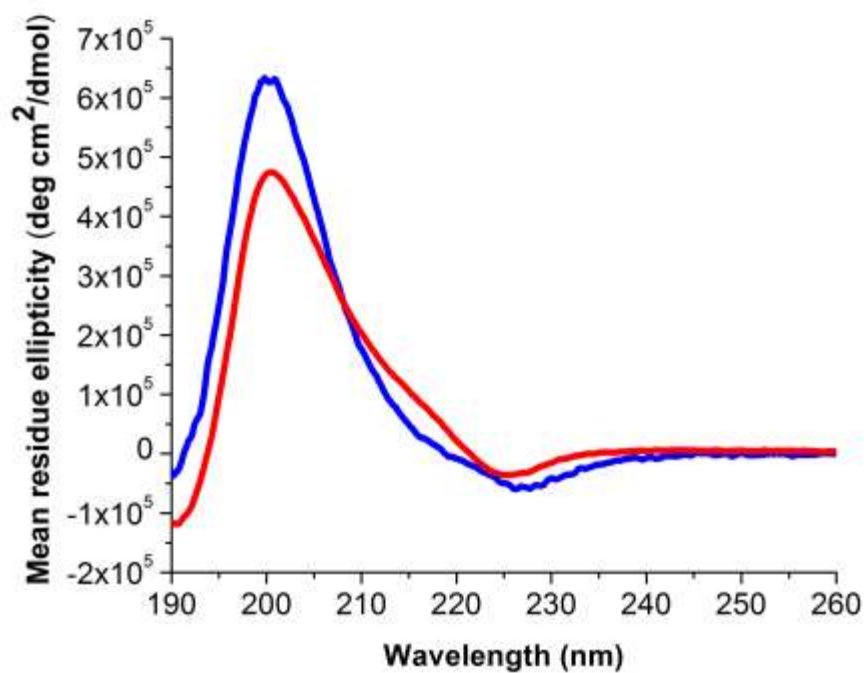


Figure 2-6 Circular dichroism of (E22L) (blue) assembled in 40% MeCN/H₂O with TFA and (K16pY)(E22L) (red) assembled in 40% MeCN/H₂O with TEAA, pH7.

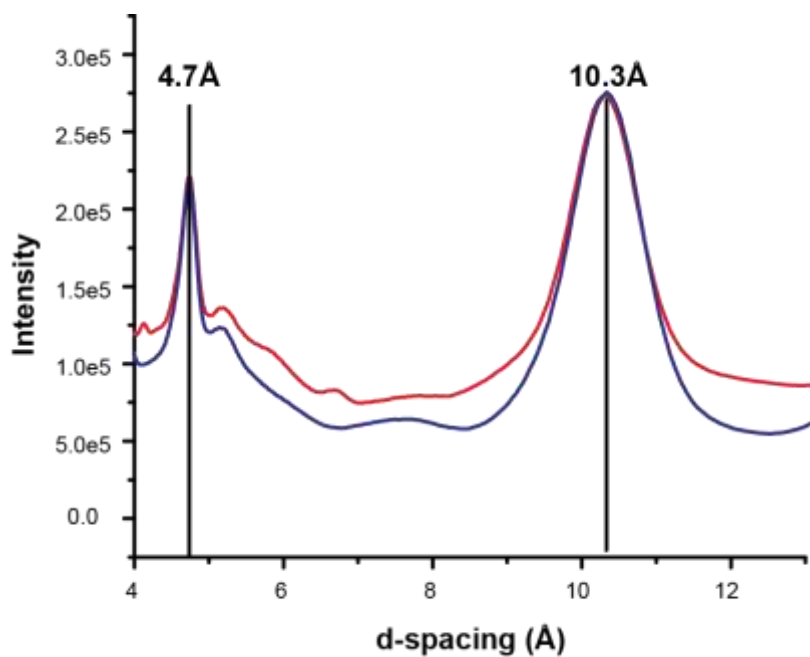


Figure 2-7 X-ray powder diffraction of (E22L) (blue) assembled in 40% MeCN/H₂O with TFA and (K16pY)(E22L) (red) assembled in 40% MeCN/H₂O with TEAA, pH7 showing reflections at d-spacing of 4.7 Å and 10.3 Å.

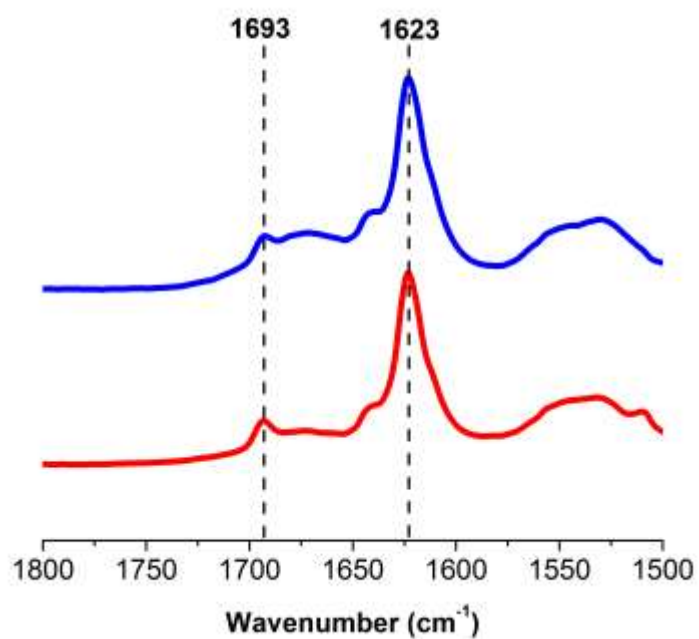


Figure 2-8 FT-IR spectra of (E22L) (blue) assembled in 40% MeCN/H₂O with TFA and (K16pY)(E22L) (red) assembled in 40% MeCN/H₂O with TEAA, pH7 showing a strong IR stretch at 1623 cm⁻¹, and a weaker band at 1693 cm⁻¹.

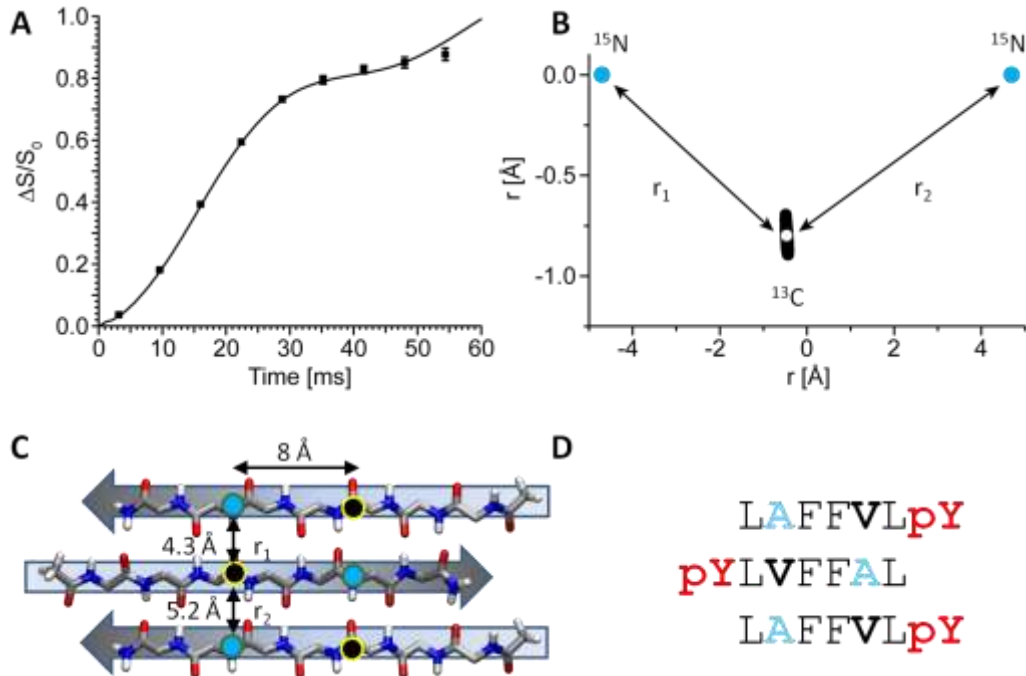


Figure 2-9 Solid-state NMR $^{13}\text{C}\{^{15}\text{N}\}$ EDOR measurements of $[1\text{-}^{13}\text{C}]\text{V18 } [^{15}\text{N}]\text{A21 (K16pY)(E22L)}$ peptides assembled as nanotubes. (A) $^{13}\text{C}\{^{15}\text{N}\}$ REDOR dephasing data fits to a (B) single ^{13}C (black circle) surrounded by two ^{15}N 's (blue circles) from adjacent H-bonded peptides. (C) Shows all ^{13}C positions that fit the experimental $^{13}\text{C}\{^{15}\text{N}\}$ REDOR data within error. The white circle corresponds to the ^{13}C position that has the best fit, with ^{13}C - ^{15}N distances of 4.2 ± 0.2 and 5.8 ± 0.2 Å and a ^{15}N - ^{13}C - ^{15}N angle of 156° . The calculated REDOR curve is shown as a solid line in (A). (D) Three H-bonded anti-parallel out-of-register peptides consistent with the NMR distance measurements.

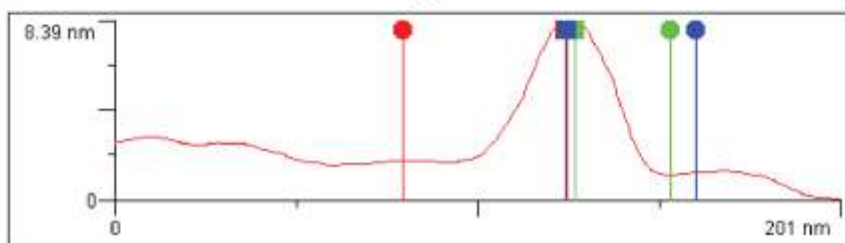
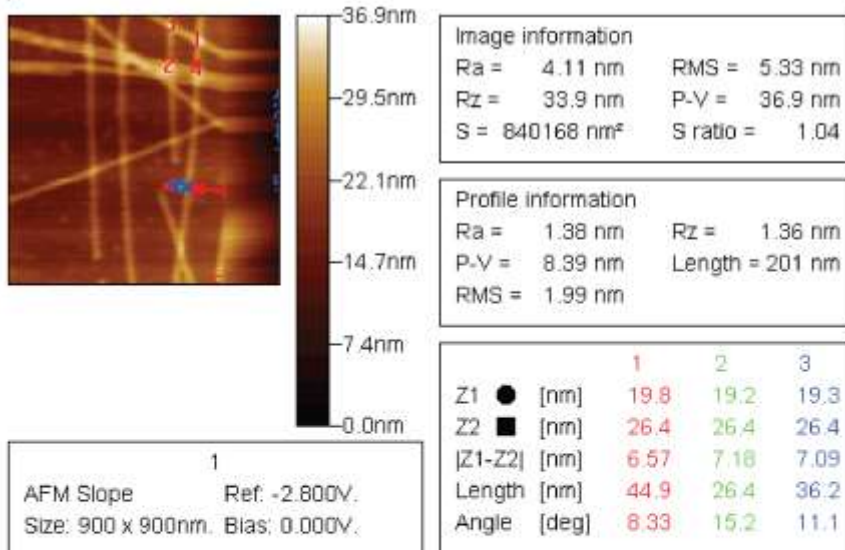
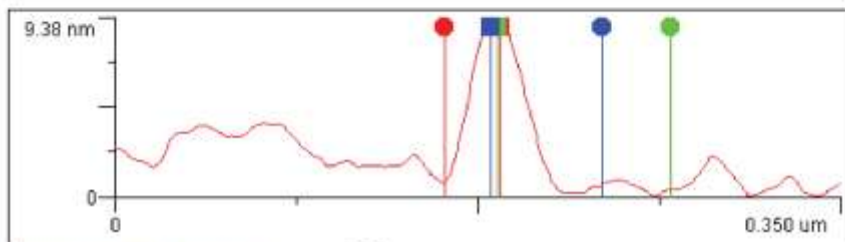
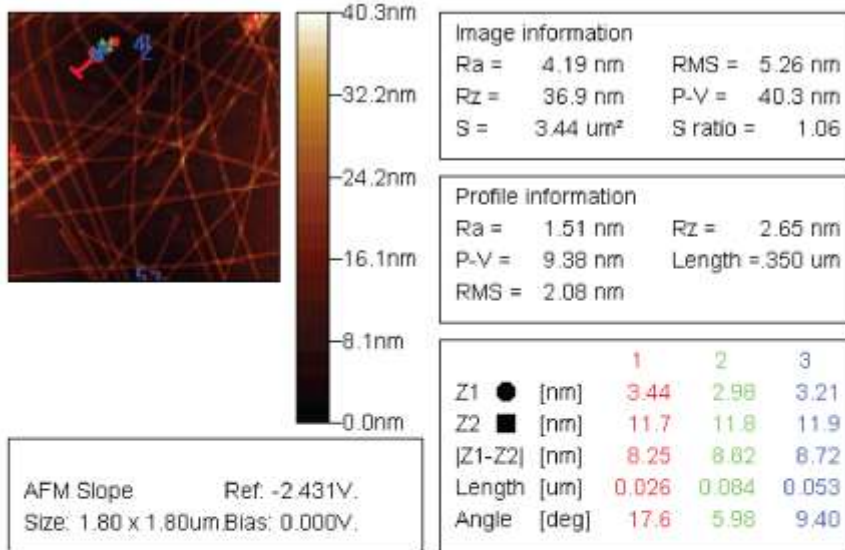


Figure 2-10 Sample AFM measurements of top: (E22L), average height = 8.6 ± 0.6 nm, and bottom: (K16pY) (E22L), average height = 8.3 ± 0.6 nm peptide assemblies. Heights are average of 10 separate measurements.

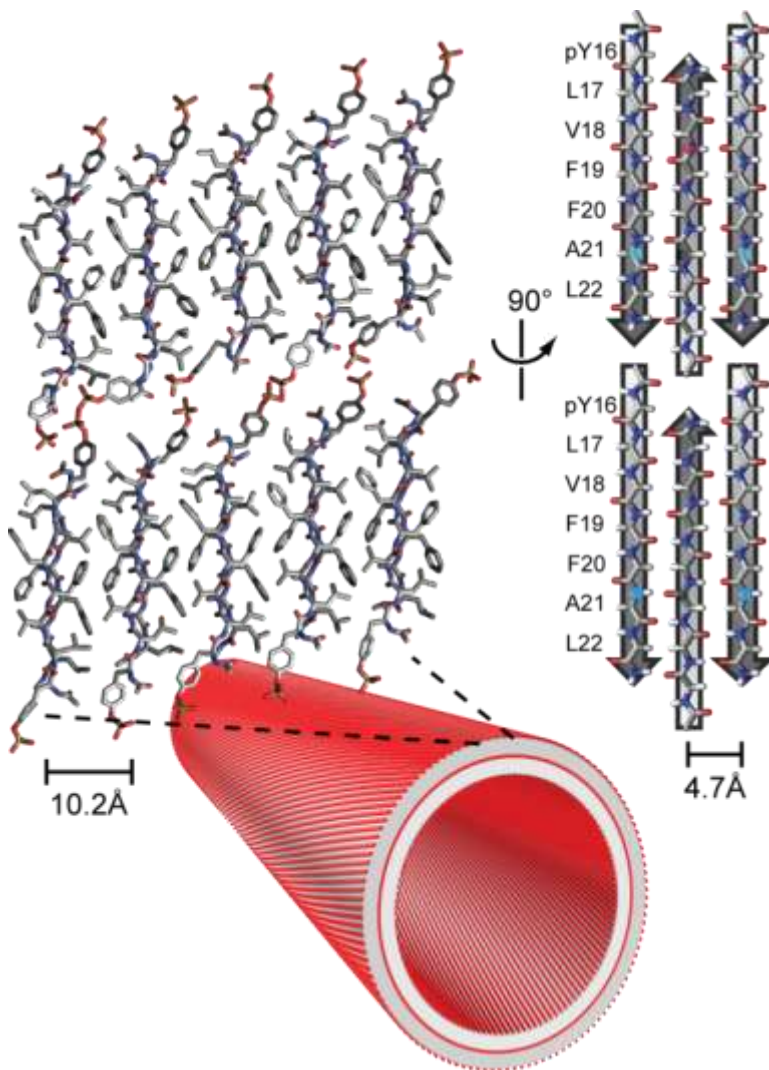


Figure 2-11 Model for (K16pY)(E22L) bilayer nanotubes with each leaflet composed of antiparallel out-of-register β -sheets. The N-terminal phosphotyrosine (pY) repeats every nanometer along each row.

Diversifying Negatively-Charged Peptide Nanotube Surfaces

The robustness of the negatively-charged peptide membranes was tested by replacing phosphotyrosine with glutamic acid and phosphoserine respectively to give Ac-ELVFFAL-NH₂ and Ac-pSLVFFAL-NH₂ peptides. These peptides assembled under 40% MeCN/TEAA at neutral pH. Both peptides self-assembled into homogeneous nanotubes

with identical tube diameters as Ac-pYLVFFAL nanotubes as shown by TEM (Figure 2-12) and tube width histogram (Figure 2-13).

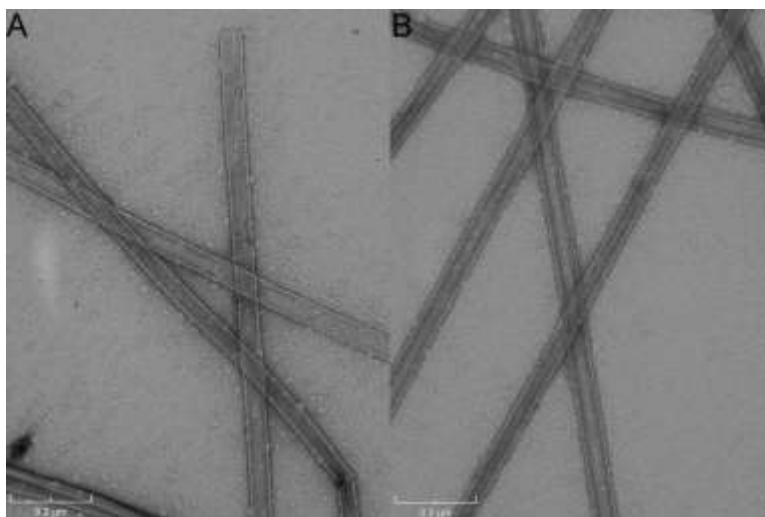


Figure 2-12 TEM micrographs of (A) Ac-ELVFFAL and (B) Ac-pSLVFFAL nanotubes assembled in 40% MeCN/H₂O with TEAA, pH7.

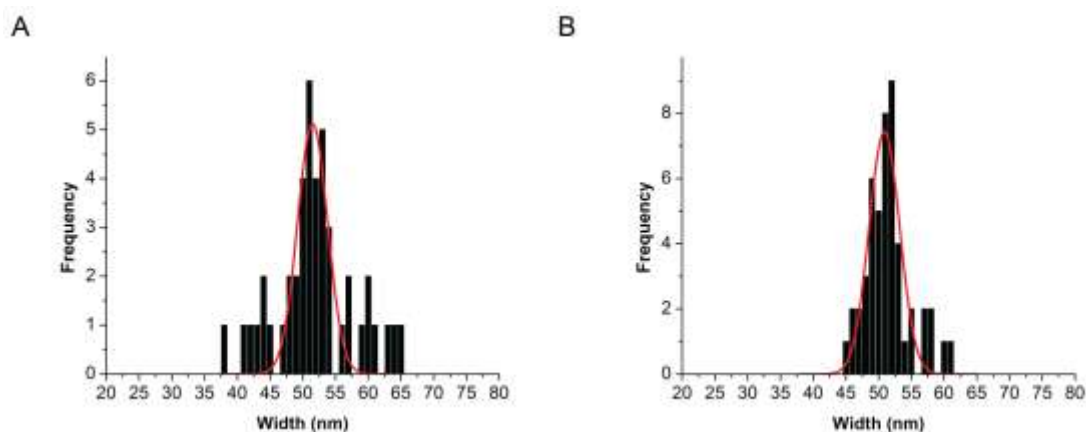


Figure 2-13 Width measurements from TEM images of A) Ac-ELVFFAL and B) Ac-pSLVFFAL nanotube assemblies. 50-100 tube widths measurements were taken with an average of 3 measurements on each single tube at different positions. The frequency was plotted against widths and fit to Gaussian distributions with center \pm width of 51.5 ± 5.4 nm and 50.9 ± 5.5 nm . Nanotube diameters can be estimated as diameter = width*2/ π to give 32 nm for both tubes.

Both Ac-ELVFFAL and Ac-pSLVFFAL nanotubes exhibit a circular dichroism (CD) ellipticity minima at 225 nm (Figure 2-14), most consistent with β -sheets. Fourier transform infrared spectra (IR) (Figure 2-15) contain a strong amide I absorption band at 1623 cm^{-1} , further supporting H-bonded β -sheet structures, and a weak band at 1693

cm^{-1} consistent with antiparallel strand arrangements. Powder X-ray diffraction (XRD) reflections with d spacing of 4.7 and 10.3 Å (Figure 2-16 and 2-17) can be assigned as β -strand and β -sheet reflections, respectively, within a cross- β assembly.

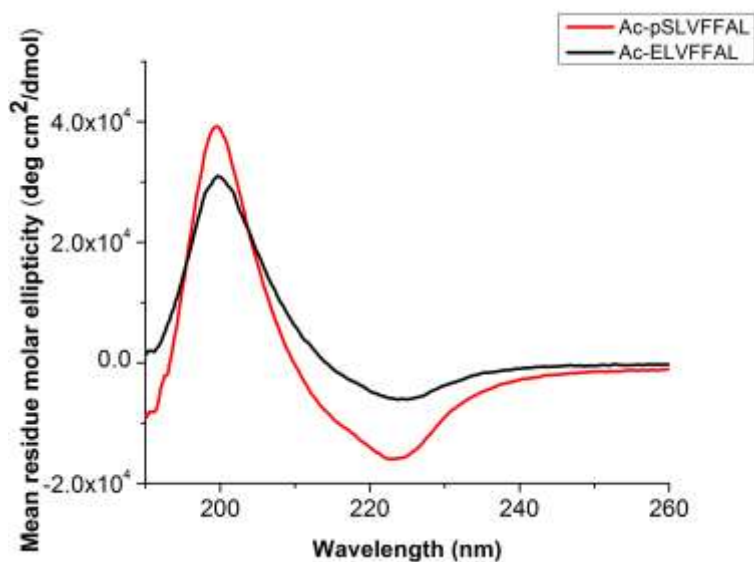


Figure 2-14 Circular dichroism of (K16pS)(E22L) (red) and (K16E)(E22L) assembled in 40% MeCN/H₂O with TEAA, pH7 with minimum at 225 nm and maximum at 202 nm.

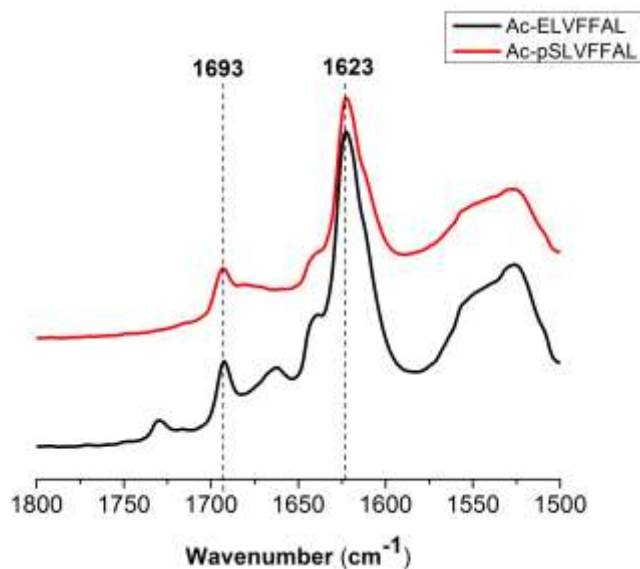


Figure 2-15 FT-IR spectra of (K16pS)(E22L) (red) and (K16E)(E22L) (black) assembled in 40% MeCN/H₂O with TEAA, pH7 showing a strong IR stretch at 1623 cm^{-1} and a weaker band at 1693 cm^{-1} .

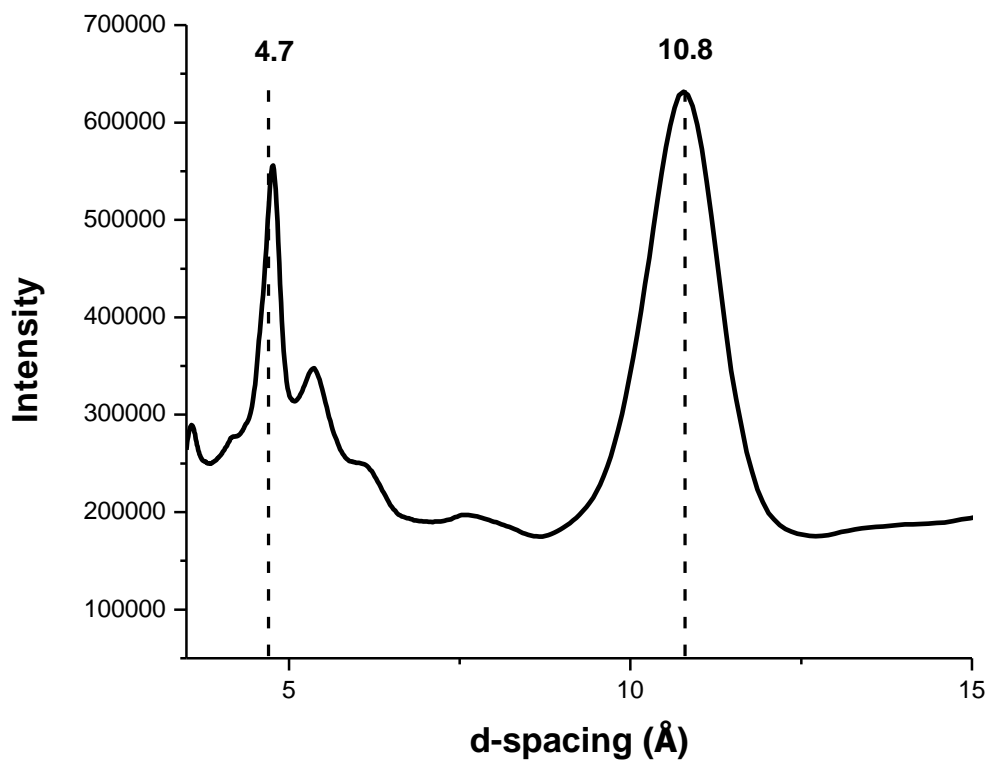


Figure 2-16 X-ray powder diffraction of (K16E)(E22L) assembled in 40% MeCN/H₂O with TEAA, pH7 showing reflections at d-spacing of 4.7 Å and 10.3 Å.

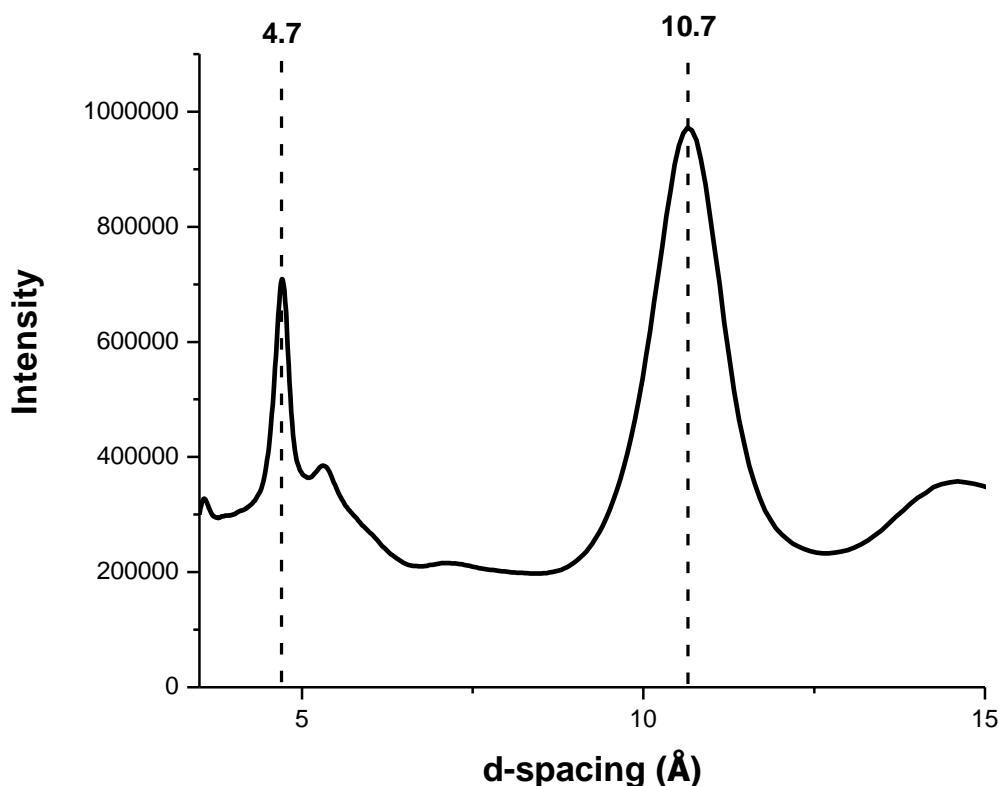


Figure 2-17 X-ray powder diffraction of (K16pS)(E22L) assembled in 40% MeCN/H₂O with TEAA, pH7 showing reflections at d-spacing of 4.7 Å and 10.3 Å.

Solvent and Temperature Dependence of Phosphorylated Peptide Membranes

Simple peptides can access diverse amphiphilic phases that appear to be etiologically relevant to several protein misfolding diseases¹⁷⁻²¹. The rich context-dependent behavior of the A β peptides nucleating core with lysine-rich surfaces has been tested in previous studies²². Solvent and temperature dependence of phosphorylated peptides assemblies are experimentally tested in this section.

Pre-assembled Ac-pYL^VFFAL-NH₂ in 40%MeCN/TEAA as mature nanotubes (Figure 2-18A) were resuspended in HPLC grade water. The assemblies remain as homogeneous nanotubes (Figure 2-18B) and within a day or two begin to unravel into ribbons and even fibers by day 3 (Figure 2-18C). After 2 weeks in water, all assemblies had turned into fibers (Figure 2-18D). The phase transition between nanotubes and ribbons/fibers may be a result of hydrophobic collapse when acetonitrile was depleted from the solvent. Such structural interchange manipulated by a simple adjustment in solvent components

demonstrates phosphorylated peptide membranes to be dynamic assemblies responsive to external environmental fluxuations.

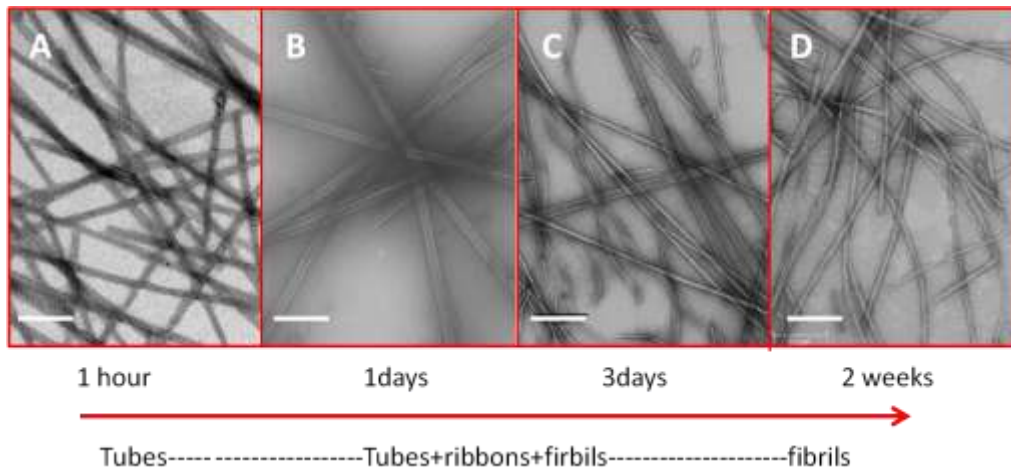


Figure 2-18 TEM micrographs of mature Ac-pYL VFFAL-NH₂ nanotubes formed 40%MeCN/TEAA and resuspend in water after A) 1 hour, B) 3 days, C) 1 week and D) 1 month. Scale bar 200nm.

Ac-pYL VFFAL-NH₂ in 40%MeCN/TEAA assemble as mature nanotubes were incubated at 75 °C for 4 hours and cooled back to room temperature. TEM showed drastic change from homogeneous nanotubes to molten globular particles (Figure 2-19), suggesting that these assemblies are temperature-dependent. As temperate is elevated, the assemblies melt from nanotubes to particles. Interestingly, the paracrystalline order appears to be preserved to some extent as smaller particles appear to be budded out from the large particles which could be the formation of new nucleating core upon re-equilibrium at room temperature²². Particles fusion which might lead to the formation of ordered structures was observed in the solution during re-equilibrium, too. Such temperature-dependent fusion behaviors reminiscent of what we seen in cell lipid membrane^{23,24} and implies plasticity of the peptide membranes structures.

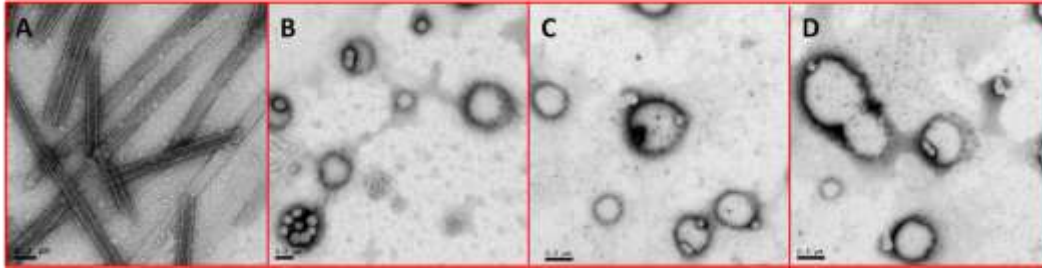


Figure 2-19 TEM images of A) matured Ac-pYLVFFAL-NH₂ nanotubes incubated under 4 °C and B) C) D) incubated under 75 °C for 4 hours and then cool back to RT.

AuNPs Binding with Peptide Membranes

Cross- β peptide membrane surfaces are known to be able to bind small molecules and metal arrays²⁵⁻²⁷. Gold-nanoparticles (AuNPs)²⁸⁻³⁰ have attracted attention in medical sciences and biotechnology because of their biocompatibility. Despite the importance of nano-bio interfaces³¹, however, the interaction between peptides and protein with gold surfaces³² is not fully understood. In order to characterize the charged surfaces of peptide membranes as well as understand the association between gold nanoparticles and peptides surfaces, gold nanoparticles with positive and negative coats were synthesized or purchased and used for association with peptide membrane surfaces in this section.

Different experimental schemes B-F as shown in Figure 2-20 were designed to test AuNPs-peptide nanotubes surfaces association (Figure 2-20). Citrate coated negatively charged gold nanoparticles with 5 nm diameter was synthesized and used for initial methodology test. Compare experiment B and C (Figure 2-20 B and C), when AuNPs and peptide nanotubes were incubated in solution for 3 hours resulted in more efficient binding of AuNPs with the nanotubes than 15 mins incubation. Both shorter and longer incubation time produced clean images without much unbound AuNPs. However, incubation of AuNPs and peptide nanotubes on the grid directly (Figure 2-20 D, E and F) led to both bound and unbound AuNPs. Drying the TEM grid in dessicators (Figure 2-19E and F) preserves binding behaviors of AuNPs better than wicking with filter paper (Figure 2-20D). Compare Figure 2-20 E and F suggests that the TEM grid with peptide nanotubes doesn't need to be dried for 24 hours before the addition of AuNPs. Although different experimental methods only have subtle differences in terms of gold binding effects, incubating in solution, resuspending the pellet and drying the grid in air generally

lead to more efficient binding of AuNPs with peptide nanotubes. Therefore, experimental schemes B (Figure 2-20 B) was chosen for further studies.

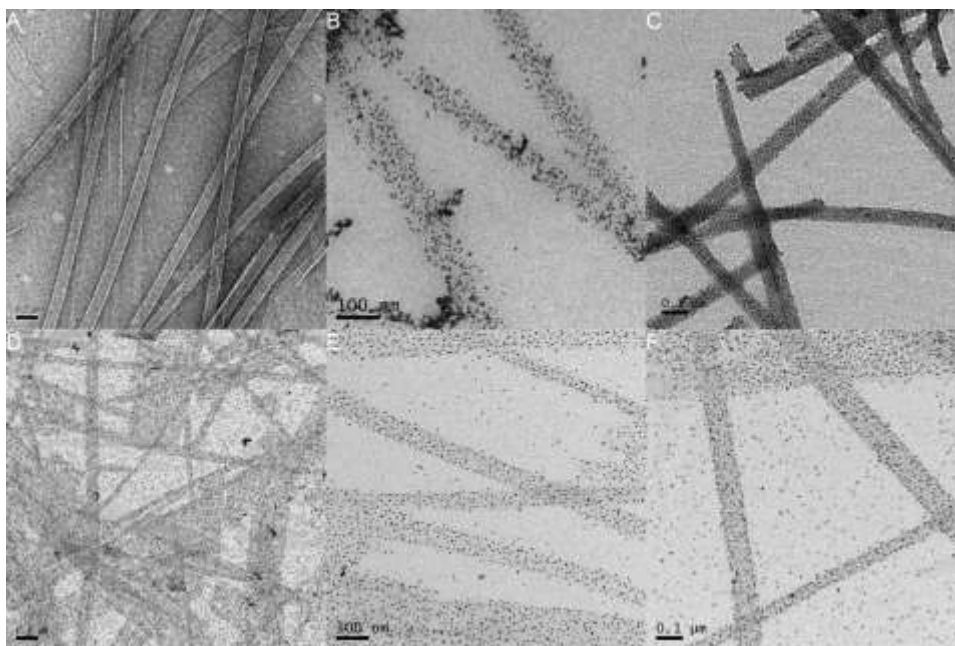


Figure 2-20 TEM micrographs of gold nanoparticles binding with Ac-KLVFFAL nanotubes with different experimental methods. (A) Ac-KLVFFAL nanotubes, stained with uranyl acetate; (B) AuNPs and peptide nanotubes were incubated in solution for 15 min, then the pellet was spun down and resuspended in solvents, and the solution was applied on the grid and dried in dessicators for 24 hrs; (C) AuNPs and peptide nanotubes were incubated in solution for 3 hrs, then the pellet was spun down and resuspended in solvents, and the solution was applied on the grid and dried in dessicators for 24 hrs; (D) AuNPs and peptide nanotubes were incubated on the carbon grid directly and dried with filter paper; (E) AuNPs and peptide nanotubes were incubated on the carbon grid directly and dried in dessicators for 24 hrs; (F) peptide nanotubes were incubated on the carbon grid and dried in dessicators for 24 hrs first and then AuNPs were added to the grid and dried for 24 hrs. No uranyl acetate stain in figure B-F.

Next, both negatively charged gold nanoparticles (functionalized with citrate) and positively charged gold nanoparticles [functionalized with (11-mercaptoundecyl)-N,N,N-trimethylammonium bromide] were prepared. Negatively charged gold nanoparticles organize specifically along the surfaces of the positively-charged (E22L) assemblies, while positively charged gold nanoparticles coat only the negatively-charged (K16pY)(E22L) assemblies (Figure 2-21). The result is consistent with positively-charged (E22L) peptide nanotube surfaces and negatively-charged (K16pY)(E22L) peptide nanotube surfaces.

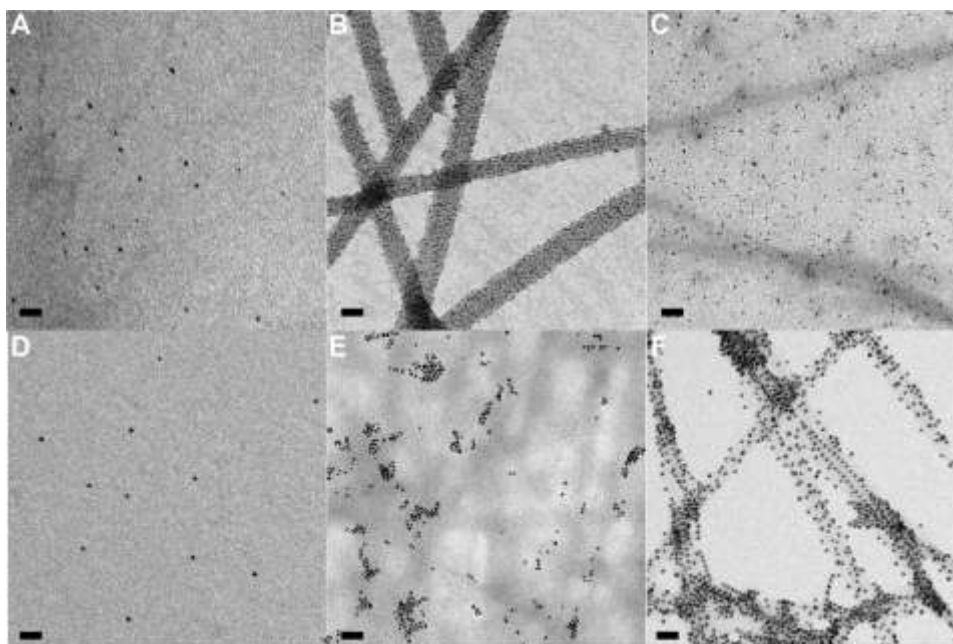


Figure 2-21 Gold nanoparticle binding to (E22L) and (K16pY) (E22L) peptide nanotubes visualized by TEM without stain. (A) 5 nm negatively-charged gold nanoparticles; (B) Negatively-charged gold nanoparticles co-incubated with (E22L) tubes; (C) Negatively-charged gold nanoparticles co-incubated with (K16pY) (E22L) tubes; (D) 10 nm positively-charged gold nanoparticles; (E) Positively-charged gold nanoparticles co-incubated with (E22L) tubes; (f) Positively-charged gold nanoparticles co-incubated with (K16pY) (E22L) tubes. Scale bars, 50 nm.

Salt-induced Macroscale Assembly of Peptide Nanotubes

Salt-induced³³ aggregation was employed to evaluate the nanotube surface charge. Induction follows the Hofmeister series³⁴, with SO_4^{2-} bundling (E22L) nanotubes³⁴ but not (K16pY)(E22L) nanotubes (Figure 2-22 B and E), consistent with (E22L) having positively charged surfaces and (K16pY)(E22L) having negatively charged surfaces. Similarly, Mg^{2+} bundles only (K16pY)(E22L) nanotubes (Figure 2-22 C and F).

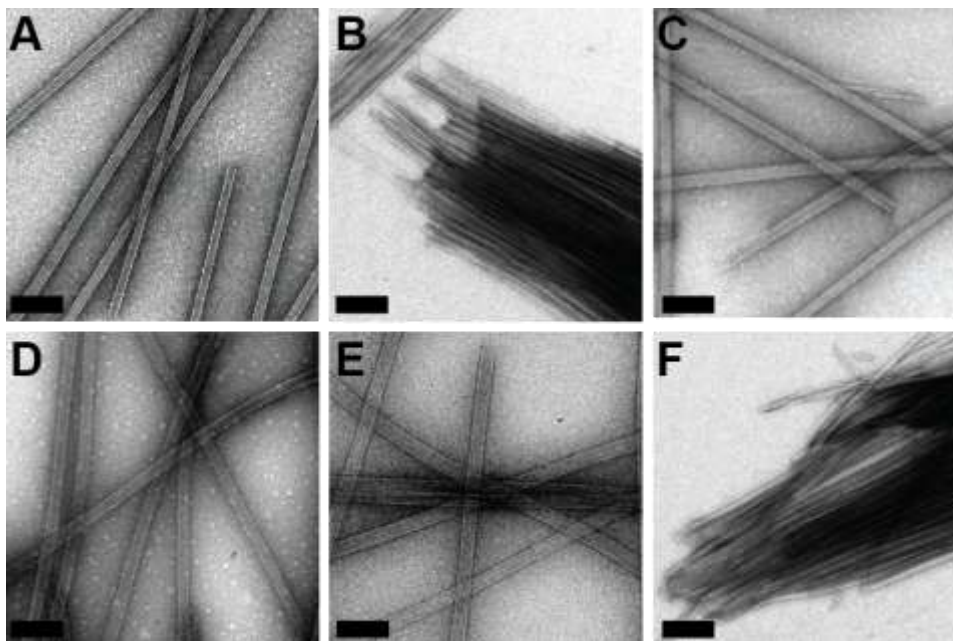


Figure 2-22 (A–F) Transmission electron microscopy micrographs of salt-induced bundling of (E22L) (top) and (K16pY)(E22L) (bottom) nanotubes: (A and D) without additional salts, (B and E) 2 h after the addition of Na₂SO₄, and (C and F) 2 h after the addition of MgCl₂. Peptide:salt molar ratio of 1:4.5 and scale bars of 200 nm.

Similar to (K16pY)(E22L) nanotubes, (K16E)(E22L) and (K16pS)(E22L) nanotubes bundled only in the presence of Mg²⁺, (Figure 2-23) suggesting they have similar negatively-charged surfaces.

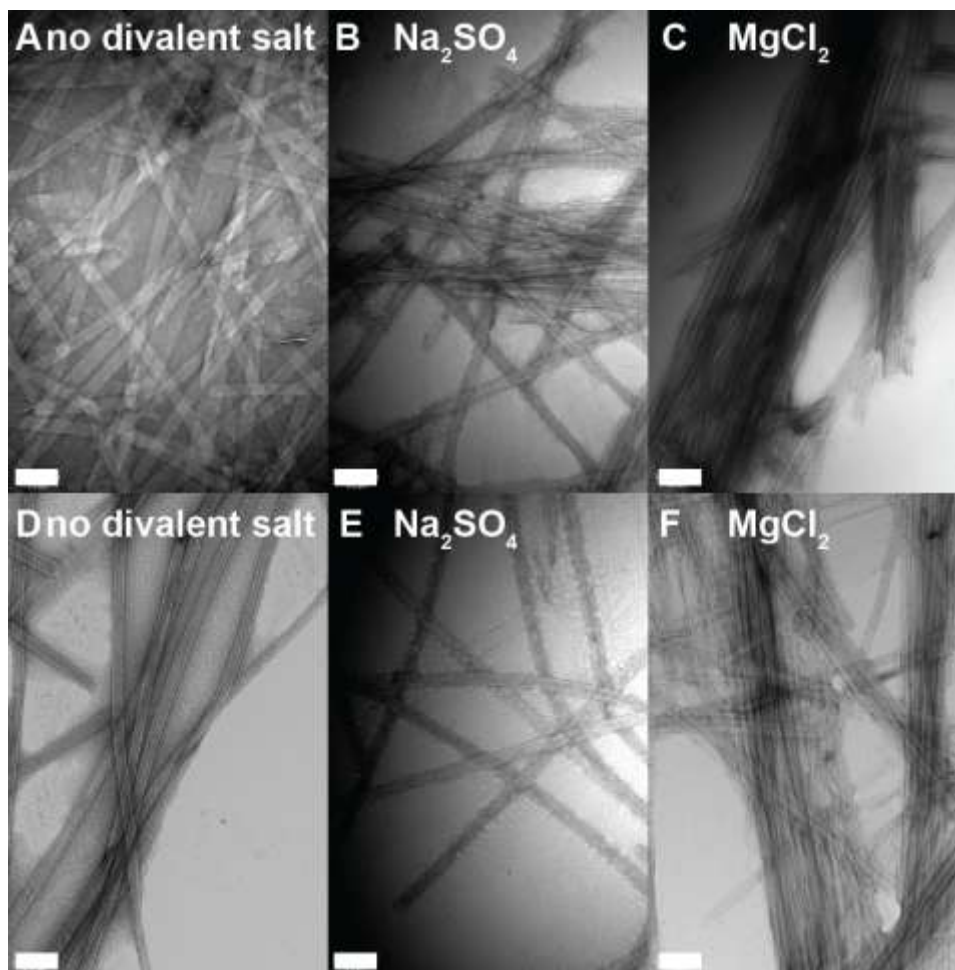


Figure 2-23 (A–F) Transmission electron microscopy micrographs of salt-induced bundling of (K16E)(E22L) (top) and (K16pS)(E22L) (bottom) nanotubes: (A and D) without additional salts, (B and E) 2 h after the addition of Na_2SO_4 , and (C and F) 2 h after the addition of MgCl_2 . Peptide:salt molar ratio of 1:4.5 and scale bars of 200 nm.

Development of Electrostatic Force Microscopy

The atomic force microscope (AFM)³⁵⁻³⁷ is one kind of scanning probe microscopes (SPM)³⁸, designed to measure local properties with a probe. Electrostatic Force Microscopy (EFM)³⁹⁻⁴¹ is a secondary imaging mode derived from AFM. A voltage is applied between the tip and the sample to create and modulate an electrostatic field. The cantilever's resonance frequency and phase change with the strength of the electric field gradient are used to construct the EFM image (Figure 2-24). The goal of an EFM experiment is not to image the surface topography as in AFM, but rather to image the electrical properties of the surface.^{42,43}

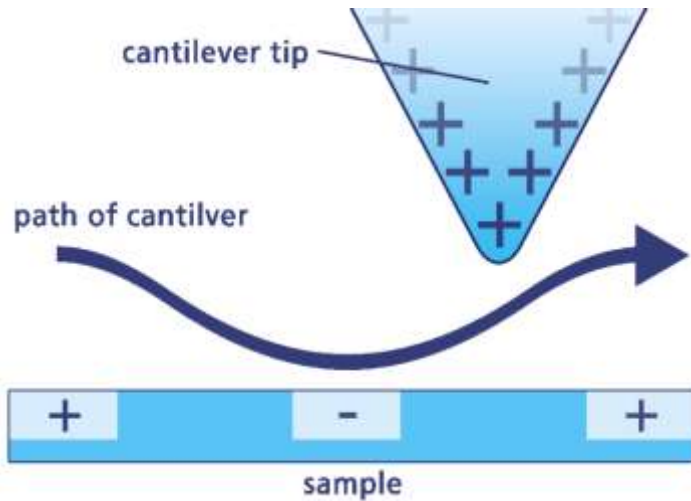


Figure 2-24 EFM maps locally charged domains on the sample surface.

EFM can be used to distinguish conductive and insulating regions in a sample. Figure 2-25 shows the standard test sample and its magnified view. The test sample consists of two comb shaped golden electrodes with each tooth of one electrode lying between teeth of the other. Each electrode has a wire connected to it. One wire is connected to the sample holder and thus sample biased, and the other wire is connected to the ground wire and thus grounded.

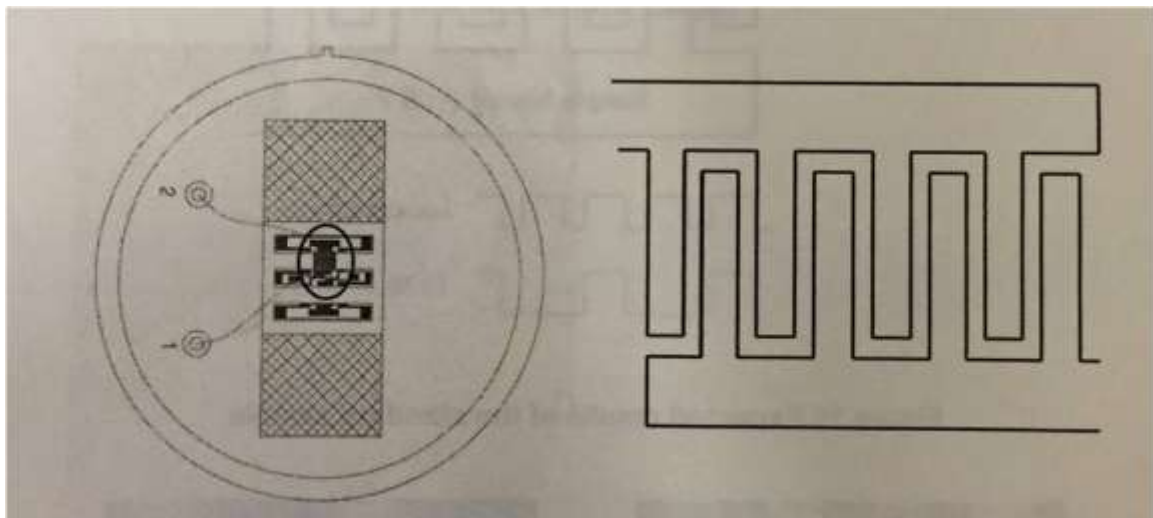


Figure 2-25 The standard sample (left) and its magnified view (right).

Figure 2-26 shows the Topography and EFM signals of the standard sample. Since all the neighboring teeth of the comb shaped electrode are the same height, the Topography signal is in the shape of a square wave. However, the neighboring electrode

differs in potential, every other peak is relatively positive compared to background in the EFM image.

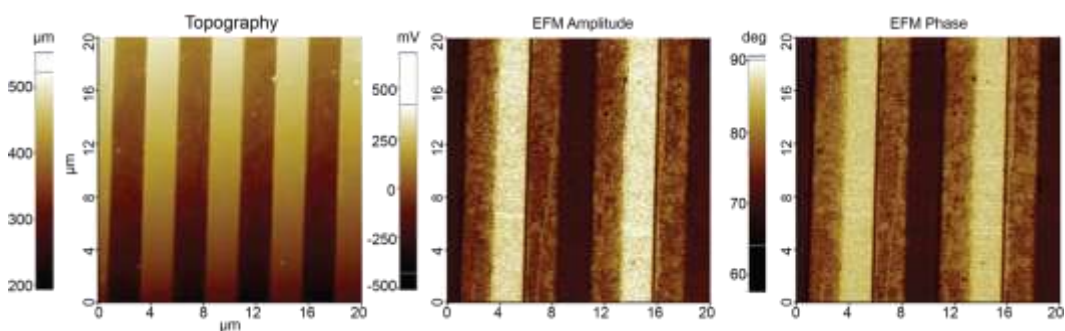


Figure 2-26 Topography (left) and EFM amplitude (middle) and EFM phase (right) signals of the standard sample.

Analysis of Supramolecular Assemblies via Electrostatic Force Microscopy

The structural models⁷ Ac-KLVFFAL and Ac-pYLVFFAL peptides present high density of ammonium ions/phosphate ions located at precise positions across a nanoscale grid on a hollow nanotube surface. Methods for mapping these charges in aqueous solutions to define positions of macromolecular adsorbents, surface imperfections, domain size, and even surface dynamics are less developed. EFM have been widely used successfully for measuring the electric field gradient distribution above dry surfaces, including mineral crystal surfaces⁴⁴, graphene layers⁴⁵, doped regions in semiconductors⁴⁶ and other solid materials⁴⁷. Attempts had been made on mapping charge distribution of simple peptide assemblies^{48,49} too, albeit none of the assemblies contain patterned charged surfaces. Here we demonstrate electrostatic force microscopy (EFM) analyses that map the charge distribution on these highly ordered self-assembled peptide membranes in a partially dried state.

Figure 2-27 A shows the partially dried (E22L) assemblies as repulsive (white) to a positive bias tip, while the (K16pY)(E22L) assemblies (Figure 2-27B) are attractive (dark) along the entire length of each assembled nanotube. The results are consistent with highly ordered positively-charged (E22L) nanotubes and negatively-charged (K16pY)(E22L) nanotubes.

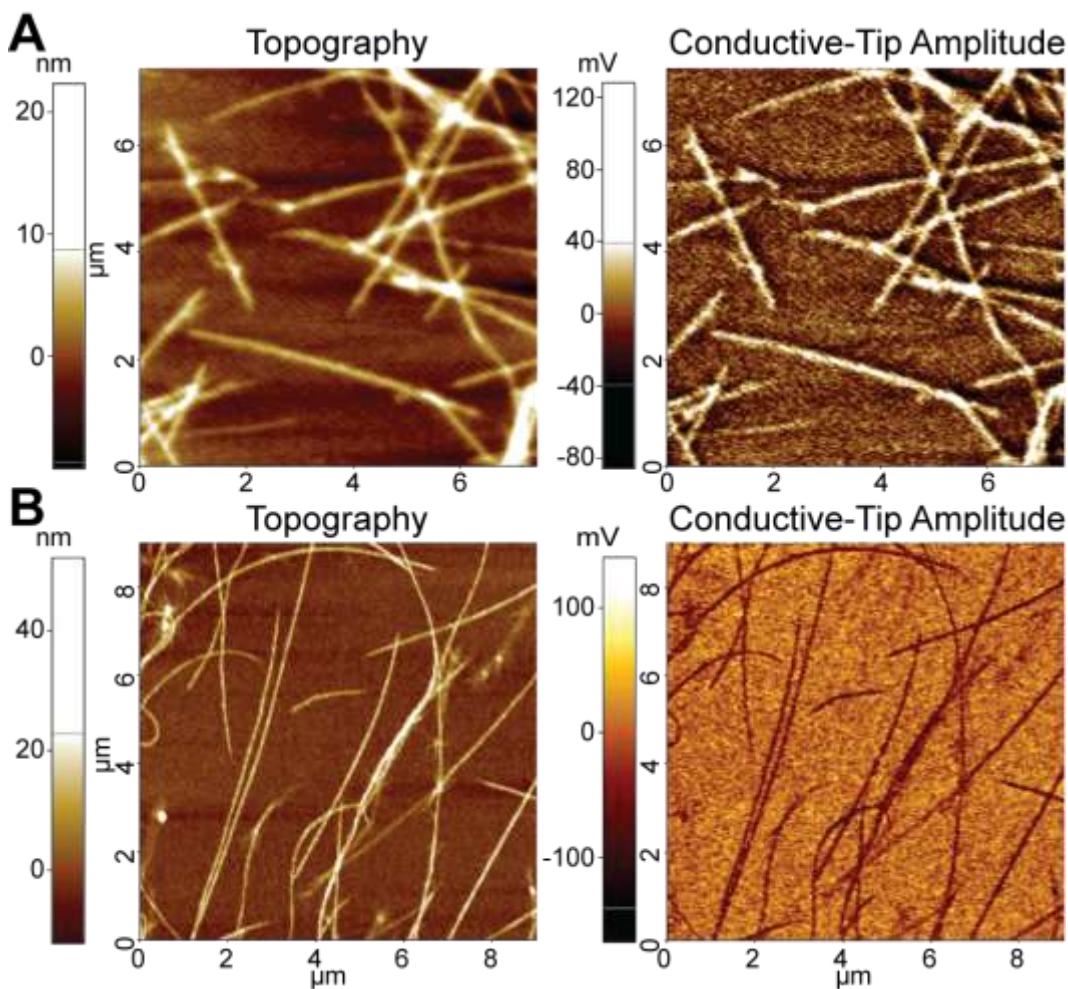


Figure 2-27 Atomic and electrostatic force micrographs of (A) (E22L) and (B) (K16pY)(E22L) nanotube assemblies. Topography (left) and EFM amplitude (right) micrographs of peptide nanotubes with a DC bias of +1 V. In the EFM amplitude micrographs, positively charged surfaces are white and negatively charged surfaces are dark.

I argue that these unique charge patterns stem from the alignment of peptide residues (lysine and phosphotyrosine) in rows along the length of the tubes and that ammonium ions/phosphate ions in solution would not make such pattern. To test this argument, salts sample of NH_4Cl and Na_2HPO_4 were analyzed by EFM. Charges were observed in these two samples, but existed as crystalline or aggregates, not as patterned charged surfaces as that of peptide nanotubes (Figure 2-28 and Figure 2-29). Together, these spectroscopic and scanning probe analyses define unique patterned peptide nanotube surfaces (Figure 2-30).

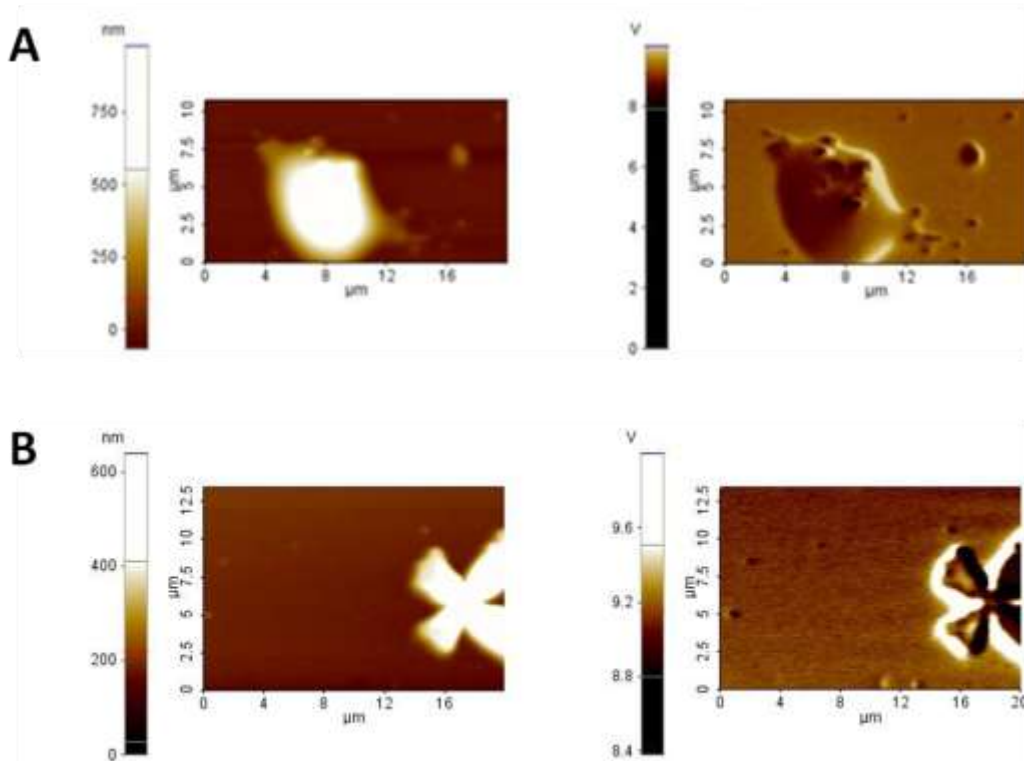


Figure 2-28 Topography (left) and EFM amplitude (right) micrographs of dried salt solutions of (A) NH_4Cl_2 and (B) Na_2HPO_4 , with a DC bias of +1 V. In the EFM amplitude micrographs, positively charged surfaces are white and negatively charged surfaces are dark.

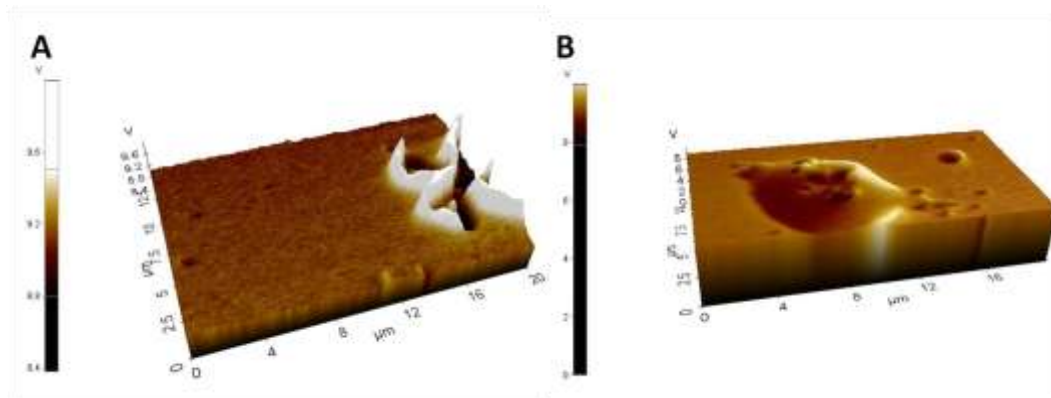


Figure 2-29 3D electrostatic force micrographs of dried salt solutions of (A) NH_4Cl_2 and (B) Na_2HPO_4 with a DC bias of +1 V. In the EFM amplitude micrographs, positively charged surfaces are white and negatively charged surfaces are dark.

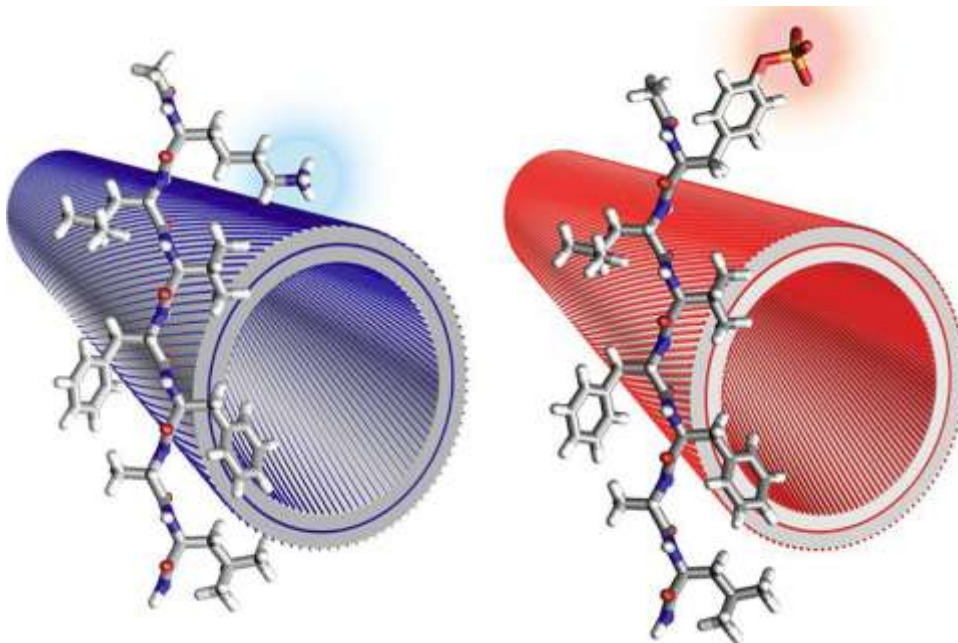


Figure 2-30 Model of Ac-KLVFFAL and Ac-pYLFFAL nanotubes, blue represents positively charged lysine residues, red represents negatively charge phosphotyrosine residues.

Small Molecules Binding with Phosphorylated Peptide Nanotube Surfaces

Congo Red (CR)^{50,51} and Thioflavin T (ThT)^{52,53} are well-known universal diagnostic indicator of amyloid structures. CR has been reported to template in amyloid's cross- β grooves and upon binding shows a red-shift in the UV²⁵. ThT is a benzothiazole dye that can exhibits enhanced fluorescence upon binding to amyloid fibrils. Nevertheless, due to the negative charges on CR and positive charges on ThT dyes, the positively-charged (E22L) peptide nanotubes are only able to bind to CR, not ThT²⁵. To further test the homogeneous charged surfaces generated by a simple N-terminal residue switch, CR and ThT binding were tested with (K16pY) (E22L) peptide nanotubes. No absorbance shift was observed when CR mixes with (K16pY) (E22L) peptide nanotubes (Figure 2-31), but ThT fluorescence intensity drastically in the presence of (K16pY) (E22L) peptide nanotubes (Figure 2-32). Consistent with ThT binding to the phosphorylated peptide membrane surfaces, very likely as a result of electrostatic association.

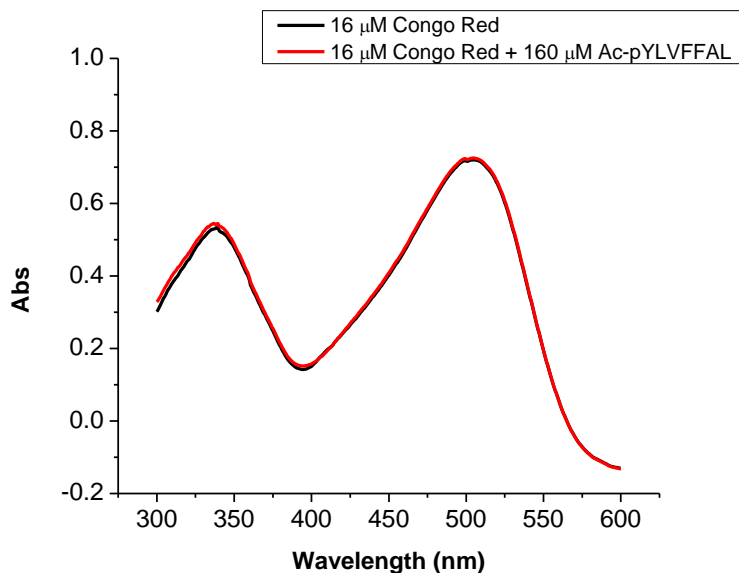


Figure 2-31 UV-Vis absorbance comparison of 16 μM CR (black), 16 μM CR + 160 μM (K16pY) (E22L) peptide nanotubes (red) in water, background corrected.

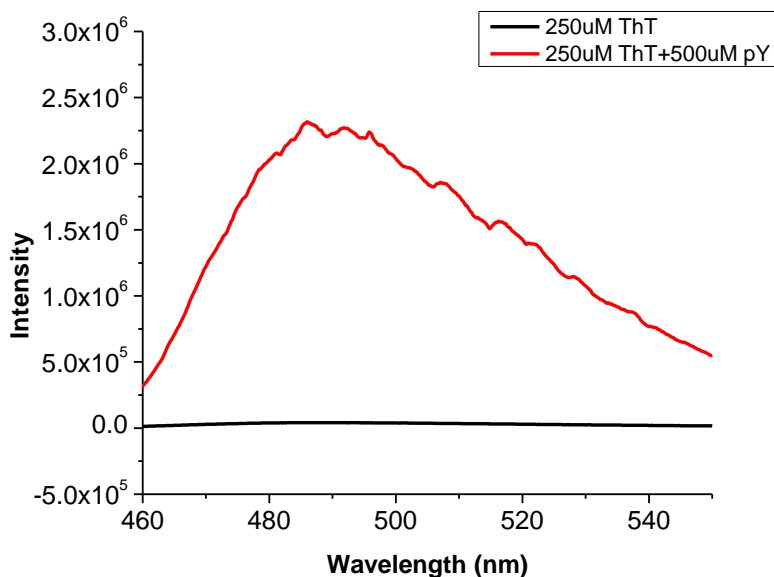


Figure 2-32 Florescence spectra of 250 μM ThT (black), 250 μM ThT μM CR + 500 μM (K16pY) (E22L) peptide nanotubes (red) in water.

Neurofibrillar Tangle Surrogates: Histone H1 Binding to Phosphotyrosine Peptide Nanotubes

The eukaryotic cell matrix presents a labyrinth of phospholipid membranes partitioning diverse compartments in a sea of ribonucleoproteins, phosphorylated metabolites, and

nucleic acid polymers. Such charged surfaces must all be navigated by the information processing cellular proteins that process nucleic acids. To further exploit the organizing potential of the peptide membranes as biomimetic surfaces, I extended small molecule binding to large protein binding in this section. Histone H1 was chosen for initial evaluation of the phosphorylated nanotube surfaces. It accumulates in the cytoplasm of neurons and astrocytes in areas impacted by neurodegenerative disease⁵⁴ and serves as a prototypical nucleic acid binding protein⁵⁵. The addition of histone H1 to (K16pY)(E22L) nanotubes does not disrupt the assemblies as visualized by transmission electron microscopy (TEM) (Figure 2-33 A), and two-photon fluorescence images in Figure 2-33 show Alexa 488 fluorophore-labeled calf thymus histone H1 specifically sequestered by the negatively charged (K16pY)(E22L) nanotubes (Figure 2-33 D), but not the positively charged (E22L) tubes (Figure 2-33 C). The precisely mapped electrochemical potential measurements on peptide assemblies appears to be independent of associated proteins as EFM are still consistent with negatively-charged peptide nanotubes. (Figure 2-34).

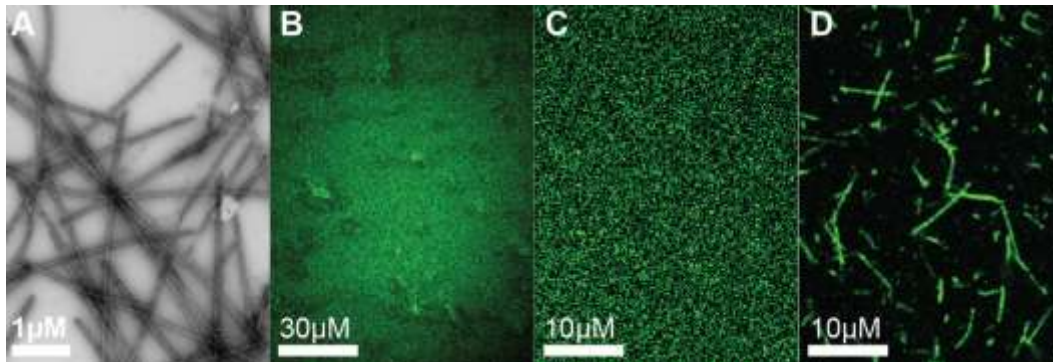


Figure 2-33 (A) TEM image of 500 μM (K16pY)(E22L) nanotube assemblies in the presence of 4.6 μM histone H1–Alexa 488 conjugate. (B–D) Single slices of the two-photon fluorescence image excited at 780 nm of 4.6 μM Alexa 488-labeled calf thymus histone H1 alone (B), in the presence of 500 μM E22L nanotube assemblies (C), and in the presence of 500 μM (K16pY)(E22L) nanotube assemblies (D).

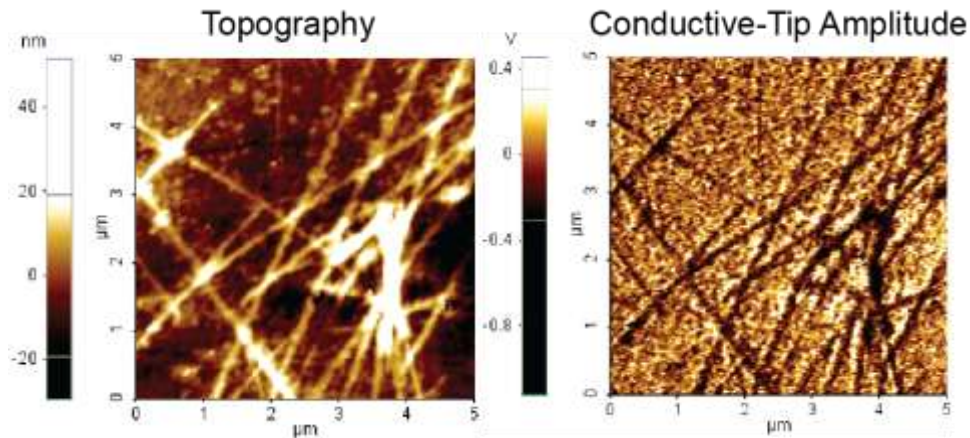


Figure 2-34 Atomic and electrostatic force microscopy images of (K16pY)(E22L) nanotube assemblies with surfaces coated by the positively charged Histone H1 protein. (Left) topography images of peptide nanotubes and (Right) EFM amplitude micrographs with a DC bias = +1V. (K16pY)(E22L) assemblies are attractive (dark) along the entire length of each assembled nanotube even in the presence of Histone H1.

Fluorescence imaging of histone H1 binding other the other two negatively-charged peptide nanotubes was also investigated. Histone H1 binds to Ac-pSLVFFAL nanotubes similarly to that of Ac-pYLVFFAL nanotubes. However, Histone H1 only causes aggregation or disassembly of Ac-ELVFFAL nanotubes (Figure 2-35), suggesting the binding interaction between histone H1 and the peptide nanotube surface is not merely electrostatic interaction, but more of specific interaction between histone H1 and phosphorylated membrane surfaces.

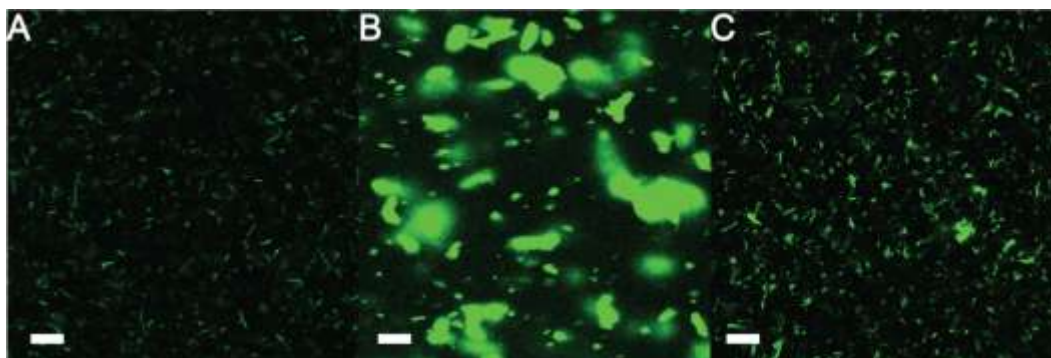


Figure 2-35 Single slices of confocal fluorescence image of 4.6 μM Alexa 488-labeled calf thymus histone H1 in the presence of 500 μM (A) Ac-pYLVFFAL nanotubes, (B) Ac-pYLVFFAL nanotubes, (D) Ac-pSLVFFALnanotubes. Scale bar 20 μm .

Isothermal titration calorimetry (ITC) thermograms show minimal heat change (Figure 3-35) between histone H1 and (E22L) assemblies. In contrast, the addition of histone to (K16pY)(E22L) nanotubes (Figure 3-36) fit to a one-site model with a large endothermic heat of binding ($\Delta H = 36.7 \pm 5$ kcal/mol) and a $-T\Delta S$ of -48 kcal/mol. This entropically driven association, with a K_a of $(2.09 \pm 0.3) \times 10^8$ M⁻¹, is remarkably 2 orders of magnitude higher than that of binding to calf thymus DNA at the same temperature.^{56,57} Even more significantly, the saturation stoichiometry of $(6.78 \pm 0.06) \times 10^{-3}$ binding sites per peptide translates into 147 ± 13 peptides per histone binding site. A binding site of 147 peptides represents an area of 11.3 nm \times 5.2 nm (59 nm²) on the nanotube surface, a large area for a 2.9 nm diameter globular protein with short unstructured N- and C termini⁵⁵.

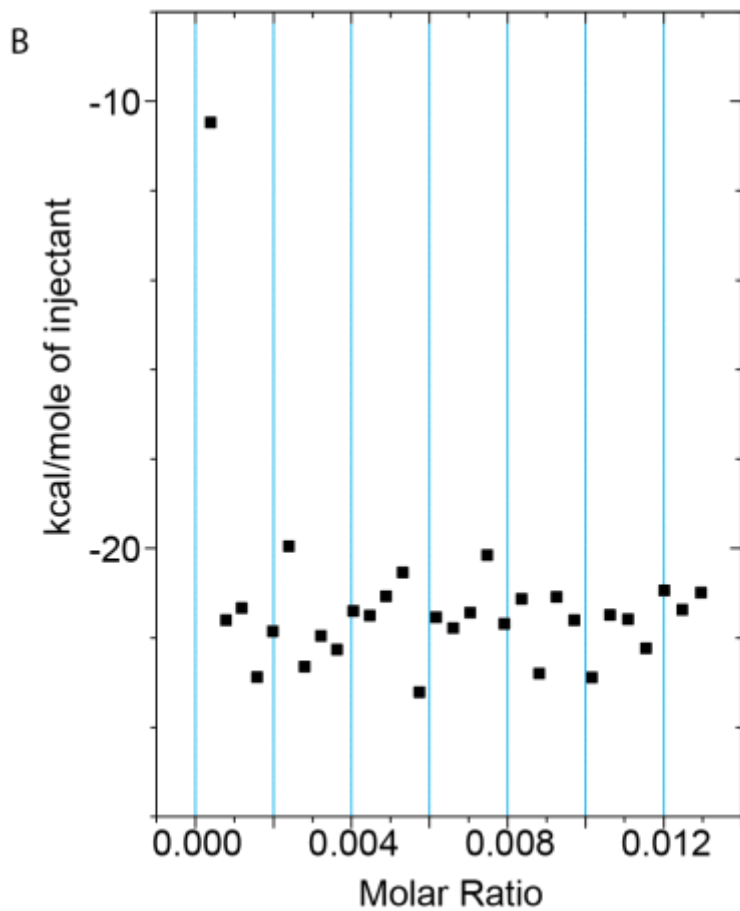
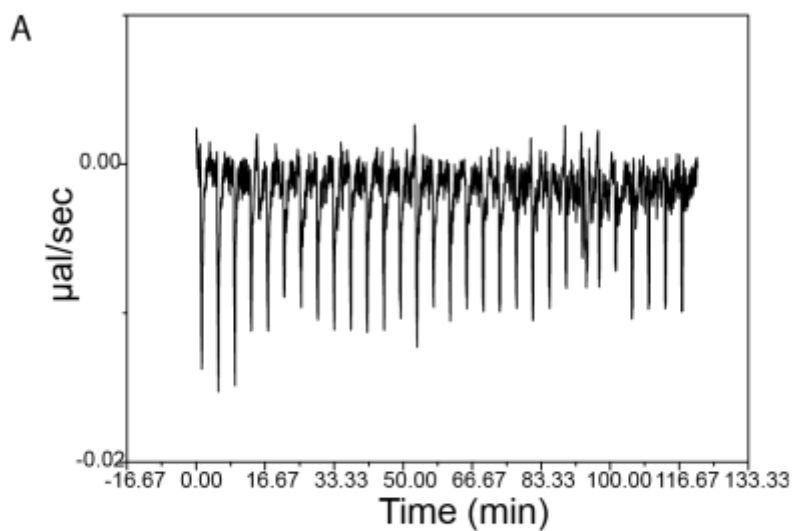


Figure 2-36 Typical ITC titration curve for the addition of Histone H1 to (E22L) nanotube solutions. (A) Baseline-corrected raw ITC signal for 30 injections of Histone H1 protein solution (300 μL of 2.25 μM) into the ITC cell filled with (E22L) nanotube solution (40 μM initial peptide concentration). (B)

Apparent ΔH for each injection, consistent with the positively charged histone not interacting with the positively charged peptide nanotube.

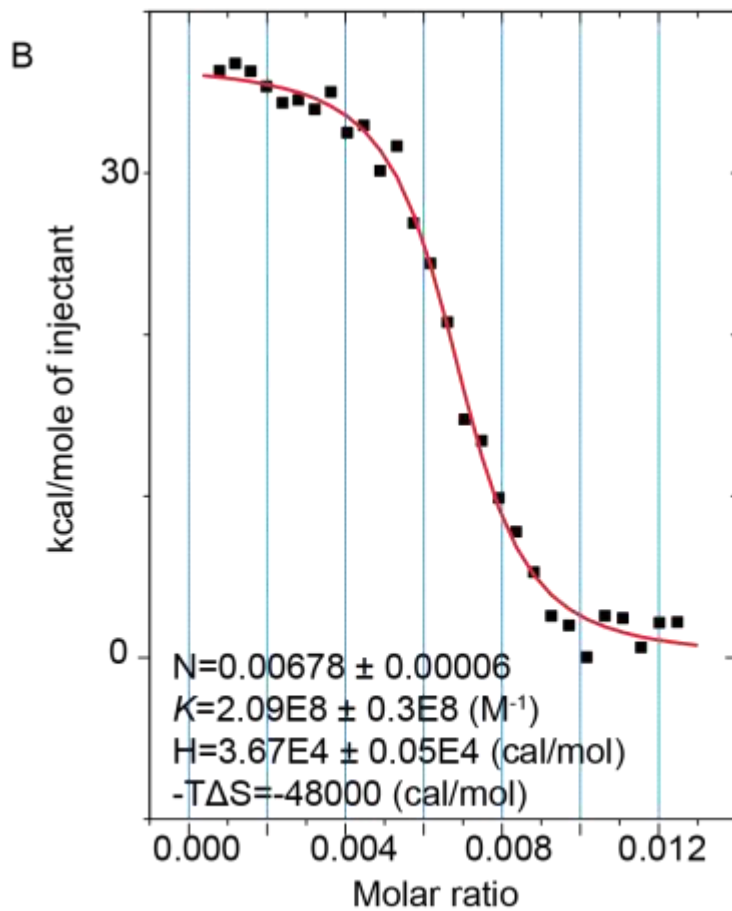
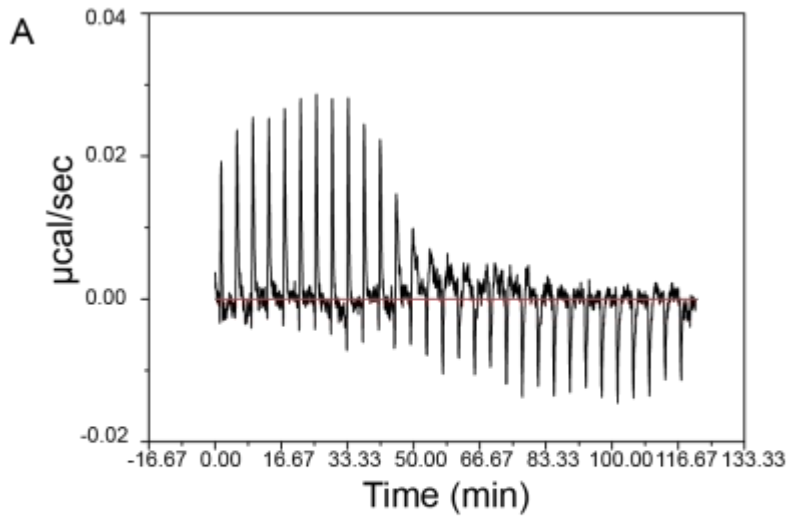


Figure 2-37 Typical ITC titration for addition of Histone H1 to (K16pY) (E22L) nanotube solutions. (A) Baseline-corrected raw ITC signal for 30 injections of a Histone H1 protein solution (300 μL of 2.25

μM) into the ITC cell filled with (K16pY) (E22L) nanotube solution ($40 \mu\text{M}$ initial peptide concentration). (B) Apparent ΔH for each injection along with the best-fit to a one-site binding model. Errors listed are the standard deviations for the best fit parameters K_d and ΔH determined in triplicate experiments.

To confirm the histone binding ITC values, fluorescence polarization (FP) is followed as (K16pY)(E22L) nanotubes are titrated into a fixed histone H1–Alexa 488 concentration (Figure 3-13). Assuming noncooperative association and 147 peptides per binding site, the K_d of $(4.8 \pm 2.9) \times 10^{-9}\text{M}$ is identical to the K_d determined by ITC [$(4.78 \pm 0.58) \times 10^{-9}\text{M}$]. A recent evaluation of the binding of histone H1 to DNA identifies a binding site of $32 \pm 1\text{ bp}$,²⁴ consistent with a histone length of 11 nm. With the 2.9 nm diameter of the globular domain, the histone coverage area can be estimated to be $11\text{ nm} \times 3\text{ nm}$ (33 nm^2), on the order of the surface area calculated for binding to the (K16pY)(E22L) nanotube surfaces and consistent with significant conformational plasticity upon binding.

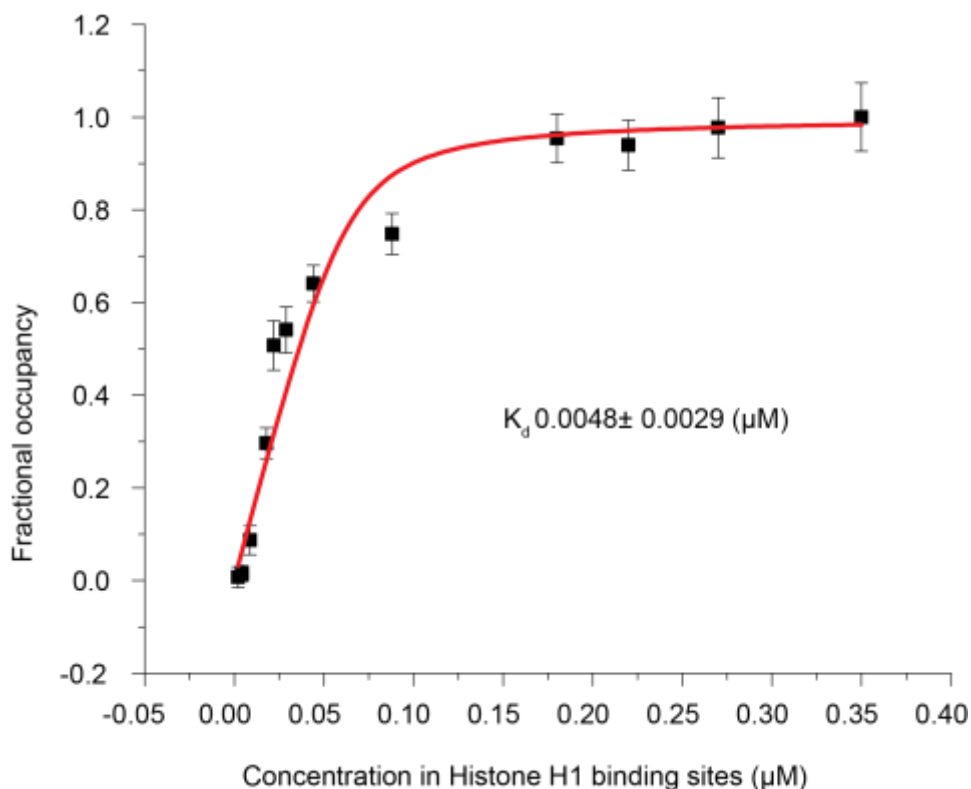


Figure 2-38 Fluorescence polarization saturation data for Histone H1–Alexa 488 conjugate and (K16pY) (E22L) nanotubes with a protein concentration of $0.0625\mu\text{M}$ and the (K16pY) (E22L) peptide concentrations of 0.32, 0.65, 1.3, 2.6, 3.2, 4.3, 6.5, 13, 26, 33, 39, 52 μM and converted to

concentration of his-tone binding sites (divided by 147 peptides per binding site). Fractional occupancy is plotted versus concentration in histone H1 binding sites.

Association of histone H1 with the DNA backbone⁵⁸ is important in gene regulation⁵⁹, chromatin condensation⁶⁰, and global control over chromatin remodeling activities⁶¹. However, H1 also permeates biological membranes and has been used to chaperone chimeric macromolecules across cell barriers⁶², highlighting the range of phosphorylated surfaces on which this protein functions. Demonstration of histone H1 binding with the phosphorylated peptide membranes opens the route for using peptide membrane as model surfaces to study protein associations.

Conclusions

In this chapter I have generated highly ordered phosphorylated peptide membrane surfaces by a simple N-terminal residue replacement of the A β (16-22) (E22L) peptide. This (K16pY)(E22L) peptide exhibits identical cross- β bilayer structure as the (E22L) peptide. AuNPs binding and salt bundling strategies were employed to test the surface charges of the two peptide nanotubes. I have further demonstrated electrostatic force microscopy (EFM) analyses that map the charge distribution on these self-assembled peptide membranes in a partially dried state. The results are consistent with homogeneously charged peptide membrane surfaces that achieve microscale order and open new opportunities for characterizing more complex and dynamic self-assembled engineered materials.

The successful characterization of surface charge properties of peptide membranes made it possible to exhibit small molecules and large proteins association with the surfaces. The synthetic accessibility and morphological tractability of these patterned peptide surfaces^{7,22} now opens entirely new possibilities for studying protein associations. For example, given that histone H1 was the first nucleic acid binding protein to be identified as mislocalized in amyloid diseases⁵⁴ and the recent implications of accumulation of other information processing proteins in disease plaques⁶³, this neurofibrillar tangle surrogate can be used for proteomic screening of AD tissues and other aberrant cellular assemblies and exploration of seeding and co-assembly in disease etiology⁶⁴.

Methods

Peptide synthesis and purification

Peptides were synthesized using a Liberty CEM Microwave Automated Peptide Synthesizer (NC, USA) and a Fmoc-Rink Amide MBHA Resin (AnaSpec, CA, USA). Fmoc-Rink Amide MBHA Resin was swollen using dimethylformamide for 15 minutes. Microwave assisted Fmoc deprotection was completed using 20% piperidine in dimethylformamide at 45-55°C for 180 sec, followed by 3X dimethylformamide flushes. Each Fmoc-amino acid coupling step was performed using 0.1M Fmoc protected amino acid and activated with 0.1 M 2-(1H-Benzotriazole-1-yl)-1,1,3,3-tetramethyluronium hexafluorophosphate (HBTU), and 0.2 M N,N-Diisopropylethylamine (DIEA) in DMF. Coupling temperatures using microwave were maintained between 75-82°C for 300 sec, then rinsed with three aliquots of dimethylformamide. Phosphotyrosine and phosphoserine was double coupled with 6W power instead of 8W for other amino acids resulting in a final temperature for coupling of 75°C. Final acetylation of the N-terminus was achieved by addition 20% acetic anhydride in dimethylformamide. Resin was filtered and washed with dichloromethane and allowed to air dry. Peptides were cleaved from the resin using trifluoroacetic acid/thioanisole/1,2-ethanedithiol/anisole (90: 5 : 3 : 2, v/v/v/v) at room temperature for 3 hrs. The cleaved peptide-TFA solution was filtered, and precipitated by drop-wise addition to cold (-20°C) diethyl ether. Precipitated product was centrifuged at 3000 rpm for 10 min, and the pellet was further washed 3 times with cold diethyl ether. Dried Ac-KLVFFAL-NH₂ peptide was dissolved in minimal volume of 40% acetonitrile/H₂O + 0.1% trifluoroacetic acid and purified by RP-HPLC using a C18-reverse phase column with an acetonitrile-water gradient. Ac-(pY)LVFFAL-NH₂, Ac-(pS)LVFFAL-NH₂ and Ac-(E)LVFFAL-NH₂ peptide was dissolved in minimal volume of 40% acetonitrile/triethylammonium acetate buffer (pH 7) and purified by HPLC with an acetonitrile-triethylammonium acetate buffer (100mM) gradient. Molecular weight was confirmed by MALDI-TOF using a 2,5-dihydroxybenzoic acid matrix.

Peptide Assembly

Peptide powders were dissolved in HFIP to make sure no pre-formed aggregates were present before assembly and dried via a centrivap concentrator. The HFIP treated peptide sample was dissolved in 40% acetonitrile/water, adjusted to pH 7 with NaOH, by vortexing and sonication at room temperature. Since TFA was present during purification

and after lyophilization of Ac-KLVFFAL-NH₂ peptide, no extra TFA was added to the assembly solvents (40% acetonitrile/water). For Ac-(pY)LVFFAL-NH₂, Ac-(pS)LVFFAL-NH₂ and Ac-(E)LVFFAL-NH₂ peptide, clear films are usually presented after lyophilization instead of commonly seen white powders. To assemble Ac-(pY)LVFFAL-NH₂, Ac-(pS)LVFFAL-NH₂ and Ac-(E)LVFFAL-NH₂ peptides 15 mM triethylammonium acetate buffer was used instead of pure water. Incubation at 4°C for 1-3 weeks was generally required for the sample maturation.

Transmission Electron Microscopy Imaging

Upon addition to TEM grid (carbon/copper), the peptide assemblies were allowed to adsorb for 1 min. Excess peptide solution was wicked away with filter paper. 2-wt % uranyl acetate was added to TEM grids and incubated for 3-5 minutes. Samples were then placed in a vacuum dessicator overnight. TEM micrographs were recorded with a Hitachi 7500 TEM at magnifications ranging from 2, 000x to 200, 000x with a Tungsten filament at an accelerating voltage of 75 kV.

Circular Dichroism

CD spectra were recorded using a JASCO J-810 spectropolarimeter fitted with a Peltier temperature controller. Samples (25 µL) were placed into a quartz cuvette with a 0.1 mm path length (Starna Cells). Each spectrum was obtained by scanning wavelength from 300 nm to 180 nm at a scanning rate of 100 nm/min with a resolution of 0.2 nm. Three successive wavelength scans were averaged for each sample. Buffer control spectra were averaged and subtracted from the sample spectra.

Fourier-Transform Infrared Spectroscopy

Sample aliquots (10µL) were dried as thin films on an ATR diamond cell. The IR spectra were acquired using a Jasco FT-IR 4100 ATR with a diamond crystal at room temperature and averaging 256 scans with 4 cm⁻¹ resolution. Background spectra were acquired immediately before each sample and were subtracted from each sample spectrum.

X-ray powder diffraction

Assembled peptide nanotubes were bundled with sulfate or magnesium with the ratio of peptide to salt 1:10. The white precipitate was collected by centrifugation.

The pellet was frozen and lyophilized to yield dry powder for X-ray diffraction. The powder spectra were obtained using a Bruker D8 Discover diffractometer, equipped with a multiposition X, Y, Z stage, a cobalt X-ray tube with Goebel mirror and a Vantec1 solid state detector. The sample was placed in a zero-background holder on the stage and the spectrum obtained using Bragg-Brentano geometry. The scan step was repeated several times to maximize the diffracted intensity and minimize noise.

Peptide Registry Determined by Solid-State NMR

Mature nanotubes were bundled with MgCl_2 with a peptide to magnesium ratio of 1:1. Previously, counter-ion bundling of nanotubes has been shown to protect assemblies from freezing and lyophilization.⁶⁵ The resulting white precipitate was pelleted by centrifugation for 10 min at 13000g to remove any unassembled peptides, frozen and lyophilized to yield dry powder. TEM confirmed the presence of only intact tubes after lyophilization. The NMR sample (~40 mg) was packed into a 4 mm solid-state NMR rotor and centered using boron nitride spacers.

All NMR spectra were collected with a Bruker (Billerica, MA) Avance 600 spectrometer and a Bruker 4 mm HCN biosolids magic-angle spinning (MAS) probe. The pulse sequence for $^{13}\text{C}\{^{15}\text{N}\}$ rotational-echo double-resonance (REDOR)⁶⁶⁻⁶⁸ consists of two parts, an S sequence that contains both ^{13}C and ^{15}N pulses, and the S_0 sequence which is identical but does not contain any ^{15}N dephasing pulses. Pulsing the dephasing ^{15}N spins interferes with the averaging of the ^{13}C - ^{15}N dipolar coupling due to magic-angle spinning. This is observed in the REDOR S spectrum, where the signal decays according to both T_2 (spin-spin relaxation) and the heteronuclear ^{13}C - ^{15}N dipolar coupling. Maximum dephasing occurs when the spacing between the ^{15}N pulses is equal to $\frac{1}{2}$ of the rotor-cycle. The sequence without any ^{15}N dephasing pulses gives the REDOR full-echo or S_0 spectra, where the magnetization decays according to only T_2 . The difference between the REDOR S and S_0 signal (ΔS) is directly proportional to the dipolar coupling, hence the distance between the two spins.

To compensate for pulse imperfections, xy8 phase cycling⁶⁹ of $^{13}\text{C}\{^{15}\text{N}\}$ REDOR⁶⁶⁻⁶⁸ 4 and 8 μs rotor-synchronized ^{13}C and ^{15}N π -pulses, respectively, and EXORCYCLE phase cycling^{70,71} of the final ^{13}C Hahn-echo refocusing pulse were applied with 128 kHz Spinal64⁷² ^1H decoupling. To minimize the effects of RF inhomogeneity^{71,73}, ^{13}C π -pulse

power level was arrayed in the REDOR S_0 pulse sequence at long REDOR evolution times (54.4 ms, corresponding to ~ 544 $4 \mu\text{s}$ ^{13}C π pulses) and choosing the power level that corresponded to the maximum signal intensity.⁷⁴ Similarly, ^{15}N π pulses were determined by arraying the ^{15}N power level using the REDOR S experiment at REDOR evolution times corresponding to a S/S_0 between 0.3 and 0.5.⁷⁴ To normalize for the decay due to T_2 , individual REDOR curves are plotted as $\Delta S/S_0$. REDOR data points are the integrated sum of center- and sideband peaks. Error bars were calculated using the noise of each spectrum as the maximum peak height deviation. REDOR data points were fit with an analytical function⁷⁵ that describes the REDOR dephasing as a function of the heteronuclear dipolar coupling, the number of rotor cycles and the rotor period for a single observe spin in the presence of multiple dephasing spins⁷⁶. ^{15}N dephasing spins were fixed at a distance of 9.4 Å, corresponding the distance from XRD, and REDOR curves were calculated as a function of the ^{13}C position.

MAS frequency was kept under active control at 10 kHz \pm 2 Hz. The cooling and spinning air exit temperature was maintained below -1 °C to ensure MAS and RF heating did not denature the samples. ^{13}C (150.8 MHz) and ^{15}N (60.8 MHz) CP-MAS spectra before and after $^{13}\text{C}\{^{15}\text{N}\}$ REDOR experiments confirmed that the samples did not change during the experiment.

Atomic Force Microscopy

20 μL of assembled peptide solutions were diluted to desired concentrations and placed on a silicon chip (4" diameter diced silicon wafer (TedPella, Inc, Redding, CA) previously cleaned by sonication in methanol for 20 min, for one minute at room temperature. Excess solution was removed with filter paper and the chip was rinsed with distilled H_2O . Tapping mode analysis on a JEOL JSPM-4210 scanning probe microscope employed ultra-sharp non-contact silicon cantilevers (MikroMasch, Wilsonville, OR) with typical frequencies between 240 and 350 kHz. Images were collected on dry samples.

Gold Nano Particle Binding

Negatively-charged gold nanoparticles were synthesized⁷⁷ by addition of freshly prepared 3mM sodium citrate solution (500 μL) to 0.3mM aqueous solution of HAuCl_4 (4.4mL), and stirred for ~ 10 min. Freshly prepared, ice-cold, 0.3M NaBH_4 (60 μL) was added while stirring. The solution immediately turned pink, indicating the formation of

gold nanoparticles. The concentration ratio of [Au]/[capping agent]/[NaBH₄] was 1:1:12. The spherical-shaped nanoparticles of dimensions 4±1 nm showed a localized surface plasmon resonance (SPR) transition at 505 nm, as measured with a Jasco V-530 UV spectrophotometer, and were further characterized by TEM. Positively-charge gold 10nm cationic gold nanoparticles (Cytodiagnosics, Canada) were surface functionalized with (11-Mercaptoundecyl)-N,N,N-trimethylammonium bromide.

For gold binding studies, 200µL of preformed gold colloid (0.3mM) was mixed with 5µL mature peptide nanotubes (1.3mM) to a final 9.2:1 ratio of gold to peptide. The mixture was incubated at room temperature for 3hrs, until a purple red precipitate gradually formed. After centrifugation, the collected pellet was resuspended in the assembly solution. Then 10µL of sample was applied to TEM grid for 2min, and excess solvent was removed with filter paper. The sample grid was stored in vacuum dessicator overnight before imaging.

Bundling Peptide Nanotubes

Salts, molar ratio to peptide 4.5:1, were added to peptides assembled as nanotubes. If white precipitation was formed (usually formed within several minutes), the solution was centrifuged and the supernatant was discarded and the pellet was dissolved in identical solvent and used for TEM imaging. If no precipitant was formed after 1 hr, this solution was used for TEM imaging directly.

Electrostatic Force Microscopy

Electrostatic Force Microscopy (EFM) was performed on Park System XE-100 AFM. Pt-Ir coated electrically conductive cantilevers were used to map electrical properties on the samples. The cantilevers had a tip radius <20nm and a force constant 2.8 N/m. EFM was operated in ambient conditions. Prior to EFM imaging, the peptide samples were deposited on Si/SiO₂ substrates. The thickness of oxide layer was 300nm. 10 µL droplets of the peptide nanotubes suspended in the liquid solution were placed on the Si substrates and air dried over 12 hours.

For EFM, the sample surface properties are electrical properties and the interaction force is the electrostatic force between the biased tip and sample. Nevertheless, one must be cautious that apart from the electrostatic force, the van der Waals forces

between the tip and the sample surface are always present⁷⁸. The magnitude of these van der Waals forces change according to the tip-sample distance, and are therefore used to measure the surface topography. Hence, the obtained signal contains both information of surface topography (called 'Topo signal') and information of surface electrical property (called 'EFM signal') generated by the van der Waals and electrostatic forces^{41,78}, respectively. Enhanced EFM (Ext)⁴⁰ is used in this thesis to separate EFM signal from the entire signal.

Atomic Force Microscopy

20uL of assembled peptide solutions were diluted to desired concentrations and placed on a silicon chip (4" diameter diced silicon wafer (TedPella, Inc, Redding, CA) previously cleaned by sonication in methanol for 20min, for one minute at room temperature. Excess solution was removed with filter paper and the chip was rinsed with distilled H₂O. Tapping mode analysis on a JEOL JSPM-4210 scanning probe microscope employed ultra-sharp non-contact silicon cantilevers (MikroMasch, Wilsonville, OR) with typical frequencies between 240 and 350 kHz. Images were collected on dry samples.

Histone Fluorescence Imaging

Alexa Fluor® 488 histone H1 conjugate (H-13188, Life technologies) was dissolved in distilled H₂O with 2mM sodium azide. Ac-(pY)LVFFAL-NH₂ nanotube assemblies were pelleted at 13,000 g and suspended in distilled H₂O. CD and EFM confirmed peptides were still assembled as nanotubes after resuspension. 500µM Ac-(pY)LVFFAL-NH₂ nanotubes were mixed with 10µg/mL histone Alexa 488 and used for fluorescence imaging. Two-photon fluorescence images were acquired on a home built two-photon microscopes as described previously.⁷⁹ All images were acquired with excitation at 780 nm and detected using photomultiplier tubes (H7421) from Hamamatsu using a 200 nm Z-stack window.

Isothermal Titration Calorimetry

Isothermal titration calorimetry (ITC) experiments were performed using a Microcal VP-ITC (Northampton, MA, USA). Histone H1 (21.5 kDa, H5505, Sigma) was dissolved in phosphate buffered saline (PBS, 10 mM, pH 7.4) and exhaustively dialyzed against PBS buffer for 24 hr at 4°C. Ac-(pY)LVFFAL-NH₂ nanotubes were pelleted and washed 5 times with protein dialysis buffer. All titrations were performed by overfilling the ITC cell

with approximately 1.5 mL of Ac-(pY)LVFFAL-NH₂ nanotube solution. During a typical ITC titration, approximately 300 µL of the Histone H1 protein solution (2.25 µM) was added to the Ac-(pY)LVFFAL-NH₂ nanotube solution (40 µM) in the micro-calorimeter cell in 30 increments delivered at 240 second intervals. All ITC experiments were performed in triplicate and at 25°C.

Non-linear regression using equations characteristic for a system exhibiting multiple sets of independent binding sites (one-site model) provided with the Microcal software yielded best fit parameters for K , ΔH and N , with:

$$K = \frac{\Theta}{(1 - \Theta)[X]}$$

$$X_t = [X] + N\Theta M_t$$

where K = binding constant, N = number of sites per peptide, V_0 = active cell volume, M_t and $[M]$ are bulk and free concentration of peptide in V_0 , X_t and $[X]$ are bulk and free concentration of ligand (histone), and Θ = fraction of sites occupied by histone.

The total heat content Q of the solution contained in V_0 at fractional saturation is:

$$Q = N\Theta M_t \Delta H V_0$$

Solving equation above equations gives

$$Q = \frac{NM_t \Delta H V_0}{2} \left[1 + \frac{X_t}{NM_t} + \frac{1}{NKM_t} - \sqrt{\left(1 + \frac{X_t}{NM_t} + \frac{1}{NKM_t}\right)^2 - \frac{4X_t}{NM_t}} \right]$$

Analysis of calorimetric titration data is performed by estimating the variable model parameters (N , K and ΔH) by fitting to the cumulative heat Q , or to the individual heat, q (where the individual heat associated with the j -th injection event is q_j such that $q_j = Q_j - Q_{j-1}$).

The number of binding sites per peptide, N , can be converted into the number of peptides per binding site = $\frac{1}{N}$.

Fluorescence Polarization

Fluorescence polarization was performed using fluoromax-3 spectrofluorometer (Horiba Jobin Yvon, Edison, NJ) with a polarizer accessory. A fixed concentration (0.0625 µM) of Histone H1 from calf thymus, Alexa fluor 488 conjugate (Life technologies, H-13188)

dissolved in PBS buffer (10 mM pH 7.4) was mixed with varied concentration of Ac-(pY)LVFFAL-NH₂ nanotube solutions and incubated for 30 min. Polarization readings typically stabilized within 20 min after mixing, (data not shown). Fractional occupancy, fB , is defined by using the equation: $fB = (P - P_{min}) / \Delta P$, where P is the measured polarization, $\Delta P (= P_{max} - P_{min})$ is the total change in polarization. K_d was determined via the following equation⁸⁰:

$$F = \frac{K_d + L_{ST} + R_T - \sqrt{(K_d + L_{ST} + R_T)^2 - 4L_{ST}R_T}}{2L_{ST}}$$

F : the fraction of bound labeled ligand (Histone H1)

L_{ST} : total input concentrations of ligands (Histone H1)

R_T : total input concentrations of receptors ((K16pY)(E22L) assemblies)

K_d : disassociation constant of the interaction.

References

- (1) Alonso, A. d. C.; Zaidi, T.; Novak, M.; Grundke-Iqbal, I.; Iqbal, K. *Proceedings of the National Academy of Sciences* **2001**, *98*, 6923.
- (2) Inoue, M.; Hirata, A.; Tainaka, K.; Morii, T.; Konno, T. *Biochemistry* **2008**, *47*, 11847.
- (3) Inoue, M.; Konno, T.; Tainaka, K.; Nakata, E.; Yoshida, H.-o.; Morii, T. *Biochemistry* **2012**, *51*, 1396.
- (4) Williams, D. R. *Intern. Med. J.* **2006**, *36*, 652.
- (5) Siddiqua, A.; Margittai, M. *J. Biol. Chem.* **2010**, *285*, 37920.
- (6) Bai, B.; Hales, C. M.; Chen, P. C.; Gozal, Y.; Dammer, E. B.; Fritz, J. J.; Wang, X.; Xia, Q.; Duong, D. M.; Street, C.; Cantero, G.; Cheng, D.; Jones, D. R.; Wu, Z.; Li, Y.; Diner, I.; Heilman, C. J.; Rees, H. D.; Wu, H.; Lin, L.; Szulwach, K. E.; Gearing, M.; Mufson, E. J.; Bennett, D. A.; Montine, T. J.; Seyfried, N. T.; Wingo, T. S.; Sun, Y. E.; Jin, P.; Hanfelt, J.; Willcock, D. M.; Levey, A.; Lah, J. J.; Peng, J. *Proc Natl Acad Sci U S A* **2013**, *110*, 16562.
- (7) Mehta, A. K.; Lu, K.; Childers, W. S.; Liang, Y.; Dublin, S. N.; Dong, J.; Snyder, J. P.; Pingali, S. V.; Thiyagarajan, P.; Lynn, D. G. *J. Am. Chem. Soc.* **2008**, *130*, 9829.
- (8) Childers, W. S.; Mehta, A. K.; Ni, R.; Taylor, J. V.; Lynn, D. G. *Angewandte Chemie-International Edition* **2010**, *49*, 4104.
- (9) Hianik, T. *Acta Physica Slovaca* **2006**, *56*, 687.
- (10) Hamley, I. W.; Nutt, D. R.; Brown, G. D.; Miravet, J. F.; Escuder, B.; Rodríguez-Llansola, F. *The Journal of Physical Chemistry B* **2010**, *114*, 940.
- (11) Astbury, W. T.; Dickinson, S.; Bailey, K. *Biochem. J* **1935**, *29*, 2351.
- (12) Kirschner, D. A.; Abraham, C.; Selkoe, D. J. *Proc. Natl. Acad. Sci. U.S.A.* **1986**, *83*, 503.
- (13) Geddes, A. J.; Parker, K. D.; Atkins, E. D. T.; Beighton, E. *J. Mol. Biol.* **1968**, *32*, 343.
- (14) Inouye, H.; Fraser, P. E.; Kirschner, D. A. *Biophys. J.* **1993**, *64*, 502.
- (15) Sunde, M.; Blake, C. C. *Q Rev Biophys* **1998**, *31*, 1.
- (16) Gullion, T.; Schaefer, J. *Journal of Magnetic Resonance (1969)* **1989**, *81*, 196.
- (17) Wiltzius, J. J. W.; Landau, M.; Nelson, R.; Sawaya, M. R.; Apostol, M. I.; Goldschmidt, L.; Soriaga, A. B.; Cascio, D.; Rajashankar, K.; Eisenberg, D. *Nat Struct Mol Biol* **2009**, *16*, 973.
- (18) Walker, L. C.; Levine, H., 3rd; Mattson, M. P.; Jucker, M. *Trends Neurosci* **2006**, *29*, 438.
- (19) Chiti, F.; Dobson, C. M. *Annu Rev Biochem* **2006**, *75*, 333.
- (20) Pedersen, J. S.; Otzen, D. E. *Protein Science : A Publication of the Protein Society* **2008**, *17*, 2.
- (21) Kodali, R.; Wetzel, R. *Curr. Opin. Struct. Biol.* **2007**, *17*, 48.
- (22) Childers, W. S.; Anthony, N. R.; Mehta, A. K.; Berland, K. M.; Lynn, D. G. *Langmuir* **2012**, *28*, 6386.
- (23) Lingwood, D.; Simons, K. *Science* **2010**, *327*, 46.
- (24) Nicolson, G. L. *Biochimica Et Biophysica Acta-Biomembranes* **2014**, *1838*, 1451.
- (25) Childers, W. S.; Mehta, A. K.; Lu, K.; Lynn, D. G. *J. Am. Chem. Soc.* **2009**, *131*, 10165.

- (26) Dong, J.; Canfield, J. M.; Mehta, A. K.; Shokes, J. E.; Tian, B.; Childers, W. S.; Simmons, J. A.; Mao, Z.; Scott, R. A.; Warncke, K.; Lynn, D. G. *Proc. Natl. Acad. Sci. U.S.A.* **2007**, *104*, 13313.
- (27) Dong, J. J.; Shokes, J. E.; Scott, R. A.; Lynn, D. G. *J. Am. Chem. Soc.* **2006**, *128*, 3540.
- (28) Kamat, P. V. *J. Phys. Chem. B* **2002**, *106*, 7729.
- (29) De, M.; Ghosh, P. S.; Rotello, V. M. *Adv. Mater.* **2008**, *20*, 4225.
- (30) Dreaden, E. C.; Alkilany, A. M.; Huang, X. H.; Murphy, C. J.; El-Sayed, M. A. *Chem. Soc. Rev.* **2012**, *41*, 2740.
- (31) Nel, A. E.; Madler, L.; Velegol, D.; Xia, T.; Hoek, E. M. V.; Somasundaran, P.; Klaessig, F.; Castranova, V.; Thompson, M. *Nat. Mater.* **2009**, *8*, 543.
- (32) Mahmoudi, M.; Lynch, I.; Ejtehadi, M. R.; Monopoli, M. P.; Bombelli, F. B.; Laurent, S. *Chem. Rev.* **2011**, *111*, 5610.
- (33) Sadeghi, R.; Jahani, F. *The Journal of Physical Chemistry B* **2012**, *116*, 5234.
- (34) Lu, K.; Guo, L.; Mehta, A. K.; Childers, W. S.; Dublin, S. N.; Skanthakumar, S.; Conticello, V. P.; Thiyagarajan, P.; Apkarian, R. P.; Lynn, D. G. *Chem. Commun.* **2007**, 2729.
- (35) Butt, H. J.; Cappella, B.; Kappl, M. *Surf. Sci. Rep.* **2005**, *59*, 1.
- (36) Giessibl, F. J. *Reviews of Modern Physics* **2003**, *75*, 949.
- (37) Binnig, G.; Quate, C. F.; Gerber, C. *Phys. Rev. Lett.* **1986**, *56*, 930.
- (38) Reich, Z.; Kapon, R.; Nevo, R.; Pilpel, Y.; Zmora, S.; Scolnik, Y. *Biotechnol. Adv.* **2001**, *19*, 451.
- (39) Paul, G. *Nanotechnology* **2001**, *12*, 485.
- (40) www.parkAFM.com.
- (41) Instruments, D. Available online: <http://nanopicolab.cnsi.ucla.edu/pages/publicview/manuals/230A-EFM.pdf>, 1996.
- (42) Xu, S.; Arnsdorf, M. F. *Proceedings of the National Academy of Sciences* **1995**, *92*, 10384.
- (43) Katano, Y.; Doi, T.; Ohno, H.; Yoh, K. *Appl. Surf. Sci.* **2002**, *188*, 399.
- (44) Bickmore, B. R.; Hochella, M. F.; Bosbach, D.; Charlet, L. *Clays Clay Miner.* **1999**, *47*, 573.
- (45) Burnett, T.; Yakimova, R.; Kazakova, O. *Nano Lett.* **2011**, *11*, 2324.
- (46) Gomez, A.; Avila, A.; Hinestroza, J. P. *J. Electrostatics* **2010**, *68*, 79.
- (47) Bonilla, R.; Ávila, A.; Montenegro, C.; Hinestroza, J. *Journal of Microscopy* **2012**, *248*, 266.
- (48) Clausen, C. H.; Dimaki, M.; Panagos, S. P.; Kasotakis, E.; Mitraki, A.; Svendsen, W. E.; Castillo-León, J. *Scanning* **2011**, *33*, 201.
- (49) Lee, G.; Lee, W.; Lee, H.; Lee, S. W.; Yoon, D. S.; Eom, K.; Kwon, T. *Appl. Phys. Lett.* **2012**, *101*, 043703.
- (50) Puchtler, H.; Sweat, F.; Levine, M. *Journal of Histochemistry & Cytochemistry* **1962**, *10*, 355.
- (51) Klunk, W. E.; Pettegrew, J. W.; Abraham, D. J. *Journal of Histochemistry & Cytochemistry* **1989**, *37*, 1273.
- (52) Biancalana, M.; Koide, S. *Biochim Biophys Acta* **2010**, *1804*, 1405.
- (53) Khurana, R.; Coleman, C.; Ionescu-Zanetti, C.; Carter, S. A.; Krishna, V.; Grover, R. K.; Roy, R.; Singh, S. *J Struct Biol* **2005**, *151*, 229.
- (54) Duce, J. A.; Smith, D. P.; Blake, R. E.; Crouch, P. J.; Li, Q.-X.; Masters, C. L.; Trounce, I. A. *J. Mol. Biol.* **2006**, *361*, 493.
- (55) Dootz, R.; Toma, A. C.; Pfohl, T. *Biomicrofluidics* **2011**, *5*, 024104.

- (56) Machha, V. R.; Jones, S. B.; Waddle, J. R.; Le, V. H.; Wellman, S.; Lewis, E. A. *Biophys. Chem.* **2014**, *185*, 32.
- (57) Xiao, B.; Freedman, B. S.; Miller, K. E.; Heald, R.; Marko, J. F. *Molecular Biology of the Cell* **2012**, *23*, 4864.
- (58) Graziano, V.; Gerchman, S. E.; Schneider, D. K.; Ramakrishnan, V. *Nature* **1994**, *368*, 351.
- (59) Dou, Y.; Gorovsky, M. A. *Mol. Cell*, *6*, 225.
- (60) Roth, S. Y.; Allis, C. D. *Trends Biochem. Sci* **1992**, *17*, 93.
- (61) Horn, P. J.; Carruthers, L. M.; Logie, C.; Hill, D. A.; Solomon, M. J.; Wade, P. A.; Imbalzano, A. N.; Hansen, J. C.; Peterson, C. L. *Nat Struct Mol Biol* **2002**, *9*, 263.
- (62) Hariton-Gazal, E.; Rosenbluh, J.; Graessmann, A.; Gilon, C.; Loyter, A. *J. Cell Sci.* **2003**, *116*, 4577.
- (63) Dammer, E. B.; Duong, D. M.; Diner, I.; Gearing, M.; Feng, Y.; Lah, J. J.; Levey, A. I.; Seyfried, N. T. *Journal of proteome research* **2013**, *12*, 3193.
- (64) Bai, B.; Hales, C. M.; Chen, P.-C.; Gozal, Y.; Dammer, E. B.; Fritz, J. J.; Wang, X.; Xia, Q.; Duong, D. M.; Street, C.; Cantero, G.; Cheng, D.; Jones, D. R.; Wu, Z.; Li, Y.; Diner, I.; Heilman, C. J.; Rees, H. D.; Wu, H.; Lin, L.; Szulwach, K. E.; Gearing, M.; Mufson, E. J.; Bennett, D. A.; Montine, T. J.; Seyfried, N. T.; Wingo, T. S.; Sun, Y. E.; Jin, P.; Hanfelt, J.; Willcock, D. M.; Levey, A.; Lah, J. J.; Peng, J. *Proc. Natl. Acad. Sci. U.S.A.* **2013**, *110*, 16562.
- (65) Lu, K.; Guo, L.; Mehta, A. K.; Childers, W. S.; Dublin, S. N.; Skanthakumar, S.; Conticello, V. P.; Thiyagarajan, P.; Apkarian, R. P.; Lynn, D. G. *Chem Commun* **2007**, 2729.
- (66) Gullion, T.; Schaefer, J. *J Magn Reson* **1989**, *81*, 196.
- (67) Gullion, T.; Schaefer, J. *Adv Magn Reson* **1989**, *13*, 57.
- (68) Christensen, A. M.; Schaefer, J. *Biochemistry* **1993**, *32*, 2868.
- (69) Gullion, T.; Baker, D. B.; Conradi, M. S. *J Magn Reson* **1990**, *89*, 479.
- (70) Rance, M.; Byrd, R. A. *J Magn Reson* **1983**, *52*, 221.
- (71) Sinha, N.; Schmidt-Rohr, K.; Hong, M. *J Magn Reson* **2004**, *168*, 358.
- (72) Fung, B. M.; Khitrin, A. K.; Ermolaev, K. *J Magn Reson* **2000**, *142*, 97.
- (73) Weldeghiorghis, T. K.; Schaefer, J. *J Magn Reson* **2003**, *165*, 230.
- (74) Ni, R.; Childers, W. S.; Hardcastle, K. I.; Mehta, A. K.; Lynn, D. G. *Angew Chem, Int Ed* **2012**, *51*, 6635.
- (75) Mueller, K. T.; Jarvie, T. P.; Aurentz, D. J.; RobertS, B. W. *Chem. Phys. Lett.* **1995**, *242*, 535.
- (76) Goetz, J. M.; Schaefer, J. *J Magn Reson* **1997**, *127*, 147.
- (77) Maiti, S.; Dutta, S.; Das, P. K. *Chemistry – A European Journal* **2011**, *17*, 7538.
- (78) Butt, H. J. *Biophys. J.* **1991**, *60*, 1438.
- (79) Wu, J.; Corbett, A. H.; Berland, K. M. *Biophysical Journal* **2009**, *96*, 3840.
- (80) Roehrl, M. H. A.; Wang, J. Y.; Wagner, G. *Biochemistry* **2004**, *43*, 16056.

Chapter 3 Generating Asymmetric Peptide Membranes

Introduction

Cellular membranes are phospholipid bilayers¹. Essentially, two single layers of phospholipid, each leaflet consisting of polar head groups and nonpolar tails, aligned parallel in a symmetrical fashion². However, the cell membrane tends to have different composition on one side of the membrane than on the other side of the membrane, introducing a degree of asymmetry³ into what is essentially stochastic assembly. Asymmetric distributions exist across the membrane of living cells via spontaneous diffusion or active ATP-dependent translocation⁴. Such asymmetrical distributions leads to intrinsic membrane potential⁵ that governs a variety of biological phenomena including membrane bending, vesicle budding and photosynthesis et, al.⁶⁻⁸ Moreover, the asymmetric distribution of proteins to distinct domains in the plasma membrane is crucial to the function of many polarized cells^{9,10}. Symmetry breaking events are widely seen in biology in response to external stimuli such as chemical gradients, electromagnetic fields and molecular signals¹¹ and it's often linked to functional diversification. In this chapter, I will present a symmetry breaking event that results simply from peptide self-assembly. By taking advantage of the charge-compensating leaflets interfaces, the asymmetric bilayer forms without any external stimulation.

Results

Model of Asymmetric Peptide Membranes

Chapter 2 established that simple phosphorylated peptides assemble into robust bilayer membranes with long-range order that are morphologically similar to lipids but structurally distinct from the traditional lipid assemblies. Peptide Ac-KLVFFAE-NH₂ and Ac-KLVFFAE-NH₂ self assemble into homogeneous cross- β nanotubes bilayer with precisely patterned lysine and phosphotyrosine side chains exposed to the surfaces and each leaflet face respectively. Therefore, both of their outer and inner surfaces as well as the leaflet interface are highly charged. These highly charged patterned leaflets interface is passivated by counterions¹² (trifluoroacetate and triethylammonium respectively), and probably the energy constraint of the self-assembly. Given the apparent energetic barrier at the leaflet interface and the effectiveness of ammonium/oxyacid inner leaflet stabilization, we explored (K16pY)(E22L) / (E22L) as co-assemblies to self-passivate. The two possible models that would stabilize the interface include a

homogeneous leaflet, Figure 3-1G or a heterogeneous leaflet, Figure 3-1H. Remarkably, both models predict a loss of bilayer symmetry (Figure 3-1E and 3-1F) where the internal and external surfaces bare high densities of opposite charge.

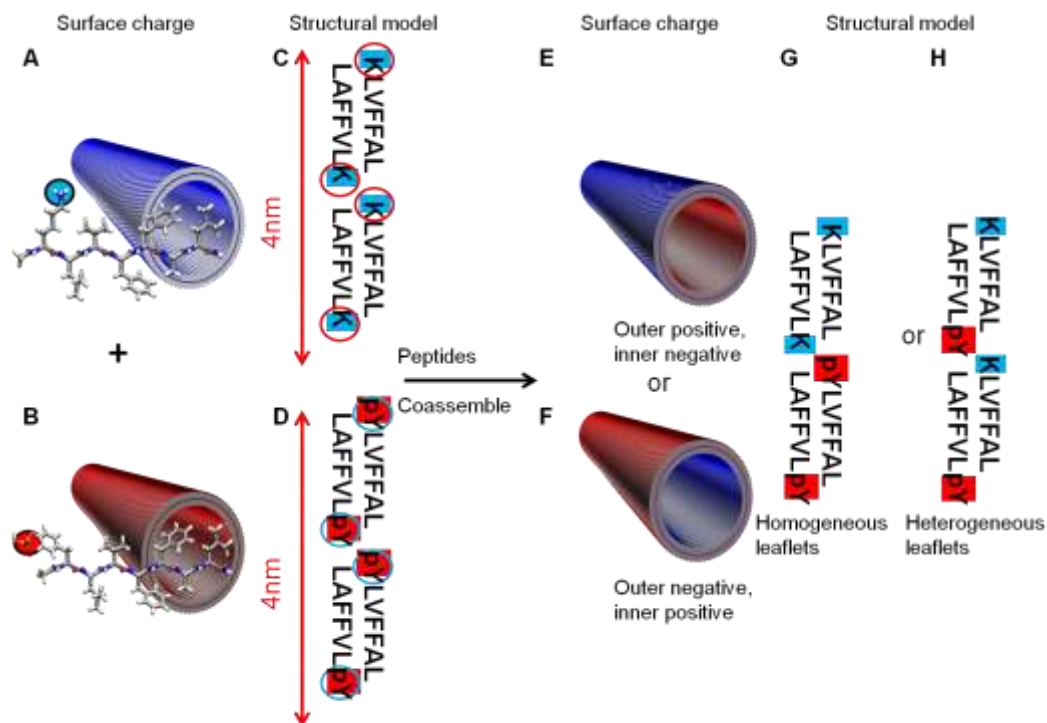


Figure 3-1 Model of asymmetric peptide membranes. Blue and red rectangular represent positive and negative charge residues respectively, blue and red circle represent counterions in the solvents respectively. Ac-KLVFFAL and Ac-pYL VFFAL peptides self-assembled into symmetric peptide membranes with positive (A) and negative charged surfaces (B) respectively with anti-parallel, out-of-register registry (C) and (D). When they're mixed for coassembly, two peptides arrangements are possible (G) homogeneous leaflets and (H) heterogeneous leaflets. Both arrangements can lead to charge separation on distinct surfaces (E) and (F).

Preliminary Evaluation of Peptide Mixing

This model was based on the assumption that K and pY can passivate each other at the interface. To test if the assumption is valid, peptide Ac-pYL VFFAK was assembled in 40%MeCN/H₂O at neutral pH. This peptide has the capacity to be zwitterionic to regulate charge compensation between the N-terminal and C-terminal residues. Ac-pYL VFFAK assembled into homogeneous nanotubes with β -sheet secondary structure (Figure 3-2 A and C). Fourier transform infrared spectra (Figure 3-2 B) contained a strong amide I absorption band at 1623 cm⁻¹, further supporting H-bonded β -sheet structures, and a

weak band at 1693 cm^{-1} consistent with antiparallel strand arrangements (Figure 3-2). The results suggested Ac-pYLFFFAK peptide exhibits similar peptide registry to Ac-KLVFFAL and Ac-pYLFFAL peptides, and an anti-parallel bilayer would place the N-terminal phosphotyrosine passivating with the C-terminal lysine residues at the interface.

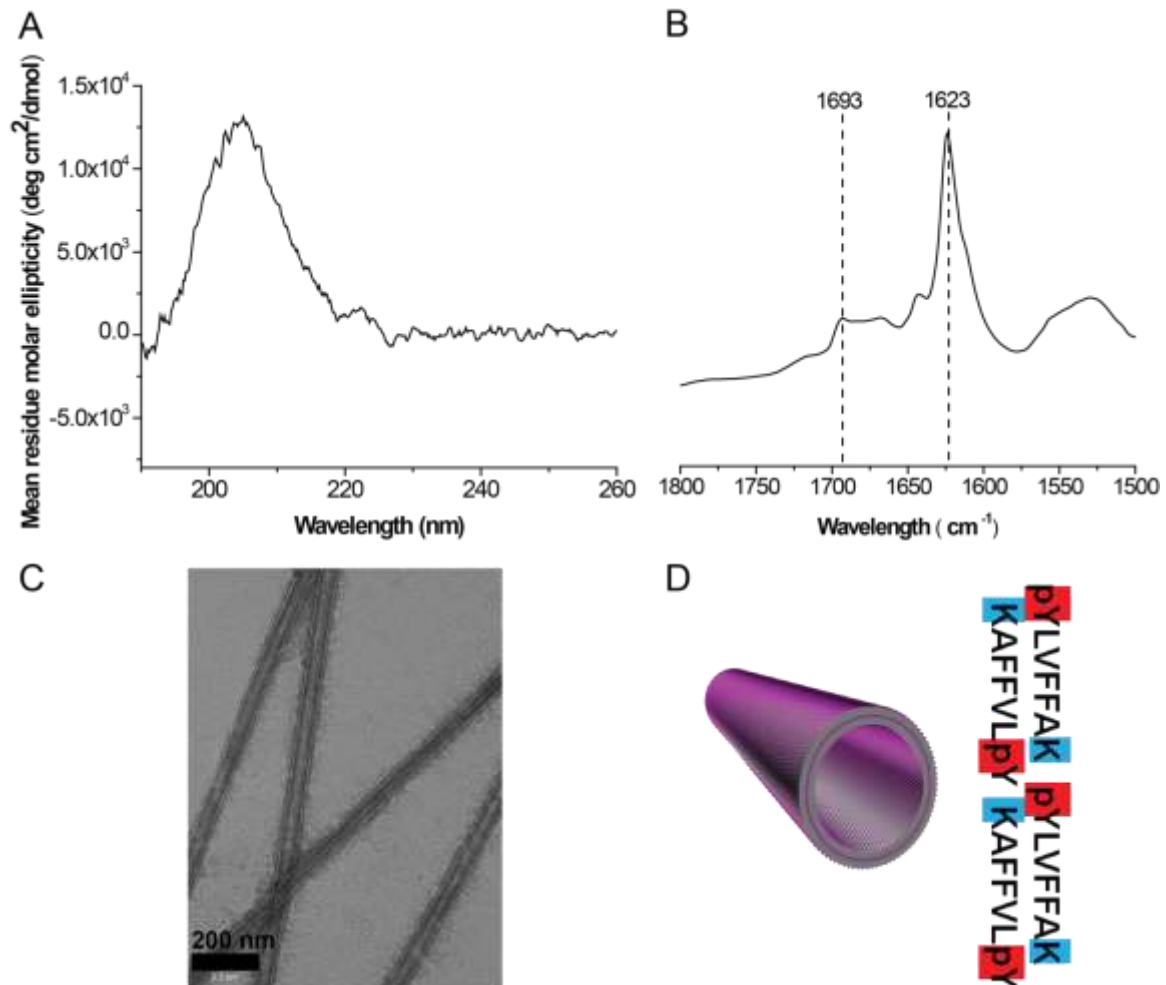


Figure 3-2 Structural characterization for Ac-pYLFFFAK. (A) Circular Dichroism of Ac-pYLFFFAK assembled in 40% MeCN/H₂O; (B) FT-IR of Ac-pYLFFFAK assemblies; (C) TEM micrograph for Ac-pYLFFFAK assembled in 40% MeCN/H₂O; (D) Illustration model for Ac-pYLFFFAK peptide bilayer registry.

Next, I conducted preliminar mixing experiments by mixing the two mature nanotubes. In the presence of TFA and TEAA respectively, the Ac-KLVFFAL and Ac-pYLFFAL peptides exhibited CD ellipticity from day 1 and assembled into mature nanotubes within

1-2 weeks. Pelleting and suspending the two assemblies together in 40% CH₃CN/H₂O gave immediate disassembly; in less than one hr, the ellipticity at 202nm and 225nm increased markedly and grew to give a stronger signature than neat K or pY nanotubes (Figure 3-3). These results suggested that the Ac-KLVFFAL and Ac-pYLFFAL peptides are able to mix and assemble into new structures that accumulate stronger β -sheets giving enough time. Judging by the disassembly upon mixing of these tubes, there might be bundling and repulsive events during early time period. To eliminate the initial bundling and repulsive events, the two peptides monomers will be co-assembled in the next step.

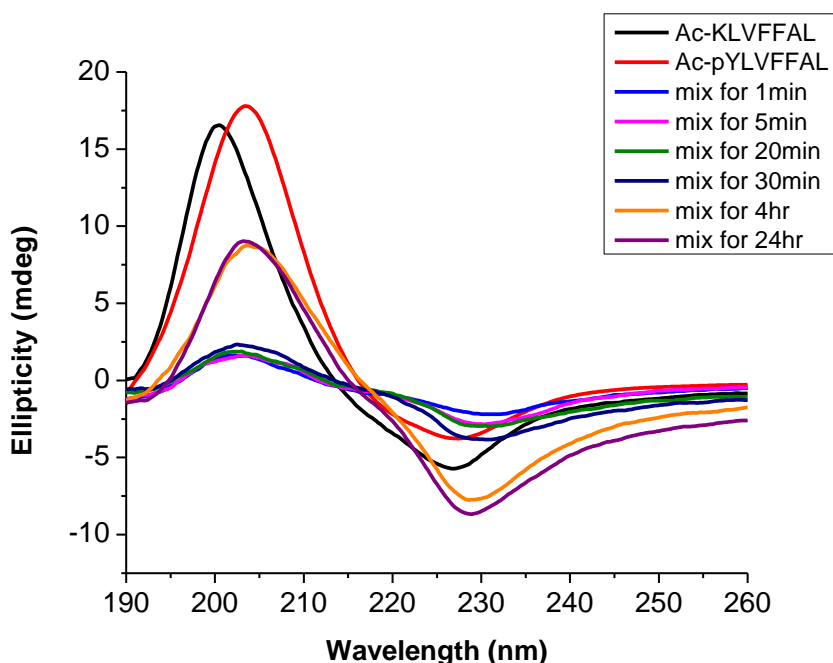


Figure 3-3 Circular Dichroism of matured Ac-KLVFFAL (black) and Ac-pYLFFAL (red) nanotubes. The two matured nanotubes assemblies were pelleted and suspended together in 40% MeCN/H₂O and monitored ellipticity at 1min, 5mins, 20 mins, 30 mins, 4hrs and 24 hrs.

Structural Characterization of the Co-Assembly

Ac-KLVFFAL and Ac-pYLFFAL peptides powders were treated by HFIP to eliminate any preformed aggregates and co-assembled in 40% MeCN/H₂O, neutral pH. The co-assemblies require at least 3 days to develop measurable ellipticity minimum at 225 nm, most consistent with β -sheets (Figure 3-4). Homogeneous micrometer long nanotubes dominate the assembly after 3-6 weeks, and FT-IR of the co-assemblies shows amide I

stretches at 1623 cm^{-1} and a weaker band at 1693 cm^{-1} (Figure 3-5), both typical of antiparallel β -sheets. Powder X-ray diffraction (XRD) reflections at 4.7 and 10.6 \AA are characteristic of β -strand and β -sheet reflections (Figure 3-6), but the lamination distance is slightly larger than neat Ac-KLVFFAL and Ac-pYLVFFAL nanotubes ($\sim 10.2\text{ \AA}$). Atomic force microscopy (AFM) measurements of the height of twice of the tube wall thickness is 7.045 nm (Figure 3-7), slightly smaller than that of E22L and (K16pY)(E22L) tubes which are $\sim 8\text{ nm}$ consistent with a $\sim 4\text{ nm}$ thick tube wall. While such 1 nm difference could still be within error, it could also be the differences in the interface created by oppositely-charged peptides that are packed closer than same-charged peptides.

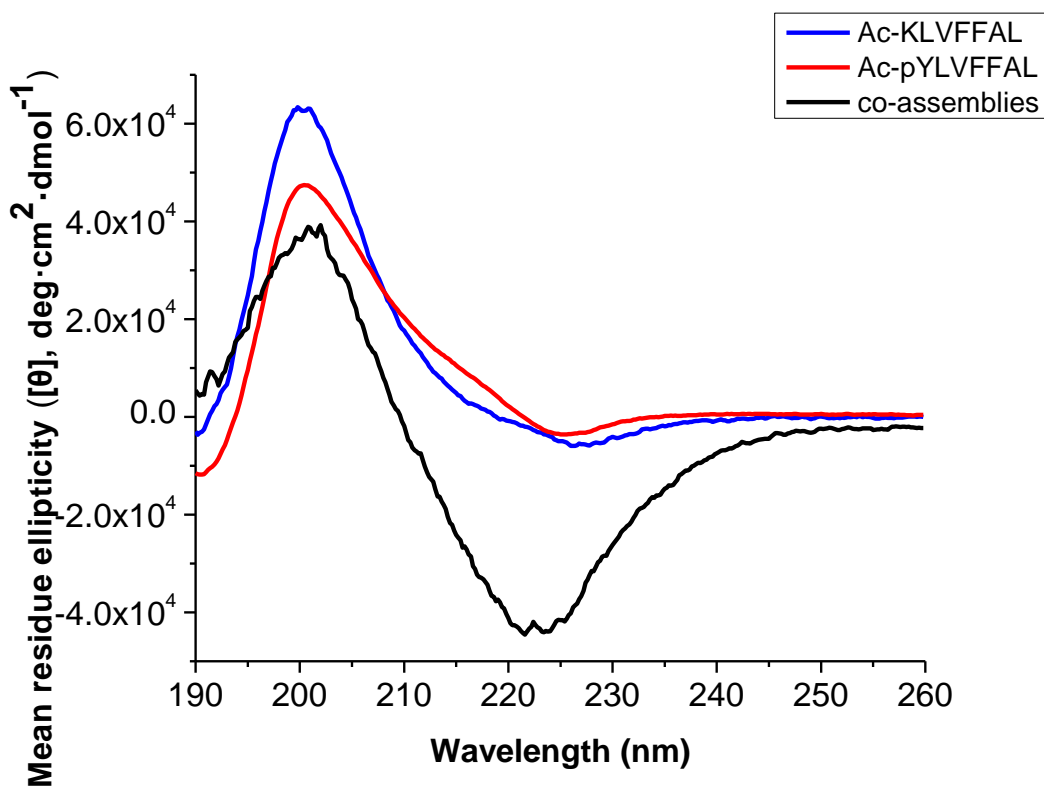


Figure 3-4 Circular Dichroism of Ac-KLVFFAL assembled in 40% MeCN/H₂O with TFA (blue), Ac-pYLVFFAL in 40% MeCN/H₂O with TEAA (red) and coassemblies in 40% MeCN/H₂O (black) at 4°C.

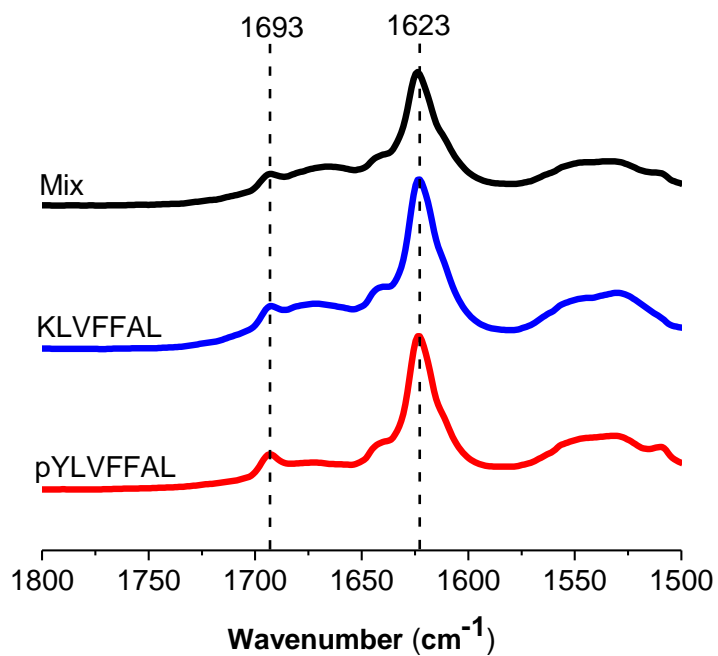


Figure 3-5 FT-IR spectra of Ac-KLVFFAL assembled in 40% MeCN/H₂O with TFA (blue), Ac-pYLVFFAL in 40% MeCN/H₂O with TEAA (red) and coassemblies in 40% MeCN/H₂O (black) at 4°C.

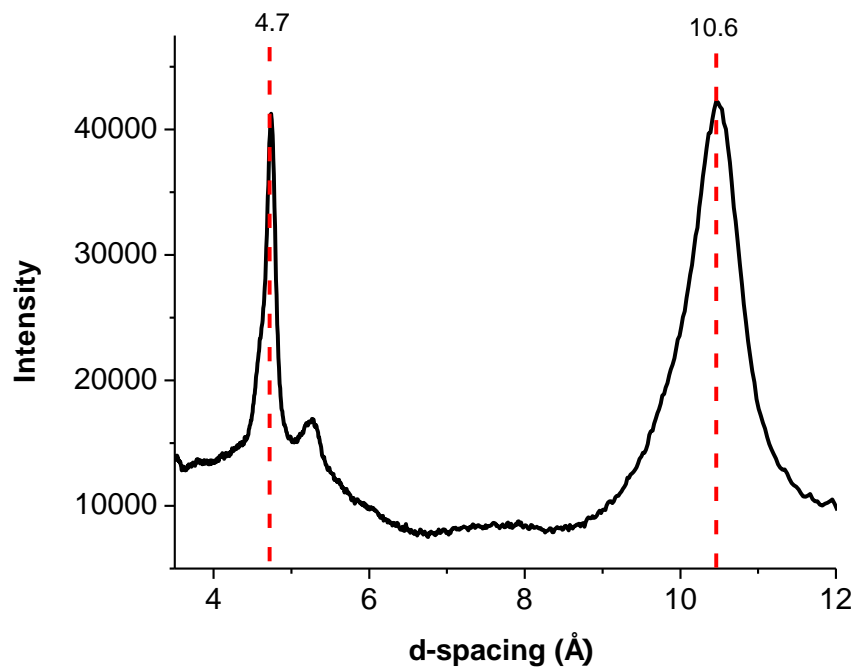


Figure 3-6 X-ray powder diffraction of coassemblies of Ac-KLVFFAL and Ac-pYLVFFAL peptides in 40% MeCN/H₂O at 4°C, showing reflections at d-spacings of 4.7 Å and 10.6 Å.

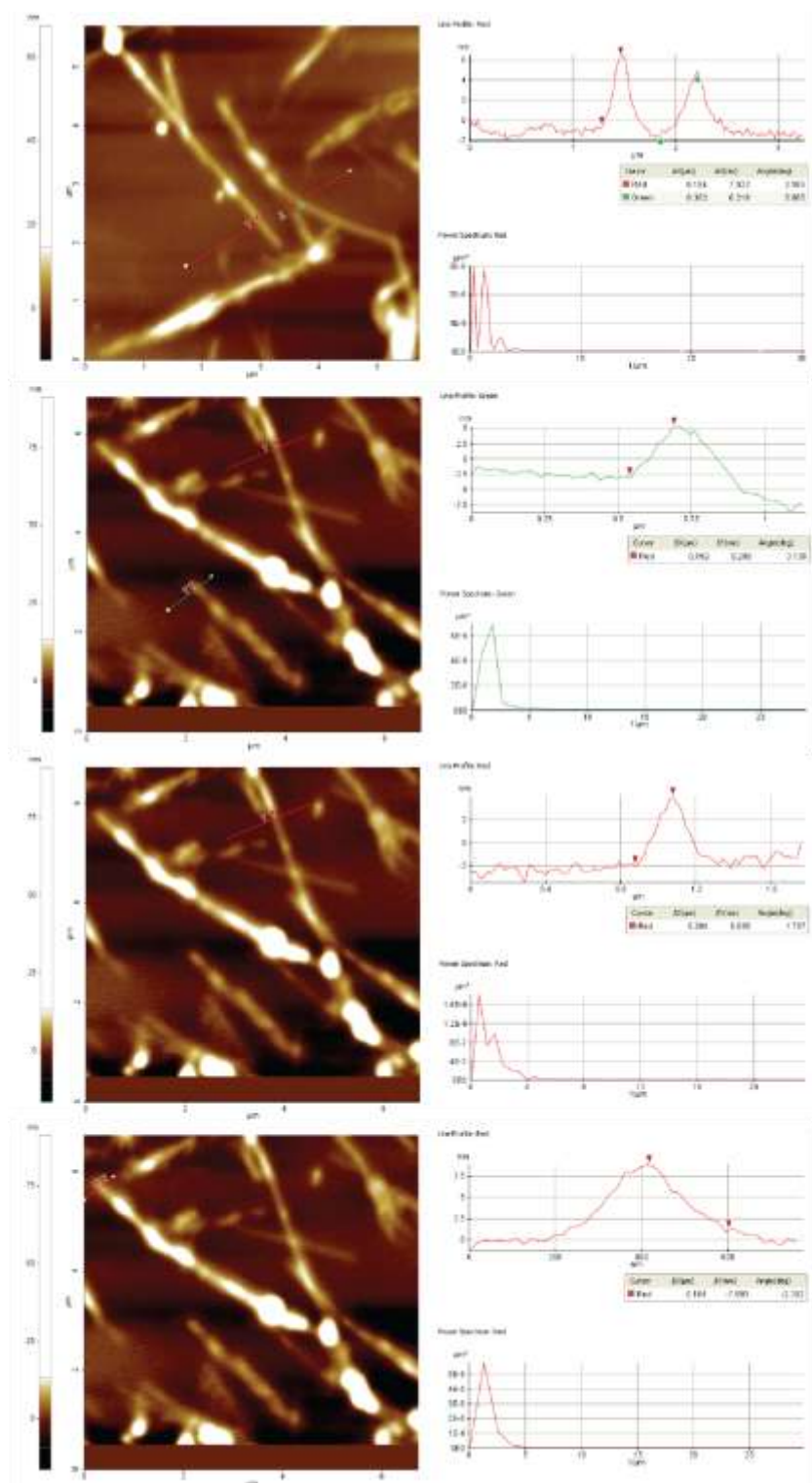


Figure 3-7 Atomic force microscopy height measurements of coassembled Ac-KLVFFAL and Ac-pYL VFFAL peptides as nanotubes in 40% MeCN/H₂O at 4°C. The measured heights from top to bottom are 7.022, 6.218, 8.288, 6.005, 7.693 nm respectively, and an average of height measurement is 7.045 nm.

Thermal Studies of the Co-Assembly

The fact that co-assemblies took longer time to mature and had stronger ellipticity is more consistent with the formation of new structures than self-sorting of the two original species. Thermodynamic stability provides clear physical evidence of homogeneous co-assembly. Melting profiles were generated by monitoring CD ellipticity at 225nm, the amide transition dipole, as a function of temperature. The resulting melting profiles were fit to the sigmoidal form of the Boltzmann equation (Equation 3-1), a melting temperature, T_m , and a measure of melting cooperativity reflected in the slope k . Each assembly displays a cooperative melting transition; however the melting temperatures (T_m) were different. Under the assembly condition (40% MeCN/H₂O), only Ac-KLVFFAL nanotubes melted at 57.6 °C, before the evaporation of the solvent acetonitrile (80 °C) (Figure 3-8).

$$\theta \propto \left(1 + \exp\left\{\frac{T_m - T}{k}\right\}\right)^{-1}$$

Equation 3-1

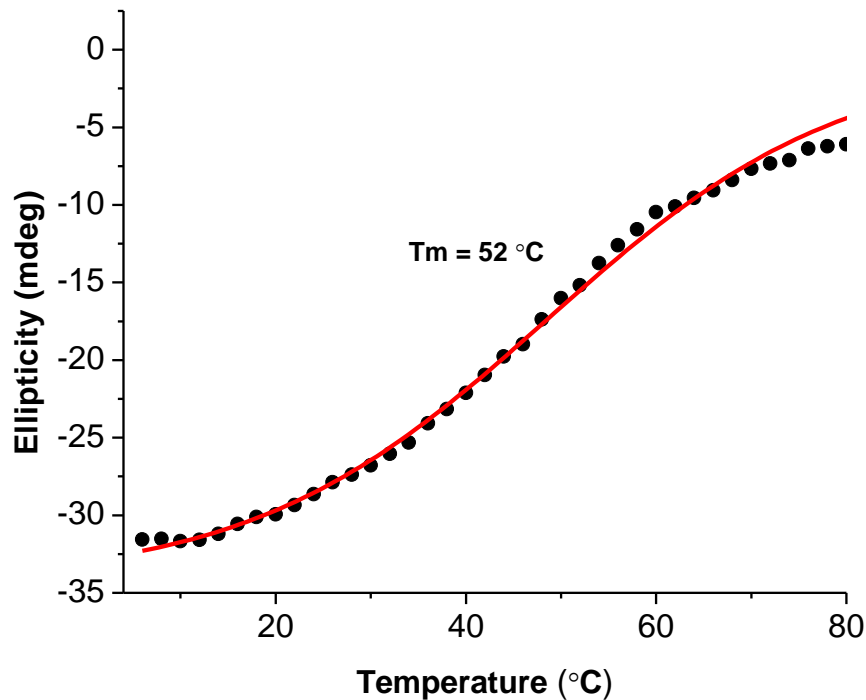


Figure 3-8 CD melting profiles for Ac-KLVFFAL peptide nanotubes formed in 40% MeCN/H₂O at 4 °C. Ellipticity at 225 nm was plotted over temperature (2 °C/min). The melting curve was fit to $y = -0.4729 + (-34.3734 + 0.4729) / (1 + \exp((T - 48.4598) / 15.5563))$, corresponding to a melting point of 48.5 ± 15.6 °C.

Ac-pYLVFFAL nanotubes remained stable in 40% and 50% MeCN/H₂O before the temperature reached 80 °C (See methods). When the nanotubes were pelleted and resuspended at higher percentage of MeCN (60%, 70% and 80% respectively), melting was observed with T_m's of 47.6, 41.6 and 25.9 °C respectively (Figure 3-9). Similar to a denaturing process, T_m decreases with increasing organic solvent. Interestingly, melting temperatures shows a linear relationship with the hydrophobicity (Figure 3-10) and the dielectric constant (Figure 3-11) of the organic solvent. As a consequence, melting temperature of nanotubes in 40% and 90% MeCN/H₂O can be estimated (Table 3-1).

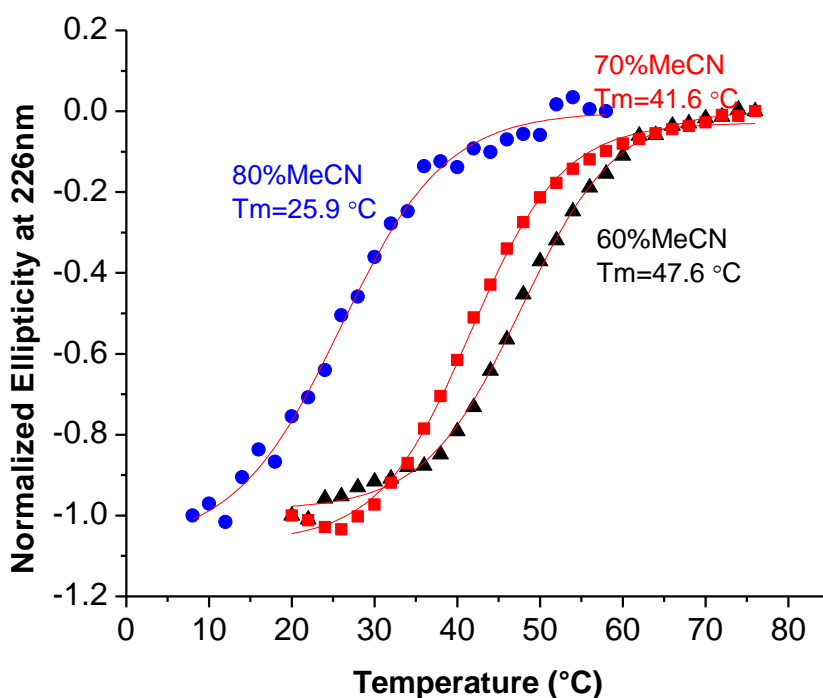


Figure 3-9 CD melting profiles for Ac-pYLVFFAL peptide nanotubes formed in 40% MeCN/H₂O at 4°C and resuspended in 60% (black), 70% (red) and 80% (blue) MeCN/H₂O respectively. E Ellipticity at 225 nm was plotted over temperature (2 °C/min). The melting curve for nanotubes in 60% MeCN H₂O was fit to the equation $y=0.0036+(-0.9853-0.0036)/(1+\exp((T-47.6493)/5.8079))$, corresponding to a melting point of 47.6±5.8 °C. The melting curve for nanotubes in 70% MeCN/H₂O was fit to the equation $y=-0.0284+(-1.0651+0.0284)/(1+\exp((T-41.6053)/5.5344))$, corresponding to a melting point of 41.6±5.5 °C. The melting curve for nanotubes in 80% MeCN/H₂O was fit to the equation $y=-0.0012+(-1.0698+0.0012)/(1+\exp((T-25.8740)/6.3733))$, corresponding to a melting point of 25.9±6.4.

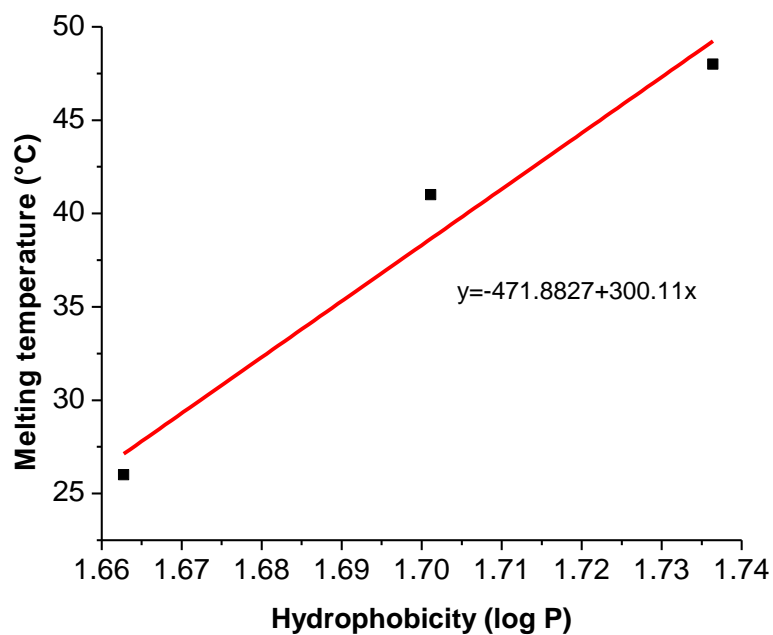


Figure 3-10 Melting temperature of Ac-pYLVEFAL in 60%, 70% and 90% MeCN/H₂O plot vs hydrophobicity of the solvent.

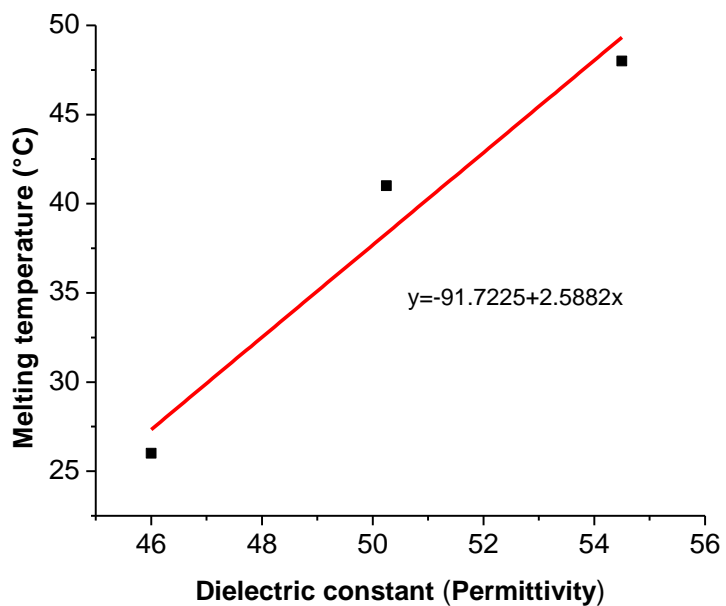


Figure 3-11 Melting temperature of Ac-pYLVEFAL in 60%, 70% and 90% MeCN/H₂O plot vs dielectric constant of the solvent.

Table 3-1 Melting temperature of Ac-pYLVFFAL at different solvent conditions.

% of MeCN/H ₂ O	Hydrophobicity (log P)	Melting temperature (°C)	Dielectric constant	Melting temperature (°C)
40	1.79934	68.1 *	63	71.3 *
60	1.7365	48	54.6	48
70	1.70114	41	50.25	41
80	1.66276	26 *	46	26 *
90	1.62066	14.5	41.75	16.3

*Calculated from plots of temperature vs hydrophobicity and temperature vs dielectric constant

Peptides co-assemblies remained stable in 70% and 80% MeCN/H₂O before 80 °C (See methods). They melt when resuspended in 90% MeCN/H₂O at 52 °C (Figure 3-12).

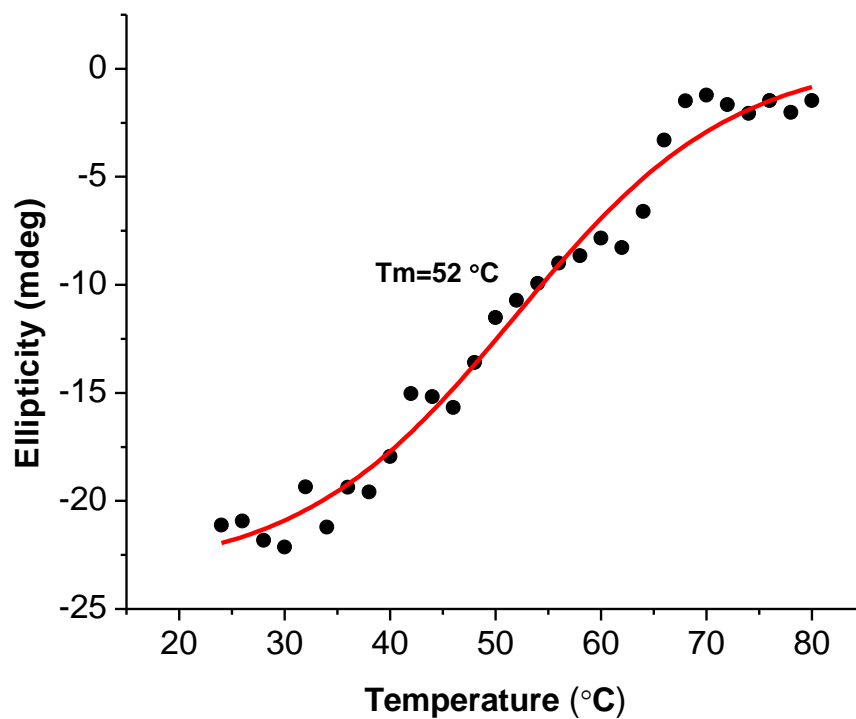


Figure 3-12 CD melting profiles for Ac-KLVFFAEL and Ac-pYLVFFAL coassemblies formed in 40% MeCN/H₂O at 4 °C and resuspended in 90% MeCN/H₂O. The melting curves were fit to the equation $y=0.6409+(-23.4538-0.6409)/(1+\exp((T-51.9535)/10.2994))$, corresponding to a melting point of 52 ± 10.3 °C.

Melting temperature of Ac-KLVFFAL and Ac-pYLVFFAL nanotubes in 40% MeCN/H₂O are comparable (Table 4-2), Ac-pYLVFFAL nanotubes melting profiles are generally more cooperative than that of Ac-KLVFFAL nanotubes, which may suggest more homogeneous Ac-pYLVFFAL assemblies. Comparison of T_m of Ac-pYLVFFAL and co-assemblies at 90% MeCN/H₂O, which are 15.4 and 52 °C respectively (Table 4-2), demonstrate greater thermal stability for the co-assemblies than either Ac-KLVFFAL or Ac-pYLVFFAL assemblies.

Table 3-2 Summary of melting temperature of Ac-KLVFFAL, Ac-pYLVFFAL and co-assemblies at different solvents conditions.

Sample	Melting condition	Melting temperature
Ac-KLVFFAL	40% MeCN/H ₂ O	48.5 ± 15.6
Ac-pYLVFFAL	40% MeCN/H ₂ O	69.7 ± 1.6*
Ac-pYLVFFAL	60% MeCN/H ₂ O	47.6 ± 5.8
Ac-pYLVFFAL	70% MeCN/H ₂ O	41.6 ± 5.5
Ac-pYLVFFAL	80% MeCN/H ₂ O	25.9 ± 6.4
Ac-pYLVFFAL	90% MeCN/H ₂ O	15.4 ± 1*
Ac-KLVFFAL and Ac-pYLVFFAL co-assemblies	90% MeCN/H ₂ O	52 ± 10.3
* Calculated from average of melting temperatures from plots of temperature vs hydrophobicity and temperature vs dielectric constant		

Surface Charge Evaluation via Salt Bundling

The co-assembly model predicts the outer surface of the mixed assembly would display high charge density and salt-induced aggregation should evaluate the charge of the nanotube surfaces. As shown in Figure 3, nanotube bundling follows the Hofmeister series, with SO₄²⁻ bundling (E22L) nanotubes and not (K16pY)(E22L) nanotubes¹³, with Mg²⁺ only bundling the (K16pY)(E22L) nanotubes. Under these conditions, the mixed assemblies only bundle in the presence of Mg²⁺, confirming that negatively-charged surfaces are exposed to solvent (Figure 3-13).

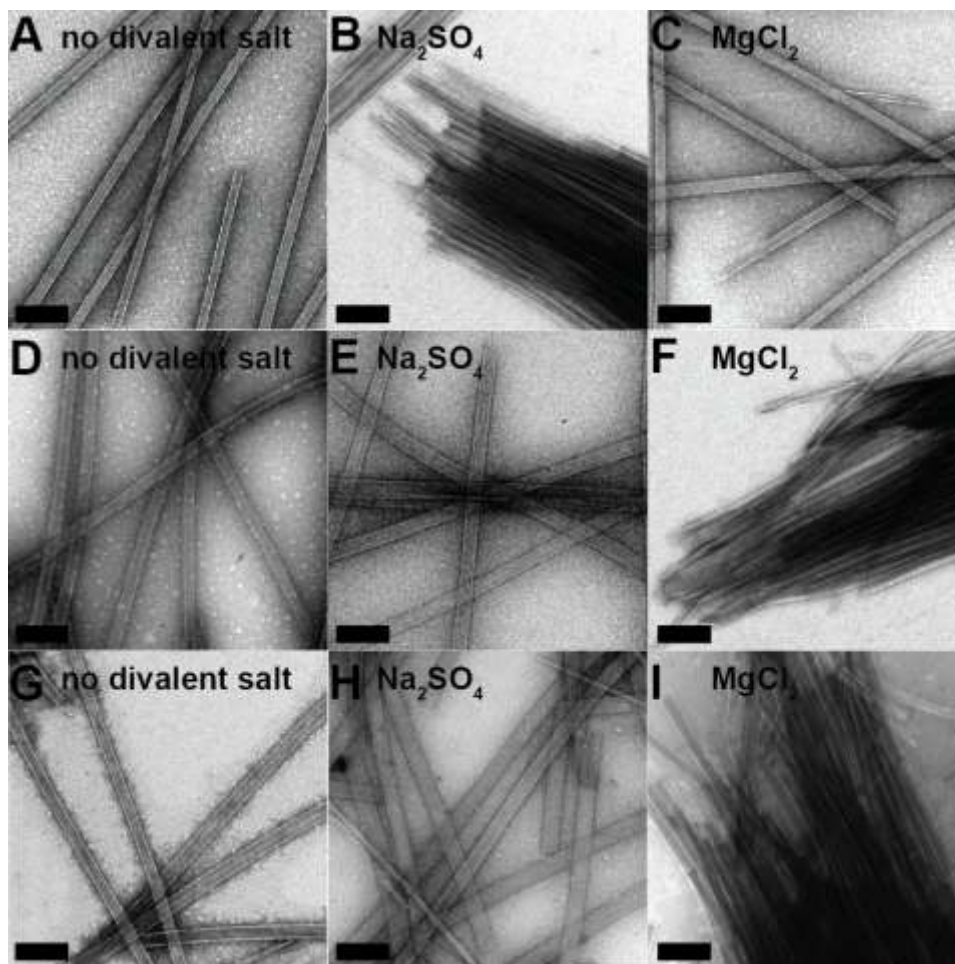


Figure 3-13 Transmission electron microscopy micrographs of salt-induced bundling of (E22L) (top), (K16pY)(E22L) (middle) and mixed peptides (bottom) nanotubes:(A, D and G) without additional salts, (B, E and H) 2 h after the addition of Na_2SO_4 , and (C, F and I) 2 h after the addition of MgCl_2 . Peptide:salt molar ratio of 1:4.5 and scale bars of 200 nm.

Surface Charge Evaluation via Electrostatic Force Microscopy

Enhanced-electrostatic force microscopy (EFM) allows the charge distribution to be mapped at higher resolution. The topographical and EFM amplitude images of the co-assembled Ac-KLVFFAL and Ac-pYL VFFAL peptides show a 1:1 correspondence, and all the nanotubes being strongly attractive (dark) along the entire length of each assembled nanotube (Figure 3-14), suggesting that the co-assemblies have homogeneous negative outer surfaces. At early points in assembly, i.e., 10min, the amorphous aggregates show positive, negative and neutral domains (Figure 3-15). These slowly mature to nanotubes during the first 20 days with a few particles remaining

on the surface of nanotubes and after 7 weeks, only nanotubes are observed (Figure 3-15).

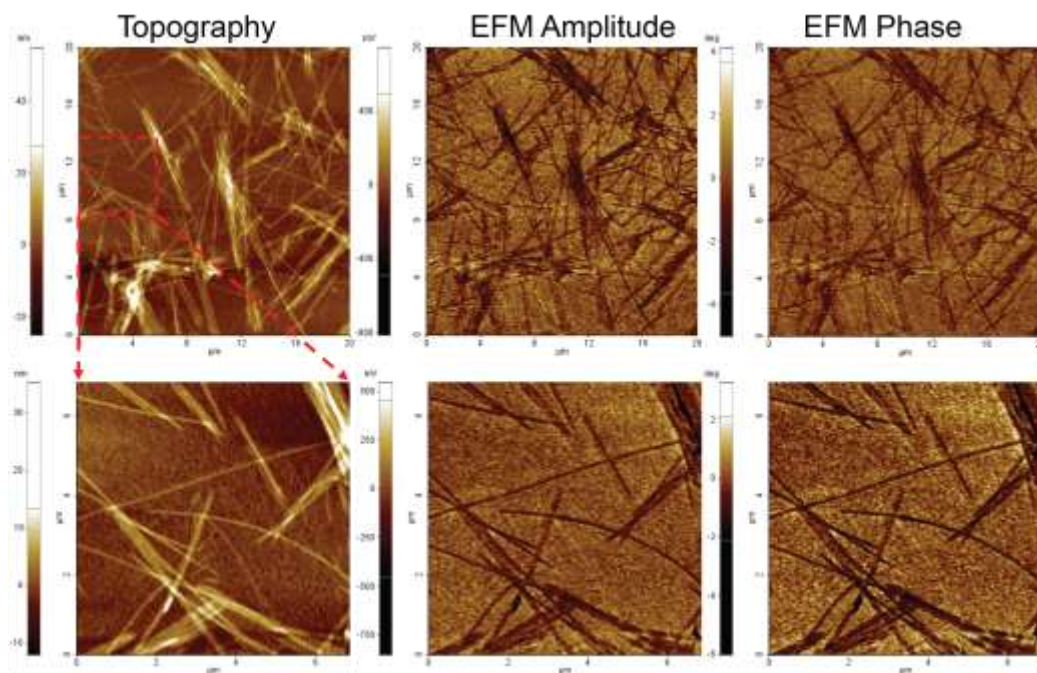


Figure 3-14 Topography (left) EFM amplitude (middle) and EFM phase micrographs (right) of Ac-KLVFFAL and Ac-pYLVFFAL peptides co-assemblies in 40% MeCN/H₂O, DC bias +1 V. In the EFM amplitude micrographs, positively charged surfaces are white and negatively charged surfaces are dark. Bottom images are zoomed in Figures of top images.

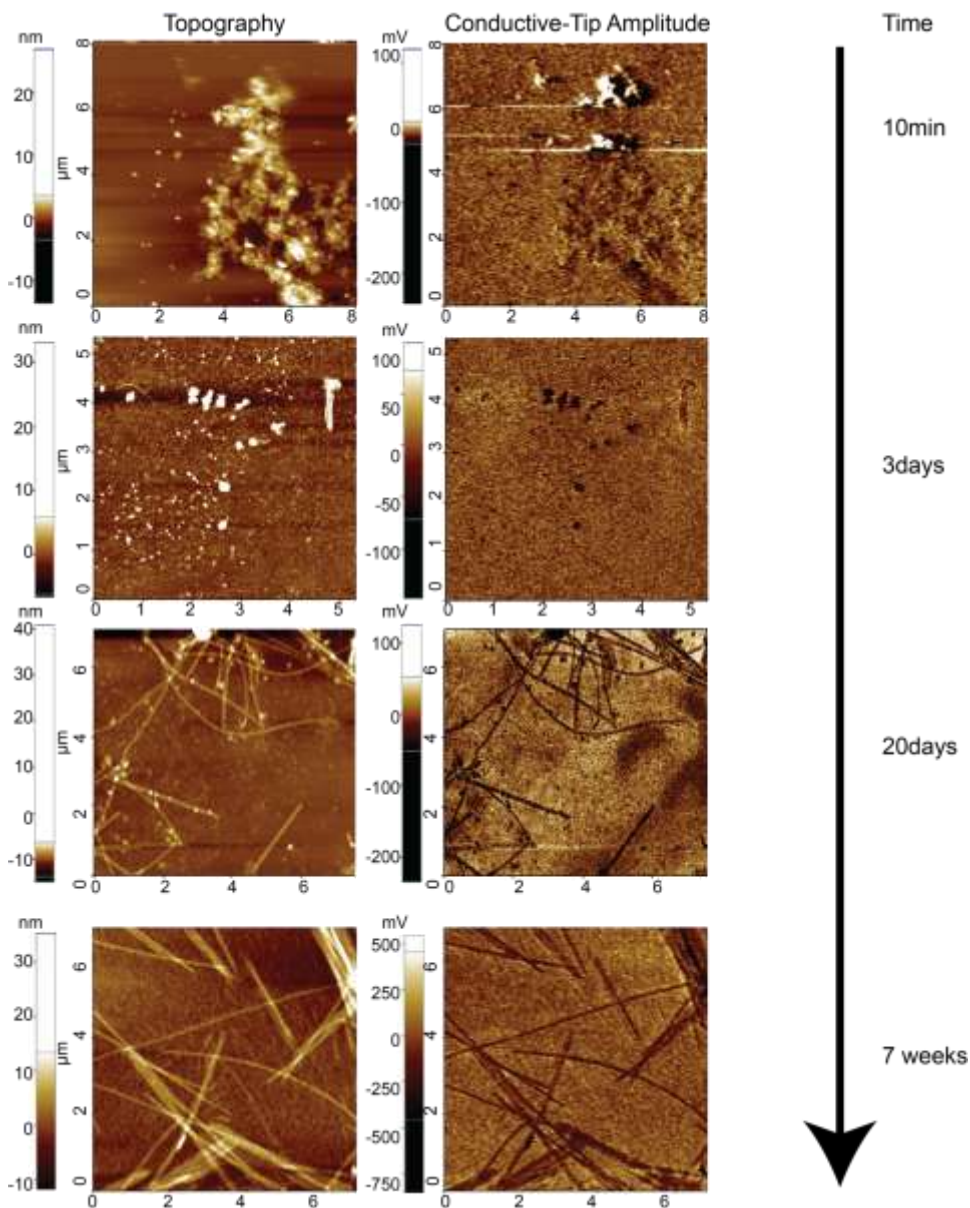


Figure 3-15 Topography (left) and EFM amplitude micrographs (right) of Ac-KLVFFAL and Ac-pYLVFFAL peptides co-assemblies in 40% MeCN/H₂O over time, DC bias +1 V. In the EFM amplitude micrographs, positively charged surfaces are white and negatively charged surfaces are dark.

Peptide Registry Characterization via Solid-State REDOR NMR

EFM and salt bundling results narrow the surface charge models to model F (Figure 3-1). However, surface charge characterization does not differentiate between the two structural models (Figure 3-1G and H). Provided anti-parallel, out-of-register peptide registry, the two peptides can either form homogeneous or heterogeneous leaflets. To further characterize peptide registry in the co-assemblies, ¹³C and ¹⁵N enriched peptides

KLVFF[1-¹³C]AL and pYL[¹⁵N]VFF[3-¹³C]AL were synthesized and co-assembled to be analyzed by solid-state REDOR NMR. If the peptides are arranged as homogeneous leaflets model, then there will be only [3-¹³C]A and [¹⁵N]V coupling (Figure 3-16 left). Likewise, only [1-¹³C]A and [¹⁵N]V coupling will be observed if the peptides are arranged as heterogeneous leaflets model (Figure 3-16 right). By plotting REDOR as $\Delta S/S_0$, the plateau (max dephasing) is directly related to the number of spins that are coupled (See methods). Therefore, if both models exist then the models partition will be reflected by experimental REDOR curve fittings, too.

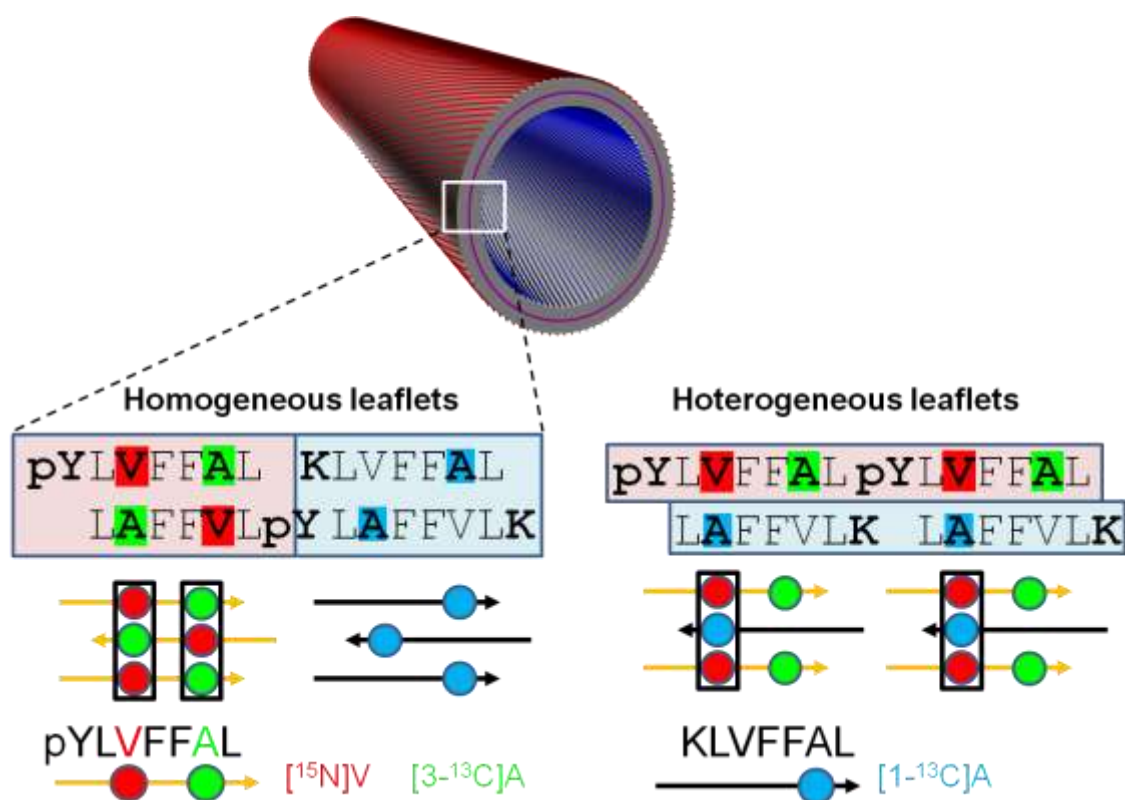


Figure 3-16 REDOR-NMR enrichment scheme for assessment of two models: homogeneous leaflets and heterogeneous leaflets. Red circle represents [¹⁵N] enriched Valine in Ac-pYL^VFFAL, green circle represents [3-¹³C] enriched Alanine in Ac-pYL^VFFAL and blue circle represents [1-¹³C] enriched Alanine in Ac-KLVFFAL. [3-¹³C]A-[¹⁵N]V coupling reports on homogeneous leaflets and [1-¹³C]A-[¹⁵N]V coupling reports heterogeneous leaflets.

Integration of the alanine ¹³CH₃ resonance to the carbonyl ¹³C resonance of the co-assemblies, with attendant sidebands, gave a pY:K peptide ratio in the assembly of 0.62 (See methods). Our previous results with neat assemblies^{14,15} as well as chapter 2 have

established $^{13}\text{C}\{^{15}\text{N}\}$ REDOR dephasing for the alanine ^{13}CO surrounded by two ^{15}N , one of them is intermolecular H-bonded, has two ^{13}C - ^{15}N distances with a defined internuclear angle. The experimental ^{13}CO dephasing of the co-assemblies (Figure 3-17) roughly fit to the dephasing curve of neat Ac-KLVFFAL assemblies. However, the dephasing curve of the neat Ac-KLVFFAL assemblies needs to be scaled down to 63% to capture the trends at plateau, suggesting there are only 63% of the ^{13}CO are surrounded by two ^{15}N . Therefore, 63% of the K peptides are hydrogen-bonded and adjacent to two pY peptides. The rest of the 37% of the K peptides must not adjacent to any pY peptides. Although the dephasing curve of the neat K assemblies captured the general shape of the co-assemblies data, it does not match all the data points within error. It suggested that the K peptide is assembled in two different environments and only partial of the ^{13}CO is coupled with ^{15}N . We argue that such fitting does not account for mutations in the propagation of the co-assembled peptide population already seen in other cross- β assemblies¹⁶. Considering the heterogeneity in a co-assembly system, the alanine ^{13}CO of K peptide could be surrounded by two ^{15}N of pY peptide, or the alanine ^{13}CO of K peptide could be surrounded by one ^{15}N of pY peptide and ^{14}N of K peptide. Such interruption in the propagation pattern introduces a 2-spin contribution into the infinite repeat represented by the 3-spin fit (See methods). When the angle and distance of the ^{13}CO and ^{15}N (^{14}N) are constrained, summation of all 3-spin and 2-spin contributions will fit the experimental data (Figure 3-18 and Figure 3-19).

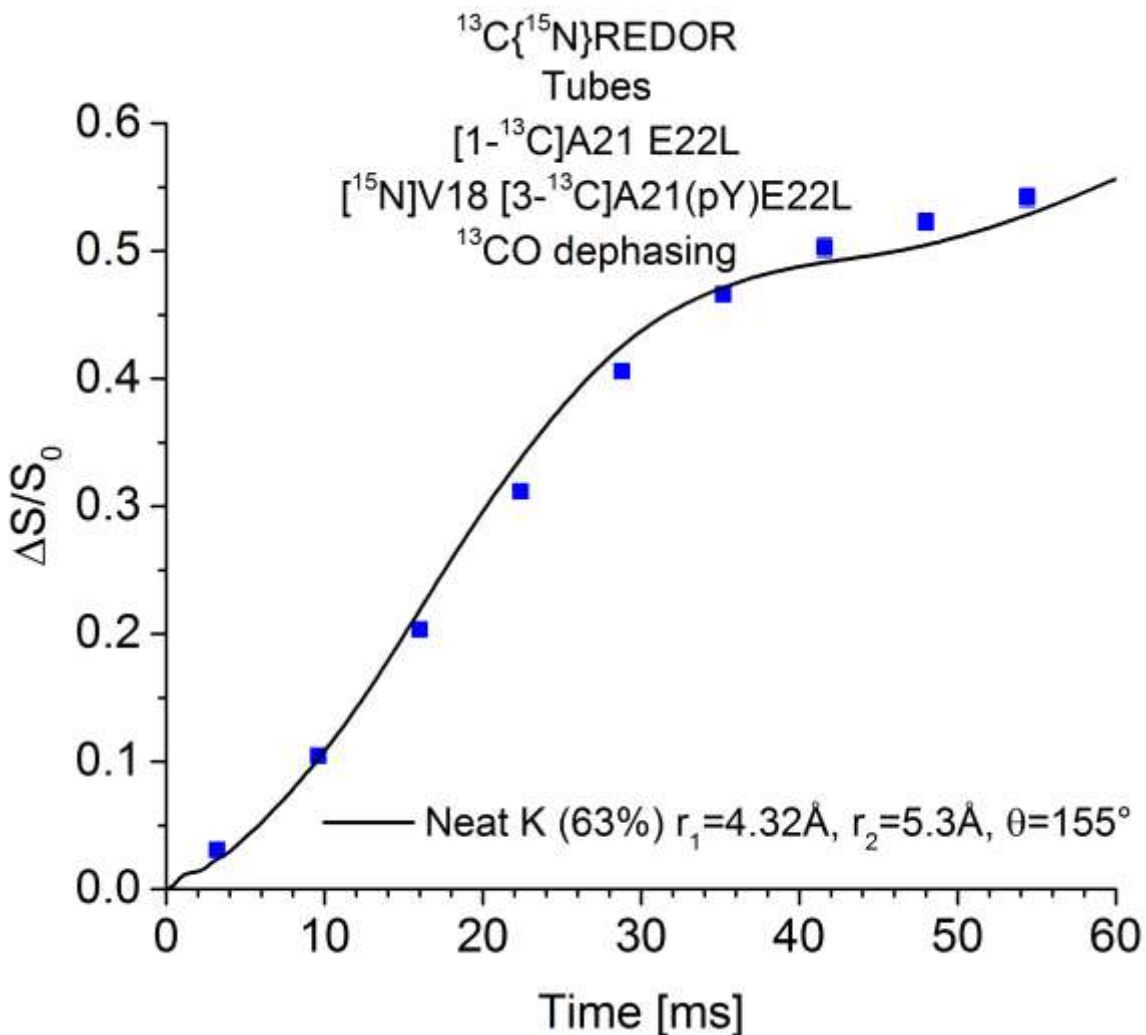


Figure 3-17 The $^{13}\text{C}\{^{15}\text{N}\}$ REDOR dephasing data points (blue) of co-assembled Ac-KLVFFAL and Ac-pYLVFFAL, compared to $^{13}\text{C}\{^{15}\text{N}\}$ REDOR dephasing curve (black) of neat Ac-KL[^{15}N]VFF[^{13}C]AL fits to ^{13}C - ^{15}N distances of 4.32 and 5.28 Å a ^{15}N - ^{13}C - ^{15}N internuclear angle of 155° .

The dephasing of $1\text{-}^{13}\text{C}\{^{15}\text{N}\}$ REDOR is shown in Figure 3-18, 65% of the [1- ^{13}C]A, which reports on K peptides (Ac-KLVFF[1- ^{13}C]AL-NH₂), are proximal to a ^{15}N containing pY peptide, and best fits are obtained with $45.4\pm 4.7\%$ of the K-peptides in extended 3-spin arrangements and $18.7\pm 6.9\%$ in 2-spin arrangements, and this leaves the rest of $35.4\pm 7.0\%$ K peptide ^{13}C do not dephase. The 3-spin and 2-spin arrangements of [1- ^{13}C] are corresponding to heterogeneous leaflets, while the no dephasing arrangement is consistent with homogeneous leaflet.

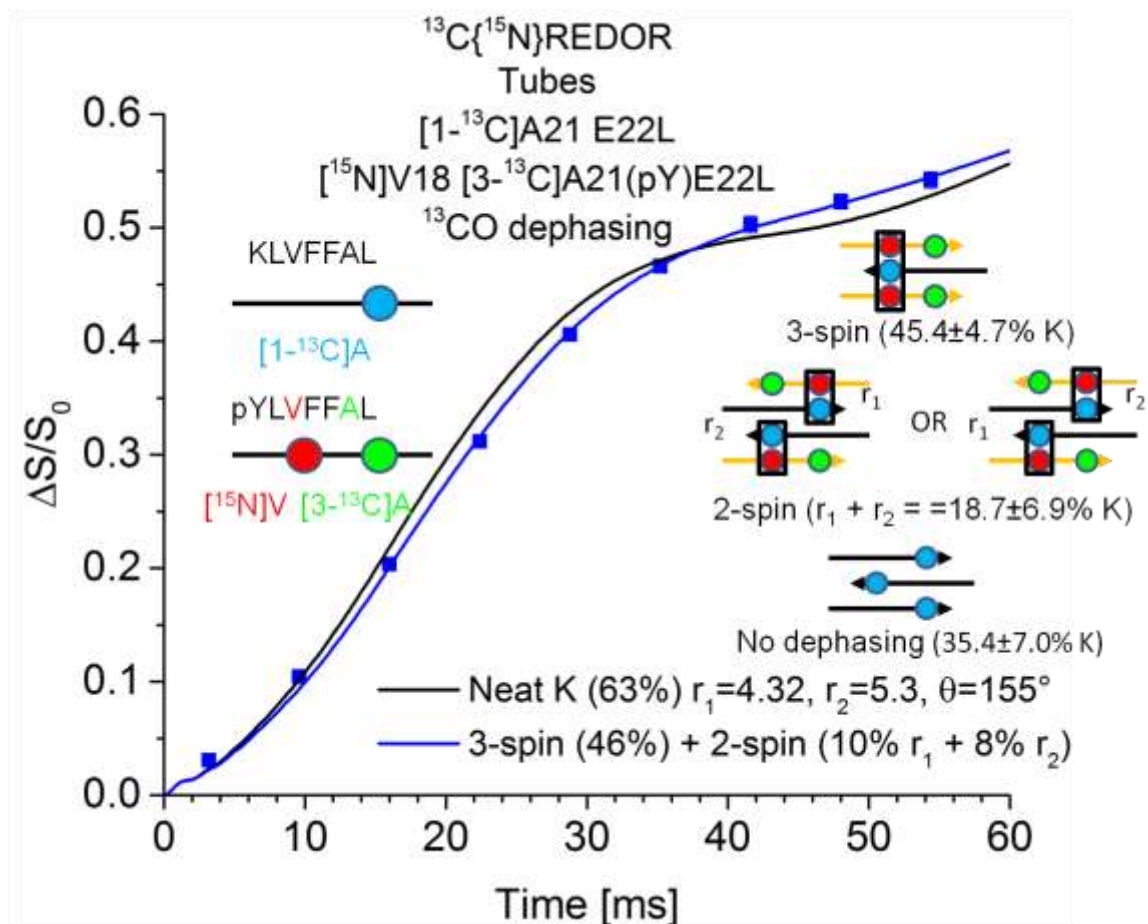


Figure 3-18 The $^{13}\text{C}\{^{15}\text{N}\}$ REDOR dephasing fits to summation of 3-spin and 2-spin systems. $^{13}\text{C}\{^{15}\text{N}\}$ REDOR dephasing fits to ^{13}C - ^{15}N distances of 4.32 and 5.3 Å a ^{15}N - ^{13}C - ^{15}N internuclear angle of 155° .

Figure 3-19 shows the $3\text{-}^{13}\text{C}\{^{15}\text{N}\}$ REDOR dephasing of the methyl carbon resonance, which reports on the pY peptides (Ac-KL ^{15}N VFF ^{13}C AL-NH $_2$). Best fits are obtained with 27.0 \pm 2.4% of the pY-peptides are in a 3-spin arrangement and 46.3 \pm 3.0% in 2-spin arrangements, and this leaves the rest of 26.7 \pm 3.8% pY peptide ^{13}C do not dephase. The 3-spin arrangements of ^{13}C are corresponding to homogeneous leaflets, while the 2-spin and no dephasing arrangements are consistent with heterogeneous leaflets.

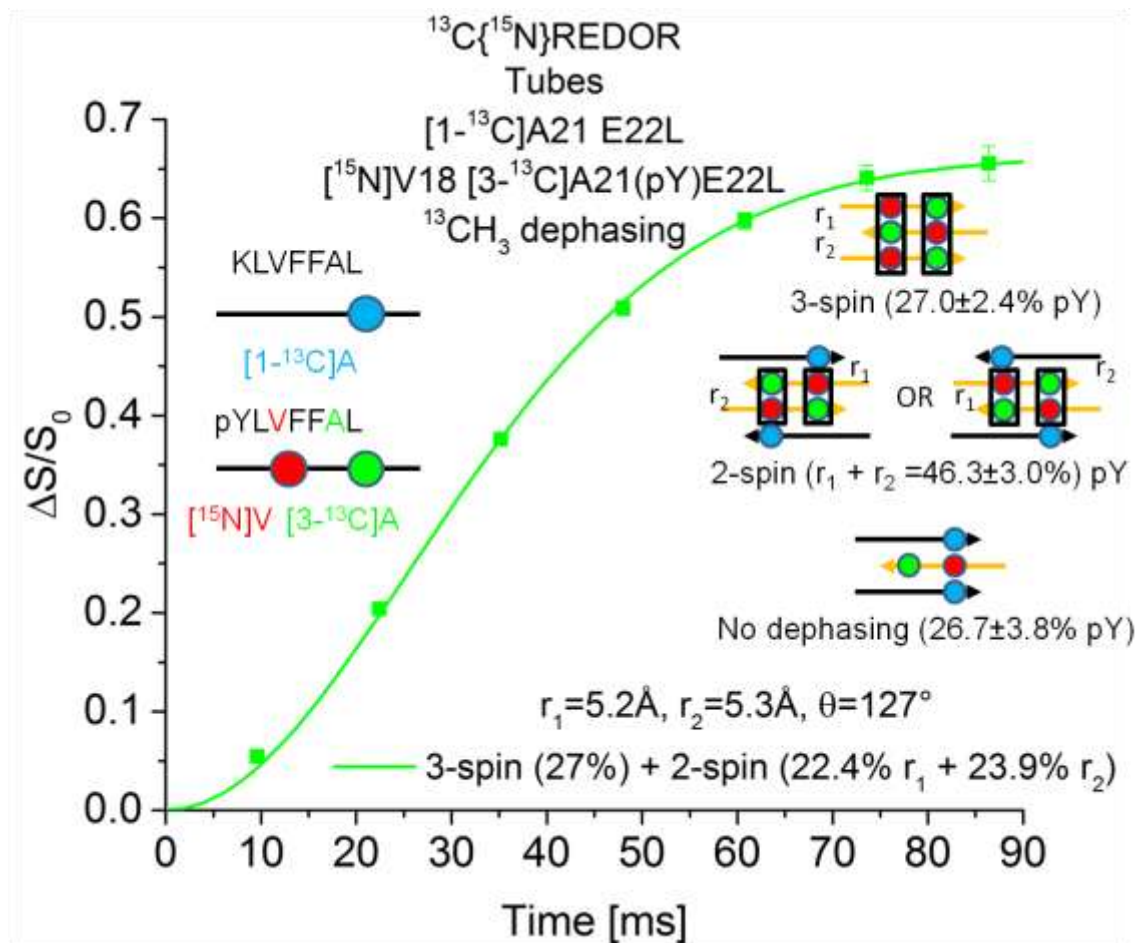


Figure 3-19 The $^{13}\text{C}\{^{15}\text{N}\}$ REDOR dephasing fits to summation of 3-spin and 2-spin systems. $^{13}\text{C}\{^{15}\text{N}\}$ REDOR dephasing fits to ^{13}C - ^{15}N distances of 5.2 and 5.3 Å a ^{15}N - ^{13}C - ^{15}N internuclear angle of 127° .

Peptide Interfaces Analysis

The $1-^{13}\text{C}\{^{15}\text{N}\}$ and $3-^{13}\text{C}\{^{15}\text{N}\}$ REDOR dephasing results are summarized in Figure 3-20. There is $35.4 \pm 7.0\%$ of the K peptides arranged in homogeneous leaflets, in correspondence $27.0 \pm 2.4\%$ of the pY peptides are arranged in homogeneous leaflets. Take into the K and pY peptides ratio of 0.62 into consideration; the numbers of K peptides that are arranged in homogeneous leaflets are about 1:1 with the numbers of pY peptides that are arranged in homogeneous leaflets ($35.4 \pm 7.0\% \times 0.62 = 22.0 \pm 4.4\%$, equal to $27.0 \pm 2.4\%$ within error), suggesting the existence of homogeneous bilayers. Moreover, $45.4 \pm 2.4\%$ of the K peptides and $26.7 \pm 3.8\%$ of the pY peptides are arranged as alternating repeats under the category of heterogeneous leaflets. The numbers of K and pY peptides that are arranged as alternating repeats are matched as 1:1 within error ($45.4 \pm 2.4\% \times 0.62 = 28.1 \pm 2.9\%$, equal to $26.7 \pm 3.8\%$ within error), revealed the formation of

heterogeneous leaflets by alternating repeats of K and pY peptides. Interestingly, REDOR NMR measurements revealed that certain amounts of peptides formed non-alternating repeats as heterogeneous leaflets and more pY peptides are falling into this category than K peptides could be an indication of more robust thermodynamic stability or self-assembly propensity of pY peptide than K peptide.




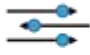
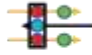
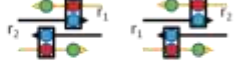



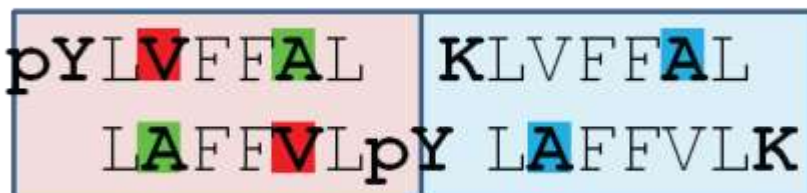
Account by % of peptides	Homogeneous leaflets		Heterogeneous leaflets	
				
			Alternating repeats	Non-alternating repeats
K	 35.4±7.0%		 45.4±4.7%	 18.7±6.9%
pY	 27.0±2.4%		 26.7±3.8%	 46.3±3.0%

Figure 3-20 Peptide leaflets analysis of Ac-KLVFFAL and Ac-pYL VFFAL co-assemblies.

In summary, the three types of leaflets can form three different bilayers based on surface charge characterization and solid-state NMR results (Figure 3-21): homogeneous bilayers consisted of K homogeneous leaflets and pY homogeneous leaflets; heterogeneous bilayers consisted of alternating repeats of K and pY peptides; and heterogeneous bilayers consisted of non-alternating repeats of K and pY peptides. The first two bilayer domains will give asymmetric peptide membranes with distinct charges on inner and outer surfaces. The third bilayer domain will form symmetric peptide membranes with same negative charges on inner and outer surfaces. This results is consistent with the fluorescence imaging analysis (see chapter 4) where both positively-charged and negatively-charged surfaces were observed in the co-assemblies.

Homogeneous bilayers



Heterogeneous bilayers consisted of alternating repeats of heterogeneous leaflets



Heterogeneous bilayers consisted of non-alternating repeats of heterogeneous leaflets

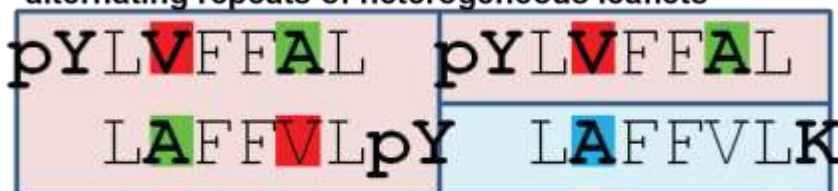


Figure 3-21 Peptide domains analysis of Ac-KLVFFAL and Ac-pYLVFFAL co-assemblies.

Domain Segregation Built upon Cross-Seeding

Although solid-state REDOR NMR successfully deciphered the partition of domain segregation on peptide nanotube surfaces, it is unclear where these domains exist, and how they form. It is intriguing whether the different domains are reflecting different nanotubes resulting from distinct nucleation events or mutations accumulate during nucleation step and propagate distinct domain architectures within single tubes. In fact, we have found some evidence with domains on single tubes in the co-assemblies (Figure 3-22). If domains can exist on single tubes, then the K and pY peptides must be able to propagate upon each other's nucleation domains to give heterogeneous leaflets. To test whether K and pY peptides can propagate with each other's nucleation domains, cross-seeding experiments were performed.

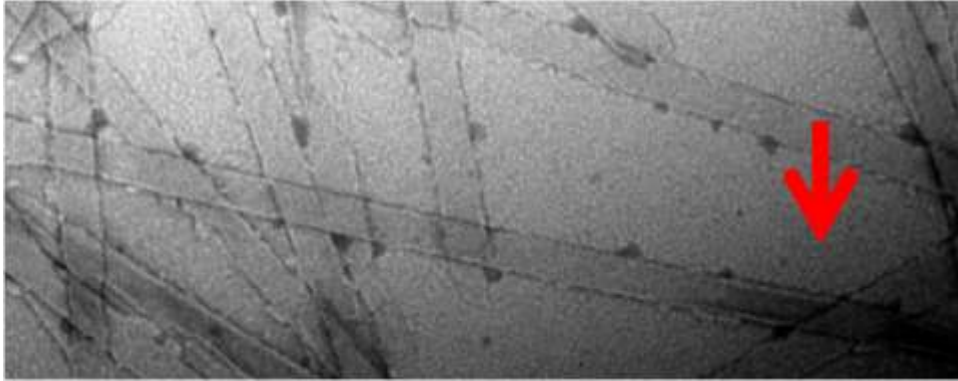


Figure 3-22 TEM micrographs of domain observed on single tubes in the co-assemblies shown by the red arrow.

Peptide nanotube seeds were prepared by sonicating one sample of mature nanotubes for 3 hours to nanotubes fragments and added to the other peptide monomers. Figure 3-23 showed CD of the K peptide monomers seeded by K, pY and mix nanotubes over 1, 4, 7 and 11 days. Figure 3-24 showed CD of the pY peptide monomers seeded by K, pY and mix nanotubes 1, 4, 7 and 11 days. All seeded samples have much higher ellipticity than K peptide monomers alone (2-7 times larger on day 11), and higher than a sum of seeds and monomers. Therefore K, pY and co-assemblies are able to cross-seed each other, although seeding efficiencies are different. Co-assembly nanotubes seeds seem to accelerate the assemblies the most: Co-assembly nanotubes seeded K monomers have 2.2 times increases in ellipticity from day 1 to day 4, and Co-assembly nanotubes seeded pY monomers have 4 times increases in ellipticity from day 1 to day 4. K nanotubes seeded K monomers, pY nanotubes seeded K monomers, K nanotubes seeded pY monomers and pY nanotubes seeded pY monomers only have 1.2, 2.6, 2 and 1.2 times increases in ellipticity respectively from day 1 to day 4. All assemblies remained relatively stable from day 4 to day 11. It's likely that cross-seeding partially bypasses the nucleation step but has little effect on tube elongation or cross-seeding only moderately affects the nucleation rate while significantly enhancing the growth of nanotubes from existing nuclei. The ability of peptides to interact with peptides of dissimilar sequences suggests cross-seeding may be a more general phenomenon.

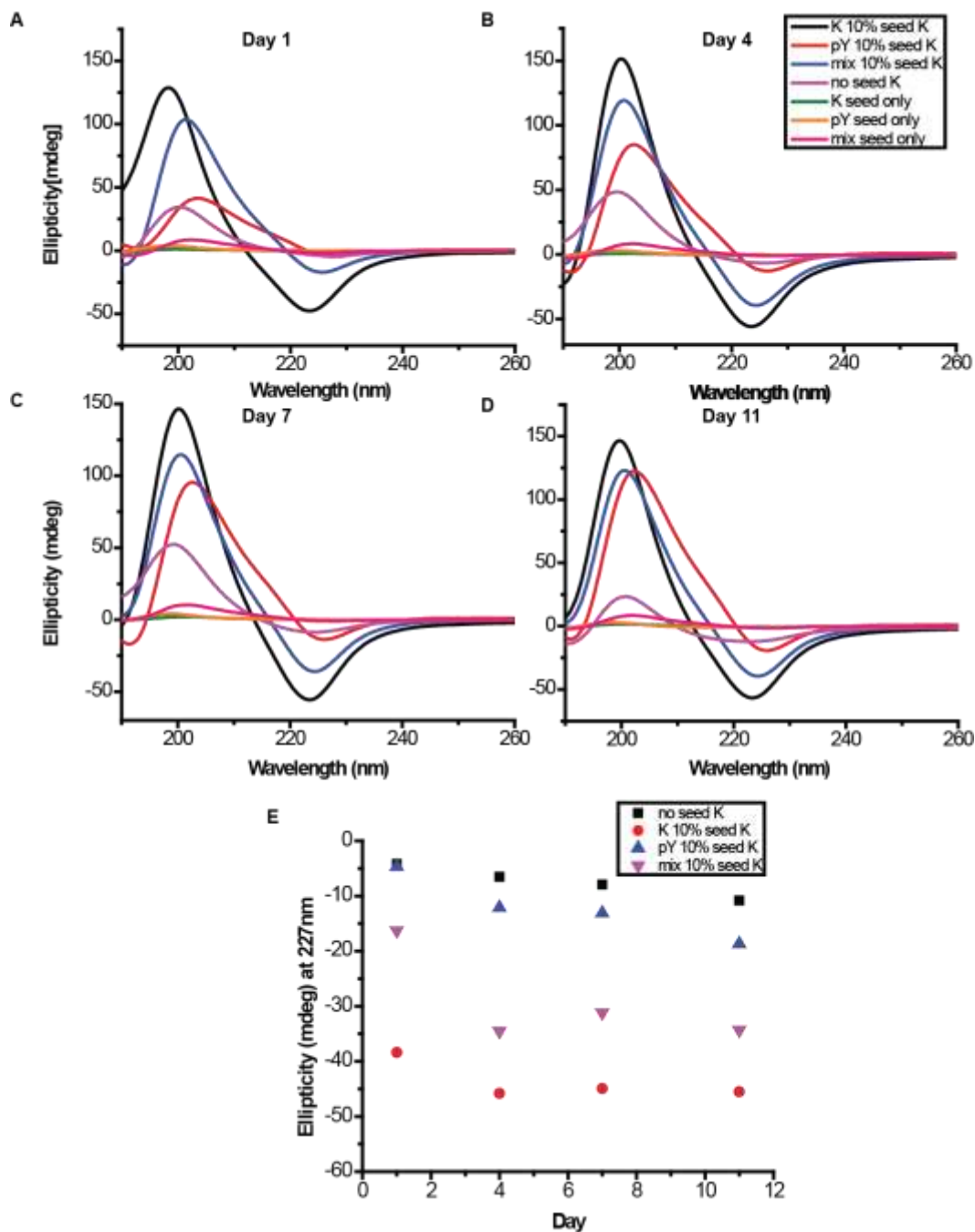


Figure 3-23 Circular Dichroism on day1 (A), 4 (B), 7 (C) and 11 (D) of Ac-KLVFFAL nanotubes as seeds for Ac-KLVFFAL monomers (black), Ac-pYL VFFAL nanotubes as seeds for Ac-KLVFFAL monomers (red), Ac-KLVFFAL and Ac-pYL VFFAL coassembled into nanotubes as seeds for Ac-KLVFFAL monomers (blue), Ac-KLVFFAL monomers (purple), Ac-KLVFFAL nanotubes seeds (green), Ac-KLVFFAL nanotubes seeds (yellow), Ac-KLVFFAL and Ac-pYL VFFAL coassembled into nanotubes seeds (magenta). Maximum ellipticity at 227 nm was plotted over time for the seeding samples in (E). Seeds vs monomer concentration ratio equals 1:9 (10% seed).

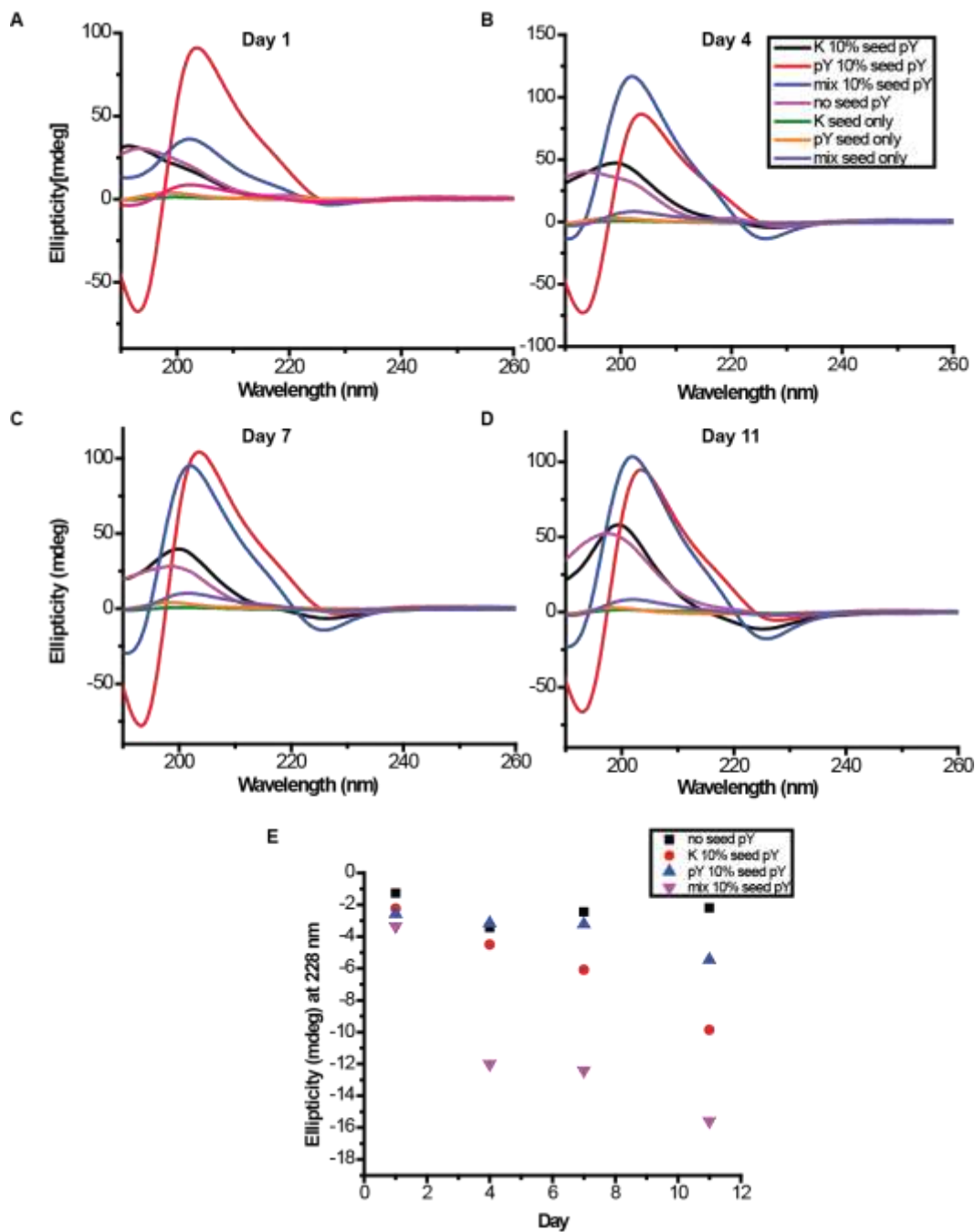


Figure 3-24 Circular Dichroism on day1 (A), 4 (B), 7 (C) and 11 (D) of Ac-KLVFFAL nanotubes as seeds for Ac-pYL VFFAL monomers (black), Ac-pYL VFFAL nanotubes as seeds for Ac-pYL VFFAL monomers (red), Ac-KLVFFAL and Ac-pYL VFFAL coassembled into nanotubes as seeds for Ac-pYL VFFAL monomers (blue), Ac-pYL VFFAL monomers (purple), Ac-KLVFFAL nanotubes seeds (green), Ac-KLVFFAL nanotubes seeds (yellow), Ac-KLVFFAL and Ac-pYL VFFAL coassembled into nanotubes seeds (magenta). Maximum ellipticity at 225 nm was plotted over time for the seeding samples in (E). Seeds vs monomer concentration ratio equals 1:9 (10% seed). All nanotubes seeds were sonicated for 3 hr before adding to peptide monomers.

K and pY tubes show similar negative stained contrast by TEM when they are stained by uranyl acetate on separate grids (Figure 3-25 A and B). Interestingly, when K and pY tubes are stained by uranyl acetate on a same grid sequentially (i.e. K nanotube are dried on EM grid followed by application of pY tubes on the same grid and then stain the grid with uranyl acetate) (Figure 3-25 C), pY nanotubes are stained relatively positive compared to the negatively stained K nanotubes, probably due to uranyl acetate's crystallization on the phosphate surfaces. To confirm the staining contrast is caused by uranyl acetate's crystalline precipitation, a same grid was prepared and stained by methylamine tungstate, another commonly used stain that does not crystallize with phosphate. No staining contrast was observed (Figure 3-26). The ability of uranyl acetate to stain differently toward K and pY peptide nanotubes provides a convenient strategy to analyze domains on single nanotubes.

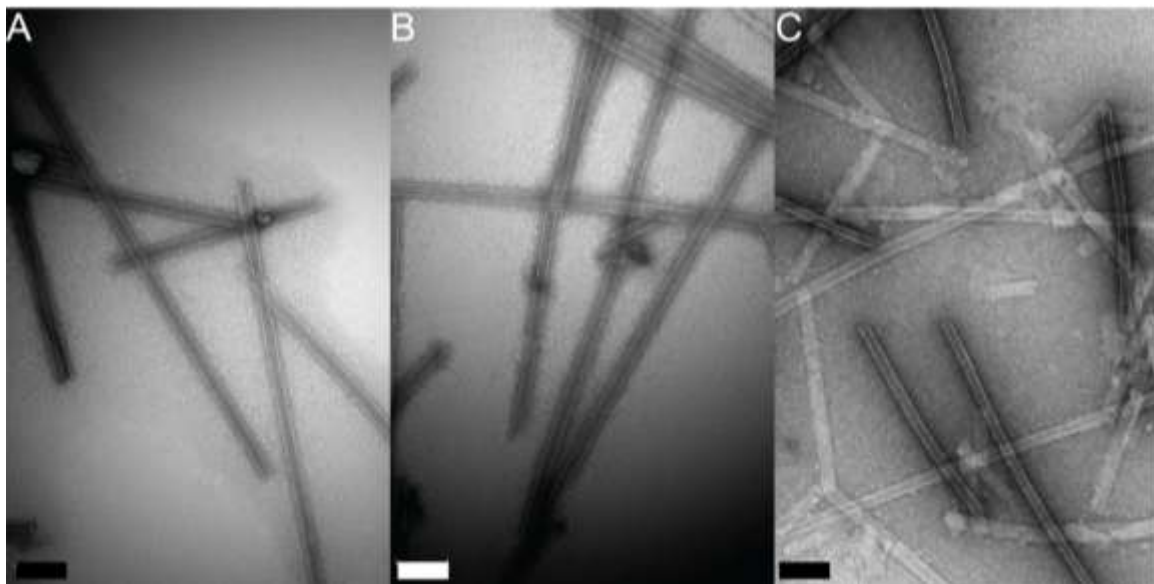


Figure 3-25 TEM micrographs of (A) Ac-KLVFFAL nanotubes, (B) Ac-pYL VFFAL nanotubes, (C) Ac-KLVFFAL and Ac-pYL VFFAL nanotubes applied on a same grid sequentially. Scale bar 200nm. Stained by uranyl acetate.

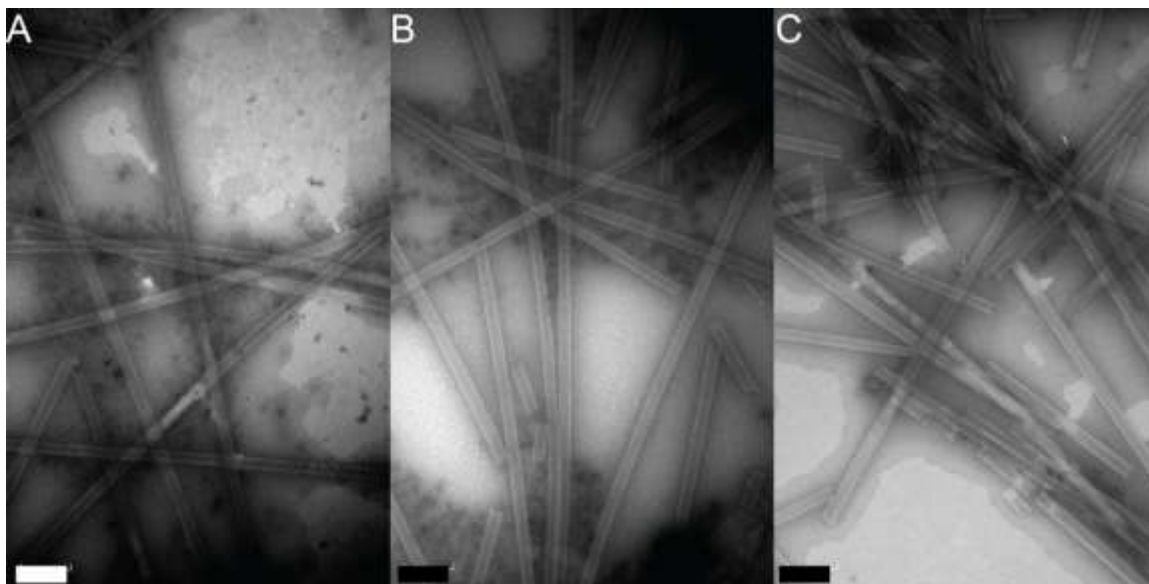


Figure 3-26 TEM micrographs of (A) Ac-KLVFFAL nanotubes, (B) Ac-pYLVFFAL nanotubes, (C) Ac-KLVFFAL and Ac-pYLVFFAL nanotubes applied on a same grid sequentially. Scale bar 200nm. Stained by methylamine tungstate.

Figure 3-27 A and B show TEM of K and pY nanotubes seeds prepared by sonication with lengths vary from 200 to 400 nm. When K and pY peptide monomers were seeded by K and pY nanotubes (10% seed), the assembled nanotubes were homogeneous from one end to the other with uranyl acetate stain (Figure 3-27 C and D). However, when K and pY peptide monomers were cross-seeded with pY and K nanotubes (10% seed) respectively, the assembled nanotubes contain segregated segments with opposite stain from the rest of the nanotubes (Figure 3-27 E and F).

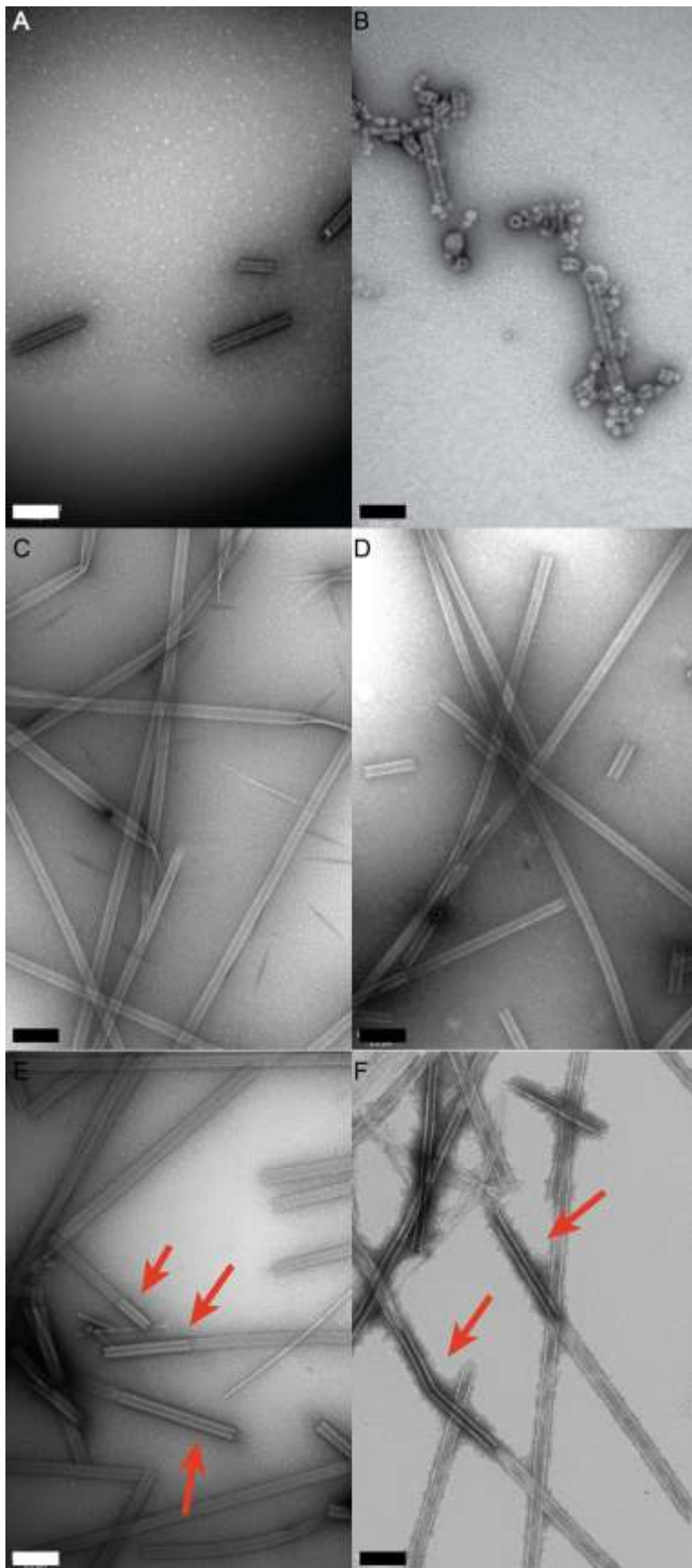


Figure 3-27 TEM micrographs of (A) Ac-KLVFFAL nanotubes seed, (B) Ac-pYLVFFAL nanotubes seed (C) Ac-KLVFFAL nanotubes seed Ac-KLVFFAL monomer, (D) Ac-pYLVFFAL nanotubes seed Ac-pYLVFFAL monomer, (E) Ac-KLVFFAL nanotubes seed Ac-pYLVFFAL monomer, (F) Ac-pYLVFFAL nanotubes seed Ac-KLVFFAL monomer. Arrows point out the domain structures with drastic contrast of the rest of the tubes. Seeds vs monomer concentration ratio equals 1:9 (10% seed). All nanotubes seeds were sonicated for 3 hr before adding to peptide monomers. Scale bar 200nm.

To confirm that the oppositely stained domains are oppositely charged from the rest of the nanotube, negatively-charged gold nanoparticles were added to the K tubes 10% seeded pY peptides sample. TEM (Figure 3-28) showed that the negatively-charged gold nanoparticles bind specifically to segments of the tubes, consistent with the hypothesis that the domains are K nanotubes seeds and the rest of the tubes are composite of pY peptide monomers. Similar growing pattern in fibers cross-seeding is known as epitaxial heteronucleation^{17,18}, growth occurs by specific structural matching between oligomeric protofibrillar aggregates and the seeding nucleus^{19,20}. In fact, cross-seeding between amyloid proteins is most efficient when the two proteins have homologous sequences²⁰. This ability to add either K or pY peptide onto either template supports the model that during propagation, mutations occur in co-assembly that initiate a new domain structure (Figure 3-29).

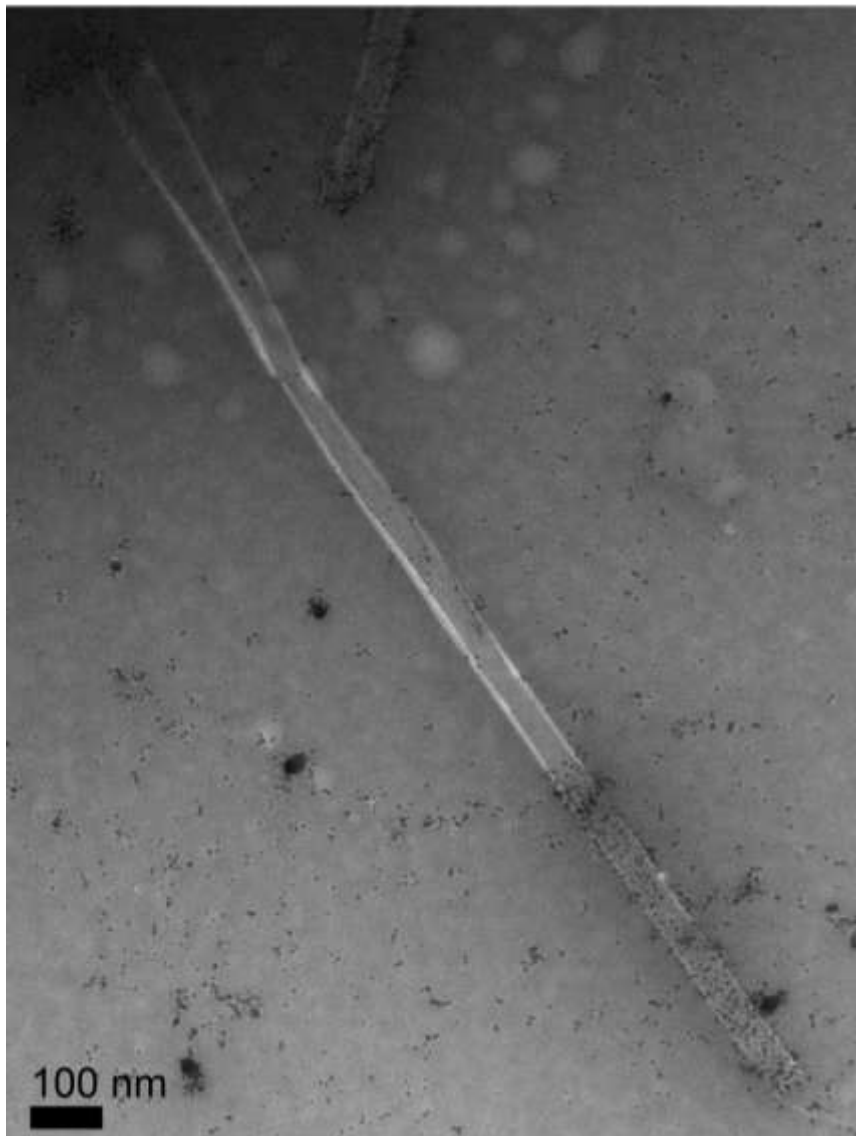


Figure 3-28 TEM micrograph of Ac-KLVFFAL nanotubes seed Ac-pYLVFFAL monomer + negatively-charged AuNPs. Peptide vs AuNPs concentration ratio is 1:12.

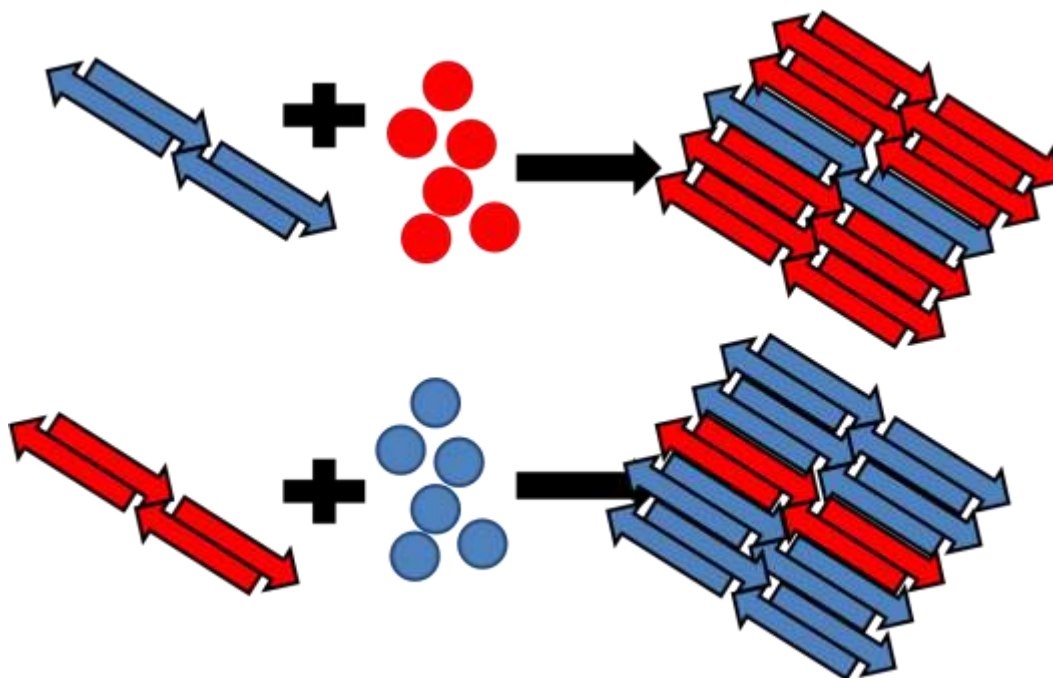


Figure 3-29 Concept illustration of cross-seeding mechanism. Arrow represent preformed β -sheet and circle represent peptide monomers. Blue is consistent with positively-charged K sheet and red is consistent with negatively-charged pY sheet.

If propagation mutation mechanism is true, then the co-assembly nanotube seeds should provide more robust templates with already propagated mutations. CD suggested that when seeded by coassemblies, both K and pY peptide assembled faster (Figure 3-23 and 3-24). Remarkably, TEM (Figure 3-30 and 3-31) presented the existence of multiple segments stained oppositely from the rest of the tube, whereas only 1-2 segments were observed on every single tube when K and pY are cross-seeded.

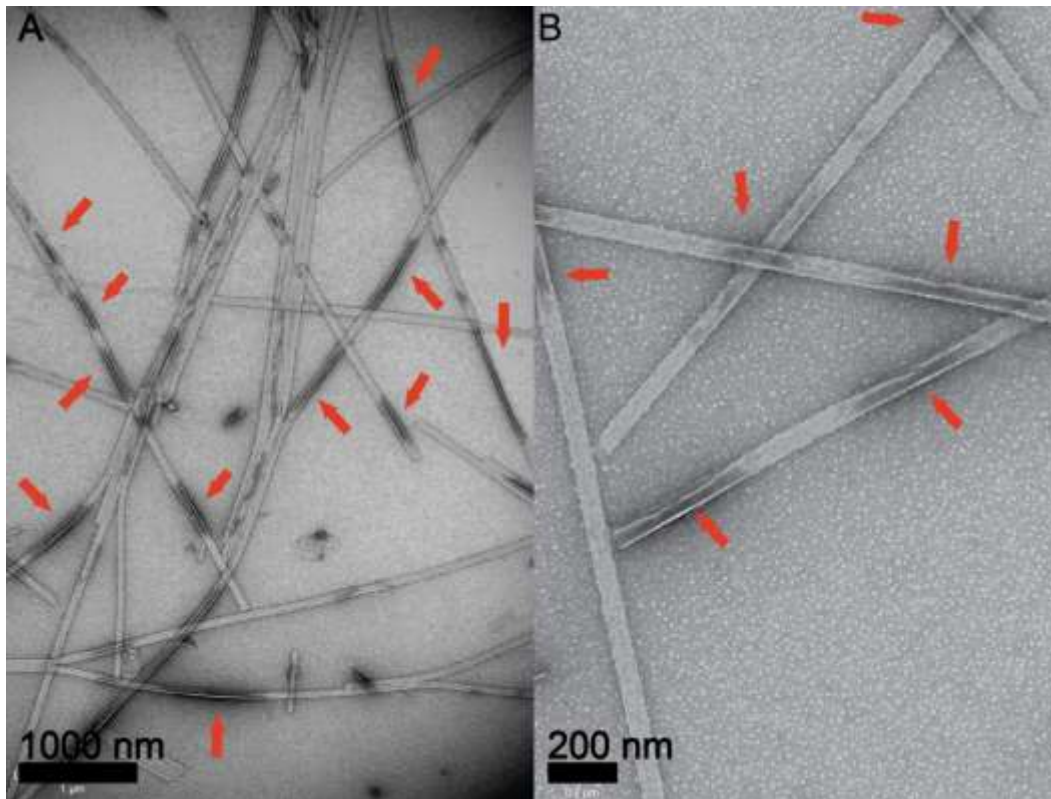


Figure 3-30 TEM micrograph of Ac-KLVFFAL peptides seeded with co-assembled peptide nanotubes. (A) Scale bar 1000nm, (B) scale bar 200nm. Arrows indicate the domain structures with drastic staining contrast compare to the rest of the tubes.

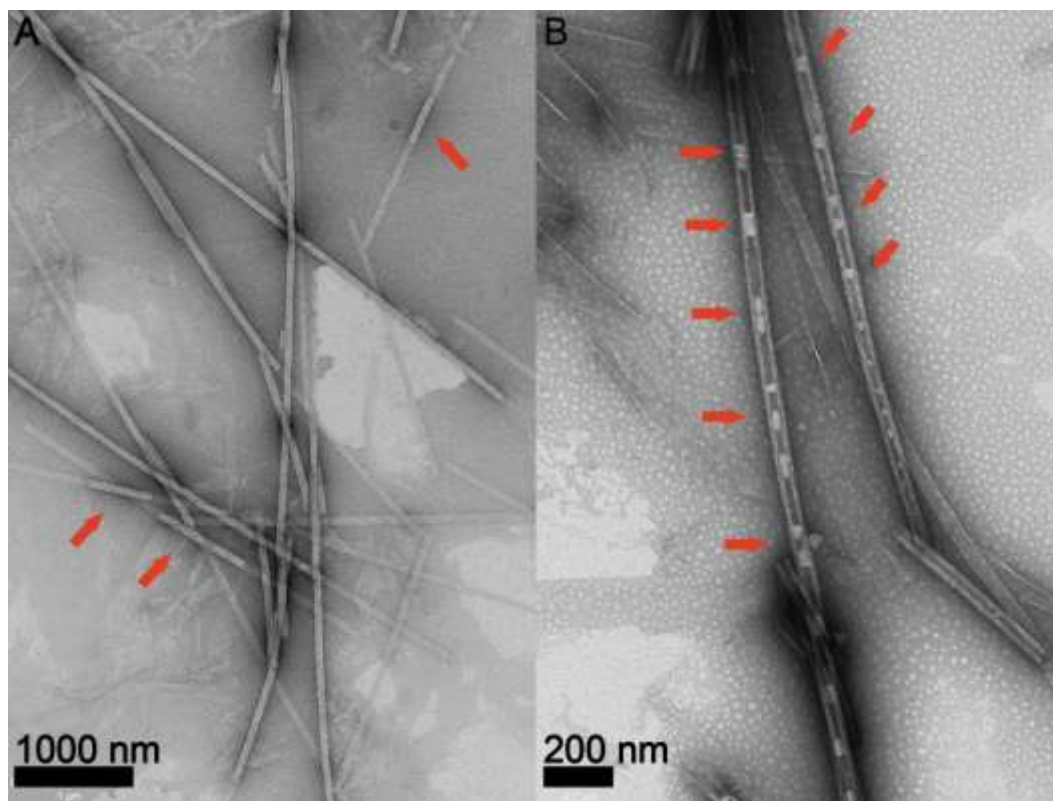


Figure 3-31 TEM micrograph of Ac-pYL VFFAL peptides seeded with co-assembled peptide nanotubes. (A) Scale bar 1000nm, (B) scale bar 200nm. Arrows indicate the domain structures with drastic staining contrast compare to the rest of the tubes.

When only one type of peptide monomer exists in solution, epitaxial heteronucleation dominates as peptides can be cross-seeded by different sequences consistent with them sharing homogeneous structures. What about when there are two types of peptide monomers exist in solution? Will peptide monomers be seeded selectively or will peptides form new oligomeric particles before being seeded? To answer this question, K nanotubes, pY nanotubes and coassembled nanotube seeds were prepared to seed 1:1 mixed K and pY peptide monomers. Kinetic results are shown in Figure 3-32 and Figure 3-33. It takes longer for the mixed peptides to grown mature (around day 45) than K or pY peptides alone (around day 7).

All seeded samples have higher ellipticity than mixed peptides alone (2-6 times higher on day 45), and the ellipticity of seeded samples is not a sum of seeds and monomers, demonstrating that that K, pY and mix assemblies are able to cross-seed each other. CD of coassembled K and pY peptides without seeds has a shoulder peak at 220 nm that disappears around day 45 (Figure 3-33). The 220nm shoulder could be the result of

disordered oligomer assemblies or particle-like aggregates implicated as nucleation and propagation centers²¹. However, when mixed K and pY peptides were seeded by coassembled nanotubes, the shoulder around 220 nm disappears around day 6. The seeds very likely bypass or speed up the nucleation and propagation step.

Seeding efficiencies are distinct with different seeds. Peptides seeded by coassembled tubes showed the largest change in CD spectrum (8.7 times) from day 1 to day 6, while peptides seeded by K tubes only increased 3.7 times and peptides seeded by pY tubes remain constant from day 1 to day 6 (Figure 3-32). Peptides seeded by K or pY tubes reach a CD ellipticity maximum at day 6. However, the CD ellipticity of peptides seeded by coassembled tubes continued to grow after day 6 until a maximum was reached around day 30, suggesting that there are multiple nucleation events or mutations during propagation.

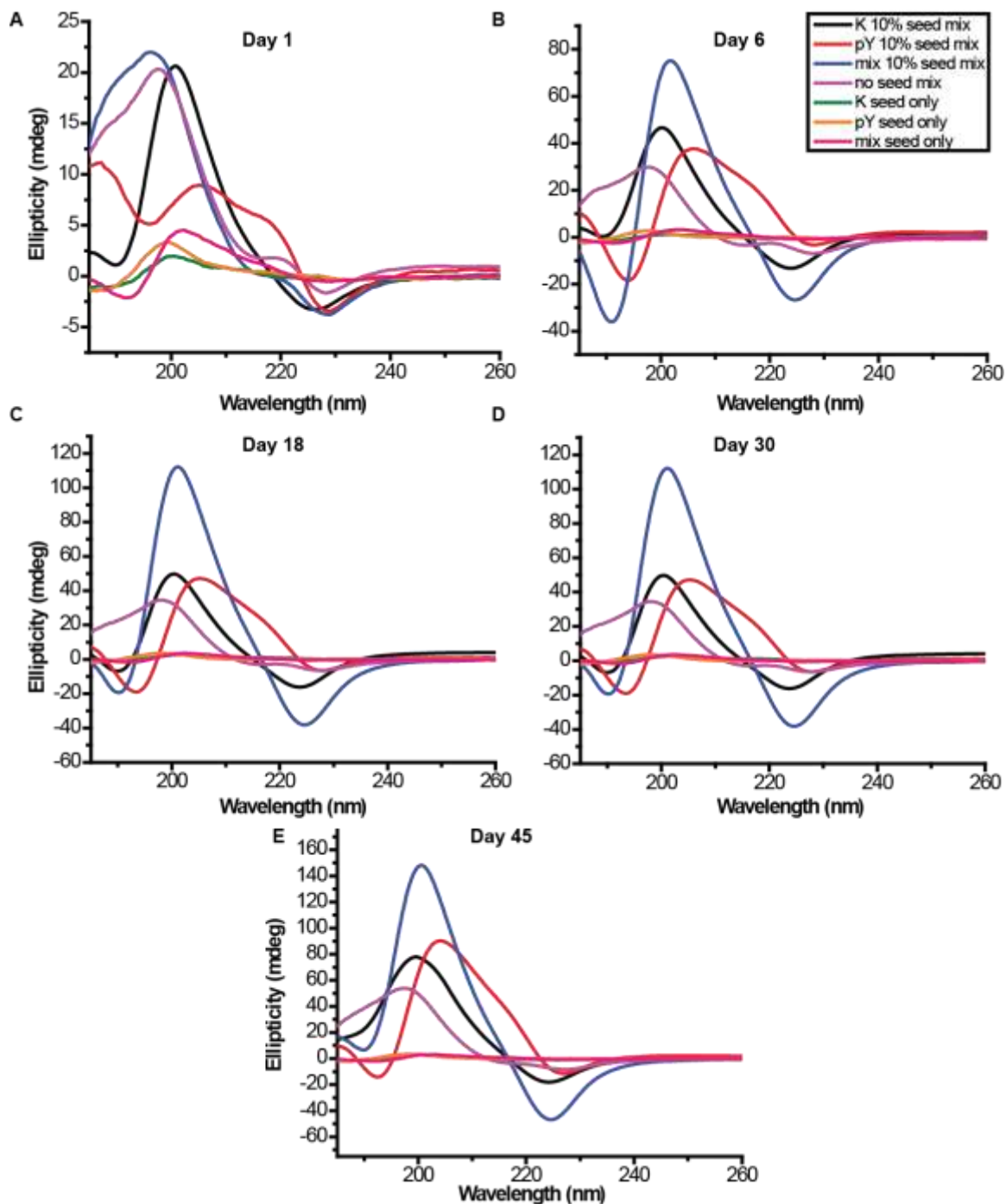


Figure 3-32 Circular Dichroism on day1 (A), 6 (B), 18 (C), 30 (D) and 45 (E) of Ac-KLVFFAL nanotubes as seeds for Ac-KLVFFAL and Ac-pYLFFAL mixed monomers (black), Ac-pYLFFAL nanotubes as seeds for Ac-KLVFFAL and Ac-pYLFFAL mixed monomers (red), Ac-KLVFFAL and Ac-pYLFFAL coassembled into nanotubes as seeds for Ac-KLVFFAL and Ac-pYLFFAL mixed monomers (blue), Ac-KLVFFAL and Ac-pYLFFAL mixed monomers (purple), Ac-KLVFFAL nanotubes seeds (green), Ac-KLVFFAL nanotubes seeds (yellow), Ac-KLVFFAL and Ac-pYLFFAL coassembled into nanotubes seeds (magenta). Maximum ellipticity at 225 nm was plotted over time for the seeding

samples in (E). Seeds: monomer concentration ratio 1:9 (10% seed). All nanotubes seeds were sonicated for 3 hr before adding to peptide monomers.

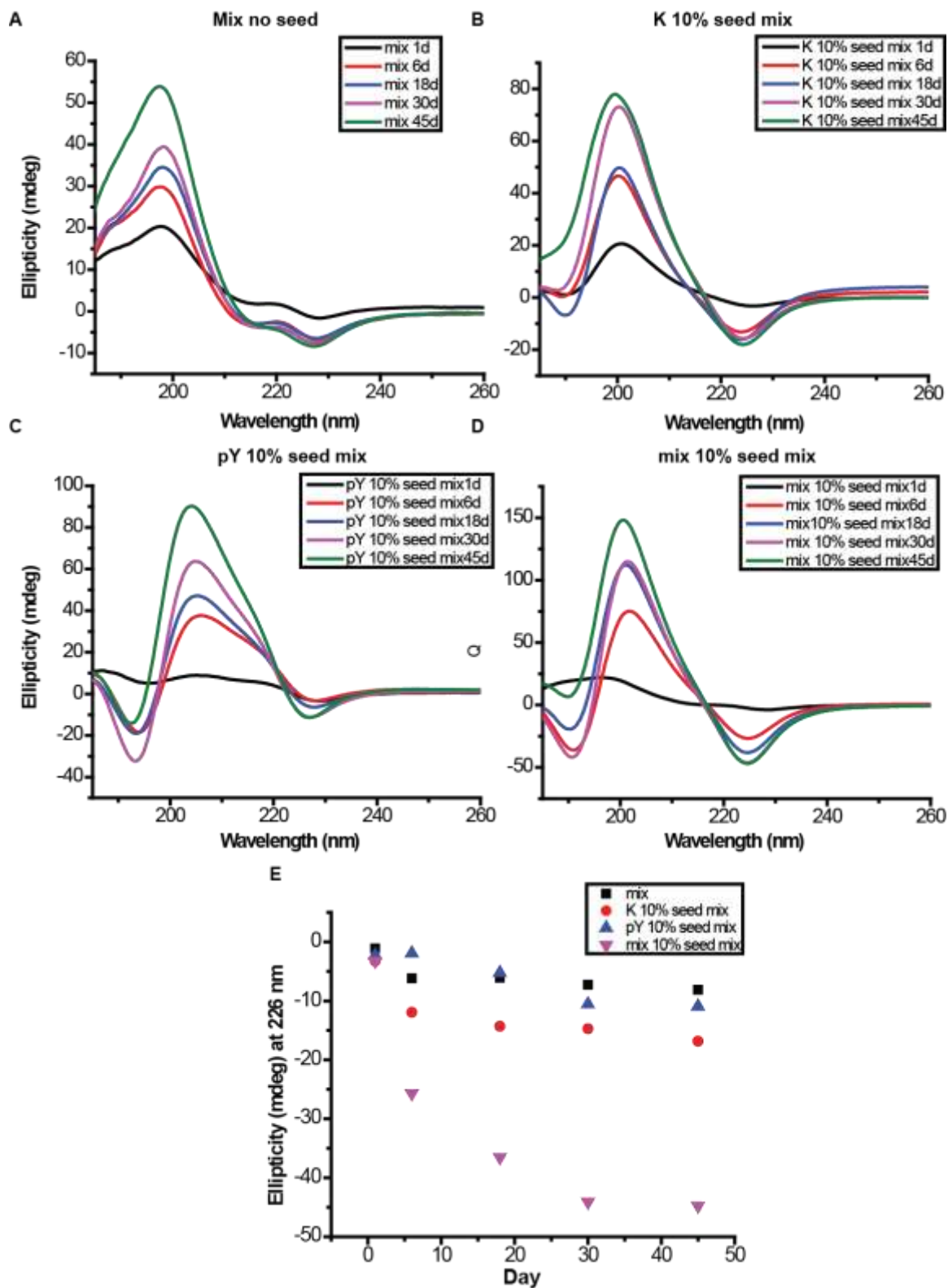


Figure 3-33 Circular Dichroism of (A) Ac-KLVFFAL and Ac-pYLFFAL mixed monomers, (B) Ac-KLVFFAL nanotubes as seeds for Ac-KLVFFAL and Ac-pYLFFAL mixed monomers, (C) Ac-pYLFFAL nanotubes as seeds for Ac-KLVFFAL and Ac-pYLFFAL mixed monomers, (D) Ac-

KLVFFAL and Ac-pYLVFFAL coassembled into nanotubes as seeds for Ac-KLVFFAL and Ac-pYLVFFAL mixed monomers Ac-KLVFFAL nanotubes as seeds for Ac-KLVFFAL and Ac-pYLVFFAL mixed monomers. Maximum ellipticity at 225 nm was plotted over time for the seeding samples in (E).

TEM micrographs of K, pY and coassembled nanotubes seed mixed K and pY peptides were shown in Figure 3-34. Homogeneous nanotubes dominate all 3 samples. However, in some images of peptides seeded by K or pY tubes, there are negatively and positively stained nanotubes, presumably pure K and pY nanotubes. Therefore, both self-seeding and cross-seeding could have taken place when mixed K and pY peptides were seeded by coassembled tubes.

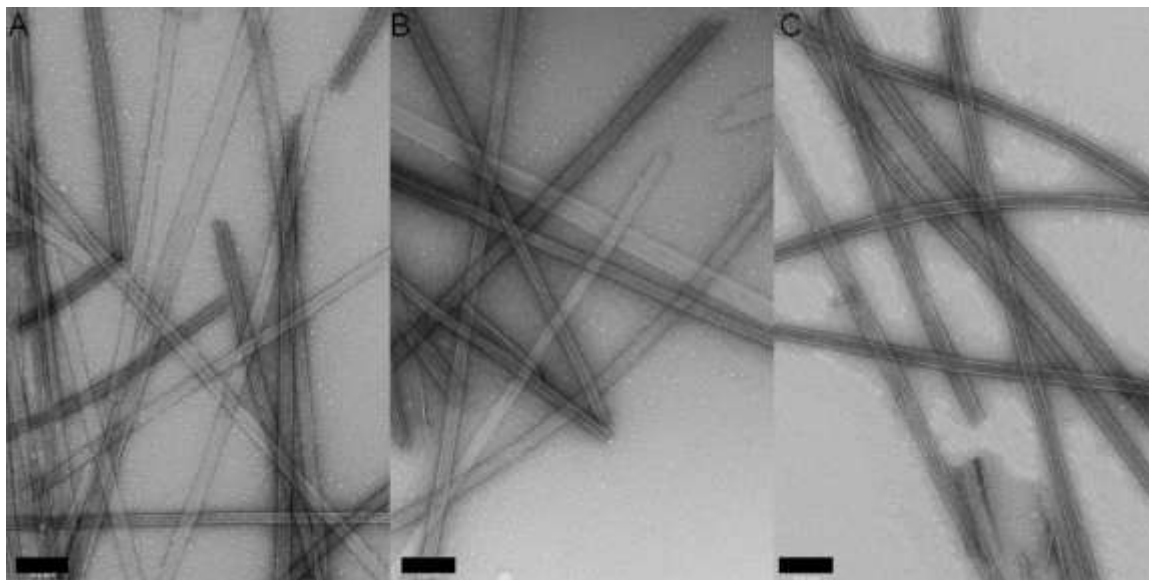


Figure 3-34 TEM micrograph for (A) Ac-KLVFFAL nanotubes as seed for mixed Ac-KLVFFAL and Ac-pYLVFFAL peptide monomers, (B) Ac-pYLVFFAL nanotubes as seed mixed Ac-KLVFFAL and Ac-pYLVFFAL peptide monomers, (C) Ac-KLVFFAL and Ac-pYLVFFAL mix peptides coassembled as nanotubes as seeds for Ac-pYLVFFAL peptide monomers. Scale bar 200nm.

Exploit Surface Charge Distribution and N-terminal Residue Sizes

Phosphotyrosine residues dominate outer surfaces in coassembly of Ac-KLVFFAL and Ac-pYLVFFAL peptides. I hypothesize that it's because phosphotyrosine is larger than lysine residue, hence they're preferable to be exposed on outer surfaces with larger radius and smaller curvature. To test this hypothesis, phosphotyrosine is replaced by negatively charged glutamic acid with smaller size. Coassembled Ac-KLVFFAL and Ac-ELVFFAL form homogeneous nanotubes in 40% MeCN/H₂O (Figure 3-35) and exhibits ellipticity minimum at 227 nm (Figure 3-36), a signature diagnostic of β -strands. Thermal melting profiles of Ac-ELVFFAL nanotubes (Figure 3-37) showed a cooperative melting

curve fitted to the equation $y=3.4972+(-66.2539-3.4972)/(1+\exp((T-57.6199)/13.73808))$, corresponding to a melting point of 57.6 ± 13.7 °C. The coassembled Ac-KLVFFAL and Ac-ELVFFAL (Figure 3-38) maintains stable until the tube pellets were resuspended in 70% MeCN/H₂O. The melting curve was fit to the equation $y=-9.303+(-16.0809+9.303)/(1+\exp((T-66.9284)/3.7767))$, corresponding to a melting point of 55.9 ± 3.8 . According to thermal stability studies in chapter 2, melting point decreases with higher percentage of MeCN. Therefore, the co-assemblies are much more stable than each peptide assemblies alone. The coassembled Ac-KLVFFAL and Ac-ELVFFAL system is similar to coassembled Ac-KLVFFAL and Ac-pYL VFFAL system in terms of thermal stability. However, the coassemblies Ac-KLVFFAL and Ac-ELVFFAL presented a homogeneous positive outer surfaces by EFM (Figure 3-39), suggested that lysine residues dominate outer surface. It's amazing that a simple switch on the residue side chain could switch the surface charges distribution.

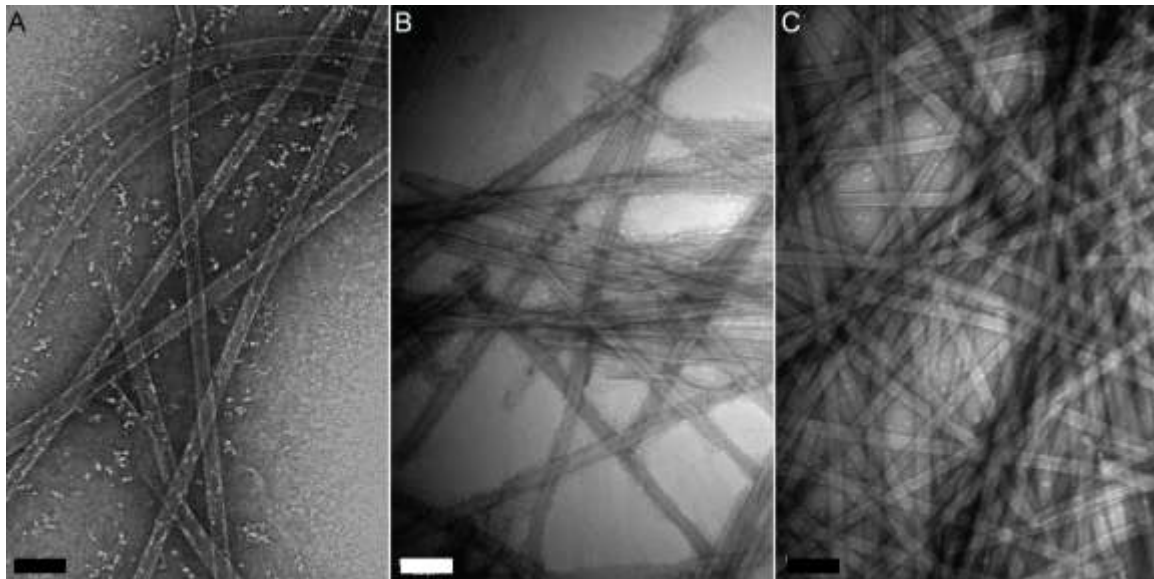


Figure 3-35 TEM micrograph of (A) Ac-KLVFFAL in 40% MeCN/H₂O with TFA, (B) Ac-ELVFFAL in 40% MeCN/H₂O with TEAA, (C) mixed Ac-KLVFFAL and Ac-ELVFFAL assembled as nanotubes in 40% MeCN/H₂O.

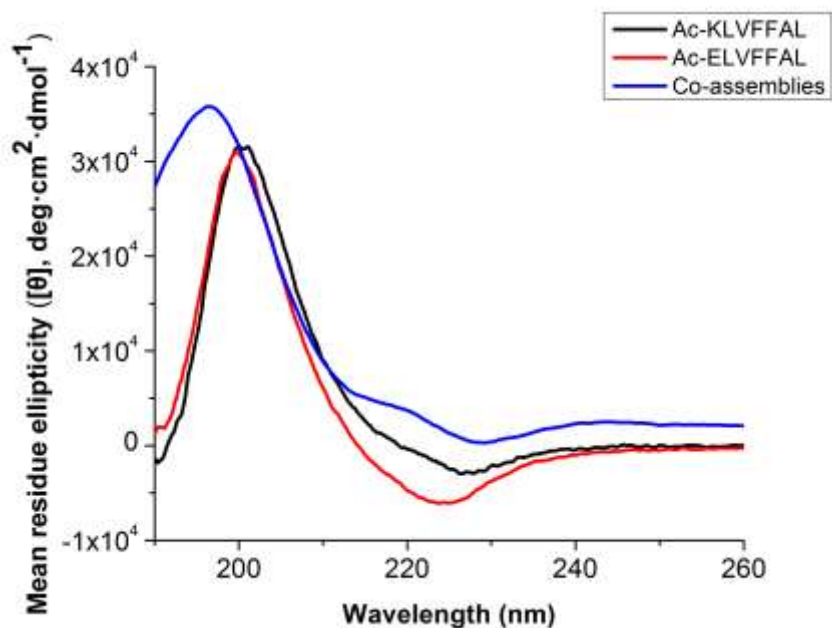


Figure 3-36 Circular Dichroism of Ac-KLVFFAL, Ac-ELVFFAL and coassembled Ac-KLVFFAL and Ac-ELVFFAL as nanotubes in 40% MeCN/H₂O.

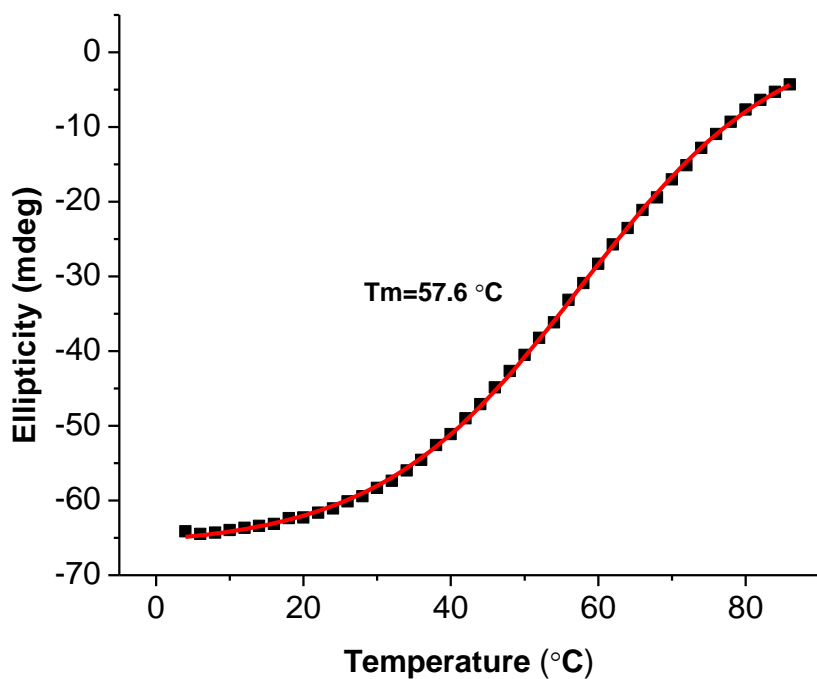


Figure 3-37 CD melting profiles for Ac-ELVFFAL peptide nanotubes formed in 40% MeCN/H₂O at 4 °C. The melting curve was fit using the sigmoidal form of the Boltzmann equation. $y=3.4972+(-66.2539-3.4972)/(1+\exp((T-57.6199)/13.73808))$, corresponding to a melting point of 57.6 ± 13.7 °C.

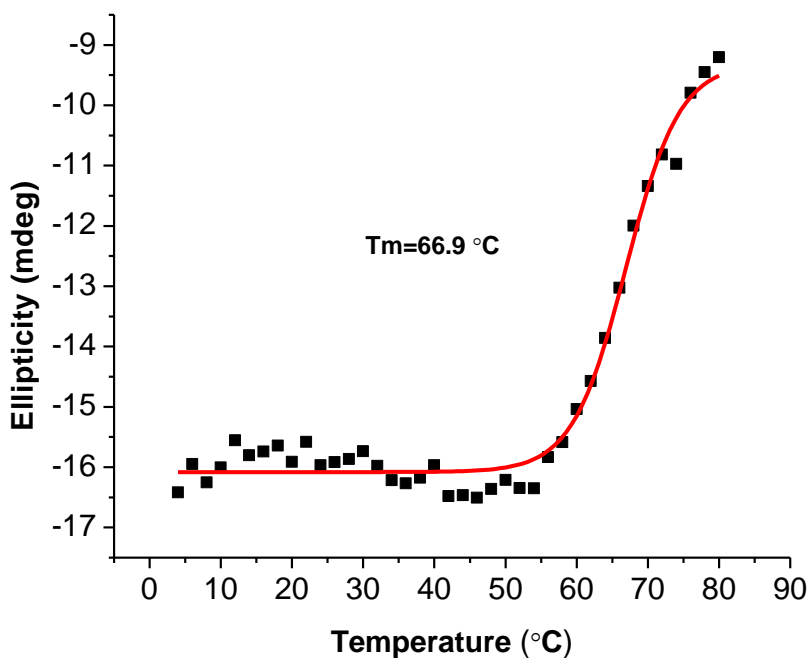


Figure 3-38 CD melting profiles for mixed Ac-KLVFFAL and Ac-ELVFFAL peptide nanotubes formed in 40% MeCN/H₂O at 4 °C and resuspended in 70% MeCN/H₂O. The melting curve was fit using the sigmoidal form of the Boltzmann equation. $y = -9.303 + (-16.0809 + 9.303) / (1 + \exp((T - 66.9284) / 3.7767))$, corresponding to a melting point of 66.9 ± 3.8 °C.

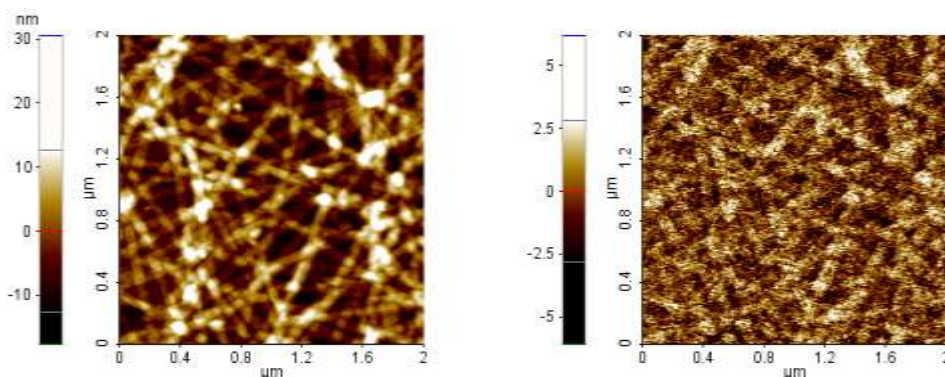


Figure 3-39 Topography (left) EFM amplitude (middle) and EFM phase micrographs (right) of Ac-KLVFFAL and Ac-ELVFFAL peptides co-assemblies in 40% MeCN/H₂O, DC bias +1 V. In the EFM amplitude micrographs, positively charged surfaces are white and negatively charged surfaces are dark.

Exploit Peptide Specificity in Co-Assembly

Nature's self-assembling systems are complex and require specificity. Recent advances have shown that mixtures of helical peptides have adequate specificity to assemble even

within complex mixtures where promiscuous coiled-coil binding could take place.^{22,23} Peptide sequence encode specificity has been studied by coassembly of Ac-KLVFFAL and its congener, Ac-KLVFFAV peptides as introduced in chapter 1. They self-sorted as separate nanotubes as well as newly nucleated as short fibers²⁴, argued that a single methylene change encodes molecular level information. To compare the molecular codes of electrostatic interaction between lysine and phosphotyrosine and peptide specificity originated from a single methylene change, Ac-KLVFFAV which self-assembles into larger nanotubes (~240nm diameter) is coassembled with Ac-pYL VFFAL which self-assembles into smaller nanotubes (~32nm diameter). A preliminary examination of coassembly was done by pelleting the two nanotubes and resuspended them together in 40% MeCN/H₂O. Ellipticity of the mixture decreased to almost 0 within minutes and did not resume back within the 24 hour detection time (Figure 3-40), implies that mixing Ac-KLVFFAV and Ac-pYL VFFAL nanotubes disassemble both, and it takes longer to reassemble than that of mixing Ac-KLVFFAL and Ac-pYL VFFAL.

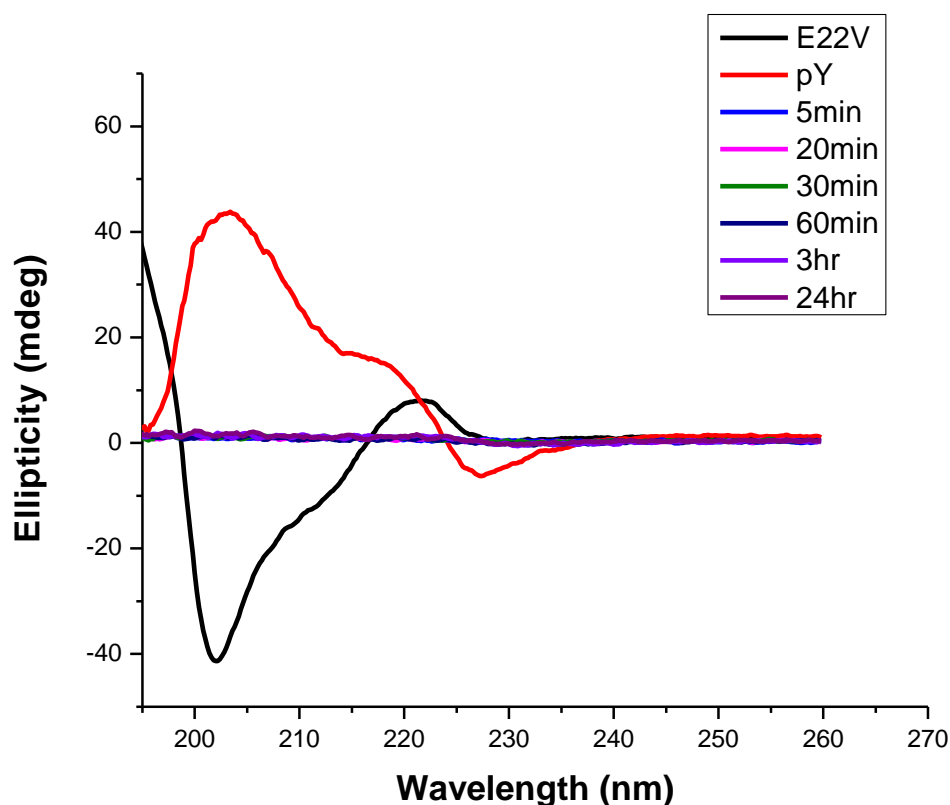


Figure 3-40 Circular Dichroism of Ac-KLVFFAV and Ac-pYL VFFAL mature nanotubes pelleted and resuspended in 40% MeCN/H₂O.

Coassembled Ac-KLVFFAL and Ac-pYLVFFAL peptides displayed β -sheet CD with ellipticity maximum at 227nm (Figure 3-41). TEM micrographs (Figure 3-42) showed that the co-assemblies contain both nanotubes (dominate by tubes with ~60 nm diameter) and fibrils, argued that electrostatic interaction code seem to drive the complicated co-assembly events even when peptides are with different specificities. The structure of the coassemblies needs further careful characterization to determine the mixing modes.

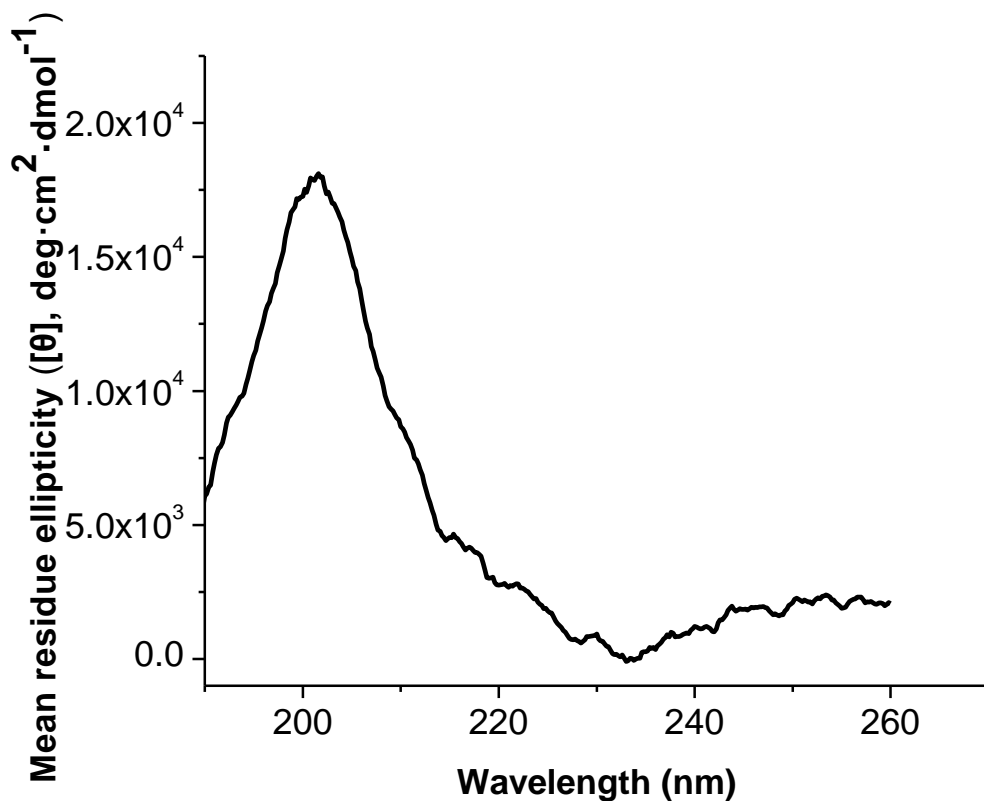


Figure 3-41 Circular Dichroism of co-assembled Ac-KLVFFAL and Ac-pYLVFFAL peptides 1:1 ratio in 40% MeCN/H₂O.

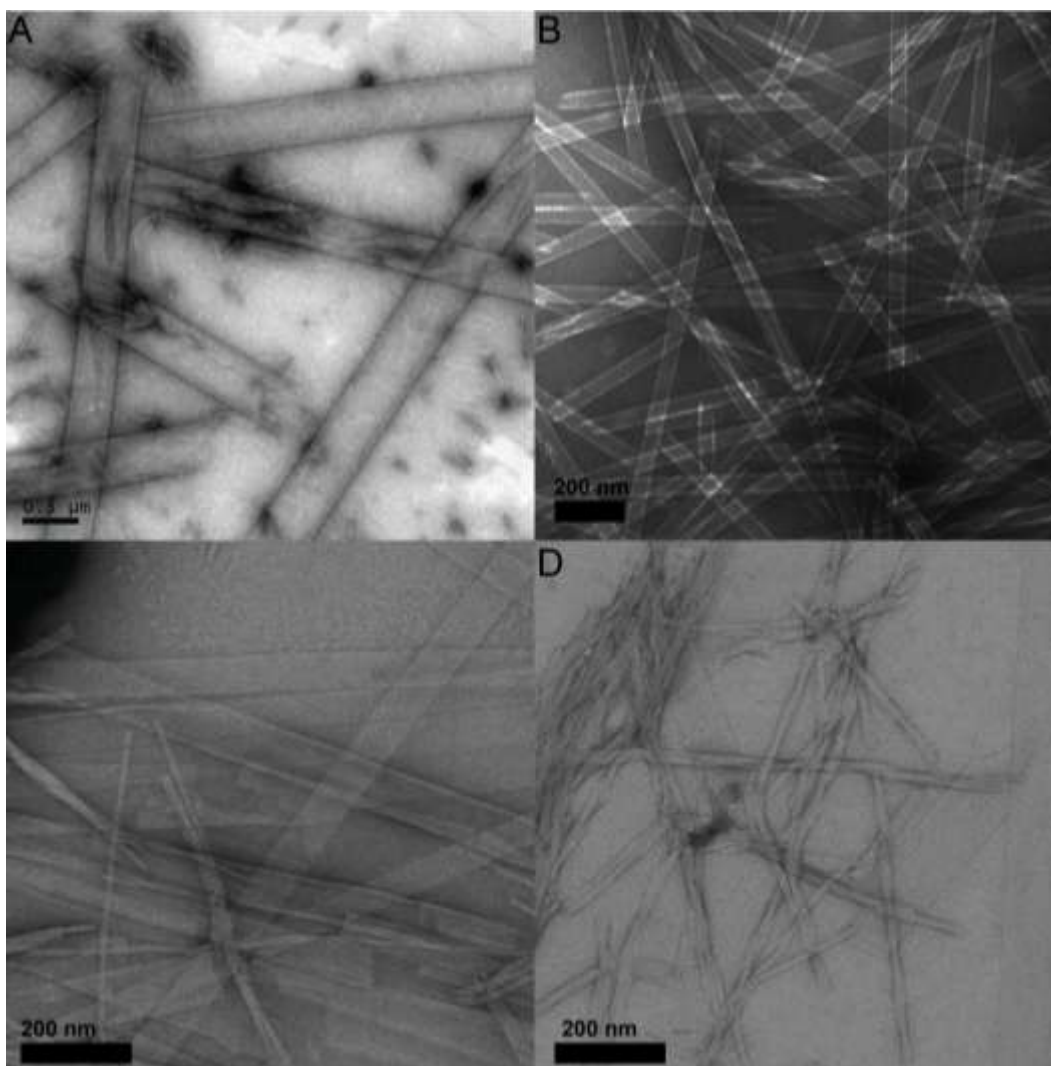


Figure 3-42 TEM micrograph of (A) Ac-KLVFFAV nanotubes in 40% MeCN/H₂O With TFA, pH2; (B) Ac-pYLVFFAL nanotubes in 40% MeCN/H₂O with TEAA; (C) and (D) coassembled Ac-KLVFFAV and Ac-pYLVFFAL peptides in 40% MeCN/H₂O for 3 weeks.

Conclusions

The loss of chiral signal upon mixing Ac-KLVFFAL and Ac-pYLVFFAL mature nanotubes implies disassembly of peptides, presumably owing to the strong electrostatic interactions between the two charged surfaces and led to collapse of partial higher-order structures. The mixture displayed ordered β -sheet structures within 24 hours, much shorter than of coassembly of peptide monomers. It could arise from the existence of tube fragments as templates or seeds to speed up the peptides reconstruction process. In both cases, however, peptides must undergo dynamic balancing of electrostatic, hydrogen-bonding and van der Waals forces. The stronger ellipticity of coassemblies than

each peptide assemblies alone suggested the formation of more robust assemblies. Indeed, the coassemblies presented much higher melting temperature than each peptide alone. Giving the molecular ordering entropy consumption at the leaflet interface by packing counterions from solvents, cooperative electrostatic interactions between lysine and phosphotyrosine residues contributes a lot to higher thermal stability. Moreover, the two peptides are structurally compatible and therefore, collaborative hydrogen-bonding and van der Waal forces further increase the thermal stability.

Biology is essentially heterogeneous: variations in structure, function and behavior exist everywhere. Heterogeneity can arise from errors in building a specific architecture or from mixing of different molecules. Stupp et al^{25,26}, Yu et al^{27,28}, and Zhuo et al²⁹ have reported mixed oppositely charged peptides can quickly self-assemble into nanofibers with β -sheet architectures or peptide hydrogels via intermolecular electrostatic attraction, provides convenient strategy to combine two bioactive signals within a single nanofiber or hydrogel. However, none of these studies have defined charge distribution in the mixtures. The utilization of EFM and solid-state NMR in this study for characterization of heterogeneous peptide coassemblies were novel strategies. EFM was proved to be effective in mapping peptide nanotube surface charges and was extended successfully to a more dynamic heterogeneous system in this study. A delicate interface analysis based on solid-state REDOR NMR revealed the existence of both homogeneous and heterogeneous interfaces, suggesting charge separation across the peptide bilayer membranes and domain segregation along the lateral dimension of the peptide membrane. Both of these techniques have great potential to be extended to other heterogeneous self-assembly systems.

The domain structures on peptide nanotubes surfaces as evidenced in uranyl acetate stained TEM discloses the cross-seeding capabilities between the two oppositely-charged peptides, and helps explain the formation of heterogeneous interfaces. Peptides monomers with opposite charges dissolve to form particles as evidenced by EFM (Figure 3-15) during the initial peptide aggregation and ordering, with numerous computational models³⁰⁻³² and experimental studies³³⁻³⁵ supported the importance of electrostatic interactions. The particles serve as the initial nucleation template for incoming peptides. Both K and pY peptides have equal probability to associate, or dock, with the template, searching for the lowest energy conformation, before it locks into that

strand orientation¹⁶. Once a mutation is built by docking and locking one peptide to the other peptide template which was proved possible by cross-seeding, it has an opportunity to propagate. The propagated domains may still switch charge if another mutation is made. In co-assemblies, the mutation rate has to be high to not able to observe distinct domains by TEM. However, when peptides are seeded by co-assembled nanotubes with propagated mutation already exist, further propagation of the same charged domain is more efficient and thus explains why now domains are long enough to be shown in TEM.

Cell membrane includes levels of asymmetry both across the lipid bilayer (lipid asymmetry) and in the lateral dimension (lipid domains). Generating asymmetry in nonbiological self-assembly systems is still an undeveloped area. We demonstrated a strategy to generate asymmetry that rivals those of extant biological membranes triggered by co-assembly of two oppositely charged peptides. The resulting coassemblies is quite unique from any previous studies in that 1) they assemble into ordered cross- β nanotube structures based on homogeneous structural elements and electrostatic interactions between oppositely-charged surface and interface exposed residues, 2) the outer surface are negatively charged and the inner surface is dominated by positive charges, the first example we known of charge separation in peptide self-assembly, 3) despite the homogeneous nanotube morphologies of the coassemblies, the peptide registry is heterogeneous with the existence of homogeneous and heterogeneous leaflets interfaces. Hence, asymmetry is generated not only across the peptide bilayer but also along the lateral dimension of the peptide membranes.

These robust charged peptide membranes have proved their capability to template small molecules, metals and even large proteins, now the unique asymmetric peptide membrane with charge separation and domain segregation opens new door for setting up system chemistry on these ordered nanomaterials.

Methods

Fmoc-protection of isotopically enriched amino acids

Isotope enriched amino acids were purchased from Cambridge Isotope Laboratories. Fmoc group was introduced by reacting the amine with Fmoc-O-succinimide (EMD Biosciences) in dioxane.

Co-assembly of peptides

Ac-KLVFFAL and Ac-pYLVFFAL peptides powders were weighed and mixed in 1:1 ratio. The mixed peptide monomers, were treated with HFIP to avoid any preformed structures before the addition of 40%MeCN/H₂O. The solution pH was adjusted to pH 7 using NaOH.

Circular Dichroism melting

CD spectra were recorded using a JASCO J-810 spectropolarimeter fitted with a Peltier temperature controller. An aliquot (50-70 μ L) of peptide assemblies was placed in 0.1mm path length demountable window cell (Starna Cells) with Teflon tape wrapped around the window edges to minimize evaporation. Initially, CD at 215 nm was recorded over a 15 minute period at controlled starting temperature (4C) until CD signature of solution stabilized. After temperature incubation, the ellipticity at 215 nm was recorded as a function of temperature in increments of 2 °C/min and fit to the sigmoidal form of the Boltzmann equation.

Ac-pYLVFFAL do not melt in 40% MeCN/H₂O before the temperature reaches 80 °C, and its melting profile is shown in Figure 3-41. Likewise, co-assemblies of Ac-KLVFFAL and Ac-pYLVFFAL do not melt in 40% MeCN/H₂O, and they don't melt when resuspended in 70% and 80% MeCN/H₂O, before the temperature reaches 80 °C (Figure 3-42 and 3-43).

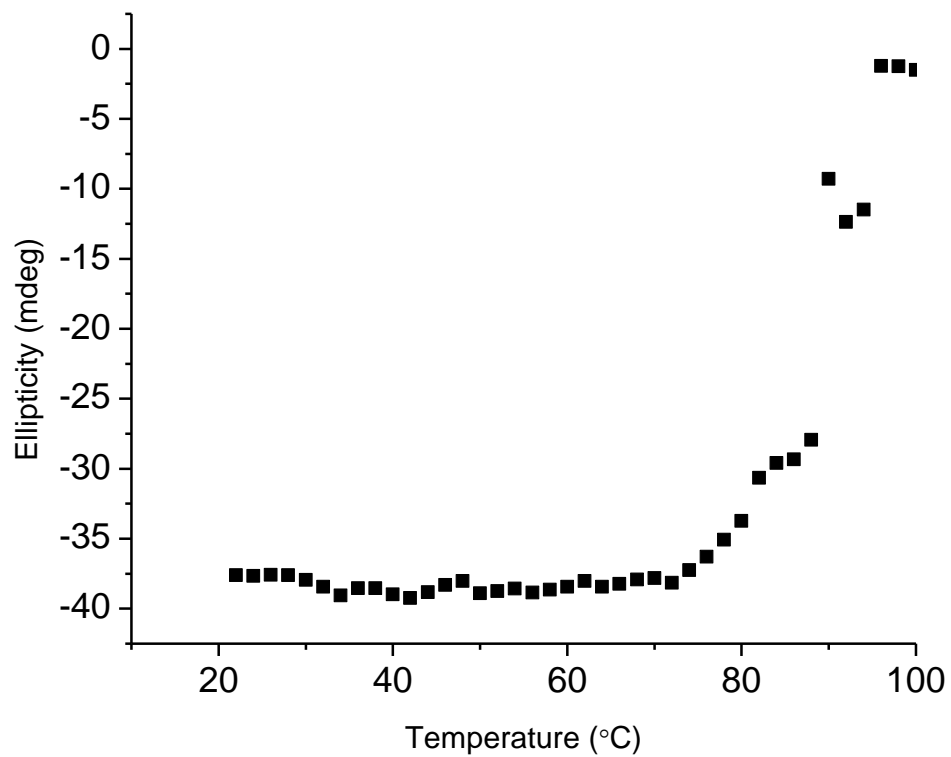


Figure 3-43 CD melting profiles for Ac-pYL VFFAL nanotubes in 40% MeCN/H₂O. The ellipticity stayed stable and changed drastically only when acetonitril started to evaporate at 80 °C.

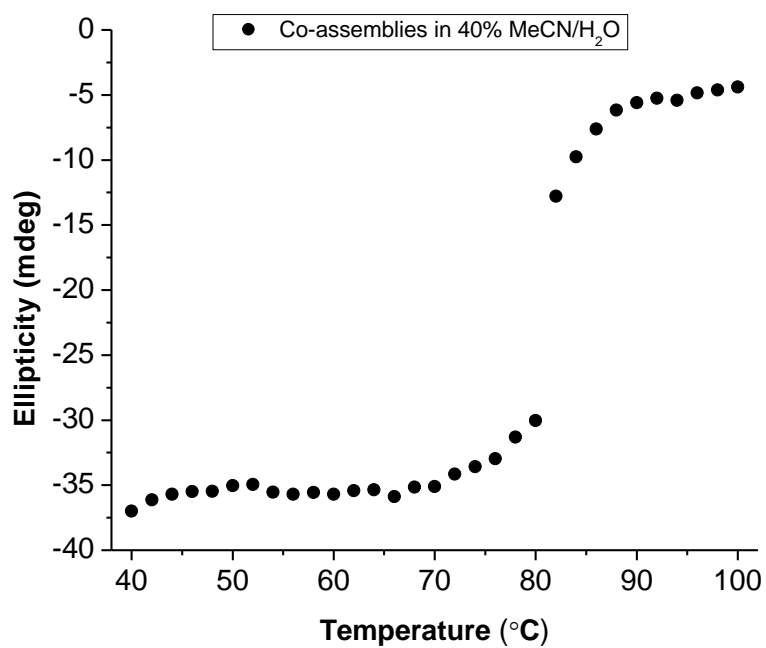


Figure 3-44 CD melting profiles for co-assembled Ac-KLVFFAL and Ac-pYLVFFAL nanotubes in 40% MeCN/H₂O. The ellipticity stayed stable and changed drastically only when acetonitril started to evaporate at 80 °C.

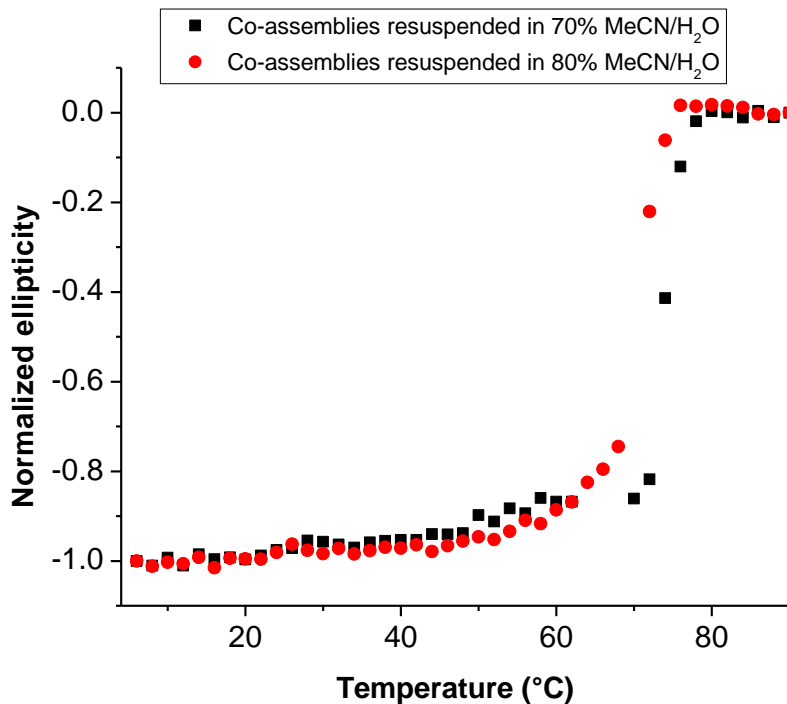


Figure 3-45 CD melting profiles for co-assembled Ac-KLVFFAL and Ac-pYL VFFAL nanotubes formed in 40% MeCN/H₂O and resuspended in 70% and 80% MeCN/H₂O. The ellipticity stayed stable and changed drastically only when acetonitril started to evaporate at 80 °C.

HPLC analysis

To ensure peptides were coassembled in 1:1 ratio, peptides powders were dissolved in minimal volume of HFIP (typically 10 to 30 μ L is enough to dissolve ~4-10mg peptides) and injected to analytical RP-HPLC using a C18-reverse phase column with an acetonitrile-water gradient. The peaks were integrated for peptide concentration calibration. Based on the integration results of HPLC peaks (Figure 3-41) of the two peptides, the two stock solution concentration can be determined relative to each other and then mixed in 1:1 ratio.

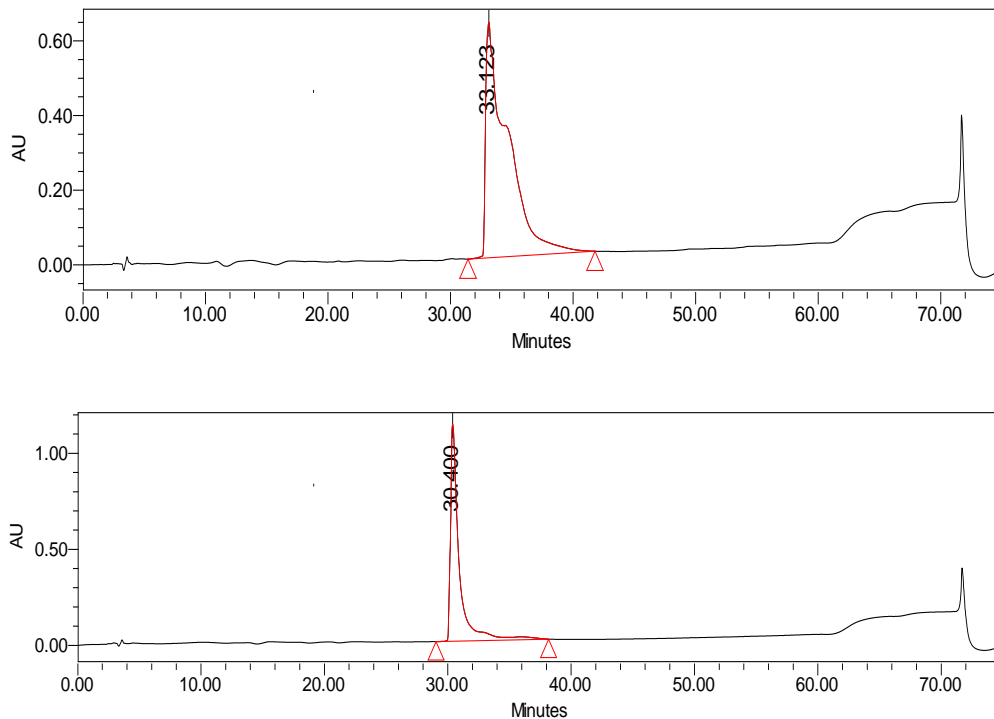


Figure 3-46 HPLC trace of Ac-KLVFF[1-¹³C]AL-NH₂) stock solution and the (Ac-pYL[¹⁵N]VFFA[3-¹³C]L-NH₂) stock solution in HFIP, method 15%-70% 55min. 100% for 10 min. 15% for 10 min.

Matrix-assisted laser desorption/ionization analysis of assembled peptides ratio

After allow the peptides mixed and coassembled as nanotubes for 6-8 weeks, MgCl₂ was added to the assemblies and the pellet was spun down for NMR analysis. A tip of the pellet was redissolved in HFIP and used for peptides amounts ratio analysis by MALDI. The m/z peaks of 879 or 902 g/mol (Ac-KLVFF[1-¹³C]AL-NH₂ or Ac-KLVFF[1-¹³C]AL-NH₂+ Na⁺) and m/z peaks of 993 or 1016 g/mol (Ac-pYL[¹⁵N]VFFA[3-¹³C]L-NH₂ or Ac-pYL[¹⁵N]VFFA[3-¹³C]L-NH₂ + Na⁺) were observed in the mixed peptides assemblies. Stock solution of Ac-KLVFFAL and Ac-pYLVFFAL peptides were dissolved in HFIP and injected to HPLC for concentration calibration. A series of samples with different ratio of mixed peptides were prepared and measured by MALDI. The m/z peaks (878 or 901 and 991 or 1014) intensity ratio were plotted vs K and pY peptides ratio determined by HPLC (Figure 3-42). The plot was fitted to $y=1.47+1.54x$. The coassembled Ac-KLVFF [1-¹³C]AL-NH₂ and Ac-pYL[¹⁵N]VFFA[3-¹³C]L-NH₂ sample contained a m/z 879/993 peak ratio of 2.33 ± 0.52 , converted to a K and pY peptides

ratio of 0.56.

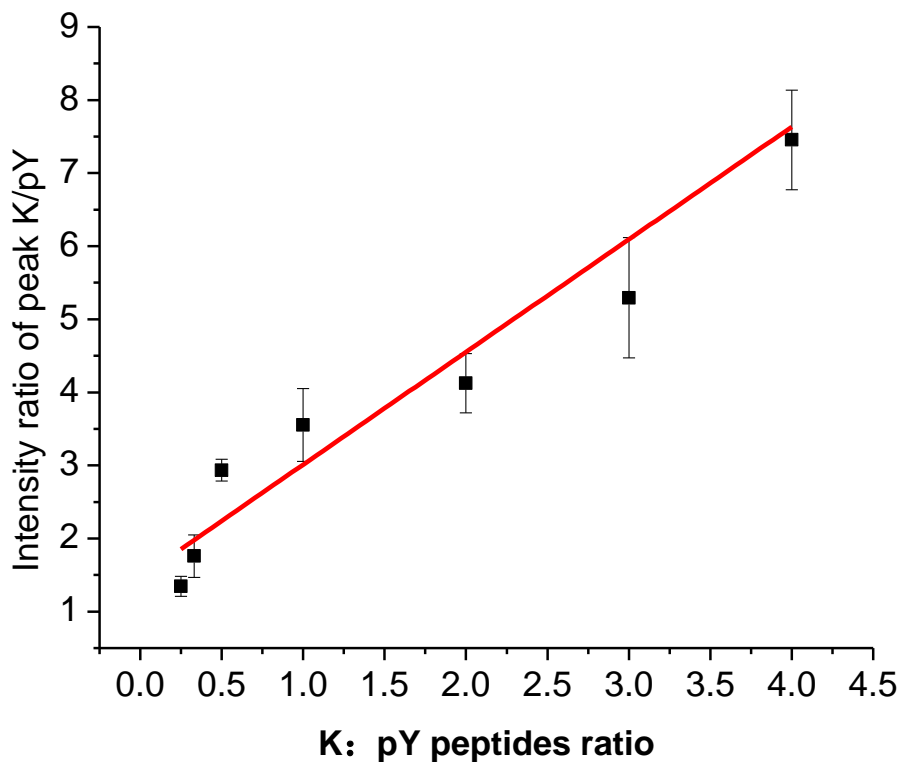


Figure 3-47 Ac-KLVFFAL and Ac-pYLVFFAL mass peak intensity ratio measured by MALDI plot vs peptides ratio.

Solid state REDOR NMR

To prepare matured samples for solid-state NMR experiments, sodium sulfate or magnesium chloride was added to Ac-KLVFFAL or Ac-pYLVFFAL, Ac-ELVFFAL, mix of Ac-KLVFFA and Ac-pYLVFFAL to a final concentration of peptide to salt ratio 1:5 to induce lateral bundling of nanotubes. Previously, sulfate bundling of nanotubes has been shown to protect assemblies from freezing and lyophilization.

Solid-state NMR experiments were conducted identical to chapter 4. As illustrated in previous chapter, the difference between the REDOR S and S0 signal (ΔS) is directly proportional to the dipolar coupling, hence the distance between the two spins.

An integration of NMR $[1-^{13}\text{C}]A$ and $[3-^{13}\text{C}]A$ peaks gives an estimation of pY: K peptide ratio of 1:0.74 (Figure 3-43). Assuming ^{13}C enriched peptide give 99 units of

magnetization and natural abundance ^{13}C 's give rise to 1.1 u of magnetization, the total ^{13}C intensities can be calculated from the concentration of pY (C_{pY}) and K (C_{K}) containing peptides as: $(^{13}\text{CH}_3)_{\text{intensity}} = 99C_{\text{pY}} + 1.1C_{\text{K}}$, assuming that the natural abundance contribution from the K-peptide is negligible, this simplifies to: $(^{13}\text{CH}_3)_{\text{intensity}} = 99C_{\text{pY}}$ $(^{13}\text{CO})_{\text{intensity}} = 99C_{\text{K}} + (1.1*6*C_{\text{K}}) + (1.1*7*C_{\text{pY}})$ Substituting $(^{13}\text{CH}_3)_{\text{intensity}} = 1$ and $(^{13}\text{CO})_{\text{intensity}} = 0.736$ gives: $C_{\text{pY}} = 1/99 = 0.01$ $C_{\text{K}} = (0.736 - 7.7*0.01)/(99 + 6.6) = 0.00624$. The result can be normalized to peptides concentration ratio of $C_{\text{pY}} = 1$ and $C_{\text{K}} = 0.62$. Comparable to the MALDI analysis result, which is $C_{\text{pY}} = 1$ and $C_{\text{K}} = 0.56$.

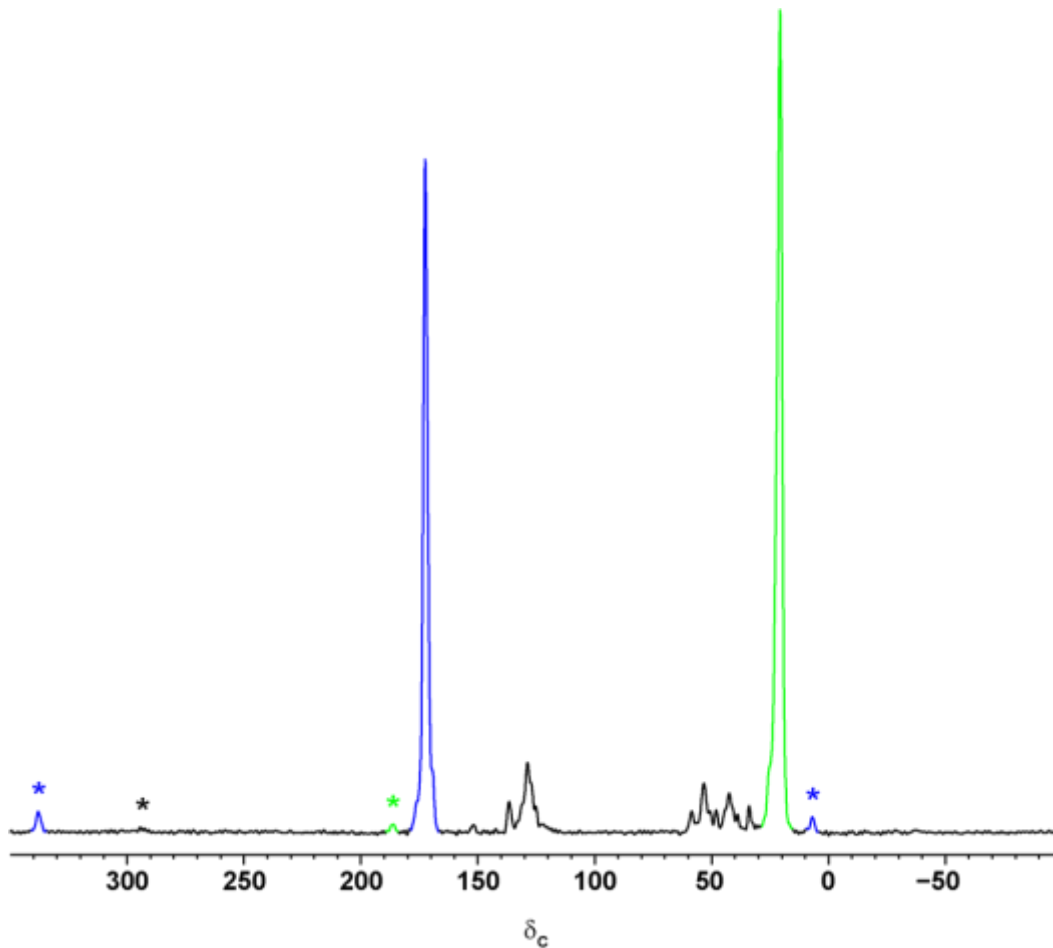


Figure 3-48 NMR spectra of $[1-^{13}\text{C}]\text{A}$ (Ac-KLVFFAL) and $[3-^{13}\text{C}]\text{A}$ (Ac-pYLVFFAL).

REDOR data points are the integrated sum of center- and sideband peaks. Error bars were calculated using the noise of each spectrum as the maximum peak height deviation. To normalize for the decay due to T2 (spin-spin relaxation), individual REDOR curves are plotted as $\Delta S/S_0$. The steeper the slope of the REDOR dephasing curves the shorter

the distance (hence stronger the dipolar coupling) between the two spins. The functional form of the REDOR curves for an isolated heteronuclear spin-pair are identical and can be overlaid on top of each other by simply scaling the x-axis, which makes fitting the REDOR data straight forward.

By plotting REDOR as $\Delta S/S_0$, the plateau (max dephasing) is directly related to the number of spins that are coupled. If only half of the observe spins (in this case ^{13}C) are coupled to a dephasing spin (in this case ^{15}N), the REDOR curve will only go to half the value observed when all the spins are coupled as illustrated in Figure 3-47.

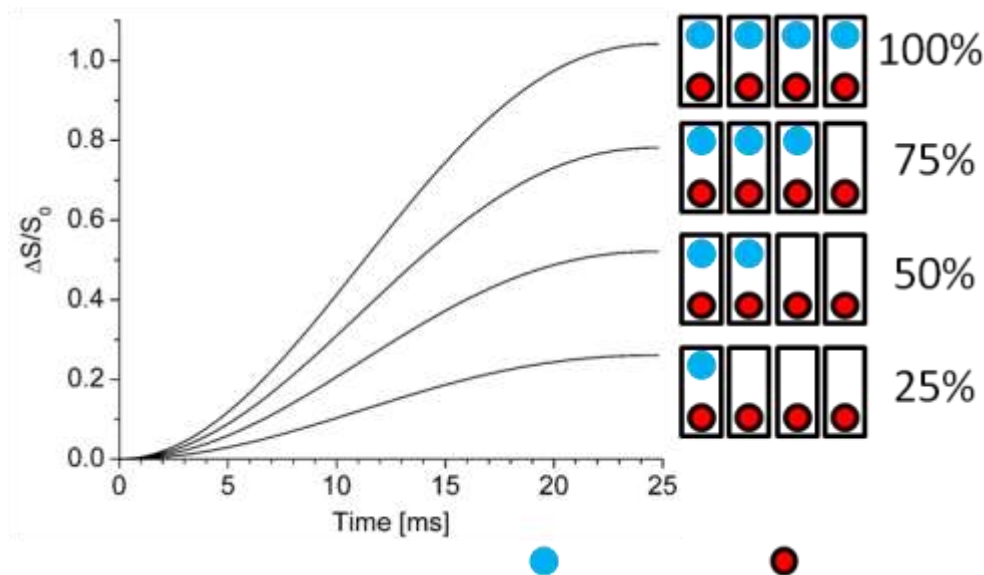


Figure 3-49 Ideal $^{13}\text{C}\{^{15}\text{N}\}$ REDOR curves that vary the percent of ^{13}C near an ^{15}N from 25% to 100%.

For dephasing of carbonyl carbon of Ac-KLVFF [$1\text{-}^{13}\text{C}$]AL-NH₂ and Ac-pYL [^{15}N]VFF [$3\text{-}^{13}\text{C}$]AL-NH₂ co-assemblies, the distance the H-bonded ^{15}N from the adjacent peptide was set to 4.32\AA (r_1) and the distance to the non-H-bonded ^{15}N was set to 5.3\AA (r_2). The angle between the two $^{13}\text{C}\text{-}^{15}\text{N}$ internuclear vectors was set to 155° , consistent with first to dephasing of pure Ac=KL [^{15}N]VFF [^{15}N]AL-NH₂ assemblies. The experimental data was fit to linear combination of 3-spin (one ^{13}C and two ^{15}N 's with distances r_1 and r_2 and angle of 155°) and $^{13}\text{C}\{^{15}\text{N}\}$ REDOR curves corresponding to the $^{13}\text{C}\text{-}^{15}\text{N}$ distances of 4.32\AA and 5.3\AA were used to fit the experimental data points using the Non-Linear Fit routine in Mathematica. Individual curves for dephasing of the carbonyl carbon of Ac-

KLVFF [1-¹³C]AL-NH₂ and Ac-pYL [¹⁵N]VFF [3-¹³C]AL-NH₂ is shown in Figure 3-48. The fit curve is a summation of 46% 3-spin, 10% 2-spin with distance r₁, 10% 2-spin with distance r₂ and natural abundance of ¹³C.

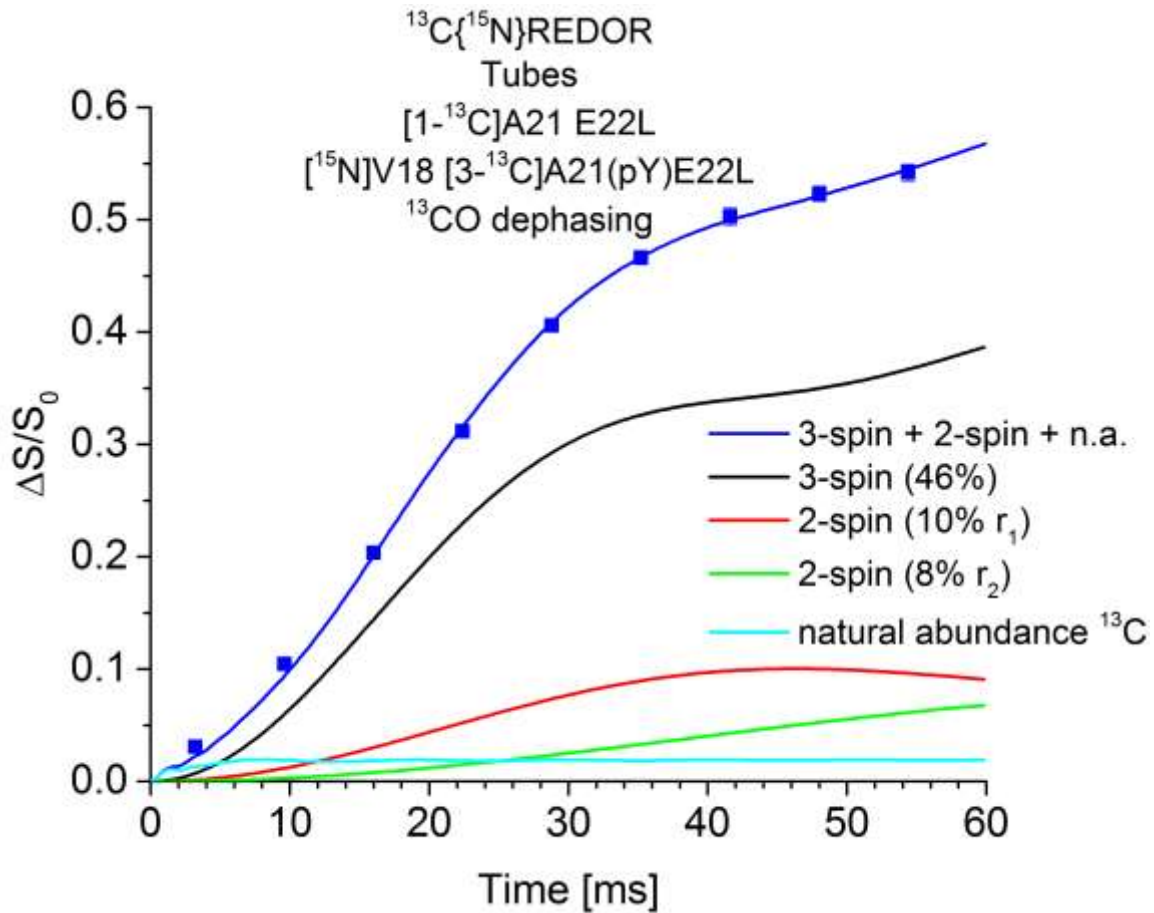


Figure 3-50 The ¹³C{¹⁵N}REDOR dephasing fits to 3-spin and 2-spin systems. The fit curve is a summation of 46% 3-spin, 10% 2-spin with distance r₁, 10% 2-spin with distance r₂ and natural abundance of ¹³C.

Seeding experiment

Ac-KLVFFAL, Ac-pYLVFFAL and mixed 1:1 peptides were allowed to assemble as mature nanotubes first. Then seeds were prepared by sonicating nanotubes for 3 hr before adding to peptide monomers. All peptide monomers were treated with HFIP to avoid any pre-formed structures. Seeds vs peptide monomer concentration ratio equals 1:9.

Reference

- (1) Alberts B, J. A., Lewis J, et al. *Molecular Biology of the Cell*; 4th edition ed.; Garland Science: New York, 2002.
- (2) Nagle, J. F.; Tristram-Nagle, S. *Biochimica et Biophysica Acta (BBA) - Reviews on Biomembranes* **2000**, 1469, 159.
- (3) Op den Kamp, J. A. F. *Annu. Rev. Biochem* **1979**, 48, 47.
- (4) Devaux, P. F. *Biochemistry* **1991**, 30, 1163.
- (5) Gurtovenko, A. A.; Vattulainen, I. *J. Am. Chem. Soc.* **2007**, 129, 5358.
- (6) Graham, T. R. *Trends Cell Biol.*, 14, 670.
- (7) Ikeda, M.; Kihara, A.; Igarashi, Y. *Biol. Pharm. Bull.* **2006**, 29, 1542.
- (8) Pomorski, T.; Lombardi, R.; Riezman, H.; Devaux, P. F.; van Meer, G.; Holthuis, J. C. M. *Molecular Biology of the Cell* **2003**, 14, 1240.
- (9) Winckler, B.; Poo, M.-m. *Nature* **1996**, 379, 213.
- (10) Mellman, I.; Yamamoto, E.; Whitney, J. A.; Kim, M.; Hunziker, W.; Matter, K. *J. Cell Sci.* **1993**, 1.
- (11) Kortholt, A.; Keizer-Gunnink, I.; Kataria, R.; Van Haastert, P. J. M. *J. Cell Sci.* **2013**, 126, 4502.
- (12) Childers, W. S.; Mehta, A. K.; Ni, R.; Taylor, J. V.; Lynn, D. G. *Angewandte Chemie-International Edition* **2010**, 49, 4104.
- (13) Lu, K.; Guo, L.; Mehta, A. K.; Childers, W. S.; Dublin, S. N.; Skanthakumar, S.; Conticello, V. P.; Thiyagarajan, P.; Apkarian, R. P.; Lynn, D. G. *Chem. Commun.* **2007**, 2729.
- (14) Mehta, A. K.; Lu, K.; Childers, W. S.; Liang, Y.; Dublin, S. N.; Dong, J.; Snyder, J. P.; Pingali, S. V.; Thiyagarajan, P.; Lynn, D. G. *J. Am. Chem. Soc.* **2008**, 130, 9829.
- (15) Li, S.; Sidorov, A. N.; Mehta, A. K.; Bisignano, A. J.; Das, D.; Childers, W. S.; Schuler, E.; Jiang, Z.; Orlando, T. M.; Berland, K.; Lynn, D. G. *Biochemistry* **2014**, 53, 4225.
- (16) Liang, C.; Ni, R.; Smith, J. E.; Childers, W. S.; Mehta, A. K.; Lynn, D. G. *J. Am. Chem. Soc.* **2014**, 136, 15146.
- (17) Kowalewski, T.; Holtzman, D. M. *Proceedings of the National Academy of Sciences* **1999**, 96, 3688.
- (18) Kellermayer, M. S. Z.; Karsai, Á.; Benke, M.; Soós, K.; Penke, B. *Proceedings of the National Academy of Sciences* **2008**, 105, 141.
- (19) Wasmer, C.; Zimmer, A.; Sabaté, R.; Soragni, A.; Saupe, S. J.; Ritter, C.; Meier, B. H. *J. Mol. Biol.* **2010**, 402, 311.
- (20) Apostol, M. I.; Wiltzius, J. J. W.; Sawaya, M. R.; Cascio, D.; Eisenberg, D. *Biochemistry* **2011**, 50, 2456.
- (21) Bonilla, R.; Ávila, A.; Montenegro, C.; Hinestroza, J. *Journal of Microscopy* **2012**, 248, 266.
- (22) Bromley, E. H. C.; Sessions, R. B.; Thomson, A. R.; Woolfson, D. N. *J. Am. Chem. Soc.* **2009**, 131, 928.
- (23) Reinke, A. W.; Grant, R. A.; Keating, A. E. *J. Am. Chem. Soc.* **2010**, 132, 6025.
- (24) Childers, S. W. T., Emory University, 2010.
- (25) Niece, K. L.; Hartgerink, J. D.; Donners, J. J. J. M.; Stupp, S. I. *J. Am. Chem. Soc.* **2003**, 125, 7146.
- (26) Behanna, H. A.; Donners, J. J. J. M.; Gordon, A. C.; Stupp, S. I. *J. Am. Chem. Soc.* **2005**, 127, 1193.

- (27) Ramachandran, S.; Flynn, P.; Tseng, Y.; Yu, Y. B. *Chem. Mater.* **2005**, *17*, 6583.
- (28) Ramachandran, S.; Taraban, M. B.; Trehwella, J.; Gryczynski, I.; Gryczynski, Z.; Yu, Y. B. *Biomacromolecules* **2010**, *11*, 1502.
- (29) Xu, X.-D.; Chen, C.-S.; Lu, B.; Cheng, S.-X.; Zhang, X.-Z.; Zhuo, R.-X. *The Journal of Physical Chemistry B* **2010**, *114*, 2365.
- (30) Yun, S. J.; Urbanc, B.; Cruz, L.; Bitan, G.; Teplow, D. B.; Stanley, H. E. *Biophys. J.* **2007**, *92*, 4064.
- (31) Buell, Alexander K.; Hung, P.; Salvatella, X.; Welland, Mark E.; Dobson, Christopher M.; Knowles, Tuomas P. *Biophys. J.* **2013**, *104*, 1116.
- (32) Tarus, B.; Straub, J. E.; Thirumalai, D. *J. Mol. Biol.* **2005**, *345*, 1141.
- (33) Konno, T. *Biochemistry* **2001**, *40*, 2148.
- (34) Raman, B.; Chatani, E.; Kihara, M.; Ban, T.; Sakai, M.; Hasegawa, K.; Naiki, H.; Rao, C. M.; Goto, Y. *Biochemistry* **2005**, *44*, 1288.
- (35) Shamma, S. L.; Knowles, T. P. J.; Baldwin, A. J.; MacPhee, C. E.; Welland, M. E.; Dobson, C. M.; Devlin, G. L. *Biophys. J.* **2011**, *100*, 2783.

Chapter 4 Energy and Electron Transfer across Asymmetric Peptide Membranes

Introduction

Light absorption, charge separation (CS) and excitation energy transfer (EET) are crucial steps in natural photosynthesis¹. Substantial attempts have been made to mimic charge separation and photoinduced electron transfer to understand photosynthesis and construct new systems. While it is challenging to construct electron transfer in covalently linked donor-acceptor systems,^{2,3} they have founded a valuable framework for the design of noncovalently assembled donor-acceptor arrays similar to nature's light-harvesting reaction centers with remarkable long-range order held by the protein environment. These systems have been constructed on on self-assembled multichromophores systems⁴⁻⁷, synthetic lipid bilayer liposomes⁸⁻¹⁰, polymeric assemblies^{11,12}, carbon nanotubes (SWCNT)^{13,14}, as well as diphenylalanine peptide nanotubes¹⁵. These previously reported scaffolds, however, are not capable of either spontaneous assembly or self-charge separating, the features in the development of an autonomous photosynthetic system.

In chapter 3, I have presented the unique asymmetric peptide membranes with distinct charges on inner and outer surfaces co-assembled from two oppositely charged amyloid peptides (Figure 4-1). The covalent coupling and noncovalent association of fluorophores to the peptide nanotubes have allowed us to achieve light harvesting, charge separation and electron transfer within the self-assembly system.

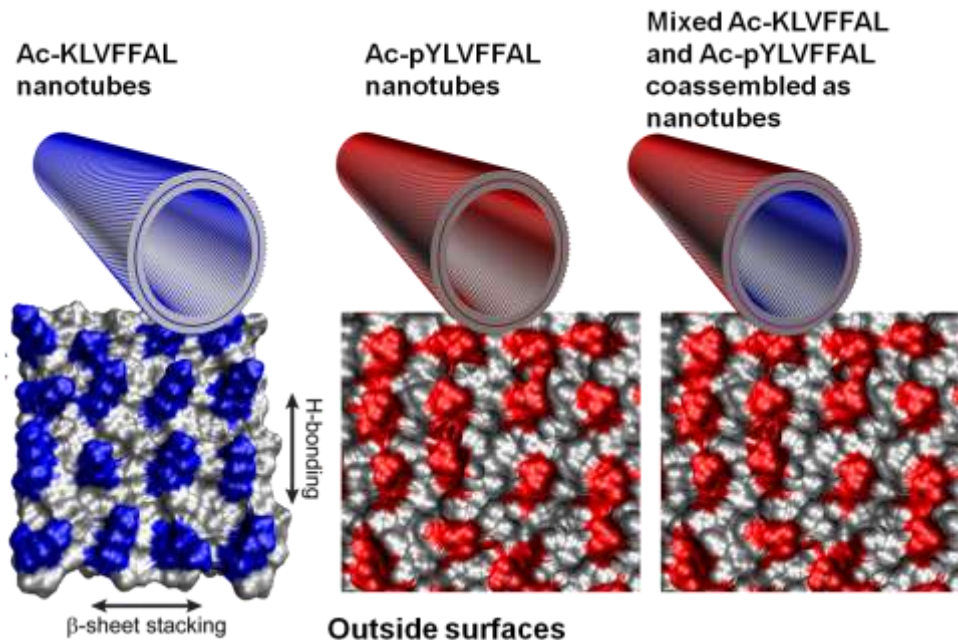


Figure 4-1 Surface charge models for Ac-KLVFFAL nanotubes with positive charges on both inner and outer surfaces (left), Ac-pYLFFAL nanotubes with negative charges on both inner and outer surfaces (middle), mixed Ac-KLVFFAL and Ac-pYLFFAL coassembled as nanotubes with negative charges on outer surfaces and both positive and negative charges on inner surfaces (right). Blue represents lysine residues with positive charges; red represents phosphotyrosine residues with negative charges.

Results

Covalent Coupling of Fluorophores to Peptide Membrane Surfaces

Previous studies have established the feasibility of decorating the N-terminus with Rhodamine 110 (Rho110) via solid phase synthetic methods to yield Rho-KLVFFAE which self-assembles into fluorescent amyloid fibrils.^{16,17} To incorporate fluorophores to asymmetric peptide nanotubes, the N-terminus of Ac-KLVFFAL peptide was replaced by Rho110, and the Rho-KLVFFAL peptide was co-assembled at 1: 250 ratios with Ac-KLVFFAL, or Ac-pYLFFAL, or mixed Ac-KLVFFAL and Ac-pYLFFAL peptides. Rho-KLVFFAL self-assembled as fibrils and ribbons by itself (Figure 4-2 A), but coassemblies with unlabeled peptides formed homogeneous nanotubes (Figure 4-2 B, C and D), morphologically identical with unlabeled peptide nanotubes. Homogeneous fluorescence nanotubes were observed by fluorescence imaging suggested that Rhodamines were

evenly decorated on the peptide nanotubes surfaces.

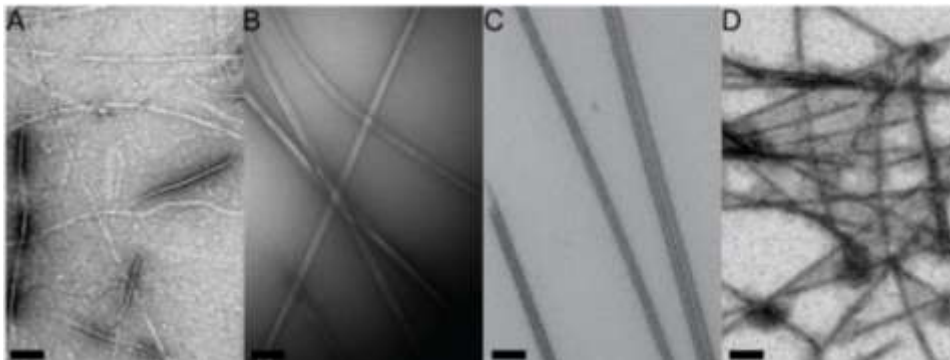


Figure 4-2 TEM micrographs of (A) Rho-KLVFFAL assemblies, (B) mixed Rho-KLVFFAL and Ac-pYLFFFAL in 1:250 ratio coassembled as nanotubes, (C) mixed Rho-KLVFFAL and Ac-pYLFFFAL in 1:250 ratio coassembled as nanotubes (D) : mixed Rho-KLVFFAL, Ac-KLVFFAL and Ac-pYLFFFAL in 1:250:250 ratio coassembled as nanotubes, scale bar 200nm.

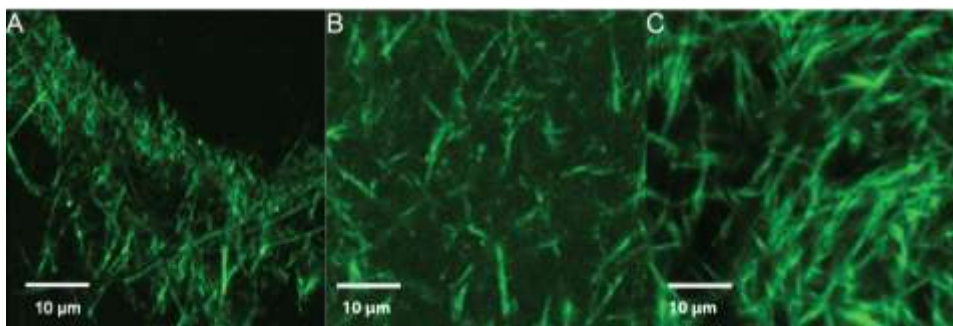


Figure 4-3 Single slices of confocal fluorescence images of (A) mixed Rho-KLVFFAL and Ac-pYLFFFAL in 1:250 ratio coassembled as nanotubes, (B) mixed Rho-KLVFFAL and Ac-pYLFFFAL in 1:250 ratio coassembled as nanotubes (C) : mixed Rho-KLVFFAL, Ac-KLVFFAL and Ac-pYLFFFAL in 1:250:250 ratio coassembled as nanotubes, scale bar 10 μ m.

Since Rh110 is zwitterionic and only incorporated at 1:250 ratios, I hypothesized that the surface charge properties of each Rho-labeled assembly should maintain the same as unlabeled assemblies. To test the hypothesis, Gold nanoparticles (AuNPs) binding with peptide nanotube surfaces, which was shown effective in chapter 2, was employed to investigate the charge properties of Rho-labeled peptide assemblies. Moreover, AuNPs are unique nanomaterials with strongly size-dependent surface plasmon resonance (SPR), high surface-to-volume ratio and good catalytic activity. Their capability as “super quenchers” for a few fluorescence dyes including Rhodamine have been utilized in DNA^{18,19} and protein detections.^{20,21} Therefore, incorporation of AuNPs could extend

possibilities for creating interacting molecules and reaction centers on peptide membranes.

As shown in Figure 4-4, Rhodamine 110 displayed fluorescence maximum intensity at 521nm. Nevertheless, the co-assemblies of Rho-KLVFFAL with Ac-KLVFFAL, Ac-pYLFFAL and mixed Ac-KLVFFAE and Ac-pYLFFAL peptides have shifted maximum wavelengths to 527, 534 and 530 nm respectively, supported the environments of the fluorophores are different in each assemblies. Negatively-charged AuNPs were then added to the peptide assemblies to evaluate surface charges. TEM section images were taken to observe whether AuNPs are bound to inner or outer surfaces. TEM images of cross-sectioning of epoxy resin embedded Ac-KLVFFAL tubes (Figure 4-5) with (-) AuNPs highlights one layer of 5nm dots around 30 nm circles. The single layer is most consistent with binding only the outer surfaces with hindered access to the inner surfaces.

Upon addition of negatively-charged AuNPs to the Rho-labeled peptide nanotubes, fluorescence intensities of all samples decreased to different scales. The quenching efficiency is accessed as fluorescence intensity in the presence of AuNPs/ in the absence of AuNPs. The differences in quenching efficiencies could reflect whether AuNPs were bound to peptide surfaces as N-terminal Rhodamine 110 were decorated on peptide nanotubes surfaces²². The coassemblies of Rho-KLVFFAL and Ac-KLVFFAL have significant quenching efficiency of 67.4%, supported coassemblies of Rho-KLVFFAL and Ac-KLVFFAL possess positively-charged outer surfaces. However, the quenching efficiencies of Rho 110, coassemblies of Rho-KLVFFAL and Ac-pYLFFAL, coassemblies of Rho-KLVFFAL, Ac-KLVFFAL and Ac-pYLFFAL are 3.4%, 8.5% and 11.4% respectively, confirmed that these peptide assemblies possess negatively-charged outer surfaces.

Covalent attachments of fluorophores do not affect the assembling properties of the peptides as long as they are incorporated in a minimum ratio. The experimental results also confirm that Ac-KLVFFAL have positively-charged surfaces, while as well as coassemblies of Ac-KLVFFAL and Ac-pYLFFAL have negatively-charged outer surfaces. Successful recruitment of outside pigments via electrostatic interactions laid foundation for building pigments arrays on peptide membrane surfaces.

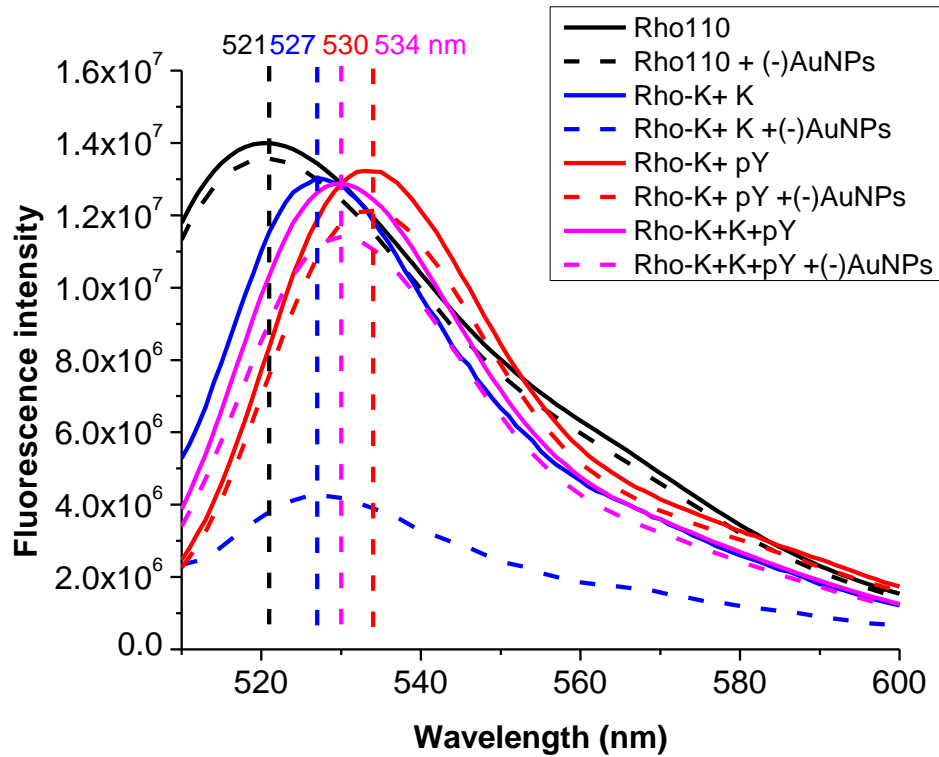


Figure 4-4 Fluorescence spectra for Rho labeled peptides assemblies. Solid lines are peptide assemblies, dashed lines are peptide assemblies with the addition of negatively charged AuNPs. Rho 110 (black): Rhodamine 110 alone; Rho-K+K (blue): mixed Rho-KLVFFAL and Ac-KLVFFAL coassembled as nanotubes; Rho-K+pY (red): mixed Rho-KLVFFAL and Ac-pYL VFFAL coassembled as nanotubes; Rho-K+K+pY (magenta): mixed Rho-KLVFFAL, Ac--KLVFFAL and Ac-pYL VFFAL coassembled as nanotubes. Each sample contains 1.8mM unlabeled peptides and Rho-KLVFFAE 0.0072mM. AuNps are 0.03mM in each sample. The maximum wavelength are 521, 527 534 and 530nm respectively, quenching efficiencies are 3.4%, 67.4%, 8.5% and 11.4% respectively.

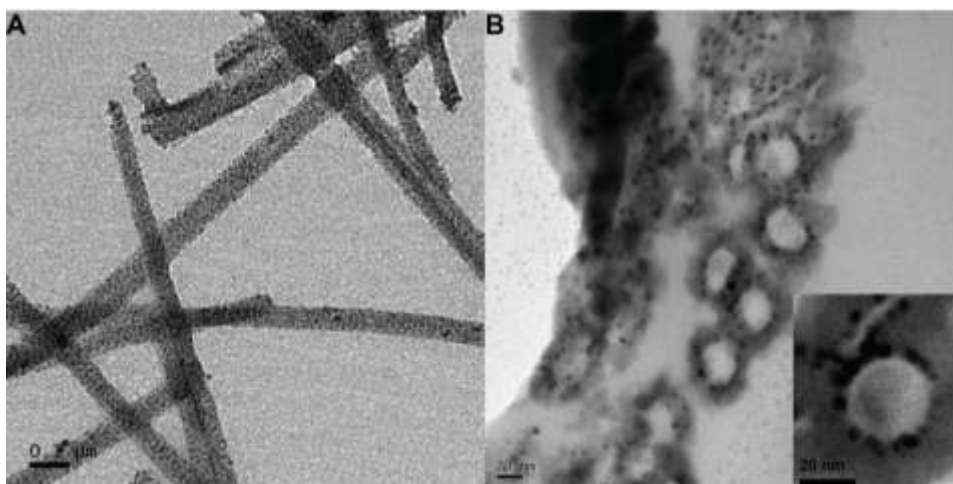


Figure 4-5 TEM micrographs of (A) Dried and flattened Ac-KLVFFAL nanotubes (bar=100 nm) bound with negatively charged AuNPs and (B) cross-sectioned, epoxy resin embedded assemblies oriented perpendicular to the tube long axis (bar=20 nm). Inset is a zoom in on one of the tubes (bar=20nm).

Noncovalent Association of Fluorophores to Peptide Membrane Surfaces

Amyloid's molecular templating capability is worth investigating for the purpose of building functional amyloid. Especially when the templated molecules are catalytical or redox-active, it will largely expand diversity of the arrays and reactions that can be set up with peptide membranes. The unique structure of cross- β nanotube, provides laminate grooves as binding sites for histochemical dye Congo Red (CR). CR bound to cross- β nanotubes display a broad red-shifted UV signature supported the existence of a precise network and linear dichroism defines the orientation of CR as parallel to the amyloid long axis and colinear with laminate grooves, illuminating the ability of the amyloid to organize molecules into extended arrays. CR, however, does not bind to negatively charged nanotube surfaces due to the negative charges on the molecule as tested in chapter 2, while positively-charged small molecule such as ThT binds to negatively-charged Ac-pYLKFFAL nanotubes. To fully take advantage of the laminate grooves of the nanotubes surfaces, Methylene Blue (MB), a heterocyclic aromatic chemical compound (Figure 4-6) with similar conjugated ring structures with CR, was chosen. Solutions of this substance are blue when oxidized and colorless if reduced. When combined with light it can be used to treat resistant plaque psoriasis,²³ AIDS-related Kaposi's sarcoma²⁴, West Nile virus²⁵. The redox properties made MB promising candidate for perform the redox activity at the nanotube surfaces.

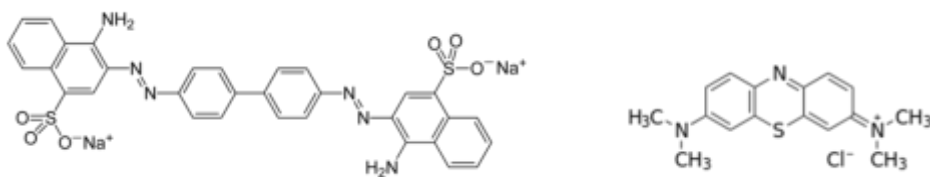


Figure 4-6 Molecular structures of Congo Red (left) and Methylene blue (right).

MB molecules do not show natural ellipticity alone, but in the presence of Ac-pYLFFAL nanotubes display cotton effect at 297 and 661 nm at the λ_{max} of each transition (Figure 4-7), supported MB binding with the surfaces of Ac-pYLFFAL nanotubes. Plot the ellipticity vs pY/MB ratio, all four peaks absolute intensity increases and reaches a plateau (Figure 4-8 and 4-9), presumably where the nanotube surfaces are saturated with MB molecules. The plateau starts at a pY/MB ratio of 2. At higher pY: MB ratio of 7.6, MB bundle pY nanotubes (Figure 4-10) just like what divalent positively-charged salt does to pY tubes.

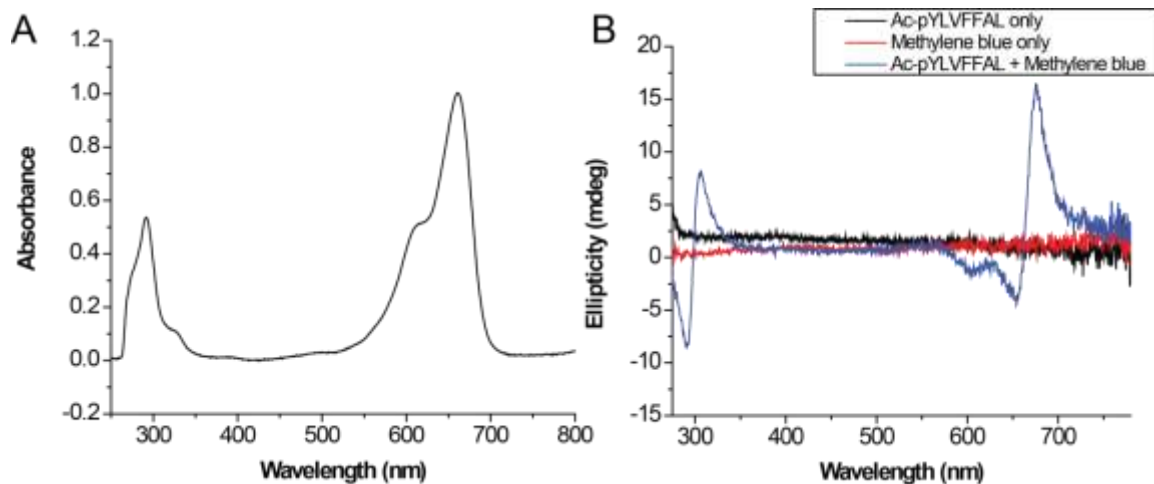


Figure 4-7 (A) UV spectra of methylene blue with strong peaks at 292 and 661nm and a shoulder peak at 610nm; (B) Circular Dichroism of Ac-pYLFFAL nanotubes alone (black), Methylene Blue alone (red) and Methylene Blue in the presence of Ac-pYLFFAL nanotubes (blue).

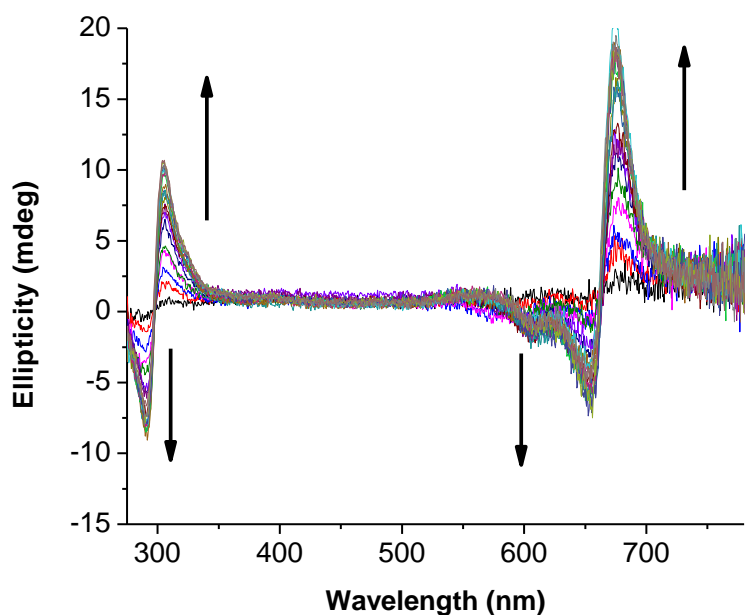


Figure 4-8 Circular Dichroism of 0.05 mM 200 μ L Methylene Blue with addition of 1, 2, 3, 4...18, 19, 20 μ L 2mM Ac-pYL VFFAL peptides nanotubes, pY/MB ratio are 0.4, 0.6, 0.8, 1...3.6, 3.8, 4.

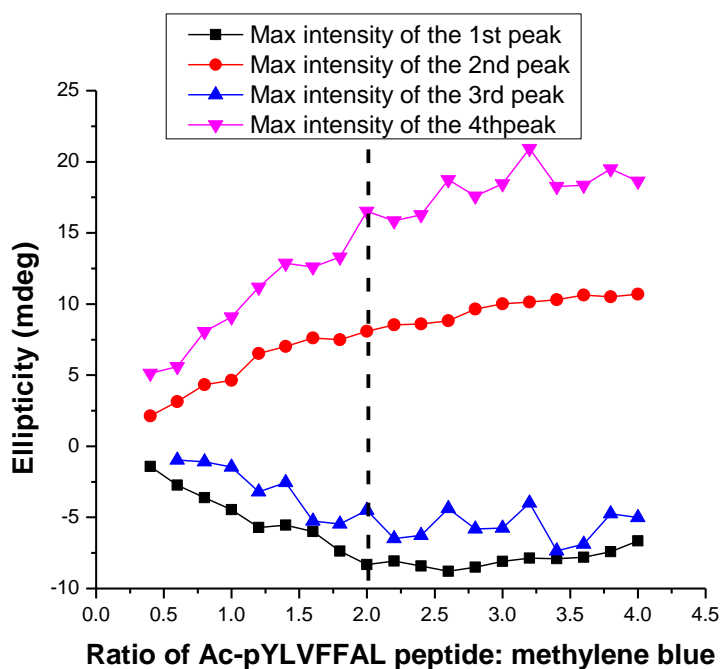


Figure 4-9 Plot the ellipticity vs pY/MB ratio, the first to fourth refer to peaks at 291, 305, 654 and 675 nm respectively. The absolute intensity of all four peaks increases and reaches a plateau and the plateau starts at a pY/MB ratio of 2.

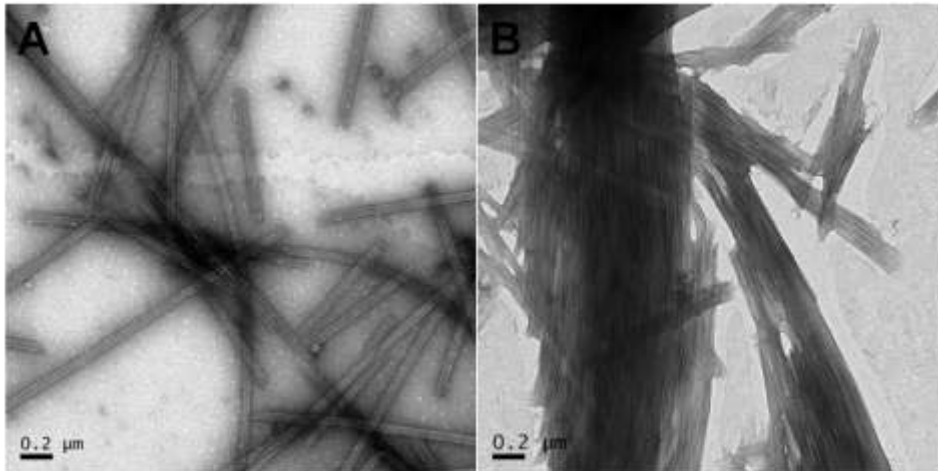


Figure 4-10 TEM micrographs of (A) Ac-pYL VFFAL in the presence of 1.1mM Methylene Blue, (B) Ac-pYL VFFAL in the presence of 8.4mM Methylene Blue.

Linear dichroism (LD) (Figure 4-11) showed the positive transition dipole of the 200 nm amide π - π^* . This positive LD indicates the amide absorption is greater parallel than perpendicular to the tube axis and orients the backbone carbonyl roughly parallel to the tube long axis.²⁶⁻²⁸ The Ac-pYL VFFAL nanotubes have no electronic transitions between 500 and 750 nm, and MB by itself displays only a weak positive LD signature, consistent with laminar flow orienting a small percentage of the linear MB molecules. The LD of MB bound to Ac-pYL VFFAL nanotubes displays a strong positive signature at 651 nm, indicating preferred absorbance parallel to the direction of flow. As both the transition dipole of MB and the backbone carbonyl of nanotubes are oriented parallel to the direction of flow, MB is oriented parallel to the tube axis.

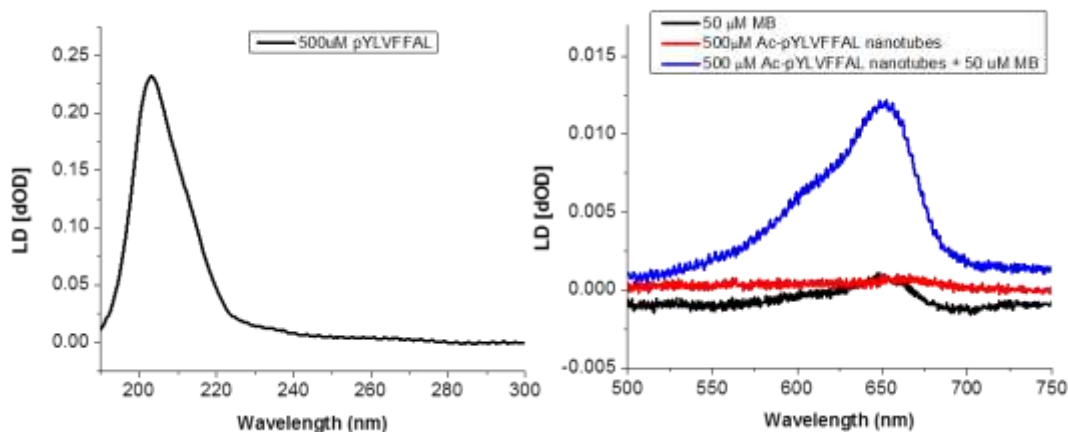


Figure 4-11 Cuvette flow LD of Ac-pYLVFFAL nanotubes. Panels show (A) the nanotube amide transition and (B) 50 μM MB (red) with (blue) and without (black) 500 μM nanotubes.

Previous studies have presented Congo Red bind positively-charged peptide nanotubes parallel to the β -sheet axis, and negatively-charged surfaces presented here bind Methylene blue in a similar mode. With this foundational insight into peptide membrane's molecular templating capability, the functionalities of the peptide scaffolds can be expanded by diversifying the binding molecules with various redox and catalytic activities.

Energy Transfer across Asymmetric Cross- β Peptide Membranes

Previous studies¹⁶ have demonstrated Fluorescence resonance energy transfer (FRET) between covalently linked Rhodamine 110 and noncovalently associated Alexa 555 on the nanotube surfaces (Figure 4-14). This extension of amyloid self-assembly to more precise supramolecular arrays containing functional pigments provides a critical first step towards constructing a self-assembling nanoscale scaffold for new applications. However, the FRET pair was recruited on the same surface in the previous study¹⁶. With the unique asymmetricly charged peptide membranes constructed in chapter 3, we are now positioned to exploit the energy transfer across the peptide bilayers.

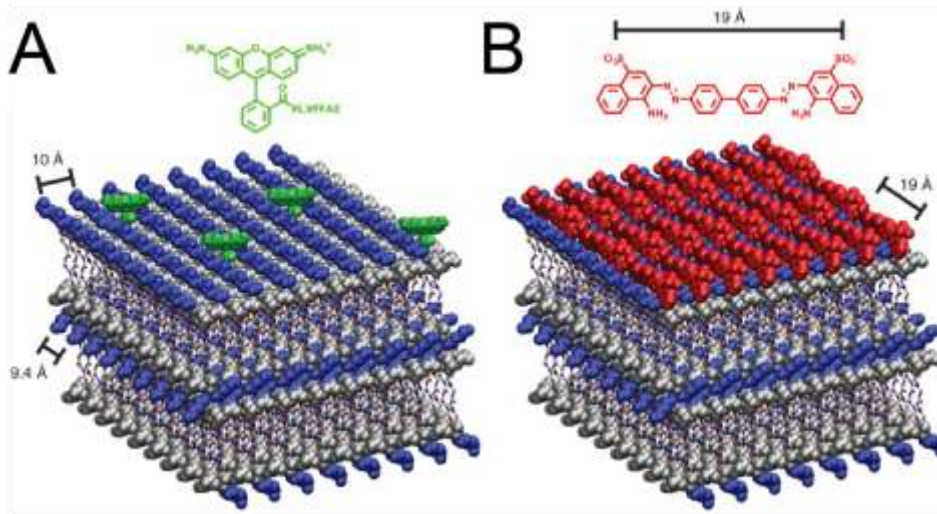


Figure 4-12 Two-photon fluorescence imaging (Ex=780nm) of Rh110-A β (16-22) donor nanotubes (A) and bound Alexa555 acceptor (Em=565nm) (B) (Reprinted from Childers, W.S. et, al. *Curr. Opin. Chem. Biol* 2009 with permission from Elsevier).

The FRET pair of Acridine orange and Alexa 633, positively- and negatively-charged respectively, were selected (Figure 4-13) to probe the negatively- and positively-charged peptide nanotube surfaces. Alexa binding with positively-charged peptide nanotube surfaces have been tested¹⁶. The absorption of Acridine orange red shifted from 494 to 500 nm in the presence of Ac-pYL VFFAL nanotubes (Figure 4-14). Acridine orange displayed positive ellipticity at 500 nm in the presence of Ac-pYL VFFAL nanotubes (Figure 4-14). These spectroscopic analyses are consistent with positive-charge fluorophore Acridine orange binding of negatively-charged phosphotyrosine peptide nanotube surfaces.

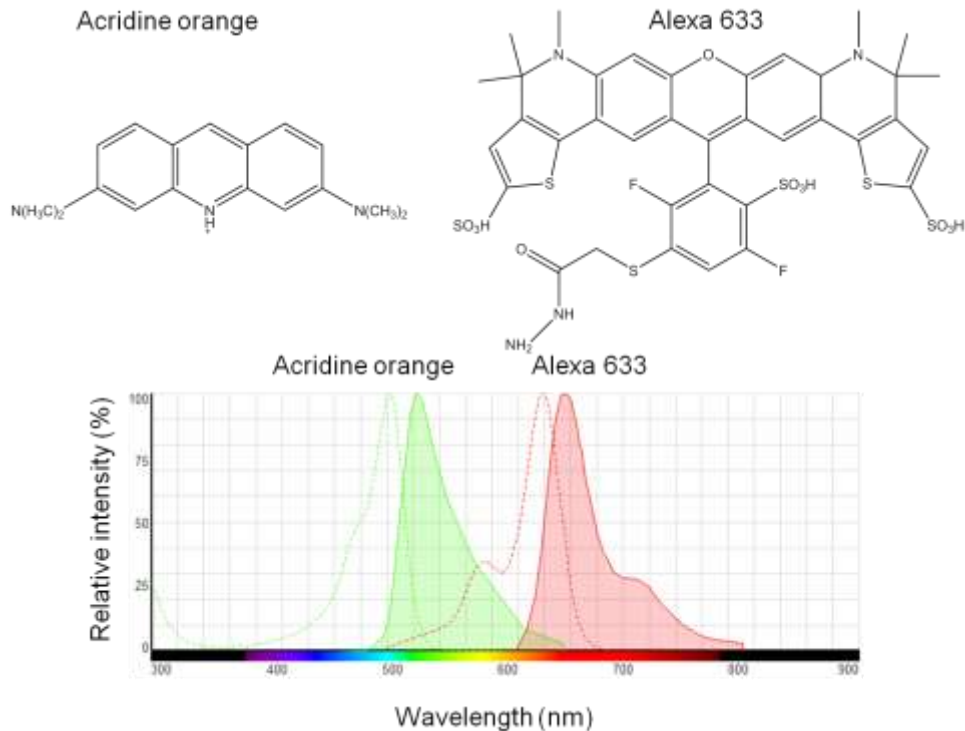


Figure 4-13 Molecular structures of Acridine orange and Alexa 633 (top), absorption (dashed line) and emission spectra (solid line) of Acridine orange and Alexa 633 (bottom). The emission spectrum of the donor (Acridine orange) has sufficient overlay with absorption spectra of the acceptor (Alexa 633). The spectra are built in fluorescence spectra viewer, life technologies.

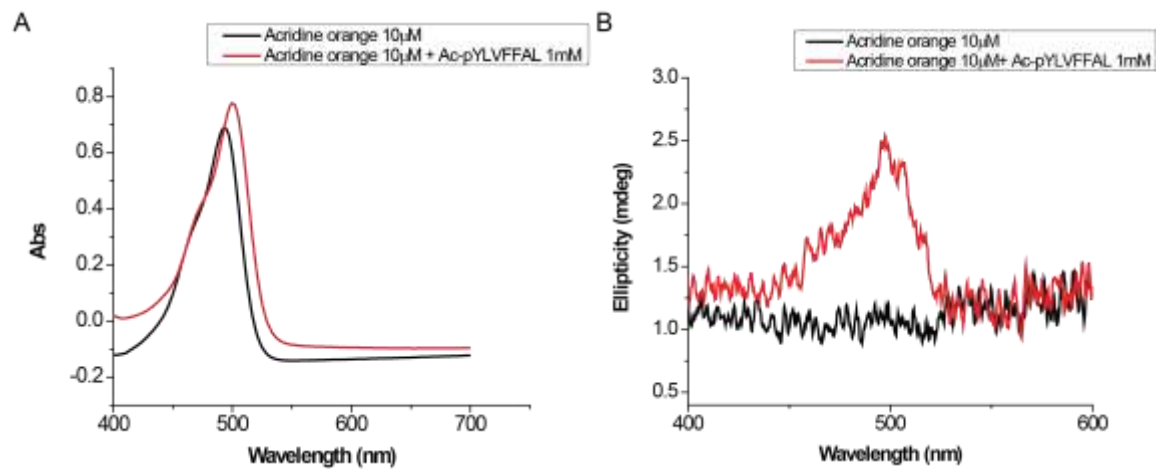


Figure 4-14 (A) UV spectra of Acridine orange 10 μM in the absence (black) and presence (red) of 1mM Ac-pYLVFAL peptide nanotubes. The maximum wavelength shifts from 493.5 to 499.5 nm; (B) Circular Dichroism of Acridine orange 10 μM in the absence (black) and presence (red) of 1mM Ac-pYLVFAL peptide nanotubes. The latter displays a positive ellipticity at 500nm.

To evaluate the homogeneity of the binding, confocal fluorescent imaging (Figure 4-13) established that negatively-charged Alexa 633 binds specifically to Ac-KLVFFAL not to Ac-pYLFFFAL (Figure 4-14). In contrast, positively-charged Acridine orange binds specifically to Ac-pYLFFFAL not to Ac-KLVFFAL (Figure 4-16). As shown in Figure 4-16, both Alexa 633 and Acridine orange bind to the co-assemblies of Ac-KLVFFAL and Ac-pYLFFFAL. An overlaid image (Figure 4-17) suggests most fluorophores are colocalized on co-assembled nanotube surfaces .

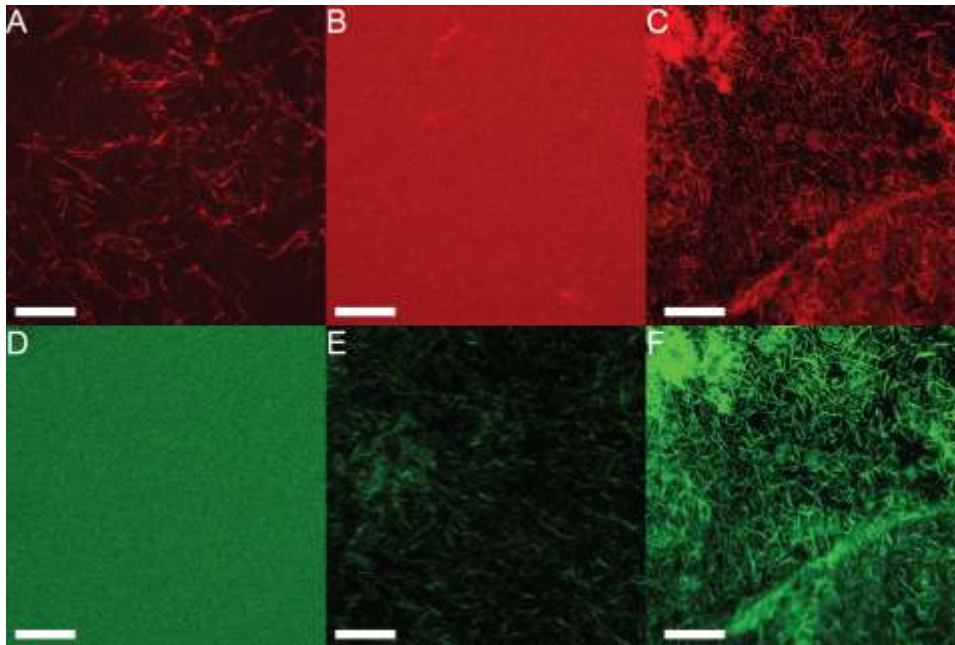


Figure 4-15 Single slices of confocal fluorescence image of (A) Alexa 633 in the presence of Ac-KLVFFAL nanotubes, (B) Alexa 633 in the presence of Ac-pYLFFFAL nanotubes, (C) Alexa 633 in the presence of mixed Ac-KLVFFAL and Ac-pYLFFFAL coassembled as nanotubes, (D) Acridine orange in the presence of Ac-KLVFFAL nanotubes, (E) Acridine orange in the presence of Ac-pYLFFFAL nanotubes, (F) Acridine orange in the presence of mixed Ac-KLVFFAL and Ac-pYLFFFAL coassembled as nanotubes. Scale bar 20 μm .

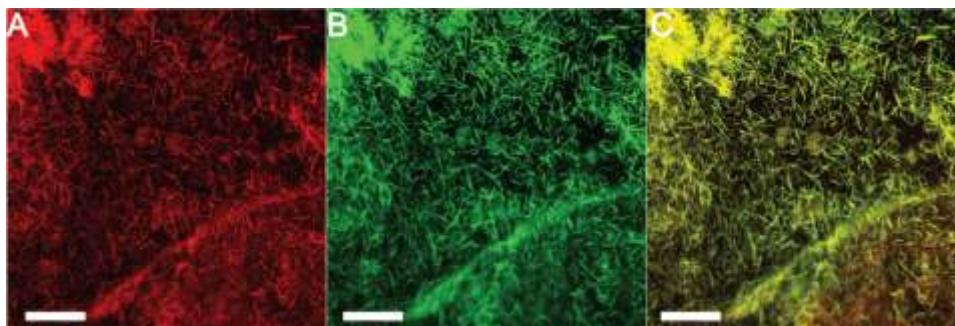


Figure 4-16 Single slices of confocal fluorescence image (A) Alexa 633 in the presence of mixed Ac-KLVFFAL and Ac-pYLVFFAL coassembled as nanotubes, (B) Acridine orange in the presence of mixed Ac-KLVFFAL and Ac-pYLVFFAL coassembled as nanotubes, (C) overlay of image (A) and (B). Scale bar 20 μ m.

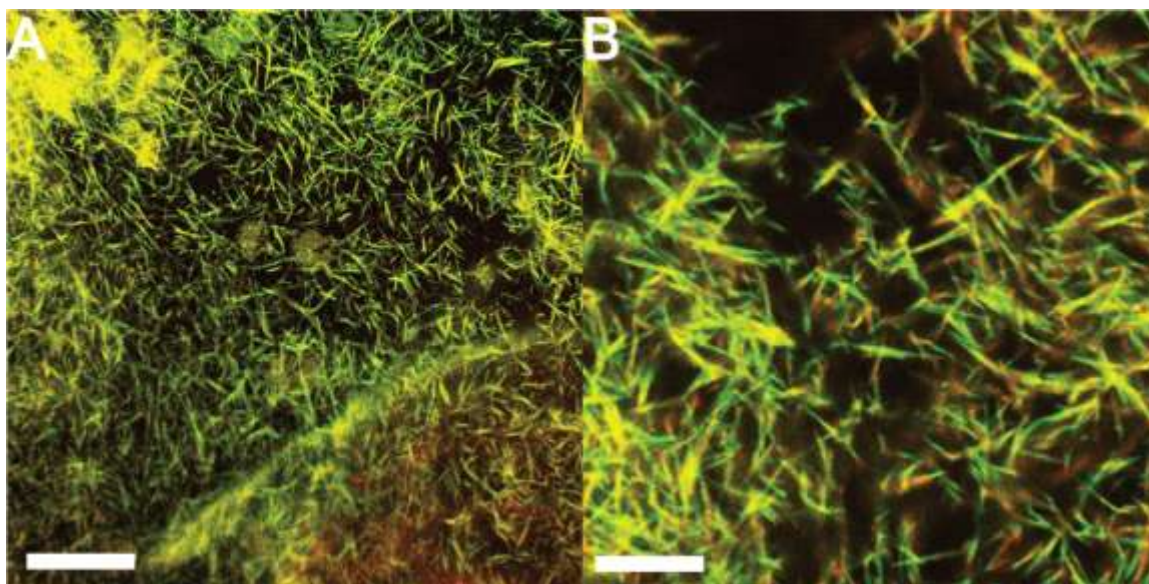


Figure 4-17 Single slices of confocal fluorescence image (A) overlay of image Alexa 633 and Acridine orange binding with the co-assemblies. Scale bar 20 μ m. (B) Zoom in on image. Scale bar 6.7 μ m.

FRET is widely used as a tool for probing molecular interactions and distances between specific sites in macromolecules. To test whether there is energy transfer between the fluorophores pair across the bilayer, the system was excited at 470 nm by single-photon fluorescence microscope. At 470 nm, only the donor Acridine orange would be excited. The emission range was set at 500-750 nm for emissions of both the donor and acceptor. In the presence of Ac-KLVFFAL nanotubes, only the emission peak of the donor Acridine orange was observed at 526 nm with or without the presence of Alexa 633 (Figure 4-18 A). In the presence of Ac-pYLVFFAL nanotubes, similar spectra were

observed (Figure 4-18 B). In the presence of co-assemblies, a drastic decrease was observed at 526 nm of the donor emission along with the appearance of a 645 nm peak of the acceptor emission (Figure 4-18 C). The results demonstrated efficient FRET between the donor and acceptor in the presence of co-assemblies, suggested the energy transfer is most likely taken place across the peptide bilayer surfaces.

Resonance Energy Transfer (FRET) Efficiencies can be calculated based from donor emission as shown in equation 4-1^{29,30}, where where I_{DA} and I_D are the total donor fluorescence intensities in presence and absence of acceptor respectively. Since the acceptor does not emit at 526 nm, the intensity values at 526 nm of the donor were used in the equation. FRET Efficiencies is calculated as $E=1-1.02182E6/2.21818E6=0.54$.

$$E = 1 - \frac{I_{DA}}{I_D}$$

Equation 4-1

Follow the procedure and the spectra overlay integral developed by Mark Hink³¹ and adapted by Antonie J.W.G. Visser³², assuming the dipole orientation factor as average of 0.67, the critical transfer distance (or Förster distance) R_0 , i.e. the D-A distance at which the FRET efficiency is 50%, is calculated as 42 Å. The donor-acceptor distance can be calculated based on equation 4-2^{29,30}, $R=38.8$ Å, which is about the same as the peptide nanotube wall thickness, suggested that the energy transfer is mostly taken place across the peptide bilayers.

$$R = R_0 \sqrt[6]{\frac{1 - E}{E}}$$

Equation 4-2

The rate constant of the energy transfer, k_{FRET} , is a simple function of the distance in between the pair, R ^{29,30}. Here, τ_D is the excited state lifetime of donor in absence of acceptor and R_0 is the critical distance. The fluorescence life time of Acridine orange is 2 ns and Alexa 633 lifetime is 3.2 ns³³, therefore the rate of transfer can be estimated as $3 \times 10^7 \text{s}^{-1}$.

$$k_{FRET} = \frac{1}{\tau_D} \left(\frac{R_0}{R} \right)^6$$

Equation 4-3

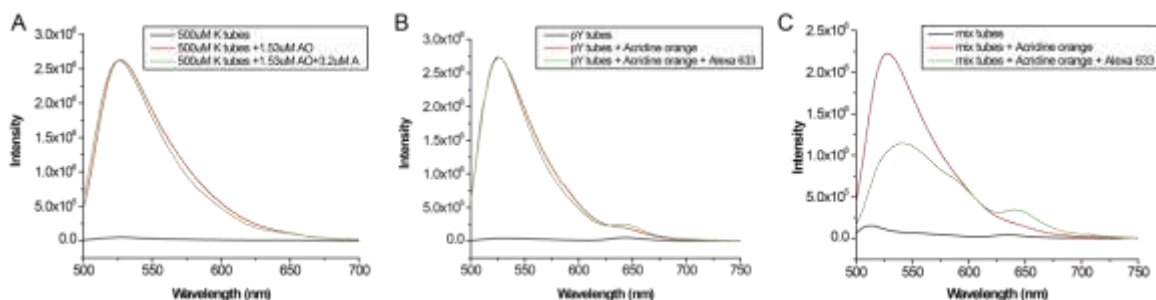


Figure 4-18 Fluorescence spectra of (A) 500 μM Ac-KLVFFAL nanotubes without the presence of dyes (black), in the presence of Acridine orange 3.2 μM (red), and in the presence of Acridine orange 3.2 μM and Alexa 633 1.6 μM (green); (B) 500 μM Ac-pYLFFAL nanotubes without the presence of dyes (black), in the presence of Acridine orange 3.2 μM (red), and in the presence of Acridine orange 3.2 μM and Alexa 633 1.6 μM (green); (C) Coassemblies of 500 μM Ac-KLVFFAL and Ac-pYLFFAL without the presence of dyes (black), in the presence of Acridine orange 3.2 μM (red), and in the presence of Acridine orange 3.2 μM and Alexa 633 1.6 μM (green).

Data in this section demonstrated functionalization of FRET pairs on asymmetric peptide membranes and the donor-acceptor energy transfer distance is aligned with the nanotube bilayer thickness, consistent with successful energy transfer across the peptide bilayer membranes (Figure 4-19). It is now possible to construct more complex, photofunctional systems on these patterned bilayer surfaces.



Figure 4-19 Conceptual figure of donor and acceptor binding on Ac-KLVFFAL (left), Ac-pYLFFAL (middle) and mixed Ac-KLVFFAL and Ac-pYLFFAL coassembled as nanotubes (right). Only in the presence of mixed nanotubes, FRET can take place across the nanotubes from negatively-charged domains to positively-charged domains.

Electron Transfer across Asymmetric Cross- β Peptide Membranes

To further exploit molecular mimicry of photosynthetic energy and electron transfer on the asymmetric peptide membranes, the FRET pair was replaced as a pair of electron donor-acceptor. In the two light reactions of photosynthesis, the critical step is the

absorption of light by a porphyrin derivative, typically a chlorophyll compound with a hydrophobic tail that embeds the molecule into the thylakoid membrane³⁴⁻³⁶. The head is a porphyrin ring that absorbs light and undergoes photon-induced electron transfer (PET). The attractive electronic properties, coupled with the ease of modification by various synthetic routes, make porphyrins good candidates as good electron donor-acceptor system³⁷ with many compounds such as fullerene^{38, 39, 40}, anthracene⁴¹ and Methyl viologen^{6, 42, 43}. Methyl viologen, a typical one-electron transfer acceptor with a low reduction potential, is able to cleave water producing hydrogen in the presence of catalysts in photochemical donor-acceptor system⁴⁴ (Figure 4-20). Here I report the development of light-harvesting peptide nanotubes and test photo-induced electron transfer between protoporphyrin IX (PPIX) and Methyl Viologen (MV) on the self-assembled peptide membranes.

UV-vis absorption spectrum of PPIX solution exhibiting four weak Q-bands (S₀→S₁ transition)⁴⁵, whereas MV has almost no absorption within 300-800 nm (Figure 4-21). Moreover, the fact that there is no spectra shift in PPIX Soret band in the presence of MV, suggests that there are few ground-state interactions between the two molecules. When excited at its Soret band 397 nm, PPIX has a fluorescence emission at 624 and 688 nm (Figure 4-22). As shown in Figure 4-23, in the presence of Ac-KLVFFAL and co-assembled Ac-KLVFFAL and Ac-pYLFFAL peptides, the maximum emission shifted slightly from 624 nm to 626 nm, whereas in the presence of Ac-pYLFFAL nanotubes, no shift was observed. Considering PPIX as a negatively-charged molecules, its binding with positively-charged nanotube surfaces that exist in Ac-KLVFFAL and mixed nanotubes in the solution suggest that binding explains the fluorescence emission shift.

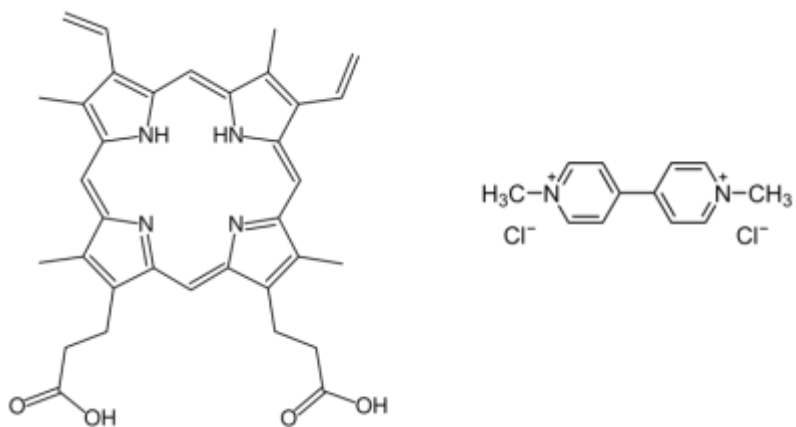


Figure 4-20 Molecular structure of Protoporphyrin IX (left) and methyl viologen (right).

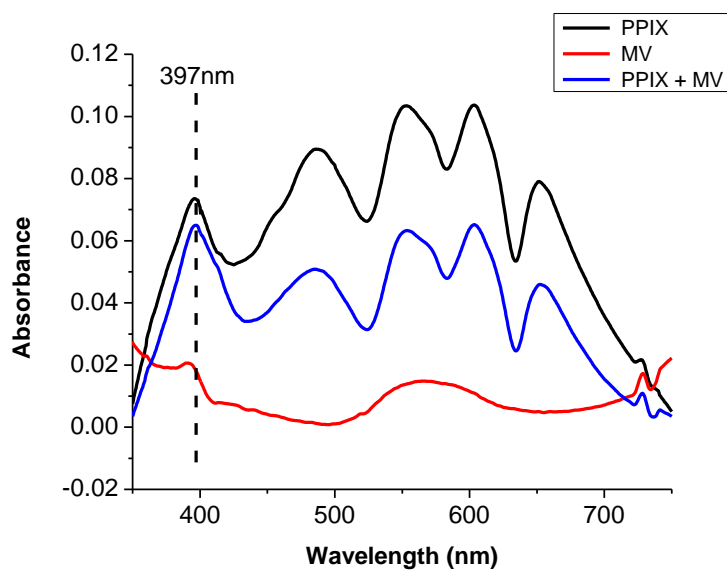


Figure 4-21 Absorption spectra of 3.33 μ M PPIX and 0.4mM Methyl viologen in TEAA.

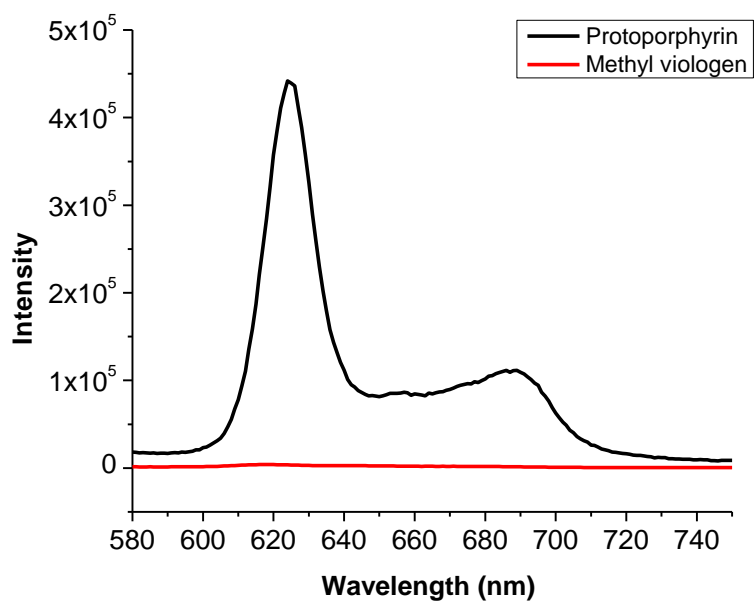


Figure 4-22 Fluorescence emission spectra of 3.33 μM PPIX with emission at 624 and 688 nm (black) and 0.4mM Methyl viologen in TEAA (red). Excitation 397 nm.

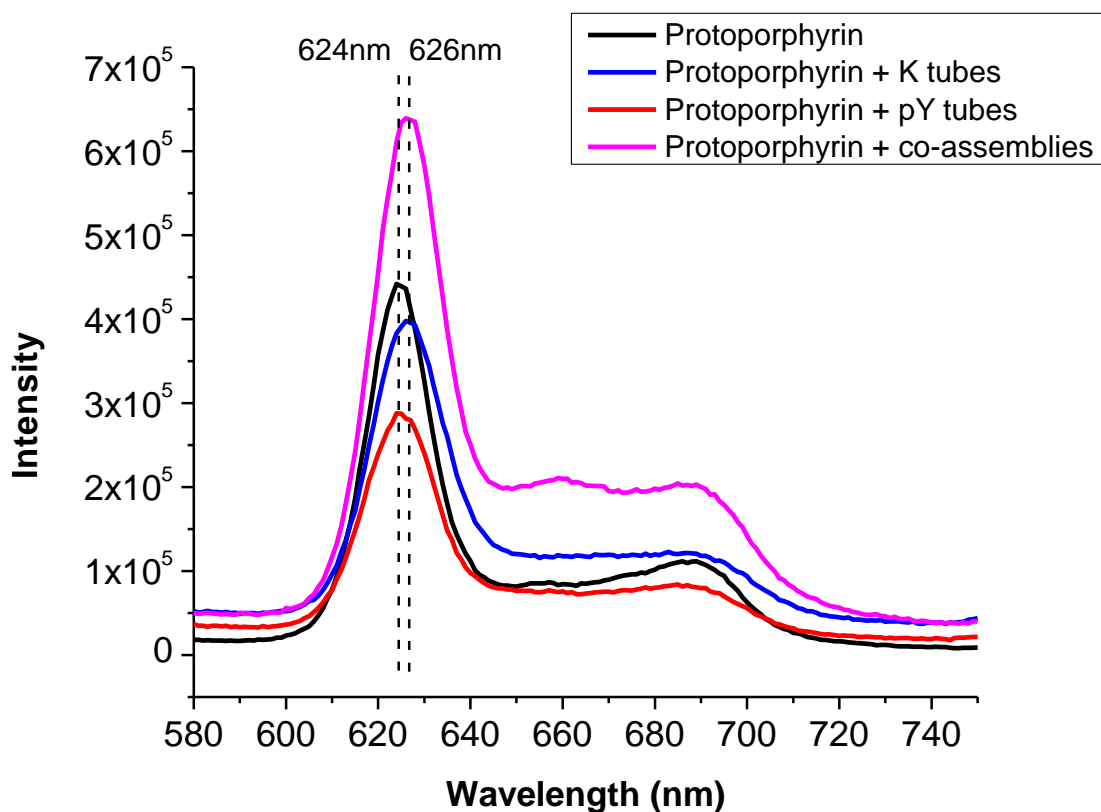


Figure 4-23 Fluorescence emission spectras of PP IX, PP IX in the presence of Ac-KLVFFAL nanotubes, PP IX in the presence of Ac-pYLVFFAL nanotubes, PP IX in the presence of mixed Ac-KLVFFAL and Ac-pYLVFFAL coassembled as nanotubes. PP IX 3.33 μ M, total peptides concentration in each sample 0.33mM. Excitation 397 nm.

Figure 4-24 shows the spectral changes upon titration of PPIX with MV^{2+} . The fluorescence emission of PPIX was quenched by the addition of MV^{2+} . Figure 4-25 shows Stern-Volmer (equation 4-4) plots for quenching of the emission from the Soret band of PPIX by MV^{2+} in the absence and presence of peptide nanotubes. The plots for the PPIX- MV^{2+} system showed efficient fluorescence quenching even in the absence of peptide nanotubes. Combining with the results from UV where the two molecules have few ground-state interactions, these data demonstrated dynamic quenching mechanism resulted from collision of an excited state fluorophore and another molecule in solution instead of a static quenching where fluorophores form a reversible complex with the quencher molecule in the ground state.

$$\frac{I_0}{I} = 1 + K_{SV}[MV^{2+}]$$

Equation 4-4

The Stern-Volmer plots (Figure 4-25 A) in the absence of peptide nanotubes fits to $I_0/I=6.94 [MV^{2+}] + 1$, $K_{sv}=6.94 \times 10^3 M^{-1}$, comparable to that of Zinc-Porphyrin to Methyl Viologen⁴⁶ ($\sim 3 \times 10^3$) and Protoporphyrin IX to fullerene⁴⁷ ($\sim 2.6 \times 10^4$). In contrast, in the presence of Ac-KLVFFAL (Figure 4-25 B), the fluorescence quenching is not linear, could be due to binding of partial PPIX on the surfaces of K tubes. Interestingly, in the presence of co-assemblies (Figure 4-25 C), the fluorescence quenching was saturated at $[MV^{2+}] \sim 0.18mM$, where the ratio of I_0/I is almost constant at 2.5. A non-linear Stern-Volmer plots can occur in both static and dynamic quenching are occurring in the sample or in the case of collisional quenching if some of the fluorophores are less accessible than others. Considering unique charge properties of the co-assembled nanotubes, this saturation behavior could be resulted from electron transfer routes different from that in solution, or could be resulted from limited access of PPIX (relatively large and conformationally constrained molecule) to the inner surfaces and decreasing the collisional opportunities of the two fluorophores.

To test these two theories, the concentration of PPIX was doubled from 3.33 μM to 6.67 μM while the concentration of peptide nanotubes and MV remained the same (Figure 4-26). In the absence of peptide nanotubes (Figure 4-27 A), the PPIX-MV²⁺ system was efficiently quenched. The Stern-Volmer plot fits to $I_0/I=5.49 [MV^{2+}] + 1$, $K_{sv}=5.49 \times 10^3 M^{-1}$. In the presence of mixed nanotubes (Figure 4-27 B), the fluorescence quenching was still saturated at $[MV^{2+}] \sim 0.18mM$, where the ratio of I_0/I is almost constant at 2.6. If the saturation behavior is resulted from limited access of PPIX, then a [PPIX] increase should increase the collisional opportunities of the two fluorophores and hence higher fluorescence quenching. Therefore, the saturation behavior due to different electron transfers routes.

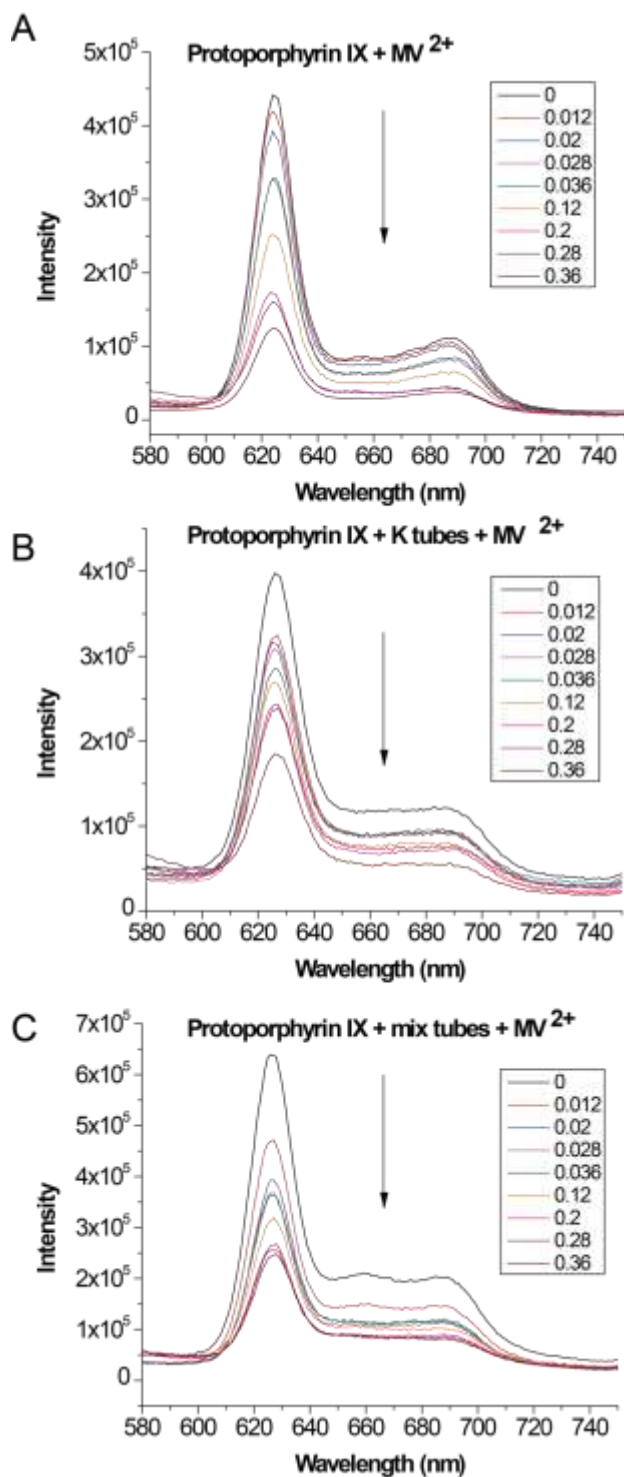


Figure 4-24 Fluorescence spectras of Protoporphyrin IX with addition of varying concentration of methyl viologen, (A) in the absence of peptide nanotubes, (B) in the presence of Ac-KLVFFAL nanotubes, (C) in the presence of mixed Ac-KLVFFAL and Ac-pYLFFFAL coassembled as nanotubes. Protoporphyrin IX 3.33 μ M, total peptides concentration in each sample 0.33mM, methyl viologen concentrations are 0.012, 0.02, 0.028, 0.036, 0.12, 0.2, 0.28, 0.36 mM respectively.

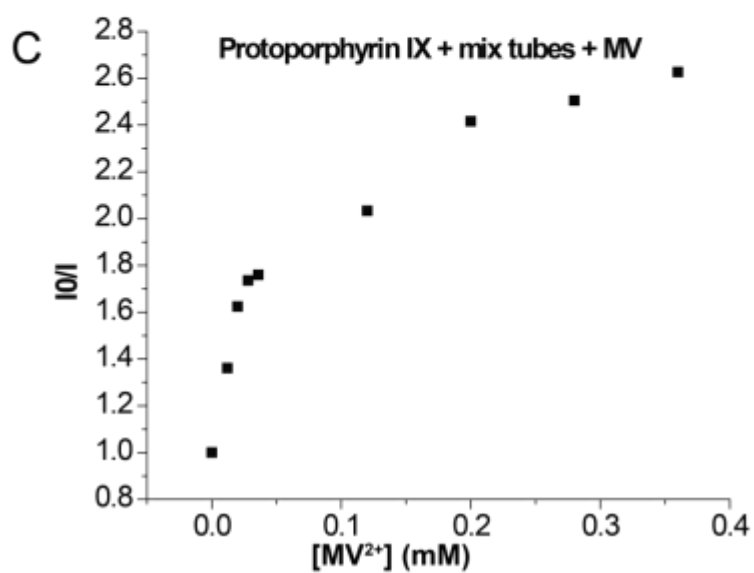
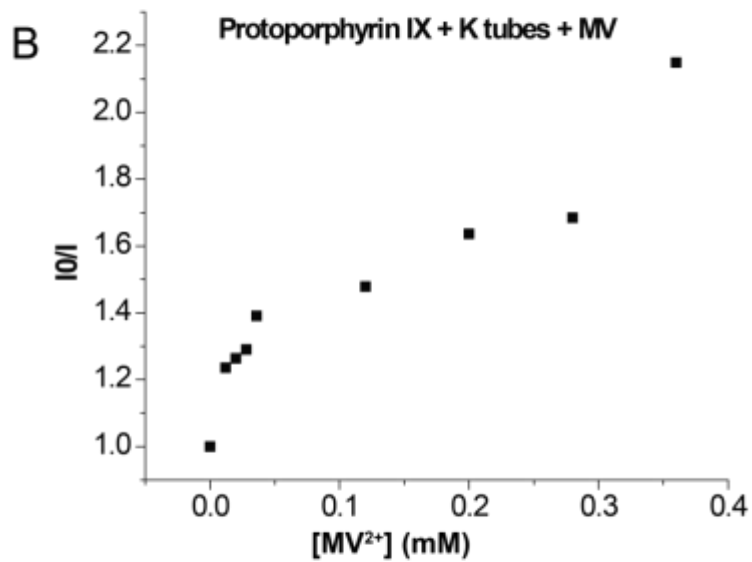
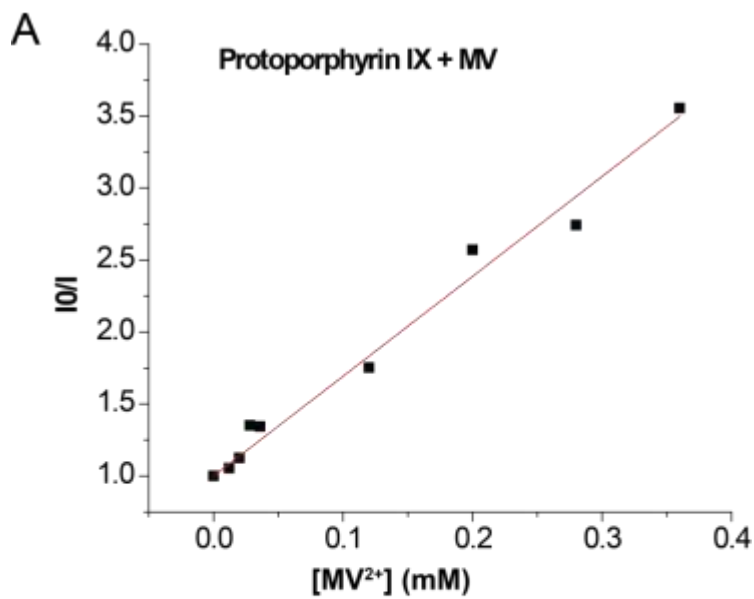


Figure 4-25 Plots of Protoporphyrin IX fluorescence intensity I_0/I vs methyl viologen concentration. I_0 : in the absence of methyl viologen, I : in the presence of methyl viologen. (A) in the absence of peptide nanotubes, (B) in the presence of Ac-KLVFFAL nanotubes, (C) in the presence of mixed Ac-KLVFFAL and Ac-pYLFFAL coassembled as nanotubes. Protoporphyrin IX $3.33 \mu\text{M}$, total peptides concentration in each sample 0.33mM , methyl viologen concentrations are $0.012, 0.02, 0.028, 0.036, 0.12, 0.2, 0.28, 0.36 \text{ mM}$ respectively. Plot A was fit to linear with intercept as 1.

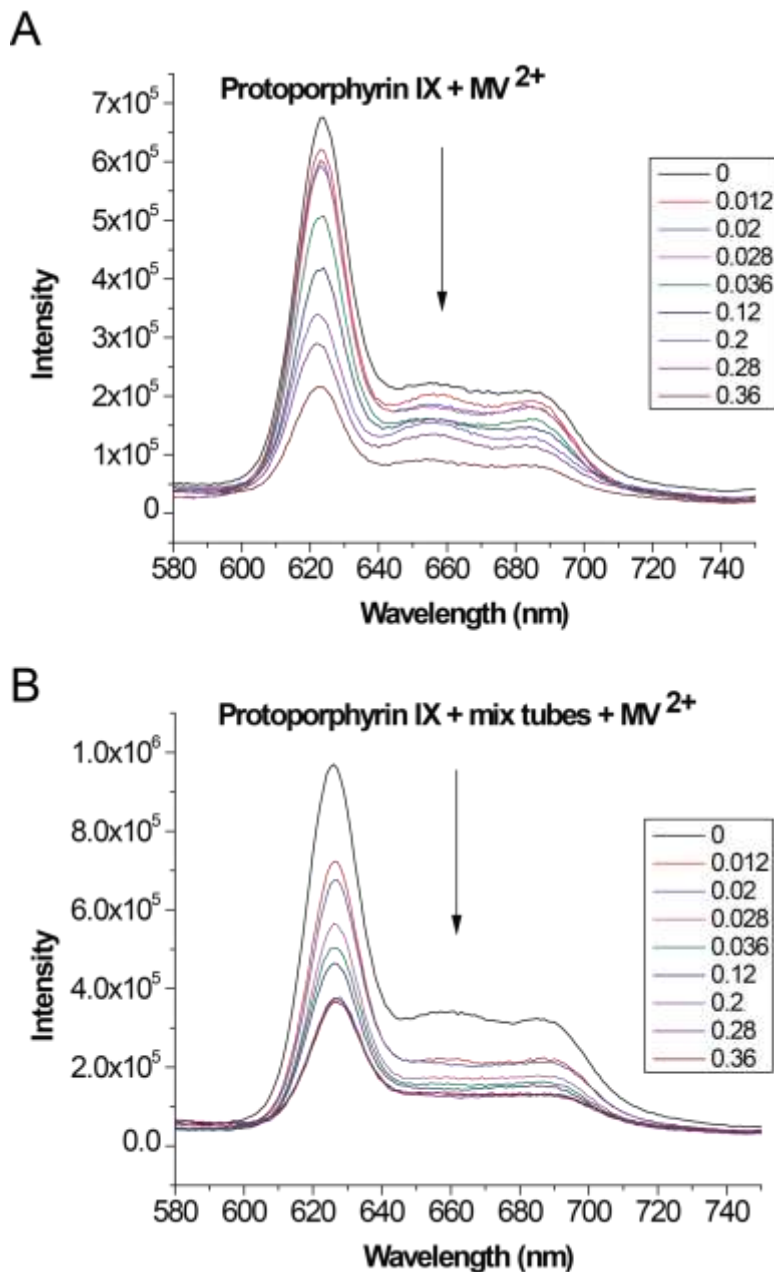


Figure 4-26 Fluorescence spectras of Protoporphyrin IX with addition of varying concentration of methyl viologen, (A) in the absence of peptide nanotubes, (B) in the presence of mixed Ac-KLVFFAL and Ac-pYLFFAL coassembled as nanotubes. Protoporphyrin IX $6.67 \mu\text{M}$, total peptides

concentration in each sample 0.33mM, methyl viologen concentrations are 0.012, 0.02, 0.028, 0.036, 0.12, 0.2, 0.28, 0.36 mM respectively.

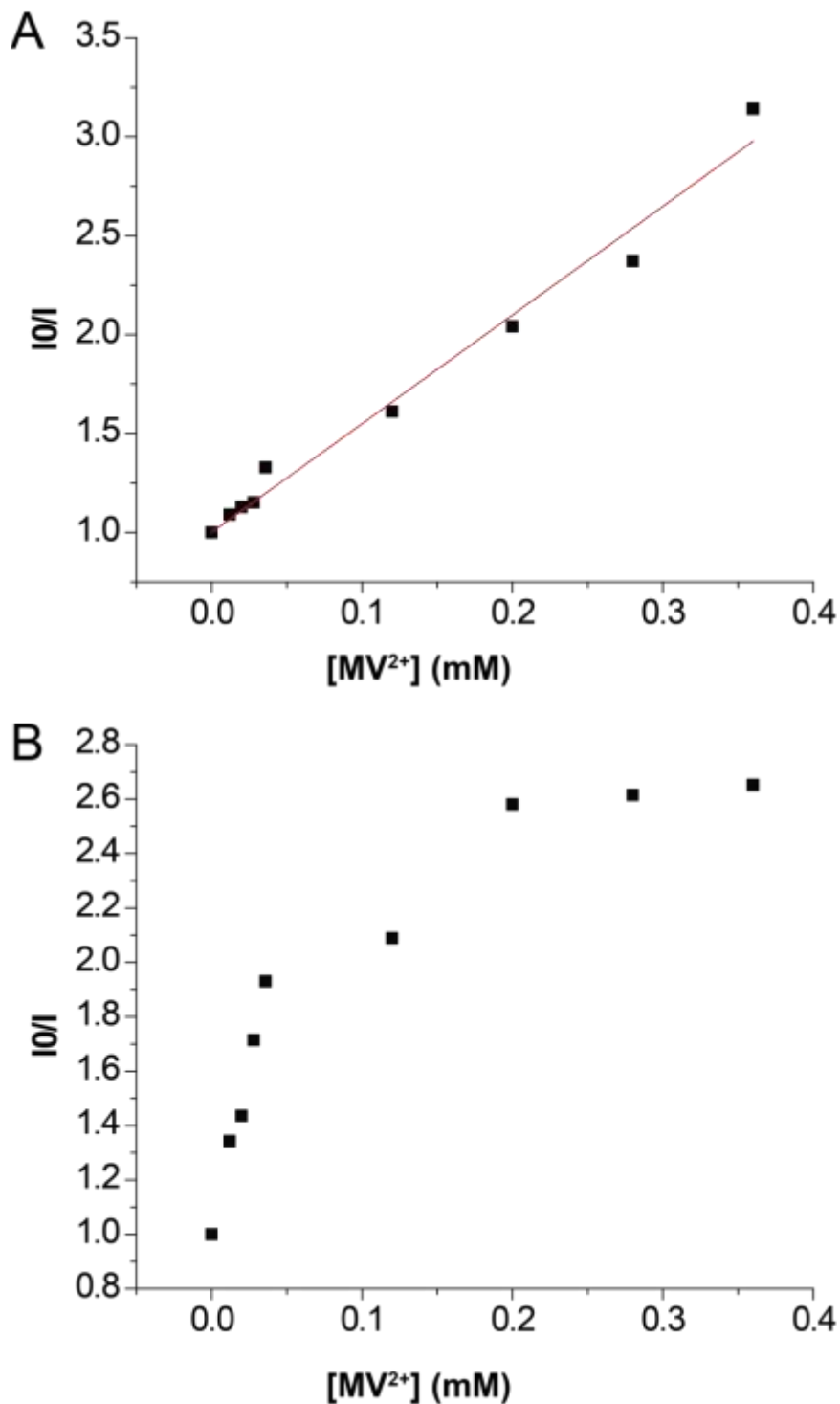


Figure 4-27 Plots of Protoporphyin IX fluorescence intensity I_0/I vs methyl viologen concentration. I_0 : in the absence of methyl viologen, I : in the presence of methyl viologen. (A) in the absence of peptide nanotubes, (C) in the presence of mixed Ac-KLVFFAL and Ac-pYLVFFAL coassembled as nanotubes. Protoporphyin IX 6.67 μ M, total peptides concentration in each sample 0.33mM, methyl

viologen concentrations are 0.012, 0.02, 0.028, 0.036, 0.12, 0.2, 0.28, 0.36 mM respectively. Plot A was fit to linear with intercept as 1.

In fact, the plots of Protoporphyrin IX fluorescence intensity I_0/I vs methyl viologen concentration in the presence of K tubes and the co-assemblies can be fitted to two-phase rates with breaking points (Figure 4-28). The plots of I_0/I vs methyl viologen are essentially measuring effective molarities of the donor and the acceptor in proximity. In the presence of K tubes, the rates are $K_1 = (12.22 \pm 1.66) \times 10^3 \text{ M}^{-1}$ and $K_2 = (2.13 \pm 0.5) \times 10^3 \text{ M}^{-1}$ respectively (Figure 4-28B). The most possible mechanism to have much higher rate than in solution ($K = (6.94 \pm 0.24) \times 10^3 \text{ M}^{-1}$) with limited acceptor concentration is when donor and donor can transfer energy between each other across the peptide bilayer tubes (Figure 4-29 A). With this model, one acceptor can effectively quench two to more donors and lead to effective donor-acceptor in proximity with limited acceptor concentration. This effect will be evened out with increasing acceptor concentration; therefore, there is a breaking point with increasing acceptor concentration. In the second stage, the electron transfer will be taken place between bound donor on tubes and the acceptor in solution, and hence similar rate to that of in solution (Figure 4-28 A).

In the presence of co-assembled tubes, the rates are $K_1 = (24.68 \pm 1.95) \times 10^3 \text{ M}^{-1}$ and $K_2 = (2.73 \pm 0.41) \times 10^3 \text{ M}^{-1}$ respectively (Figure 4-28C). The most possible mechanism to have much higher rate than in solution ($K = (6.94 \pm 0.24) \times 10^3 \text{ M}^{-1}$) with limited acceptor concentration is when donor and acceptor can transfer energy between each other across the peptide bilayer tubes (Figure 4-29 B). Considering a 4nm electron transfer is rarely seen unless the transfer pathway is conductive, this model suggests the asymmetric peptide membranes may possess conductivity. Similar, the effect of increased molarities of donor-acceptor in proximity will be evened out with increasing acceptor concentration; therefore, there is a breaking point with increasing acceptor concentration. In the second stage, the electron transfer will be taken place between bound donor on tubes and the acceptor in solution, and hence similar rate to that of in solution.

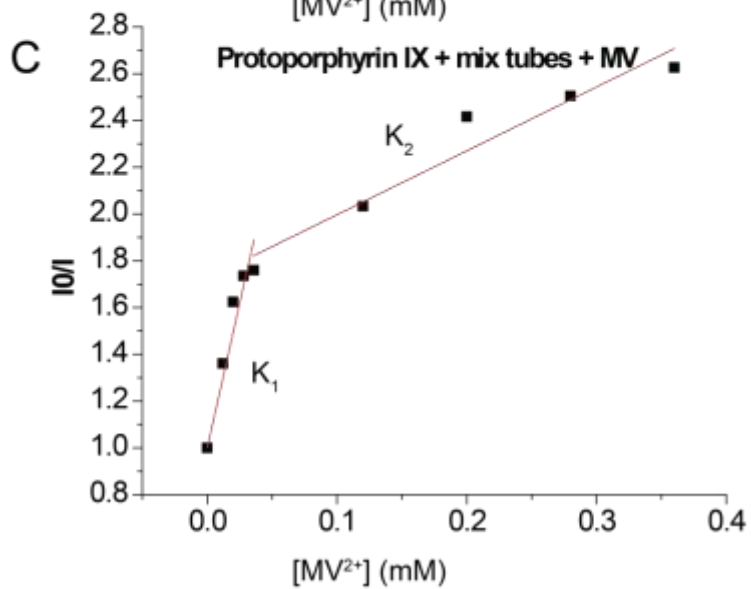
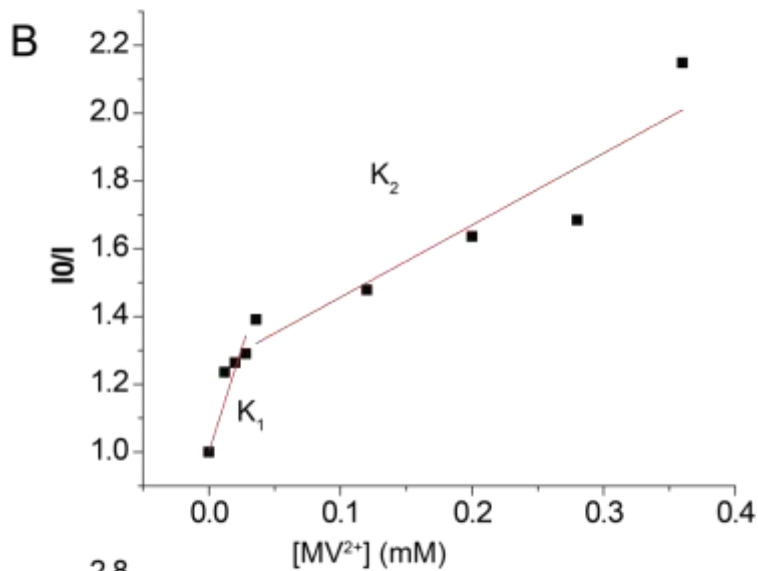
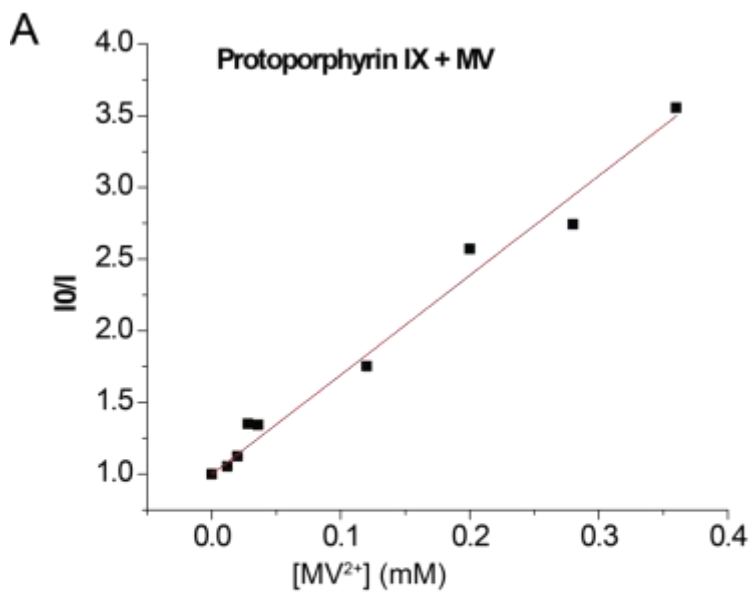


Figure 4-28 Plots of Protoporphyrin IX fluorescence intensity I_0/I vs methyl viologen concentration. I_0 : in the absence of methyl viologen, I : in the presence of methyl viologen. (A) in the absence of peptide nanotubes, (C) in the presence of mixed Ac-KLVFFAL and Ac-pYLVFFAL coassembled as nanotubes. B and C are fitted with two slopes as two stages. Protoporphyrin IX 3.33 μM , total peptides concentration in each sample 0.33mM, methyl viologen concentrations are 0.012, 0.02, 0.028, 0.036, 0.12, 0.2, 0.28, 0.36 respectively.

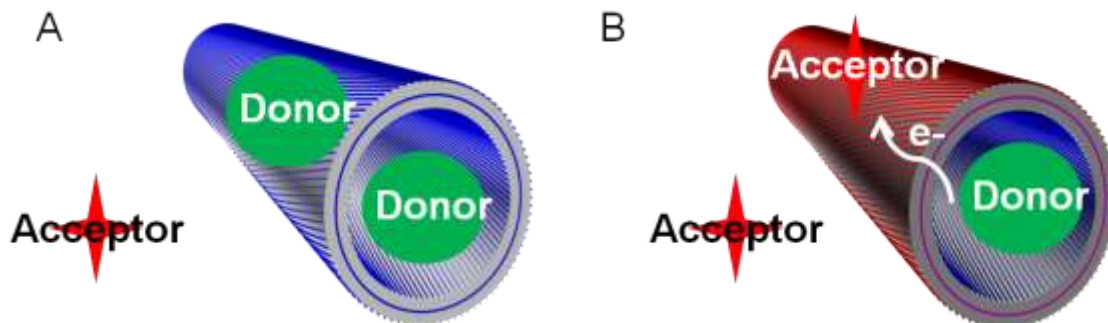


Figure 4-29 Electron transfer models between Protoporphyrin IX and Methyl viologen in the presence of Ac-KLVFFAL tubes (A) and in the presence of co-assembled Ac-KLVFFAL and Ac-pYLVFFAL peptides (B).

In order to estimate the electron transfer rate in the presence of asymmetric peptide nanotubes, the fluorescence decays of PPIX in the absence of peptide nanotubes were measured and expressed with a monoexponential curve with a lifetime of 9.35 ns (Figure 4-30 and Table 4-1). The addition of co-assembled nanotubes led to a slightly decrease in the lifetime to 8.81 ns (Figure 4-30 and Table 4-1). Addition of MV^{2+} to PPIX in the absence of co-assembled peptide nanotubes caused a shortening of the lifetime to 5.5 ns. Addition of MV^{2+} to PPIX in the presence of co-assembled peptide nanotubes caused the largest shortening of the lifetime to 3.6 ns. The electron transfer rate can be estimated as the reciprocal of the donor lifetime difference in the absence and presence of the acceptor. Therefore, the electron transfer rate (k) from PPIX to MV in the absence of peptide nanotubes was estimated as $k_{\text{et}} = (\tau[\text{MV}^{2+}])^{-1} - (\tau[\text{none}])^{-1} = 7.49 \times 10^7 \text{ S}^{-1}$, where $\tau[\text{MV}^{2+}]$ and $(\tau[\text{none}])$ are the fluorescence lifetimes of PPIX with and without addition of MV^{2+} , respectively. Similarly, the rate constant for the electron transfer (k) from PPIX to MV in the presence of co-assembled peptide nanotubes was estimated as $k_{\text{et}}' = (\tau[\text{MV}^{2+}])^{-1} - (\tau[\text{none}])^{-1} = 1.64 \times 10^8 \text{ S}^{-1}$, where $\tau[\text{MV}^{2+}]$ and $(\tau[\text{none}])$ are the fluorescence lifetimes of PPIX with and without addition of MV^{2+} , respectively. The

electron transfer rate is higher in the presence of peptide nanotubes, demonstrated peptide nanotubes as robust scaffold are able to organize electron-donor pairs for light-harvesting and electron transfer.

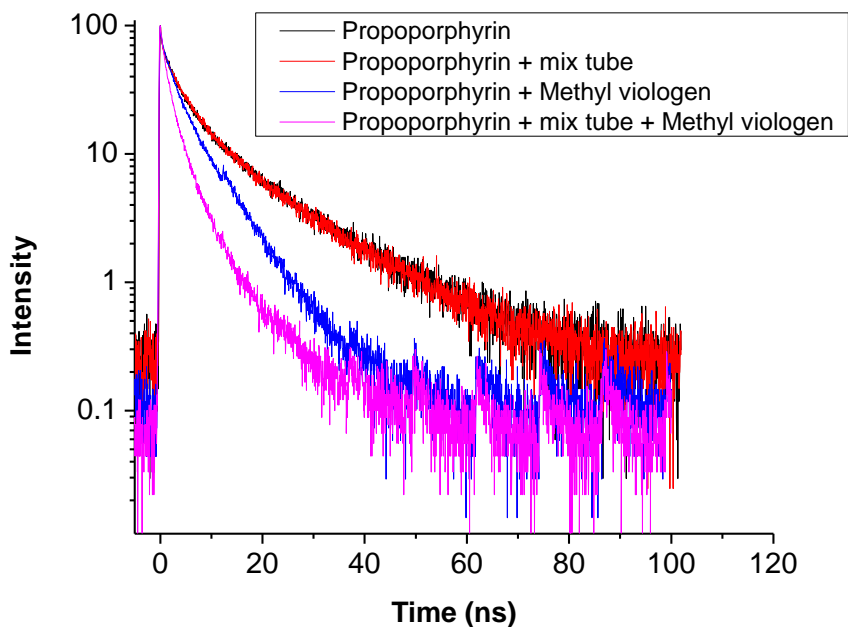


Figure 4-30 Fluorescence lifetime decay of Protoporphyrin IX, Protoporphyrin IX in the presence of mixed Ac-KLVFFAL and Ac-pYLVFFAL coassembled as nanotubes, Protoporphyrin with the addition of methyl viologen, Protoporphyrin IX in the presence of mixed Ac-KLVFFAL and Ac-pYLVFFAL coassembled as nanotubes with the addition of methyl viologen Protoporphyrin IX 3.33 μM , total peptides concentration in each sample 0.33mM, methyl viologen 0.12mM.

Table 4-1 Lifetime measurements and electron transfer rate.

	Lifetime (ns)	Error (ns)	$k_{\text{et}} (\text{S}^{-1})$	Error (S^{-1})
Protoporphyrin	9.35	0.11		
Protoporphyrin + mix tubes	8.81	0.12		
Protoporphyrin + methyl viologen	5.5	0.1	7.49×10^7	2.17×10^7
Protoporphyrin + mix tubes + methyl viologen	3.6	0.1	1.64×10^8	2.42×10^7

Conclusions

In this chapter, a unique asymmetric peptide membrane with distinctly charged inner and outer surfaces is utilized as a self-assembled scaffold to array pigments and electron donor-acceptor pairs. A variety of qualitative and quantitative methods were developed to characterize their ability to recruit fluorophores and molecules. The cross- β grooves appear to have some of the features of small molecule binding sites in proteins and certainly capture some of the ability to access the long-range order inherent in lipids and membranes. Such unique surfaces created from supramolecular assemblies were exploited by building energy and electron transfer systems on peptide nanotube surfaces. These experiments expands the light-harvesting FRET taken place on the same surfaces of symmetric peptide membrane, to complicated FRET and electron transfer processes that are taken place not only on the the same peptide membrane surface, but also across the cross- β bilayer of the asymmetric peptide membrane. The self-assembly of asymmetric peptide membranes offer an effective strategy to integrate light harvesting and charge separation in artificial photosynthetic systems.

Methods

Reagents

Acridine orange, Methylene blue, Protoporphyrin IX, Methyl viologen dichloride hydrate were purchased from Sigma-Aldrich. Alexa Fluor® 633 NHS Ester (Succinimidyl Ester) was purchased from life technology. All the fluorophores were dissolved in 40% MeCN/H₂O or buffer in consistence with peptide assemblies.

Synthesis of Rho-KLVFFAL

Peptide was prepared on a solid support resin using Fmoc microwave-assisted peptide synthesis with final deprotection of the Fmoc, leaving a free –NH₂ on the N-terminus of the peptide. The resin was washed with DCM before the coupling reaction. For coupling of Rhodamine 110, a 3x molar equivalent (assuming a 0.1mmol scale for peptide synthesis) of Rhodamine 110 was added to a minimal 173 volume of DCM and stirred to dissolve. To this solution were added 8 equivalents of DIEA. After 10 minutes, 3 equivalents of HBTU were added to the Rhodamine solution for activation. After another 10 minutes, the resin slurry was added to this Rhodamine solution. Reaction was stirred overnight under N₂ gas in an ice bath and was monitored by TLC. Following either

reaction, the resin was washed with 1:1 DMF:DMSO (2x), DMF (2x) and DCM (2x) to remove excess Rhodamine 110 from the resin. Resins were then dried and the peptides cleaved as previously described.

UV-Vis Absorption, Circular Dichroism and Fluorescence Emission measurements

UV-vis absorption spectra were recorded with a Jasco V-530 UV spectrophotometer using a 2 mm cuvette path length. UV spectra were background subtracted using peptide nanotubes in the absence of CR to minimize scattering effects. CD spectra were measured on a Jasco V-810 CD polarimeter with a 1 mm cuvette. Fluorescence Emission was measured using fluoromax-3 spectrofluorometer (Horiba Jobin Yvon, Edison, NJ, USA) using a 3mm cuvette length.

FRET calculations

The emission of the donor Acridine orange and the absorption of the acceptor Alexa 633 were measured (Figure 4-31) to calculate R_0 . Follow the procedure and the spectra overlay integral developed by Mark Hink³¹ and adapted by Antonie J.W.G. Visser³², and input the spectra data results, assuming the dipole orientation factor as average of 0.67, the critical transfer distance is calculated as 42 Å.

The rate constant of the energy transfer, k_{FRET} , is a simple function of the distance in between the pair, R . Here, τ_D is the excited state lifetime of donor in absence of acceptor and R_0 is the critical distance, i.e. the D-A distance at which the FRET efficiency is 50%.

$$k_{FRET} = \frac{1}{\tau_D} \left(\frac{R_0}{R} \right)^6$$

Equation 4-5

The FRET efficiency is defined as the quantum yield of the process:

$$E = \frac{k_{FRET}}{k_{FRET} + \sum k_i} = \frac{k_{FRET}}{k_{FRET} + \sum k_i} = \frac{R_0^6}{R_0^6 + R^6}$$

Equation 4-6

Therefore, the energy transfer distance can be calculated from FRET efficiency by:

$$R = R_0 \sqrt[6]{\frac{1 - E}{E}}$$

Equation 4-7

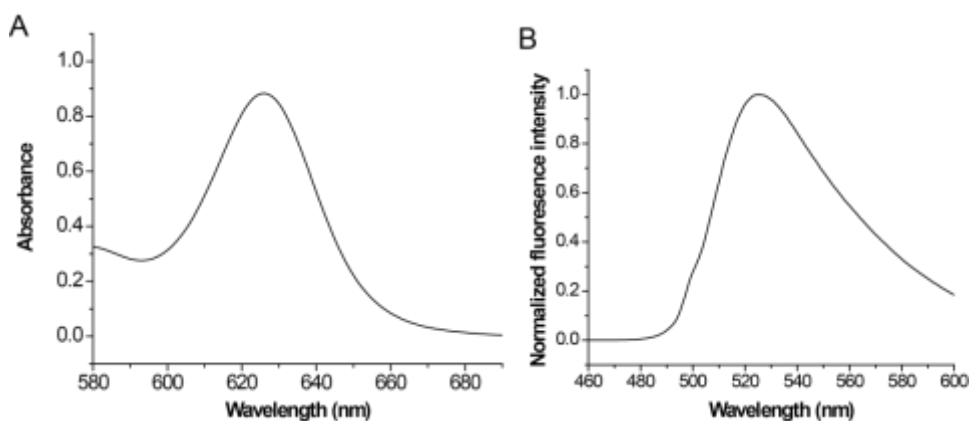


Figure 4-31 (A) UV spectra of Alexa 633 absorbance, (B) fluorescence spectra of Acridine orange emission.

Electron transfer sample preparation

PPIX, MV and peptide nanotubes pellets were dissolved or resuspended in triethylammonium acetate buffer, pH7. A stock solution of 10 and 20 μM PPIX were prepared. A series of MV solution were prepared with concentrations of 0.036, 0.06, 0.084, 0.108, 0.36, 0.6, 0.84, 1.08 mM. Total peptides concentration in stock solution is 1mM. A typical sample is prepared by mixing 50uL of each stock solution of PPIX, MV and peptides. The fluorescence excitation wavelength is 397nm with integration time 0.1 s and increment 1nm. Figure 4-32 shows the excitation spectra of PPIX with the maxima excitation at 397nm and was used as the excitation wavelength for all fluorescence

emission measurements.

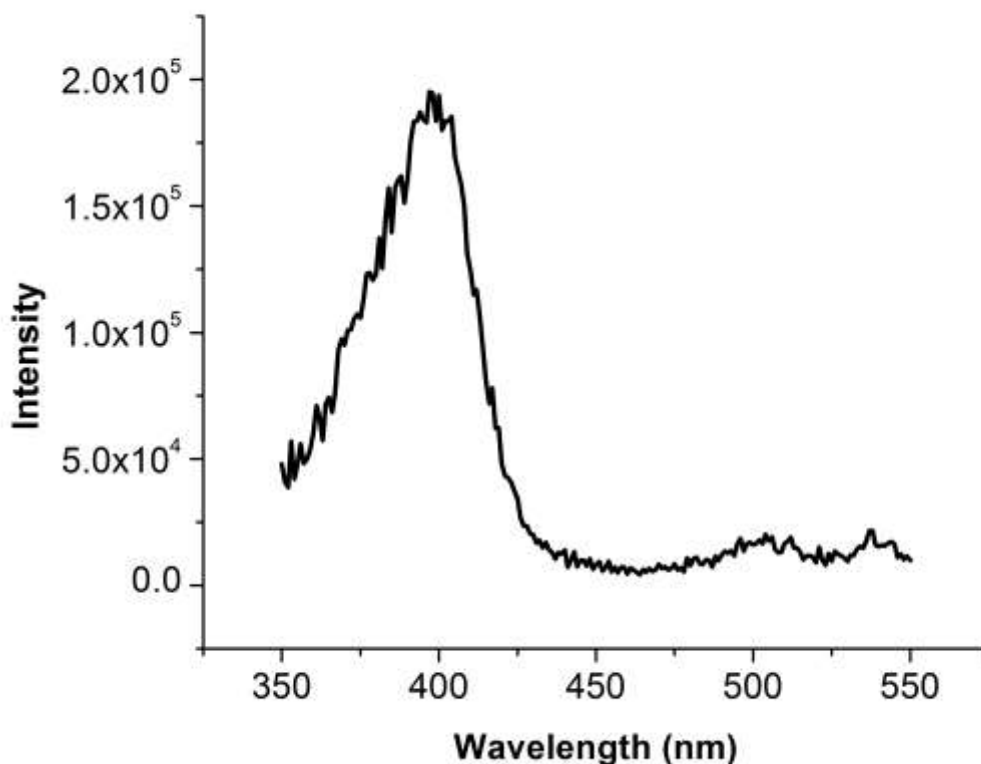


Figure 4-32 Excitation spectra of Protoporphyrin IX.

Time-Resolved Fluorescence Lifetime Measurements

Time-correlated single photon counting (TCSPC) method was used to measure the fluorescence decay of the PPIX. Samples were held in a 1 cm cuvette and measured at the right angle geometry. The output pulses centered at 800 nm (~ 100 fs, 80 MHz) from a mode-locked Ti:Sapphire laser (Tsunami oscillator pumped by a 10 W Millennia Pro, Spectra-Physics) were passed through a pulse picker (Conoptics, USA) to reduce the repetition rate by a factor of 20 and then frequency-doubled in a BBO crystal to generate pump pulses at 400 nm and used to excite PPIX samples. The emissions from PPIX were detected by a microchannel-plate photomultiplier tube (Hamamatsu R3809U-51), the output of which was amplified and analyzed by a TCSPC board (Becker & Hickel SPC 600).

Linear Dichroism

This was recorded using a microvolume cuvette with a path length of 50 μm ⁴⁸ and a rotation speed of 3000 rpm to establish Couette flow. The background scattering for each sample was obtained from the LD spectra of samples at 0 rpm.

Fluorescence imaging

Samples were loaded onto a 22 × 50 mm #1.5 coverslip in custom holder and enclosed with a 22 × 30 mm coverslip. Fluorescence imaging was taken on an Olympus Fluoview 1000 Confocal Microscope using an Olympus 60X oil immersion (PlanApo N, 1.42 NA) objective lens. Each fluorescence intensity acquisition consisted of one frame at 256×256 pixels with dimensions 212 × 212 μm , 106×106 μm or 70×70 μm and the images were acquired approximately 2 μm below the glass surface. The image data was analyzed by Olympus Fluoview and FIJI.

Corss-section embedded TEM

Ac-KLVFFAL peptide sample solution (15 μL) was placed on a glass slide and inverted over a 50% glutaraldehyde solution at 60°C for 30 minutes, then placed further over 4% OsO₄ for 30 minutes in a closed glass Petri dish. The resulting sample was incubated in 2.5% glutaraldehyde in 0.1 M phosphate buffer (pH 7.4) for 30 minutes, followed by a H₂O rinse, and further incubation in 2% OsO₄ for 30 minutes. This sample was washed with H₂O, stained with 4% uranyl acetate in 50% ethanol for 10 minutes, dehydrated through an ethanol series, ending at 100% and gradually embedded with 812 Epoxy resin by: (1) 60 minute incubation in 1:1 Ethanol: 812 epoxy resin, (2) 60 minutes 1:2 Ethanol: 812 epoxy resin, and (3) 60 minutes in 100% 812 epoxy resin. Samples were then thin (70 to 80nm) sectioned using a diamond knife and a RMC MT-7000 ultramicrotome, placed on TEM grids and post-stained with uranyl acetate and Reynold's lead citrate stain. TEM micrographs were recorded with a Philips 410 TEM using a tungsten filament at an accelerating voltage of 75 kV.

References

- (1) Archer MD, B. J. *Photosynthesis and photoconversion*. ; Imperial College Press: London, UK, 2004
- (2) Collado, D.; Perez-Inestrosa, E.; Suau, R. *The Journal of Organic Chemistry* **2003**, *68*, 3574.
- (3) Ahrens, M. J.; Sinks, L. E.; Rybtchinski, B.; Liu, W.; Jones, B. A.; Giaimo, J. M.; Gusev, A. V.; Goshe, A. J.; Tiede, D. M.; Wasielewski, M. R. *J. Am. Chem. Soc.* **2004**, *126*, 8284.
- (4) Berman, A.; Izraeli, E. S.; Levanon, H.; Wang, B.; Sessler, J. L. *J. Am. Chem. Soc.* **1995**, *117*, 8252.
- (5) Sessler, J. L.; Wang, B.; Harriman, A. *J. Am. Chem. Soc.* **1993**, *115*, 10418.
- (6) Hayashi, T.; Takimura, T.; Ogoshi, H. *J. Am. Chem. Soc.* **1995**, *117*, 11606.
- (7) van der Boom, T.; Hayes, R. T.; Zhao, Y.; Bushard, P. J.; Weiss, E. A.; Wasielewski, M. R. *J. Am. Chem. Soc.* **2002**, *124*, 9582.
- (8) Páli, T.; Garab, G.; Horváth, L. I.; Kóta, Z. *CMLS, Cell. Mol. Life Sci.* **2003**, *60*, 1591.
- (9) Bahatyrova, S.; Frese, R. N.; Siebert, C. A.; Olsen, J. D.; van der Werf, K. O.; van Grondelle, R.; Niederman, R. A.; Bullough, P. A.; Otto, C.; Hunter, C. N. *Nature* **2004**, *430*, 1058.
- (10) Scheuring, S.; Sturgis, J. N.; Prima, V.; Bernadac, A.; Lévy, D.; Rigaud, J.-L. *Proc. Natl. Acad. Sci. U.S.A.* **2004**, *101*, 11293.
- (11) Wang, X.; Maeda, K.; Chen, X.; Takanabe, K.; Domen, K.; Hou, Y.; Fu, X.; Antonietti, M. *J. Am. Chem. Soc.* **2009**, *131*, 1680.
- (12) Kaneko, M. *Prog. Polym. Sci.* **2001**, *26*, 1101.
- (13) Najafpour, M. M.; Rahimi, F.; Fathollahzadeh, M.; Haghghi, B.; Holynska, M.; Tomo, T.; Allakhverdiev, S. I. *Dalton Transactions* **2014**, *43*, 10866.
- (14) Calkins, J. O.; Umasankar, Y.; O'Neill, H.; Ramasamy, R. P. *Energy & Environmental Science* **2013**, *6*, 1891.
- (15) Kim, J. H.; Lee, M.; Lee, J. S.; Park, C. B. *Angew. Chem. Int. Ed.* **2012**, *51*, 517.
- (16) Liang, Y.; Guo, P.; Pingali, S. V.; Pabit, S.; Thiyagarajan, P.; Berland, K. M.; Lynn, D. G. *Chem. Commun.* **2008**, 6522.
- (17) Anthony, N. R.; Mehta, A. K.; Lynn, D. G.; Berland, K. M. *Soft Matter* **2014**, *10*, 4162.
- (18) Zhang, H.; Wang, L.; Jiang, W. *Talanta* **2011**, *85*, 725.
- (19) Dubertret, B.; Calame, M.; Libchaber, A. J. *Nat Biotech* **2001**, *19*, 365.
- (20) Ao, L.; Gao, F.; Pan, B.; He, R.; Cui, D. *Anal. Chem.* **2006**, *78*, 1104.
- (21) Mayilo, S.; Kloster, M. A.; Wunderlich, M.; Lutich, A.; Klar, T. A.; Nichtl, A.; Kürzinger, K.; Stefani, F. D.; Feldmann, J. *Nano Lett.* **2009**, *9*, 4558.
- (22) Childers, W. S.; Ni, R.; Mehta, A. K.; Lynn, D. G. *Curr. Opin. Chem. Biol.* **2009**, *13*, 652.
- (23) Salah, M.; Samy, N.; Fadel, M. *J Drugs Dermatol* **2009**, *8*, 42.
- (24) João P. Tardivo, A. D. G., Luis H. Paschoal, and Dr. Mauricio S. Baptista *Photomedicine and Laser Surgery* **2006**, *24(4)*, 528.
- (25) Papin, J. F.; Floyd, R. A.; Dittmer, D. P. *Antiviral Res.* **2005**, *68*, 84.
- (26) Rodger, A.; Marrington, R.; Geeves, M. A.; Hicks, M.; de Alwis, L.; Halsall, D. J.; Dafforn, T. R. *PCCP* **2006**, *8*, 3161.

- (27) Childers, W. S.; Mehta, A. K.; Lu, K.; Lynn, D. G. *J. Am. Chem. Soc.* **2009**, *131*, 10165.
- (28) Dafforn, T. R.; Rajendra, J.; Halsall, D. J.; Serpell, L. C.; Rodger, A. *Biophys. J.* **2004**, *86*, 404.
- (29) Lakowicz, J. R. *Principles of Fluorescence Spectroscopy*, 3rd Ed ed.; Springer: New York, 2006.
- (30) Valeur, B. *Molecular Fluorescence: Principles and Applications*; 2nd Ed ed.; Wiley-VCH: Weinheim, 2012.
- (31) Hink, M.; Visser, N.; Borst, J.; van Hoek, A.; Visser, A. W. G. *Journal of Fluorescence* **2003**, *13*, 185.
- (32) Visser, A. J. W. G. Available online: <http://www.photobiology.info/Experiments/Biolum-Expt.html>.
- (33) Instrumentation, I. Available online: <http://www.iss.com/resources/pdf/datatables/LifetimeDataFluorophores.pdf>, Lifetime Data of Selected Fluorophores
- (34) Croce, R.; van Amerongen, H. *Nat Chem Biol* **2014**, *10*, 492.
- (35) Carapellucci, P. A.; Mauzerall, D. *Ann. N.Y. Acad. Sci.* **1975**, *244*, 214.
- (36) Panda, M. K.; Ladomenou, K.; Coutsolelos, A. G. *Coord. Chem. Rev.* **2012**, *256*, 2601.
- (37) Hayashi, T.; Ogoshi, H. *Chem. Soc. Rev.* **1997**, *26*, 355.
- (38) El-Khouly, M. E.; Ito, O.; Smith, P. M.; D'Souza, F. *Journal of Photochemistry and Photobiology C: Photochemistry Reviews* **2004**, *5*, 79.
- (39) D'Souza, F.; Ito, O. *Coord. Chem. Rev.* **2005**, *249*, 1410.
- (40) Guldi, D. M. *Chem. Soc. Rev.* **2002**, *31*, 22.
- (41) Seixas de Melo, J.; Sobral, A. J. F. N.; Gonsalves, A. M. d. A. R.; Burrows, H. D. *J. Photochem. Photobiol. A: Chem.* **2005**, *172*, 151.
- (42) Rougee, M.; Ebbessen, T.; Ghetti, F.; Bensasson, R. V. *The Journal of Physical Chemistry* **1982**, *86*, 4404.
- (43) Togashi, D. M.; Costa, S. M. B. *New J. Chem.* **2002**, *26*, 1774.
- (44) Miller, D. S.; McLendon, G. *J. Am. Chem. Soc.* **1981**, *103*, 6791.
- (45) Kathiravan, A.; Raghavendra, V.; Ashok Kumar, R.; Ramamurthy, P. *Dyes and Pigments* **2013**, *96*, 196.
- (46) Harada, A.; Yamaguchi, H.; Okamoto, K.; Fukushima, H.; Shiotsuki, K.; Kamachi, M. *Photochem. Photobiol.* **1999**, *70*, 298.
- (47) Kathiravan, A. *Synth. Met.* **2014**, *194*, 77.
- (48) Marrington, R.; Dafforn, T. R.; Halsall, D. J.; MacDonald, J. I.; Hicks, M.; Rodger, A. *Analyst* **2005**, *130*, 1608.

Chapter 5 Assembly of Lipid-Peptide Chimeras

Introduction

Nature's phospholipids are known to self-assemble spontaneously into supramolecular structures with diverse morphologies and achieve remarkable long-range order in aqueous environments. Lipid molecules contain both polar and apolar elements and such amphiphilicity is one of their main driving forces for self-assembly in aqueous environment.

Similar to spontaneous self-assembled phospholipids, other amphiphiles including single chain surfactants, peptides and proteins can achieve long-range order in aqueous solution. Simple amphiphilic peptides composed of alternating hydrophobic and hydrophilic residues assemble into "membrane-like" β -sheet bilayers by effectively sequester hydrophobic faces. Diverse morphologies including fibers, tubes, ribbons and vesicles, reminiscent of lipid surfactants, can be assembled from four to 20 residue peptides. The nucleating core of the A β peptide of the Alzheimer's disease was known to organize into bilayer architectures with dimensions similar to biological membranes. Although the dynamics of the hydrogen-bonded peptides are certainly different from the flexible alkanes of the lipid membranes, the plasticity of laminate packing and their potential to respond dynamically to environmental fluctuations suggested peptide membranes have organizing potential.

Intense research has focused on incorporation functionality into amphiphilic peptides. Apart from all amino-acid peptide amphiphiles, peptides containing non-amino acid hydrophobic elements, including one or more long alkyl chains, are known as lipid-peptide amphiphile or lipid-peptide chimera. Specifically, N-terminally alkylated peptides are commonly seen in nature such as the marine siderophores¹ and peptaibols². Protein-lipid interactions are often seen in membrane protein anchoring and reconstruction^{3,4} too. The Fields⁵ and Tirrell⁶ labs have investigated monoalkylated peptides and found that alkyl chains elevate thermal stability of the original peptide structures and induce novel helical structures, which the peptides would not form otherwise. Stupp et, al have designed amphiphiles built up from four different segments: hydrophobic tail, beta-sheet forming segment, charged head groups and bioactive epitope⁷. Their amphiphiles self-assemble into high-aspect-ratio cylindrical nanofibers under specific solution conditions (controlled pH, ionic strength, and temperature). They

have proposed the combined effect of intermolecular hydrogen bonding among the peptide segments and hydrophobic collapse of alkyl tails⁸. The incorporation of bioactive elements has made the nanostructures of great interest in tissue engineering and drug delivery applications. Other groups have taken advantage of lipid-peptide amphiphiles to anchor the peptides into membranes to expose the peptides as receptors for proteins, sugars and metal ions.^{9,10} In all these examples, lipid hydrophobic collapse dominates the assemblies to form worm-like micelles. Recently, Lynn and coworkers demonstrated that A β peptides, not lipid alkanes, dominate self-assembly of lipid-peptide chimeras. Covalently coupling various length alkyl chains to the N-terminus of the amphiphilic nucleating core of the Alzheimer's disease peptide---A β (16-22), K¹⁶LVFFAE²²-NH₂ form ribbons, fibers and nanotubes¹¹. Among them, N-lauroyl-A β (16-22) (C12-KLVFFAE) (Figure 5-1) was selected to be characterized thoroughly. Transmission electron microscopy and high-resolution cryo-SEM¹² had shown that C12-KLVFFAE self-assemble as homogeneous nanotubes with slightly larger diameters of 56 \pm 8 nm (Figure 5-1) compared to 52 \pm 5 nm of the C2-KLVFFAE tubes. Further powder X-ray diffraction revealed similar anti-parallel out-of-register cross- β structures with increased lamination distances from 9.8 \AA to 11.5 \AA . REDOR NMR ¹³C-¹⁵N distance measurements managed to distinguish between extended and bent lauroyl chains. The REDOR NMR fittings restrict the chain within the laminated β -sheets consistent with the ω -CH₃ placed within the laminate groves¹².

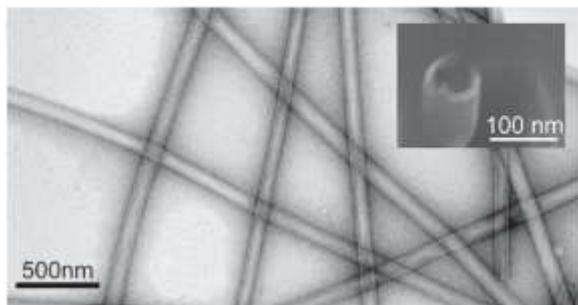
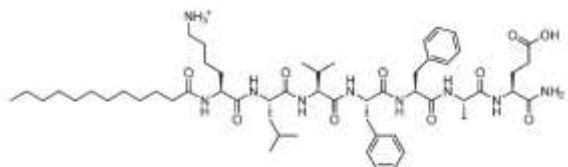


Figure 5-1 Structure of N-lauroyl-Ab(16-22) (top) and TEM, cryo-SEM (inset) (bottom) of 1.2 mm N-lauroyl-Ab(16-22) assembled in 40% acetonitrile/water with 0.1% trifluoroacetic acid for 1–2 weeks. Adapted from Ni, R. et. al. *Angew. Chem.* 2012 with permission from John Wiley and Sons.

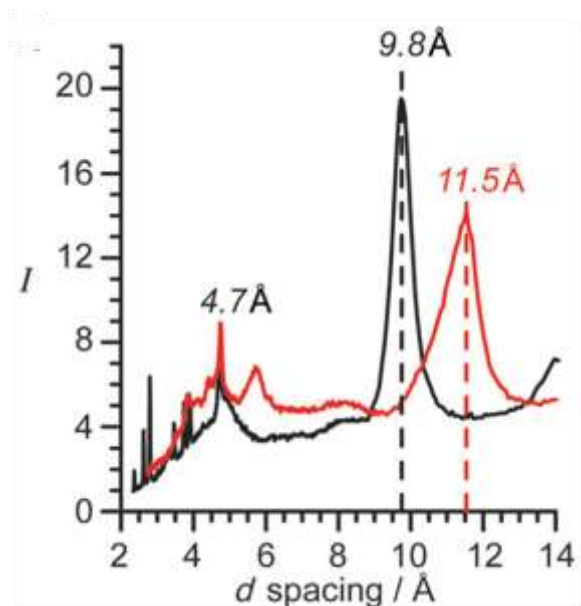


Figure 5-2 Powder and oriented electron diffraction of N-acyl-Ab(16-22) peptide assemblies. a) X-ray powder diffraction of N-lauroyl-Ab(16-22) (red) and N-acetyl-Ab(16-22) tubes (black), indicating that each has a 4.7 Å H-bonding d spacing but differ in lamination d spacing (9.8 Å vs. 11.5 Å). Adapted from Ni, R. et. al. *Angew. Chem.* 2012 with permission from John Wiley and Sons.

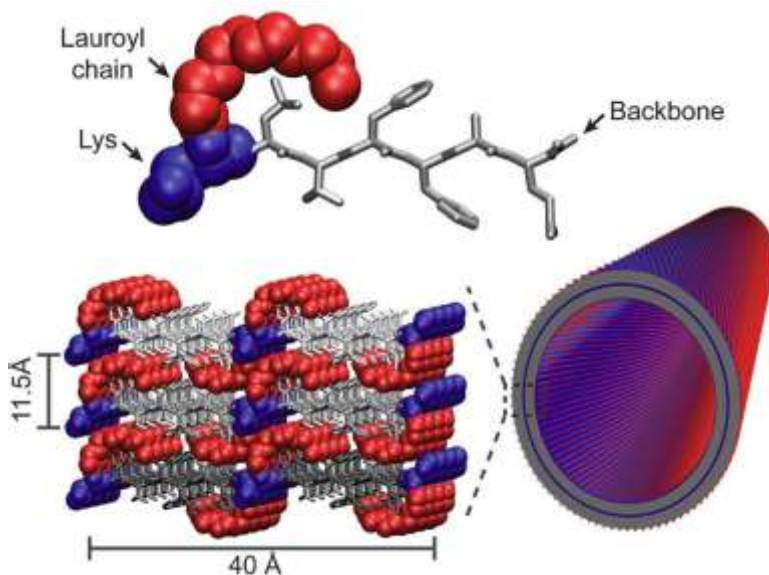


Figure 5-3 Model of lauryl chain packing (red) within β -sheet laminates. Position of lysine residues are colored blue, β -sheet backbone shown as grey pleats. Adapted from Ni, R. et, al. *Angew. Chem.* 2012 with permission from John Wiley and Sons.

The hybrid architecture model highlights the interactions between alkane and the peptide. This “accordion like” expansion of the laminate packing to accommodate lipid chains suggests that peptide membranes could display dynamic properties and respond dynamically to environmental fluctuations. The most interesting discovery is the unexpected plasticity of the cross- β fold to accommodate acyl chains within the stacks of the β -sheet laminate. However, the plasticity of these structures is unknown. The occupancy of the cavity by shorter C5 to C10 chains¹¹ seem not sufficient to make thermodynamically stable assemblies, while longer acyl chains give what appears to be more heterogeneous assemblies. Lipid-peptide chimera is a promising area for exploring molecular interactions within a heterogeneous complex system and could another powerful strategy for generating asymmetry apart from coassembly of peptides.

In my attempts to better understand the interplay between lipids and peptides in lipid-peptide chimeras, the dynamic of cross- β fold plasticity was explored using conformationally more constrained unsaturated lipid chains. Along with the discovery of stabilization effects of lipid chains on assembled peptides, the peptides elements were changed to unassembled ones to test the limits of stabilizing effects of lipid chains. At last, lipid-peptide chimeras were allowed to cross-seed or coassemble with peptides as initial studies for molecular interactions within complex environments.

Results

Accommodating Unsaturated Lipid Chains within A β Peptide Membranes

Membrane phospholipids are fatty acids with varying lengths and degrees of saturation to adjust fluidity of the membrane with different packing arrangements¹³. Unsaturated chain disrupts packing by putting kinks into otherwise straight hydrocarbon chain and consequences lower melting points.

To further evaluate dynamic properties of lipid-peptide chimeras, one double bond was placed at positions 2, 5 and 11 with trans and cis conformations of a 12-carbon alkyl chain and attached to the N-terminal of A β (16-22), K¹⁶LVFFAE²²-NH₂ peptide. They're named as C12:1 (cis-5)-KLVFFAE, C12:1 (trans-5)-KLVFFAE, C12:1 (cis-2)-KLVFFAE, C12:1 (trans-2)-KLVFFAE and C12:1 (11)-KLVFFAE, with (C12:1) refers to 12-carbon chain and 1 degree of unsaturation following unsaturated phospholipids nomenclature (Figure 5-4). Among all five unsaturated lipid-peptide chimeras, C12:1 (trans-2)-KLVFFAE and C12:1 (11)-KLVFFAE have almost identical conformation with the C12-KLVFFAE. C12:1 (cis-5)-KLVFFAE, C12:1 (trans-5)-KLVFFAE and C12:1 (cis-2)-KLVFFAE exhibit more constrained conformations.

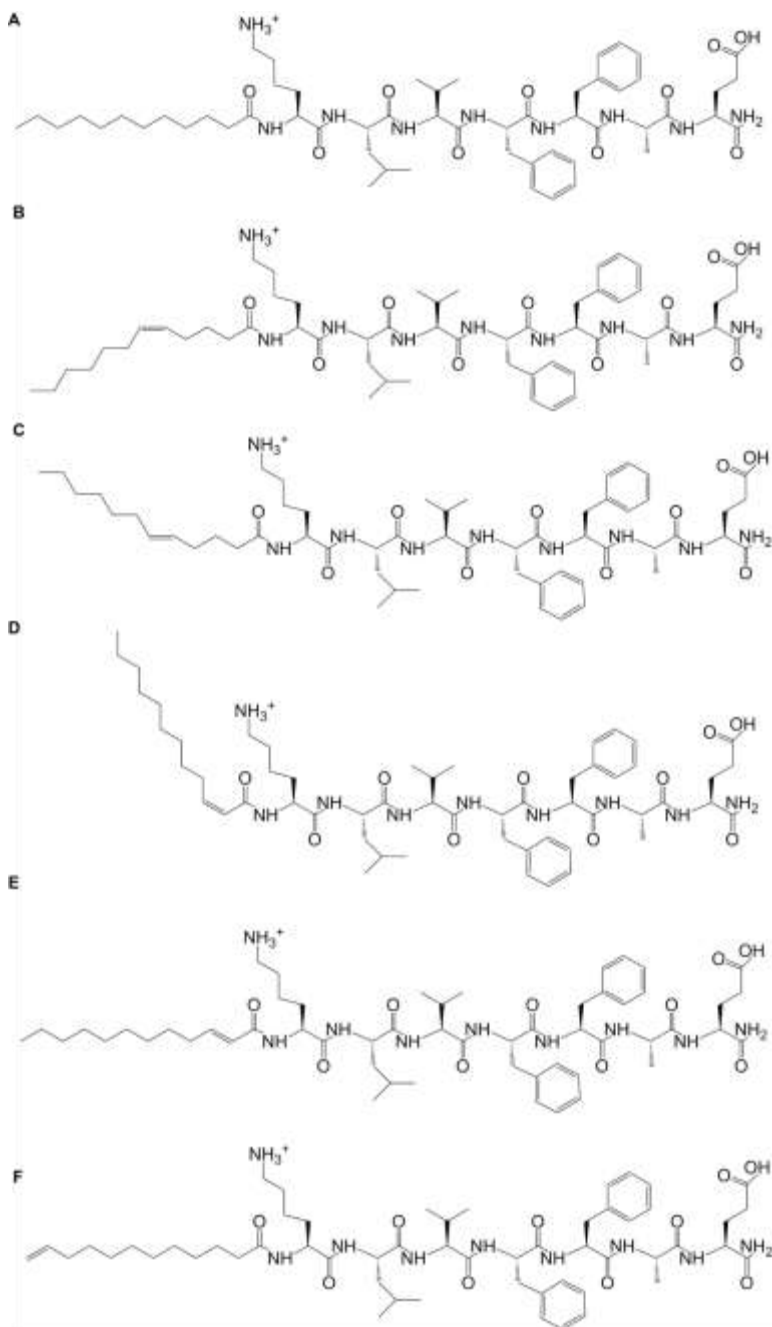


Figure 5-4 Molecular structure of (A) C12-KLVFFAE, (B) C12:1 (cis-5)-KLVFFAE, (C) C12:1 (trans-5)-KLVFFAE, (D) C12:1 (cis-2)-KLVFFAE, (E) C12:1 (trans-2)-KLVFFAE and (F) C12:1 (11)-KLVFFAE

The MMFFs force field was used to construct a family of structures within 19kJ/mol of lowest energy structure of macromodel conformational search. Three anti-parallel out-of-register peptides, consistent with previous isotope-edited IR results were constructed in the search with a protonated glutamic acid side chain. The N-lauroyl or N-dodecenoyl groups were attached to only the middle chain to approximate an infinitely long- β sheet.

All atoms except for the lysine attached to the lauroyl or dodecenoyl chain and the lauroyl and dodecenoyl chain were frozen. No distance restraints were used, yet all C12-KLVFFAE structures had lauroyl chain carbonyl carbon distance of $3.7\text{\AA}\pm 0.3\text{\AA}$ from the leucine nitrogen. All other C12:1-KLVFFAE structures showed similar lauroyl chain carbonyl carbon distances to the peptide backbone leucine nitrogen despite different positions of double bonds. For reference, a fully extended chain, analogous with the worm-like micelle model, would have a lauroyl carbonyl carbon distance to the leucine nitrogen of 4.5\AA .

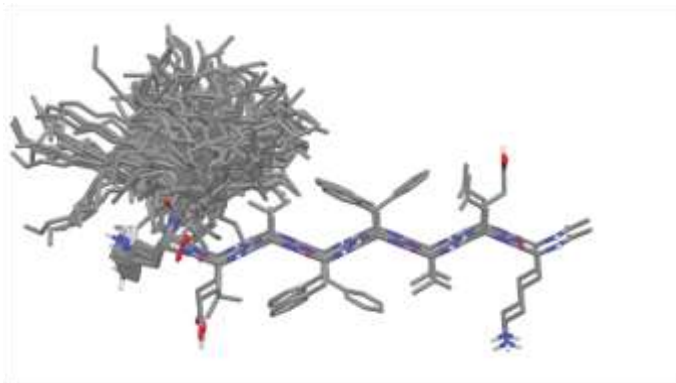


Figure 5-5 Family of structures within 19kJ/mol of lowest energy structure of macromodel conformational search using the MMFFs force field, for C12-KLVFFAE peptides.

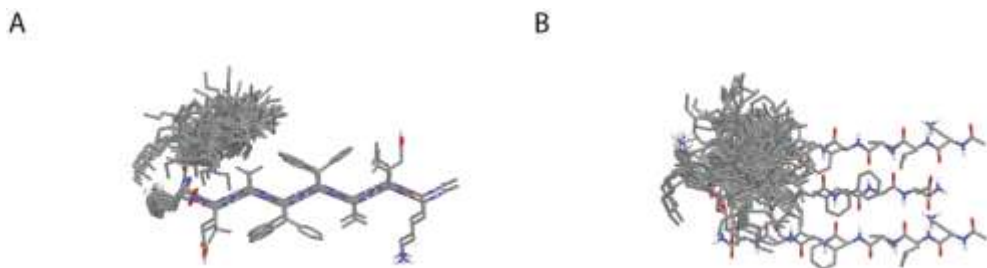


Figure 5-6 Family of structures within 19kJ/mol of lowest energy structure of macromodel conformational search using the MMFFs force field, for C12:1 (cis-5)-KLVFFAE peptides. (A) Side view and (B) top view.

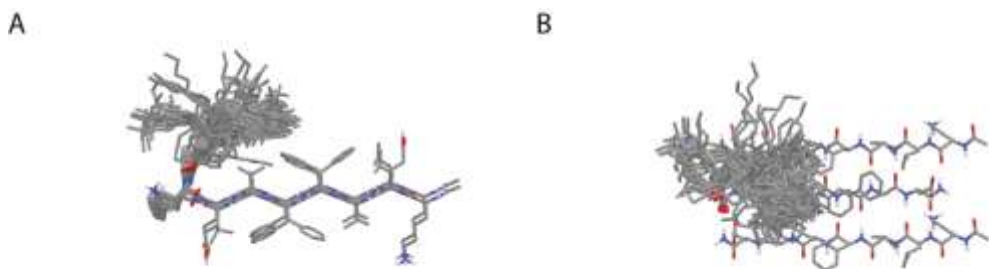


Figure 5-7 Family of structures within 19kJ/mol of lowest energy structure of macromodel conformational search using the MMFFs force field, for C12:1 (trans-5)-KLVFFAE peptides. (A) Side view and (B) top view.

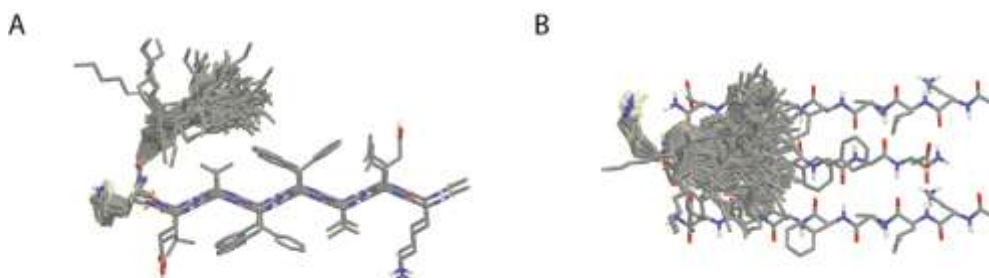


Figure 5-8 Family of structures within 19kJ/mol of lowest energy structure of macromodel conformational search using the MMFFs force field, for C12:1 (cis-2)-KLVFFAE peptides. (A) Side view and (B) top view.

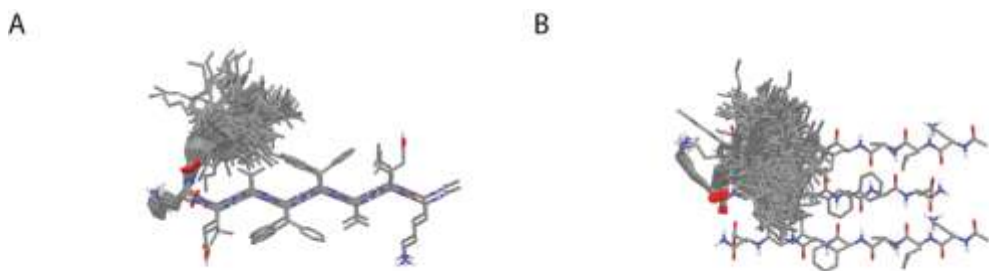


Figure 5-9 Family of structures within 19kJ/mol of lowest energy structure of macromodel conformational search using the MMFFs force field, for C12:1 (trans-2)-KLVFFAE peptides. (A) Side view and (B) top view.

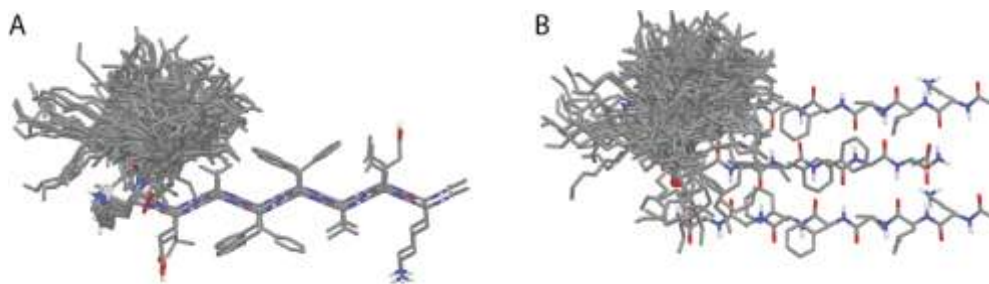


Figure 5-10 Family of structures within 19kJ/mol of lowest energy structure of macromodel conformational search using the MMFFs force field, for C12:1 (11)-KLVFFAE peptides. (A) Side view and (B) top view.

Molecular modeling discovered that saturated and unsaturated lipid cross- β peptide chimeras seem to adopt the same molecular packing strategy by bending the lipid chains in the interior of β -sheets laminates. The cross- β fold possesses remarkable potential in structural plasticity.

Self-assembly and Structural Characterization of Lipid-Peptide Chimeras

To experimentally test the self-assembly of unsaturated lipid-peptide chimeras, *cis*-5-dodecenoic acid was synthetically coupled to the N-terminal of uncapped-KLVFFAE peptide to give the C12:1(*cis*-5)-KLVFFAE chimera. C12:1 (*cis*-5)-KLVFFAE was chosen because its conformation is among those different from C12-KLVFFAE in molecular modeling studies. 1mM C2-KLVFFAE, C12-KLVFFAE and C12:1(*cis*-5)-KLVFFAE amphiphiles were allowed to self-assemble in 40% acetonitrile/water + 0.1% TFA pH2. They all displayed positive maximum ellipticity at 197nm and negative maximum at 217nm by Circular Dichroism (Figure 5-11) after 1-2 weeks incubation at 4°C. While all of their CD spectra features are consistent with known β -sheet secondary structures, their ellipticities were different. C2-KLVFFAE has the highest ellipticity, followed by C12-KLVFFAE and C12:1(*cis*-5)-KLVFFAE displayed the lowest among the three. Ellipticity at 215 nm of C2-KLVFFAE assemblies is 4 and 14 times of C12-KLVFFAE and C12:1(*cis*-5)-KLVFFAE assemblies, respectively. These differences in ellipticity could be both a function of the degree of assembly, and/or the nature of the structures.

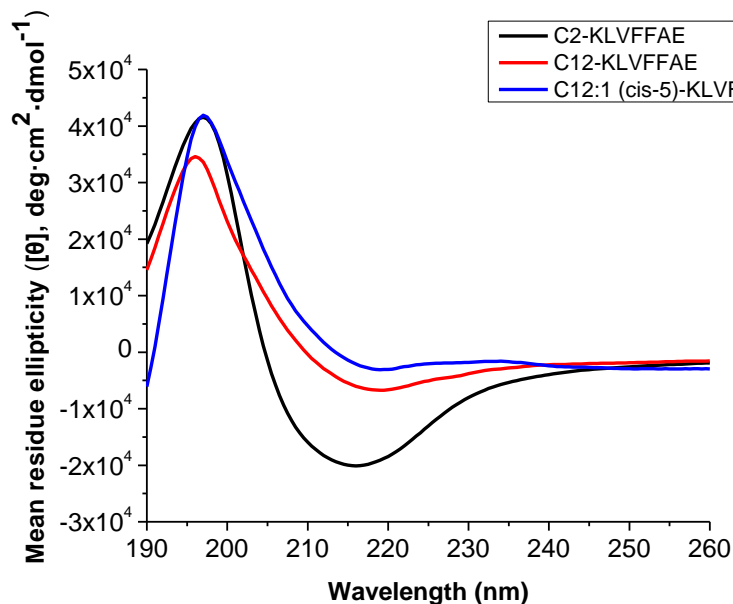


Figure 5-11 Circular dichroism of 1mM C2-KLVFFAE (black), C12-KLVFFAE (red) and C12:1 (cis-5)-KLVFFAE (blue) assemblies in 40% MeCN/H₂O, 0.1% TFA, pH2

Transmission electron microscopy revealed that all three amphiphiles self-assemble into homogeneous nanotubes (Figure 5-12). C2-KLVFFAE and C12-KLVFFAE have similar diameters of 48.2 ± 4.1 nm and 51.5 ± 9.6 nm, consistent with previous analyses¹². However, C12:1 (cis-5)-KLVFFAE self-assembled into significantly larger nanotubes with an estimated diameter of 81.7 ± 10.1 nm. In addition, C2-KLVFFAE is the most homogeneous assembly (± 6.5 nm) while C12-KLVFFAE and C12:1 (cis-5)-KLVFFAE have more dispersed distribution of tube width (± 12 nm and 12.7 nm). Higher homogeneity of C2-KLVFFAE may contribute for its higher ellipticity (Figure 5-11).

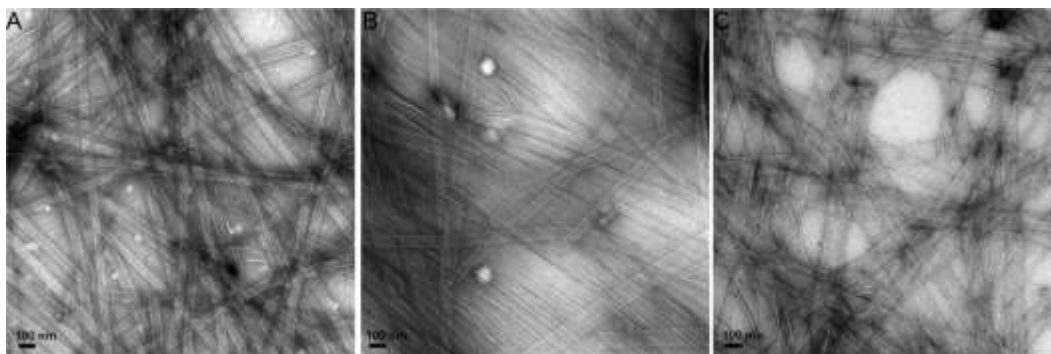


Figure 5-12 TEM micrographs of (A) C2-KLVFFAE, (B) C12-KLVFFAE and (C) C12:1 (cis-5)-KLVFFAE self-assembled as homogeneous nanotubes in 40%MeCN/H₂O, 0.1% TFA, pH2

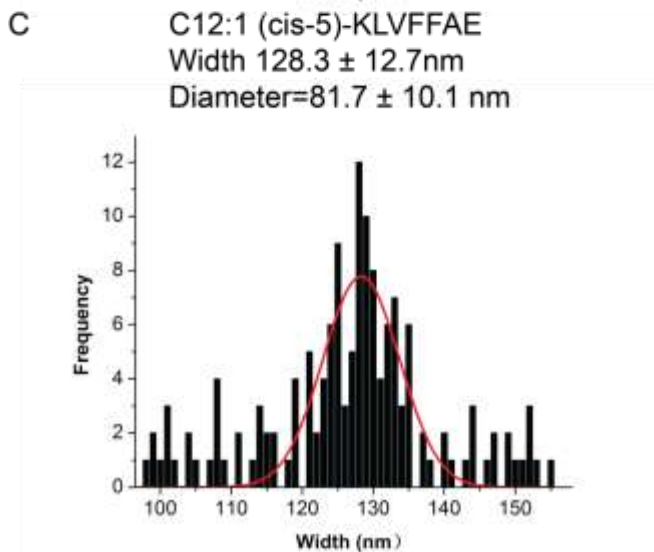
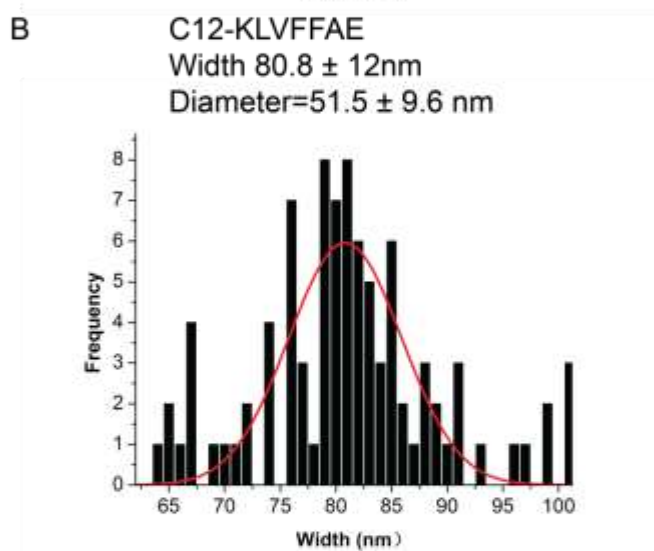
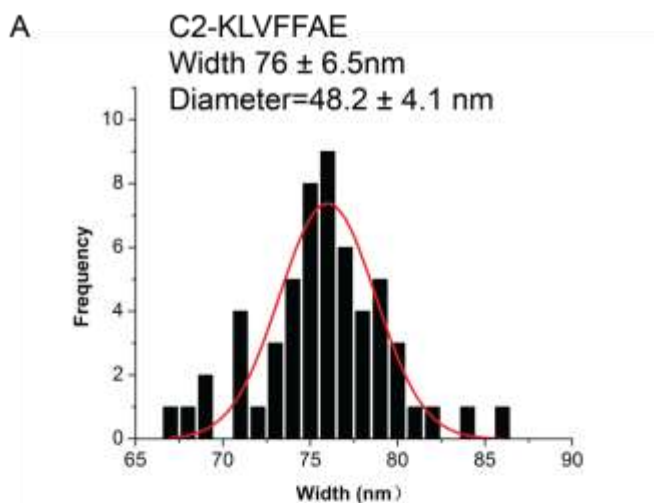


Figure 5-13 Nanotube widths distribution of A) C2-KLVFFAE, B) C12-KLVFFAE and C) C12:1(cis-5)-KLVFFAE. 50-100 tube widths measurements were taken with an average of 3 measurements on

each single tube at different positions. The frequency was plotted against widths and fit to Gaussian distributions and the diameters were estimated as $\text{width} \times 2/\pi$

Powder X-ray diffraction (XRD) reflections on C12:1 (cis-5)-KLVFFAE showed d-spacing of 4.7 Å and 11.6 Å (Figure 5-14), corresponding to hydrogen-bonded β -strands and laminations between β -sheets respectively. The lamination distance is similar to that of C12-KLVFFAE¹² and larger than C2-KLVFFAE¹⁴, consistent with molecular modeling of N-dodecenoyl chains being incorporated within β -sheets laminations (Figure 5-6). The molecular model for C2-KLVFFAE, C12-KLVFFAE/C12:1(cis-5)-KLVFFAE were shown in Figure 5-15.

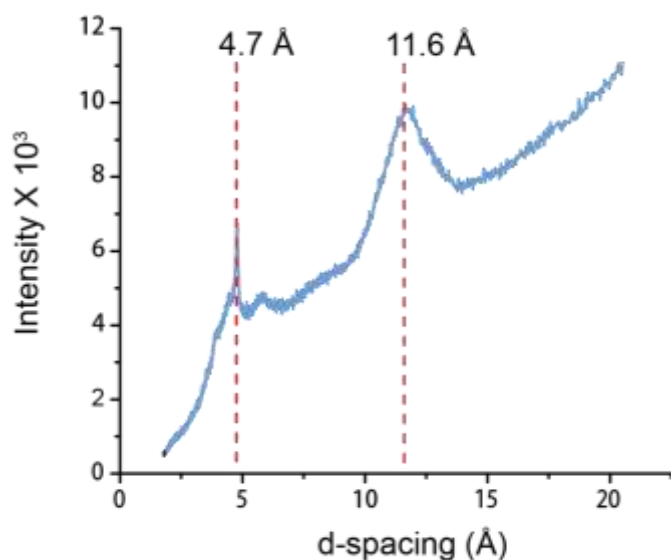


Figure 5-14 Powder X-ray diffraction of C12:1 (cis-5)-KLVFFAE showing reflections at d-spacings of 4.7 Å and 10.6 Å

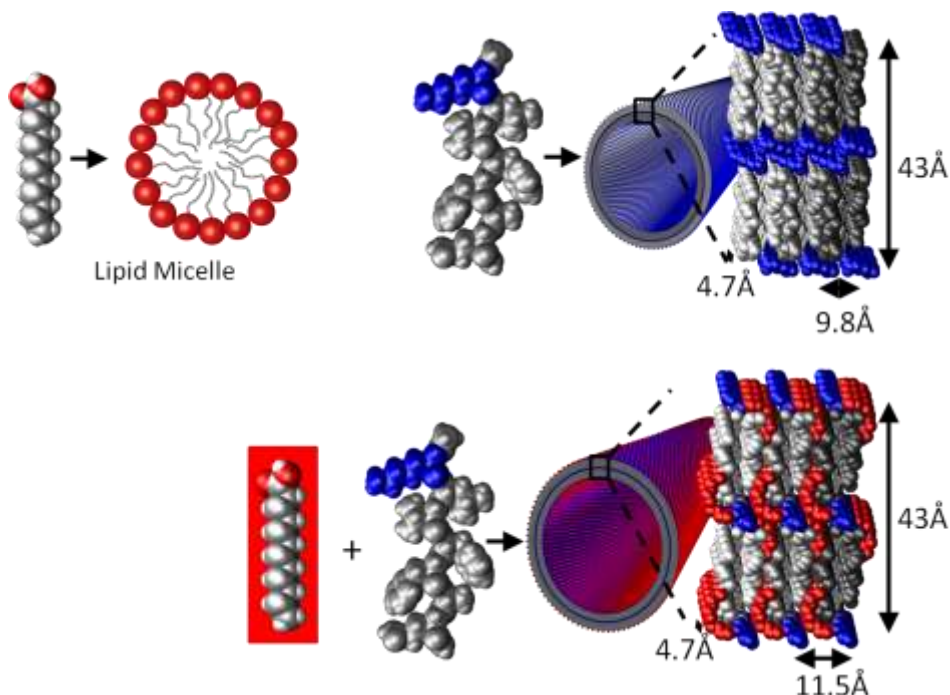


Figure 5-15 Cartoon model of C2-KLVFFAE (top) and C12-KLVFFAE, C12:1(cis-5)-KLVFFAE (bottom) nanotubes. Lipid polar heads are shown in red, positively-charged lysine residues are shown in blue. Nonpolar N-lauryol or N-dodecenoyl tails and non-charged rest of the peptide residues are shown in grey

Thermal Studies of Lipid-Peptide Chimeras

Each of the mature lipid-peptide assemblies gives significant circular dichroism (CD) with ellipticity minimum at 215 nm (Figure 5-11), a transition diagnostic of β -strands. The ellipticity was monitored as temperature increases. The CD melting profiles (Figure 5-16) was fit to the sigmoidal form of the Boltzmann equation (eq 1), a melting temperature, T_m , and the slope k . Each assembly displayed a cooperative melt on heating.

$$\theta \propto \left(1 + \exp \left\{ \frac{T_m - T}{k} \right\} \right)^{-1} \quad (1)$$

T_m of C2-KLVFFAE is 48.6 ± 8 C, consistent with previous analyses¹⁵. C12-KLVFFAE and C12:1(cis-5)-KLVFFAE melted at $55.5 \pm 8.3^\circ\text{C}$ and $51.4 \pm 7.7^\circ\text{C}$ respectively. Lipid-peptide chimeras melted at higher temperatures than the peptide assemblies, revealed a stabilizing effect of hydrophobic alkyl chains, which is very likely resulted from more stable hydrophobic collapses.

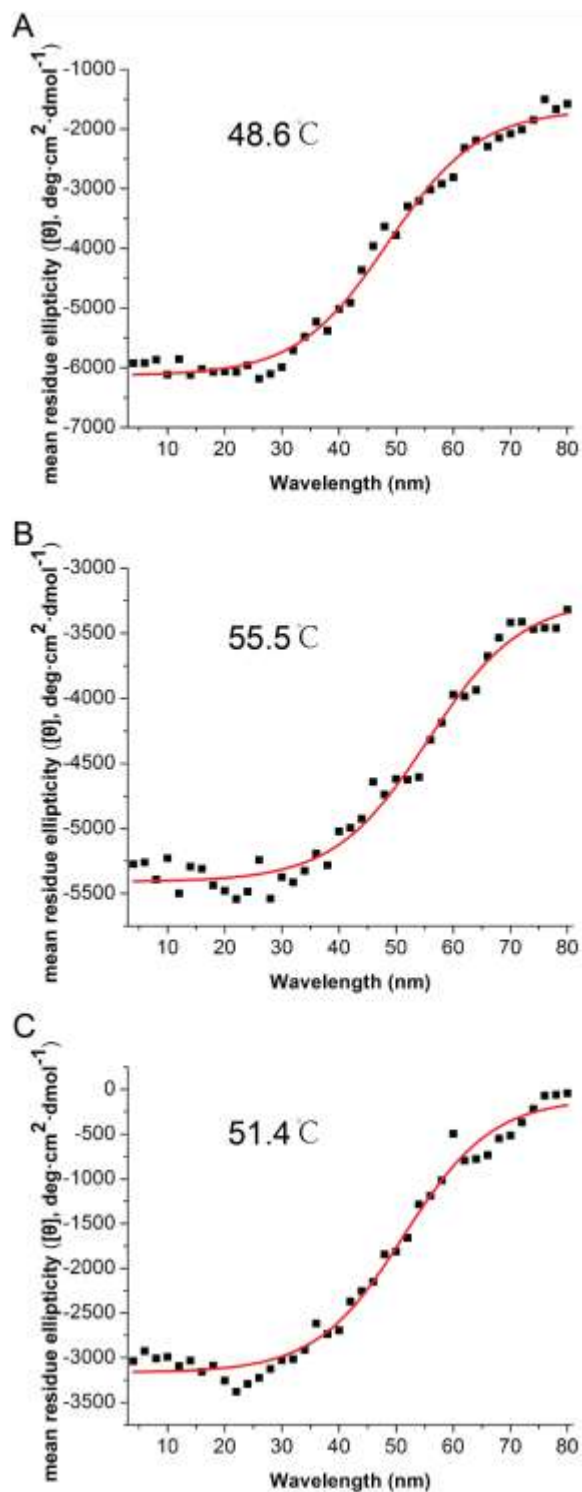


Figure 5-16 Melting profiles for (A) C2-KLVFFAE with T_m 48.6 °C; (B) C12-KLVFFAE with T_m 55.5 °C; (C) C12:1(cis-5)-KLVFFAE T_m 51.4 °C. Fitting equations are $y = -1671.6 + (-6131.8 + 1671.6)/(1 + \exp((T - 48.6)/8))$, $y = -3233 + (-5410.5 + 3233)/(1 + \exp((T - 55.5)/8.3))$ and $y = -102.7 + (-3165.6 + 102.7)/(1 + \exp((T - 51.4)/7.7))$

Surfactant molecules can display complex phase behavior when dispersed as a liquid colloid in aqueous environments.¹⁶ The condition for C2-KLVFFAE nanotube assembly has been optimized in 40% acetonitrile acidified with trifluoroacetic acid (TFA), and subtle changes to these conditions induce transitions through different phase barriers. To investigate the temperature dependence of the transition barriers, each peptide is solubilized in 40% acetonitrile containing 0.1% TFA and split into three equal aliquots to incubate at 4 °C, 37°C or 55 °C until thermodynamic equilibrium is achieved by CD (Figure 5-17). All assemblies exhibited maximum ellipticity at 215 nm at 4°C. C12-KLVFFAE and C12:1(cis-5)-KLVFFAE's β -structure ellipticities maintained stable when temperature is elevated to 37 °C, whereas ellipticity of C2-KLVFFAE at 37 °C decreased by 10% of the 4°C nanotubes, consistent with minimum paracrystalline structures (Figure 5-17) . TEM micrographs demonstrated that spherical particle structures were found at 37 and 55 °C in C2-KLVFFAE (Figure 5-18). High temperature clearly inhibits the propagation of any preformed aggregates into nanotubes for C2-KLVFFAE. With the addition of alkyl chains, C12-KLVFFAE and C12:1(cis-5)-KLVFFAE nanotubes had higher thermal stability and stayed as nanotubes when assembled at 37 °C. At 55 °C, At 55 °C, no ellipticity was apparent for all assemblies and they all failed to assemble into paracrystalline ordered structures (Figure 5-19).

Thermal studies show that lipid-peptide chimeras have higher thermal stability than peptides. When temperature is raised above melting temperature, peptides tend to undertake phase transitions from nanotubes to particles, while lipid-peptide chimeras seem to disassemble.

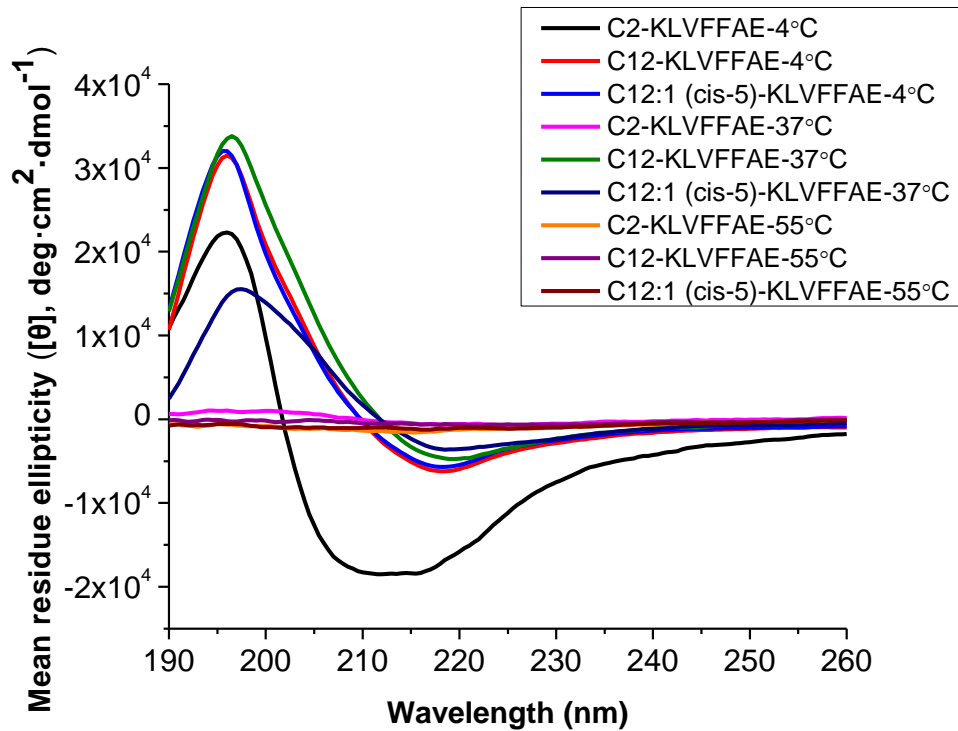


Figure 5-17 Circular Dichroism of C2-KLVFFAE, C12-KLVFFAE and C12:1(cis-5)-KLVFFAE assembled from monomer under 4, 37 or 55 °C respectively for a week

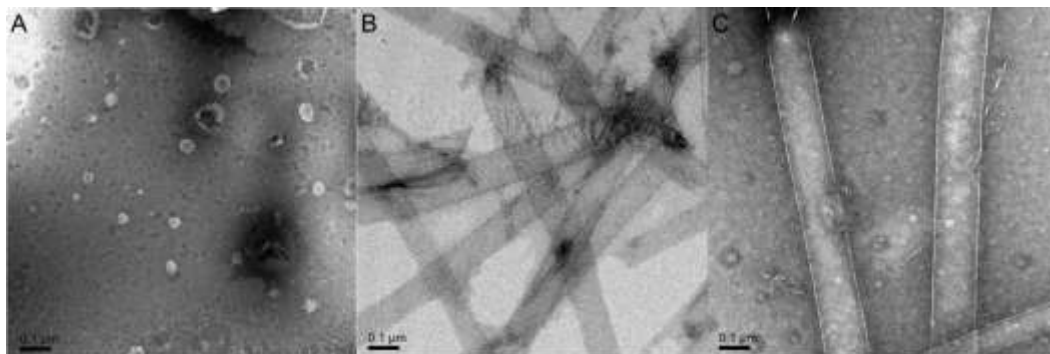


Figure 5-18 TEM micrographs of (A) C2-KLVFFAE assembled as particles (B) C12-KLVFFAE assembled as nanotubes and (C) C12:1(cis-5)-KLVFFAE assembled as nanotubes at 37 °C

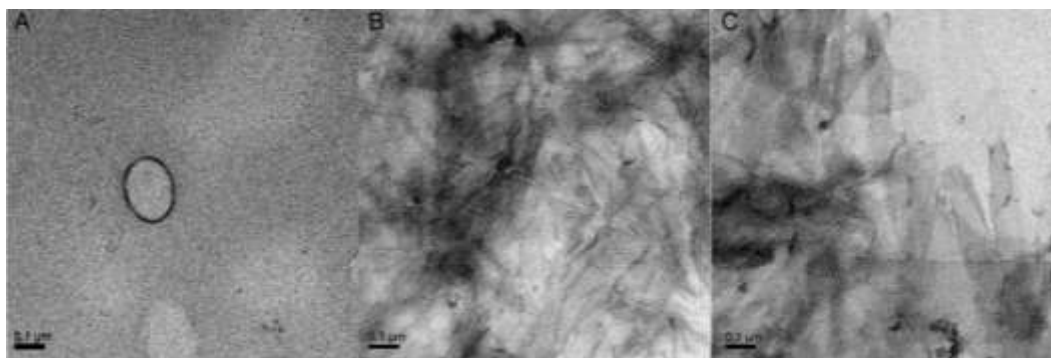


Figure 5-19 TEM micrographs of (A) C2-KLVFFAE assembled as particles, (B) C12-KLVFFAE with no ordered assemblies and (C) C12:1(cis-5)-KLVFFAE with no ordered assemblies at 55 °C

To further confirm the spherical particles are transitioned through phase barriers, matured nanotubes were formed first at 4 °C and spun down to be resuspended in fresh solvents. The new solutions were reincubated at 37 °C for 3 days. Spherical particles were seen again in C2-KLVFFAE assemblies, confirmed that the particles can be transformed from nanotubes (Figure 5-20). C12-KLVFFAE and C12:1(cis-5)-KLVFFAE stayed stable as nanotubes under same temperature transitions.

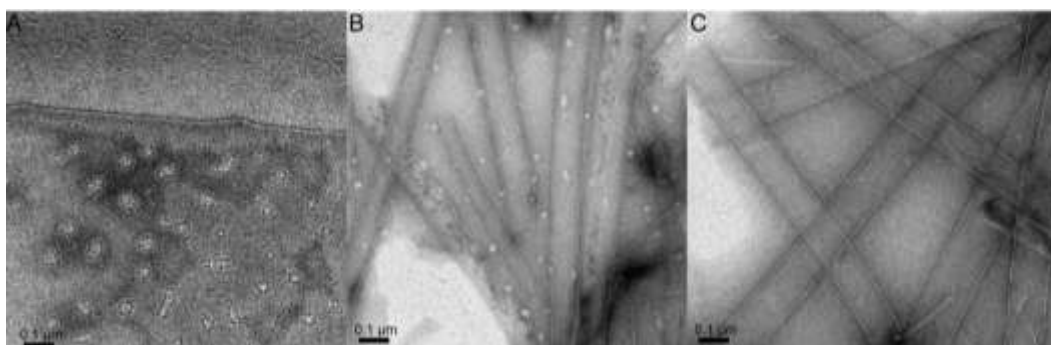


Figure 5-20 TEM micrographs of mature nanotubes formed at 4°C and reincubated at 37 °C: (A) C2-KLVFFAE transformed from nanotubes to spherical particles, (B) C12-KLVFFAE and (C) C12:1(cis-5)-KLVFFAE stayed as nanotubes

Modulating Conformation and Aggregation Capability of Peptides via Lipidation

The sequence properties of peptide region in the peptide-amphiphiles are critical for the formation of unique assemblies. For example, our lipid-peptide amphiphiles are structurally distinct from the cylindrical fibrils models¹⁷⁻¹⁹ presented by Stupp's lab. The N-terminal palmitoylated peptide used in Stupp's lab contains IKVAV, which can not form a hydrophobic pocket to desolvate alkyl chains. In contrast, the central five hydrophobic residues in A β (16-22) (KLVFFAE) peptide could create a hydrophobic environment to bury alkyl chains. As a result, the lipid-peptide chimera C12-KLVFFAL self-assembles as homogeneous ordered nanotubes with increased lamellations compared to the C2-

KLVFFAE peptide nanotubes. In this section, peptides will be modulated as unstructured assemblies to test how lipidation controls conformation and aggregation capability of the peptides.

Previous MD simulations predicted the aromatic stacking within the Phe-Phe core of A β (16-22) (KLVFFAE), includes edge-to face interactions between F19/F20 in the fibers and F19/F19 and F20/F20 in the tubes, as well as Phe-Phe offset stacked interaction between adjacent strands from different sheets¹⁴. The experimental studies supported this argument when FF dyad in A β (16-22) (KLVFFAE) peptide was replaced with isoleucine (II), tyrosine (YY) and tryptophan (WW) dyad.^{14,20} Under identical assembly conditions, all C2-KLVIIAE, C2-KLVYYAE and C2-KLVWWAE peptides failed to assemble²⁰. It's hypothesized that addition of alkyl chains to these peptides will increase the aggregation capability by both increasing the hydrophobicity and compensating the packing cavity with bulky alkyl chains.

N-lauroyl chains were synthetically coupled to the N-terminal of uncapped-KLVIIAE, -KLVYYAE, and -KLVWWAE peptides to give C12-KLVIIAE, C12-KLVYYAE and C12-KLVWWAE chimeras. 1mM lipid-peptide amphiphiles were allowed to self-assemble in 40% acetonitrile/water with 0.1% TFA (pH2) at 4°C. C2-KLVIIAE, C2-KLVYYAE and C2-KLVWWAE were assembled under the exactly same condition as controls. All of the peptides didn't display obvious β -sheet ellipticity after 3 weeks incubation except that C2-KLVIIAE showed a dispersed peak at 210nm (Figure 5-21). On the opposite, all the lipid-peptide chimeras displayed positive maximum ellipticity at 197nm and negative maximum at 218nm within 1 week, consistent with β -sheet secondary structures (Figure 5-21), supported the hypothesis that lipidation increases the aggregation capability of the peptides.

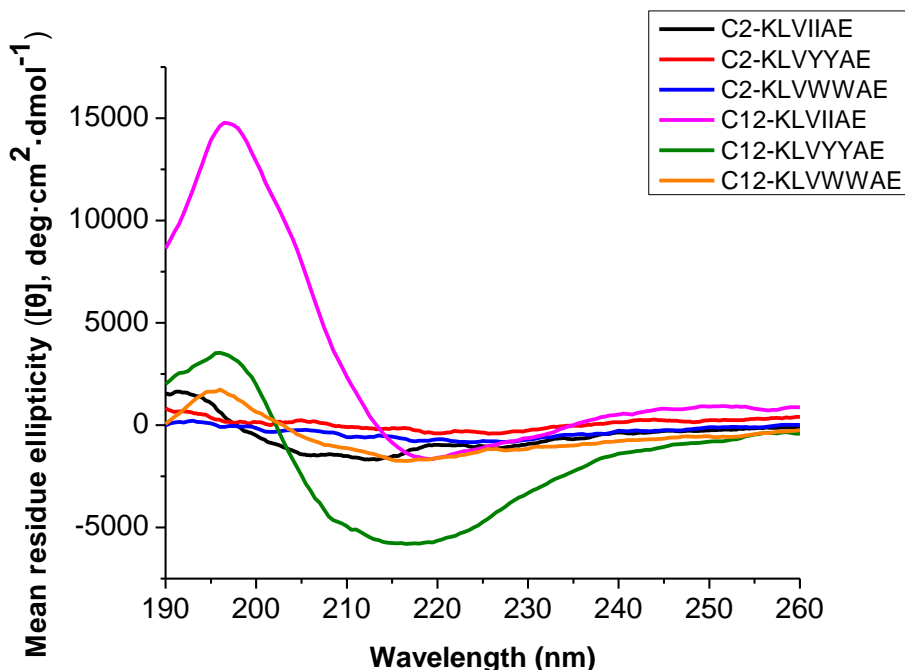


Figure 5-21 Circular dichroism of C2-KLVIIAE (black), C2-KLVYYAE (red) and C2-KLVWWAE (blue). C12-KLVIIAE (magenta), C12-KLVYYAE (green) and C12-KLVWWAE (orange). All lipid-peptide chimeras and peptides were incubated in 40% MeCN/H₂O with 0.1% TFA (pH2) at 4°C

After 3 weeks incubation in 40% MeCN/H₂O, Ac-KLVIIAE formed amorphous filaments (Figure 5-22A), consistent with the broad negative ellipticity (Figure 5-21). With the addition of acyl chain, however, C12-KLVIIAE self-assembled into quite homogeneous nanotubes (Figure 5-22B). The diameter of C12-KLVIIAE nanotubes was estimated as 55.5 ± 7 nm, comparable to that of C12-KLVFFAE nanotubes. The 1mM Ac-KLVYYAE peptide lost the self-assembly ability completely in 40% MeCN/H₂O (Figure 5-22C). Considering the relative less hydrophilicity of Y compared with F, even in water, the YY peptide didn't assemble into twisted fibrils until the concentration was increased to 4 mM²⁰. Nevertheless, C12-KLVYYAE was able to assemble into bundled fibers with an average bundle widths of 10-20nm (Figure 5-22D) within a week of incubation in 40% MeCN/H₂O. Similar to Ac-KLVYYAE, Ac-KLVWWAE peptide didn't manage to assemble in 40% MeCN/H₂O at pH2 (Figure 5-22E). C12-KLVWWAE self-assembled into both fibrils (Figure 2-24F) particles (Figure 5-22G). The fibrils have average widths of 5-10nm. The particles have two sizes of 80.8 ± 21.1 and 177.6 ± 26.2 nm respectively (Figure 5-24), an order of magnitude smaller than the transient intermolecular molten globules reported at room temperature²¹. These results revealed that based on different

molecular geometry, charge distribution and hydrophobic residue sizes of the peptides, lipidation could modulate the conformation of the assemblies.

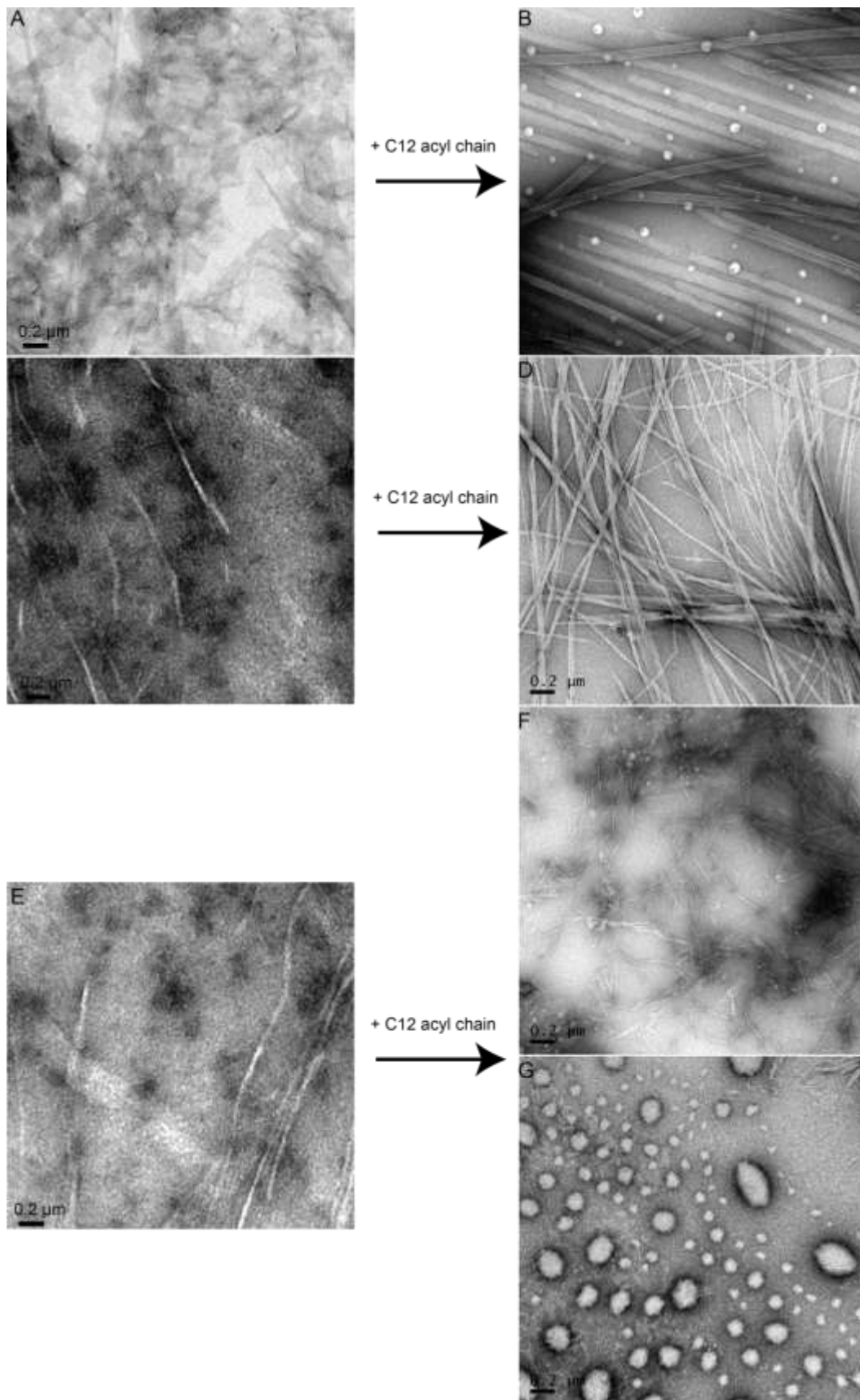


Figure 5-22 TEM micrographs of (A) C2-KLVIIAE; (B) C12-KLVIIAE; (C) Ac-KLVYYAE; (D) C12-KLVYYAE, (E)Ac-KLVWWAE; (F) and (G) C12-KLVWWAE. All lipid-peptide chimeras and peptides were incubated in 40% MeCN/H₂O with 0.1% TFA (pH2) at 4°C

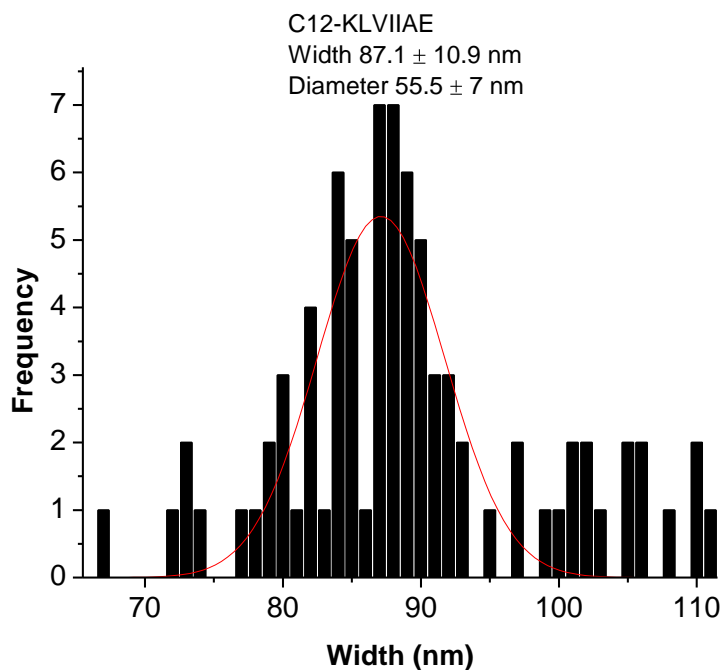


Figure 5-23 Width measurements from TEM images of C12-KLVIIAE. 50-100 tube widths measurements were taken with an average of 3 times measurements on a single tube at different positions. The frequency was plotted against width and fit to Gaussian distribution with a center at 87.1 nm and a distribution width of 10.9nm. The diameter was estimated as $\text{width} \cdot 2/\pi$ as 55.5 ± 7 nm

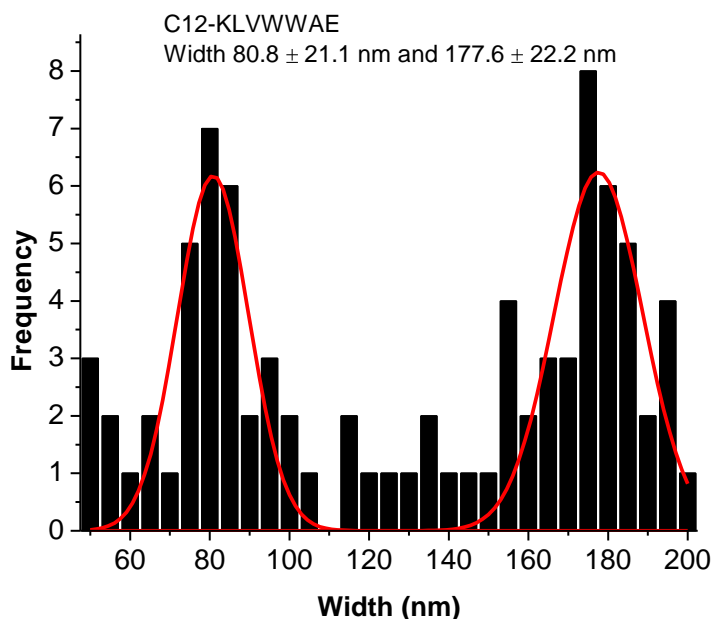


Figure 5-24 Width measurements of particles from TEM images of C12-KLVWWAE. 50-100 particle widths measurements were taken. The frequency was plotted against width and fit to bimodal Gaussian distribution of 80.8 ± 21.1 and 177.6 ± 26.2 nm

X-ray diffraction patterns for C12-KLVIIAE and C12-KLVYYAE showed two sharp, intense diffraction rings at 4.7 and 10.5 Å (Figure 5-25 and 5-26) suggesting the sample polycrystallinity. The 4.7 Å reflection is consistent with the typical β -sheet hydrogen-bonding repetitive structure. The 10.5 Å is consistent with lamination distances. Despite the remarkable morphological differences between nanotubes and fibers, the same cross- β structures are conserved in C12-KLVIIAE and C12-KLVYYAE assemblies.

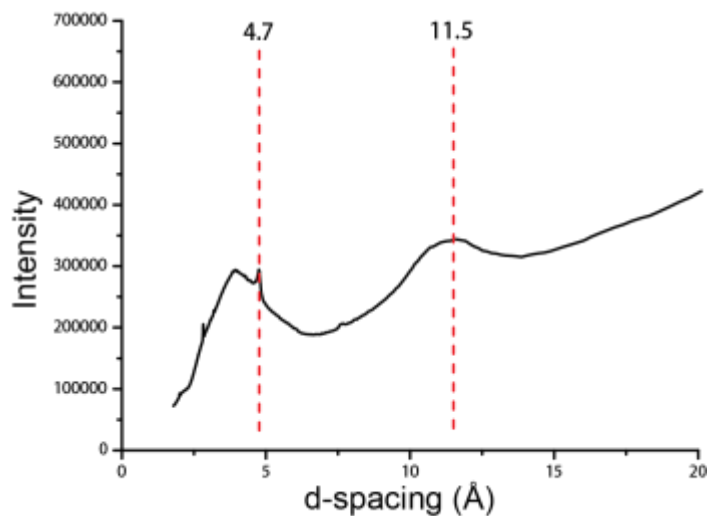


Figure 5-25 Powder X-ray diffraction of C12-KLVIIAE showing reflections at d-spacings of 4.7 Å and 11.5 Å

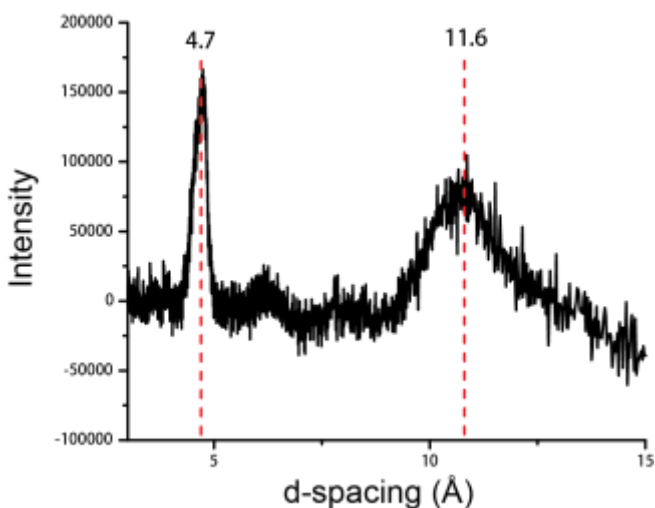


Figure 5-26 Powder X-ray diffraction of C12-KLVYYAE showing reflections at d-spacings of 4.7 Å and 11.6 Å

Next, the charged residue lysine switched from N-terminal to C-terminal and 1) the hydrophobic core LVFFA was reversed to give EAFFVLK or 2) the hydrophobic core LVFFA was maintained the same to give ELVFFAK.

N-lauroyl chain was synthetically coupled to the N-terminal of uncapped-EAFFVLK, ELVFFAK peptides to give C12- EAFFVLK, and C12-ELVFFAK chimeras. 1mM lipid-peptide amphiphiles were allowed to self-assemble in 40% acetonitrile/water with 0.1% TFA (pH2) at 4 °C. C2- EAFFVLK, and C2-ELVFFAK peptides were assembled under

the exactly same condition as controls. Neither peptides (C2-EAFFVLK and C2-ELVFFAK) managed to self-assemble in 40% acetonitrile/water. Instead, C2-ELVFFAK formed nanotubes (~ 130 nm) and thin ribbons and C2 EAFFVLK assembled into twisted fibrils in pH2 water²⁰. Interestingly, upon addition of alkyl chains, both lipid-peptide chimeras achieved strong self-assemble propensity as shown in figure 5-27. C12-EAFFVLK and C12-ELVFFAK exhibited diagnostic β -sheet ellipticity(Figure 5-27). Both CD spectras are more resemblance to β -sheet fibrils instead of β -sheet nanotubes, as β -sheet nanotubes tend to have stronger negative ellipticity peak than the positive ellipticity peak and β -sheet fibrils usually have similar ellipticity intensities at both positive and negative peaks. TEM micrographs supported the CD spectras as both assemblies form homogeneous fibrils. However, C12-EAFFVLK assembled into short straight fibrils (Figure 5-28) while C12-ELVFFAK assembled into longer and twisted fibrils (Figure 5-29).

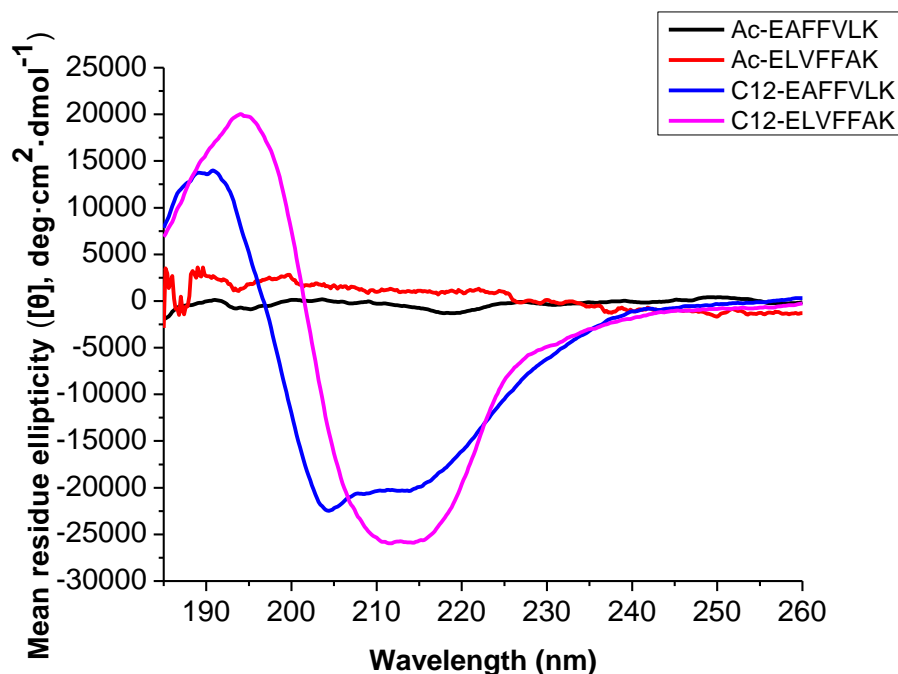


Figure 5-27 Circular dichroism of C2-EAFFVLK (black) and C2-ELVFFAK (red), C12-EAFFVLK (blue) and C12-ELVFFAK (magenta). All lipid-peptide chimeras and peptides were incubated in 40% MeCN/H₂O with 0.1% TFA (pH2) at 4°C. C12-EAFFVLK displayed maximum at 193 nm and minimum at 205, C12-ELVFFAK displayed maximum at 197 nm and minimum 213 nm

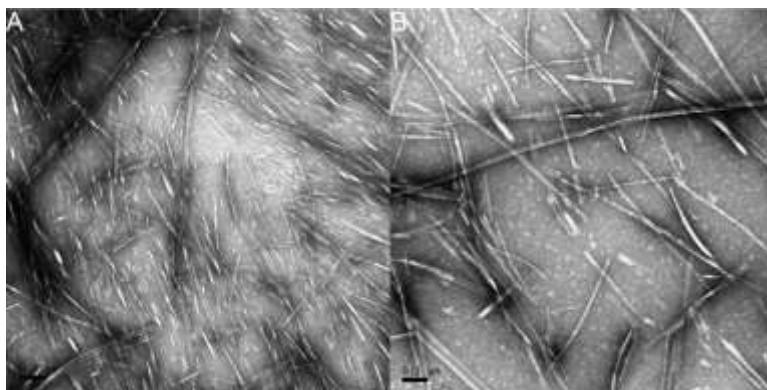


Figure 5-28 TEM micrograph of C12-EAFFVLK self-assembled as fibers in 40% MeCN/H₂O, pH2. Scale bar are 0.2 (left) and 0.1 μm (right) respectively

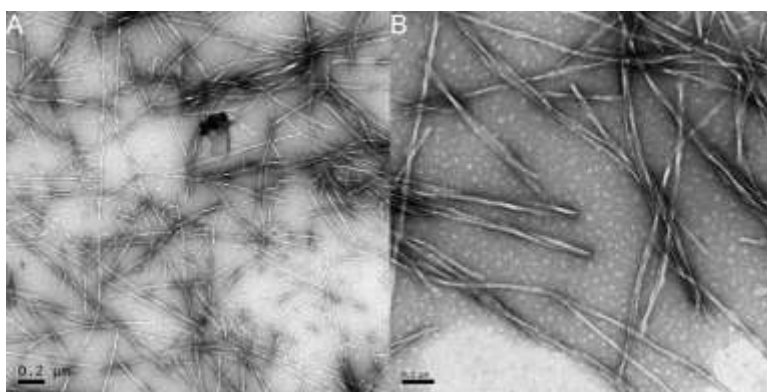


Figure 5-29 TEM micrograph of C12-ELVFFAK self-assembled as fibers in 40% MeCN/H₂O, pH2. Scale bar are 0.2 (left) and 0.1 μm (right) respectively

Differed from previous C12-KLVIIAE and C12-KLVYYAE assemblies, X-ray powder diffraction of C12-EAFFVLK and C12-ELVFFAK showed only one sharp, intense diffraction rings at 4.7 consistent with hydrogen-bonding distances. However, the lack of extended β -sheet laminations suggested these two assemblies might undergo completely different assembly patterns. They are very likely assembled into worm-like micelle structures with lipid tails dominating the assembly when the peptides completely lost their assembly propensity.

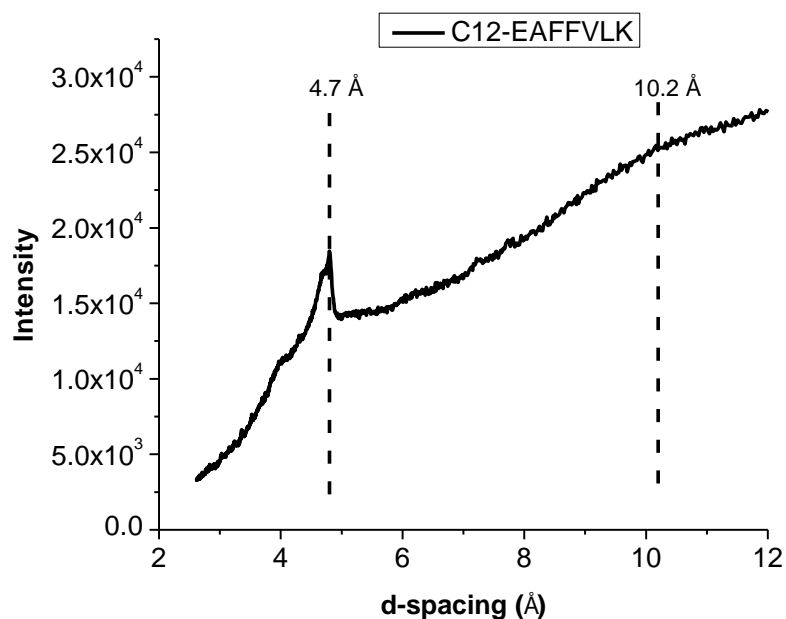


Figure 5-30 Powder X-ray diffraction of C12-EAFFVLK showing a strong reflection at d-spacings of 4.7 Å and a weak broad reflection at 11.2 Å

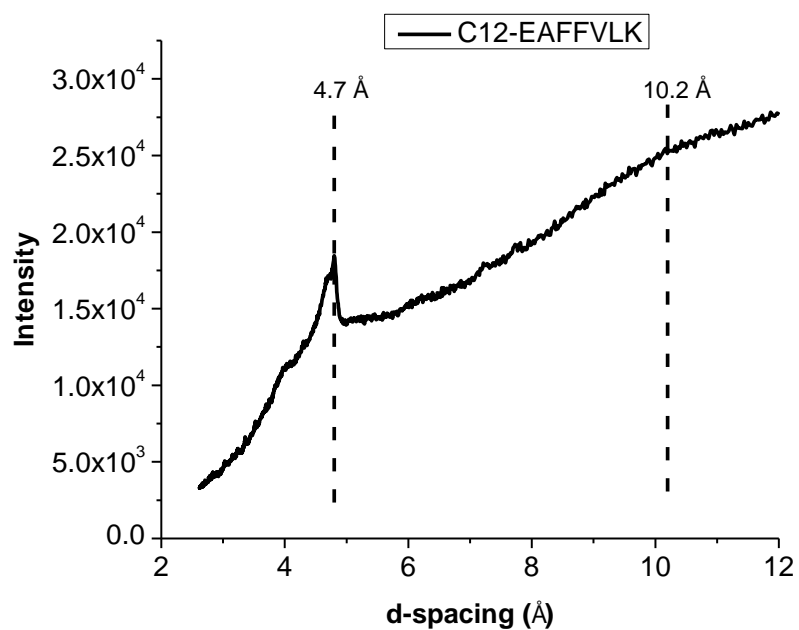


Figure 5-31 Powder X-ray diffraction of C12-ELVFFAK showing a strong reflection at d-spacings of 4.7 Å and a weak broad reflection at 11.2 Å

In order to further test if lipid chains dominate the assembly at pH 2, the C12-ELVFFAK peptide was allowed to assemble at pH7. Strikingly, it assembled into homogeneous

nanotubes and showed typical nanotube cross- β signature (Figure 5-32). At pH 2, only lysine is charged and the assembly is mostly driven by V-A and F-F packing. At neutral pH, both K16 and E22 residues are charged, and the K-E salt-bridge, which is a strong pairing code, appears to direct assembly, highlighted K-E analog code is more powerful than V-A and F-F analog code. The K-E code is so strong that it made peptides dominate in the lipid-peptide chimera self-assembling process.

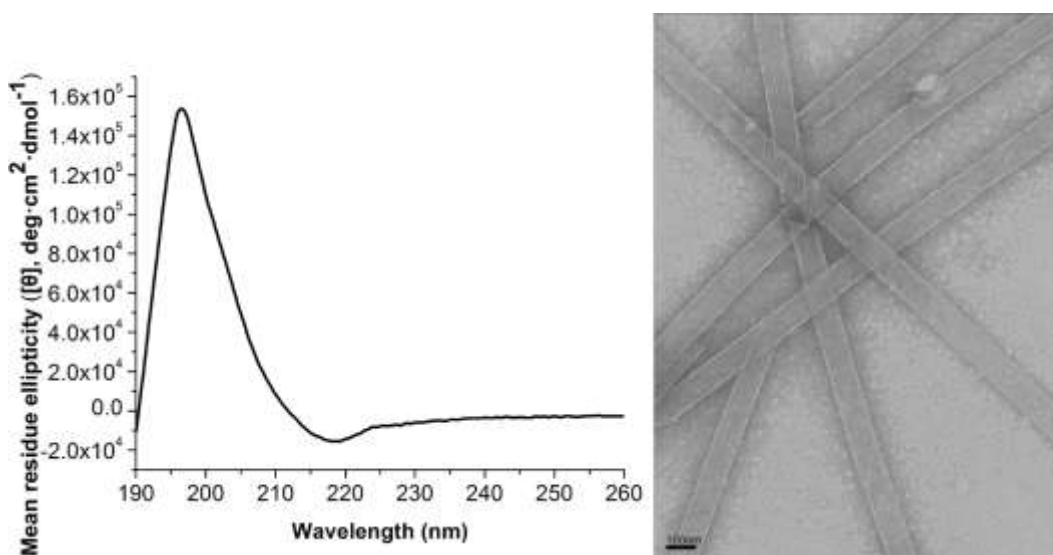


Figure 5-32 Circular dichroism and TEM micrograph of C12-ELVFFAK in 40%MeCN/H₂O, pH7

Coassembly of Lipid-Peptide Chimeras

Intricately complex multi-component assemblies are seen everywhere in nature. In order to better understand peptide specificity and further examine the plasticity of lipid-peptide chimeras, C2-KLVFFAE and C12-KLVFFAE are allowed to coassemble in 40% MeCN/H₂O pH2 at 1:1, 9:1 and 99:1 ratios. Both peptides were treated with HFIP to ensure no preformed aggregates. Quite a few insights can be drawn from Circular Dichroism, TEM and diffraction studies.

- 1) All coassemblies exhibited β -sheet ellipticity. The coassembly ellipticity is not a simple sum of each components, but much larger than a sum of each components, suggesting a mutual stabilization relationship (Figure 5-33, 5-34 and 5-35).
- 2) When total peptides concentration is maintained the same as 1.3mM, 9:1 and 99:1 coassemblies exhibited higher ellipticity than 1:1 coassemblies. Therefore, the coassemblies could be heterogeneous structures with different β -sheet propensities (Figure 5-33, 5-34 and 5-35).

3) TEM of the coassemblies showed the existence of tubes with same sizes of C2-KLVFFAE and C12-KLVFFAE (Figure 5-36 C and D), ribbons (Figure 5-36 E and F) and amorphous structures (Figure 5-36 G). All structures were observed in co-assemblies despite ratio differences. Self-sorting events clearly took place during coassembling. In addition, new nucleation events have taken place as supported by the formation of ribbons.

4) X-ray powder diffraction (Figure 5-37) of the coassembly at 1:1 ratio confirms the existence of both 9.8 β -sheet hydrogen-bonding distances and 11.5 \AA β -sheet laminations, consistent with the self-sorting events. However, the reflections of other structures such as ribbons were not shown, possibly masked by the tubes paracrystalline features.

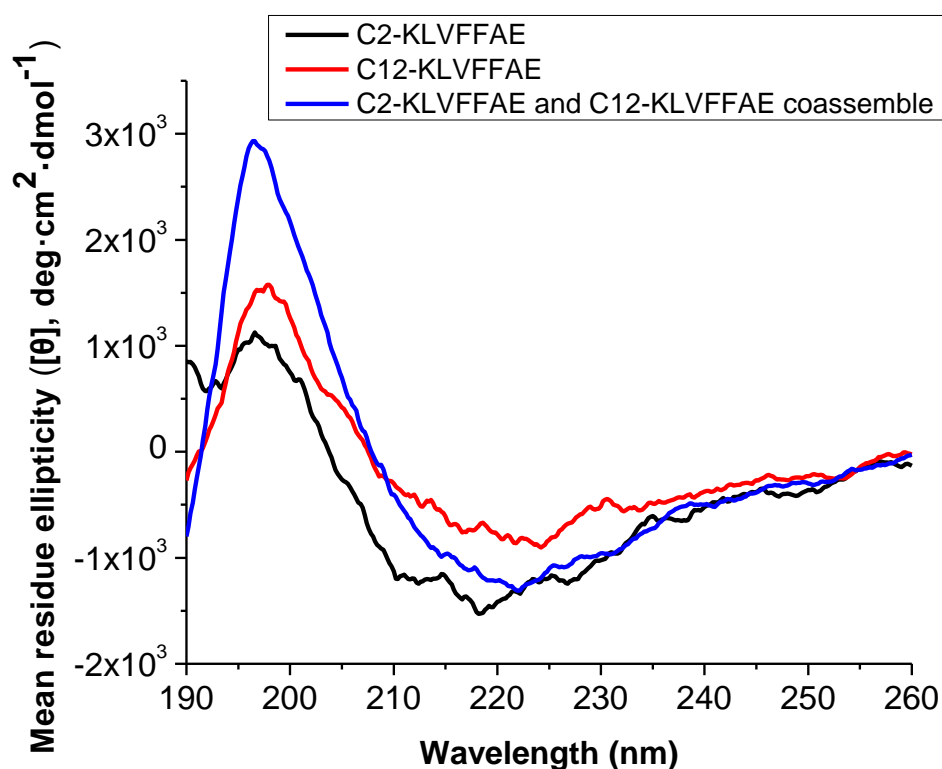


Figure 5-33 Circular Dichroism of C2-KLVFFAE 0.65mM alone (black), C12-KLVFFAE 0.65mM alone (red) and mixed peptides coassemblies in 1:1 ratio, 0.65mM each (blue). All display minimum at 220 nm and maximum at 197 nm, consistent with β -sheet secondary structure

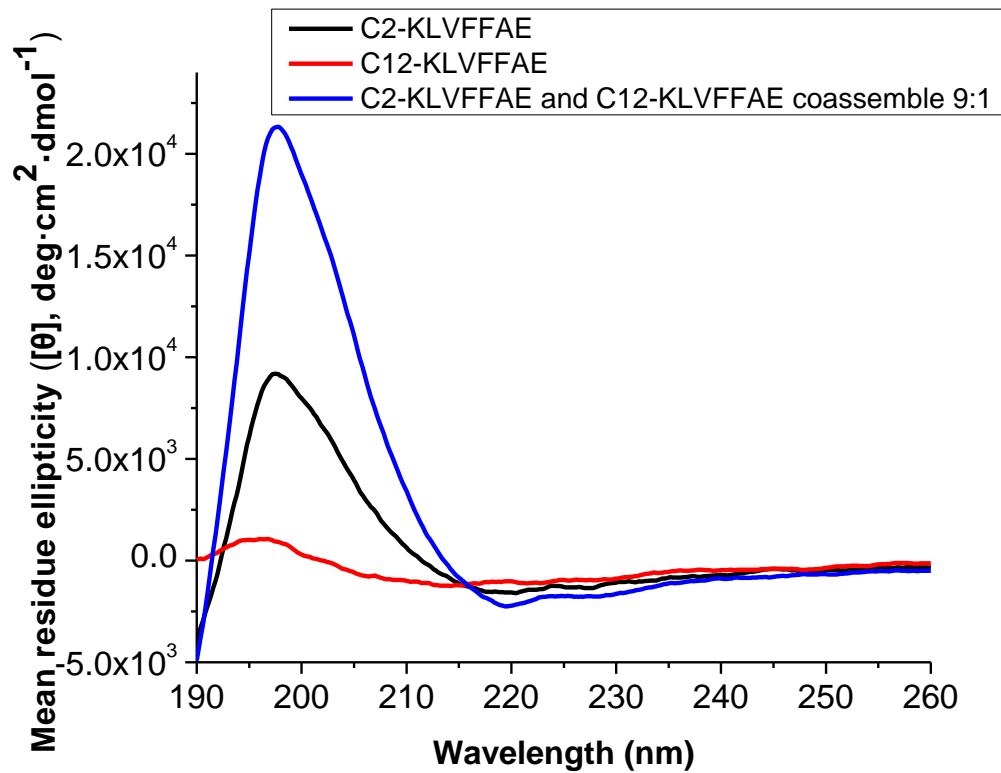


Figure 5-34 Circular Dichroism of C2-KLVFFAE 1.17mM alone (black), C12-KLVFFAE 0.13mM alone (red) and mixed peptides coassemblies in 9:1 ratio, 1.17mM and 0.13 mM respectively (blue). 0.13mM C12-KLVFFAE barely assembled with weak ellipticity, 1.17 mM C2-KLVFFAE and coassemblies display minimum at 220 nm and maximum at 197 nm, consistent with β -sheet secondary structure

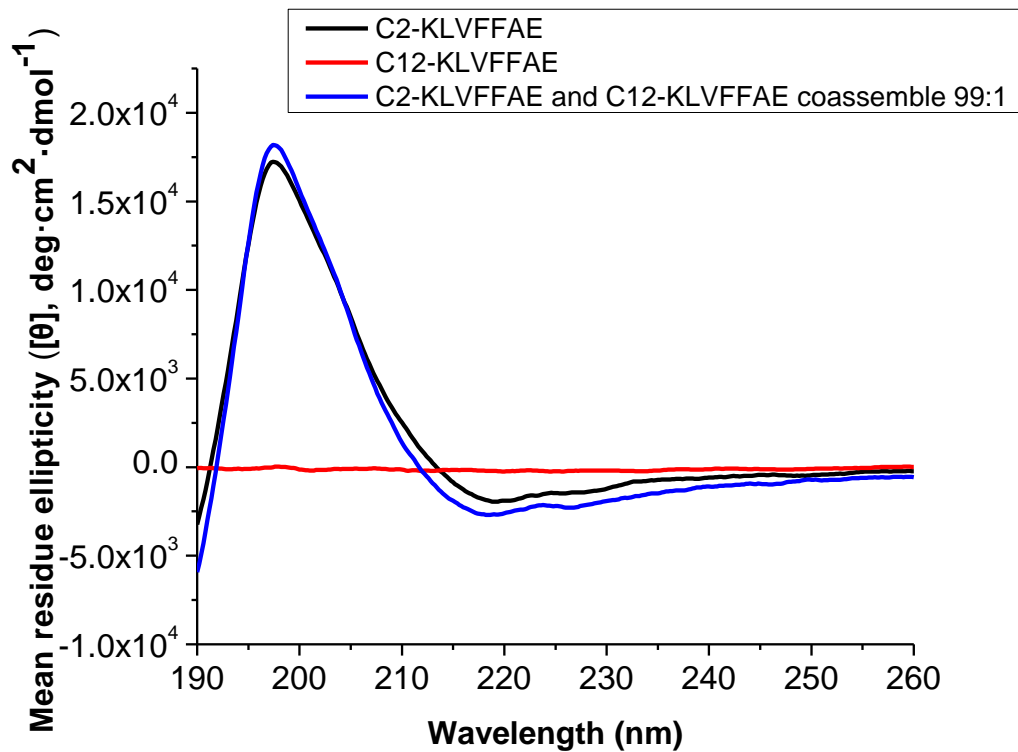


Figure 5-35 Circular Dichroism of C2-KLVFFAE 1.287mM alone (black), C12-KLVFFAE 0.013mM alone (red) and mixed peptides coassemblies in 99:1 ratio, 1.287mM and 0.013 mM respectively (blue). 0.013mM C12-KLVFFAE barely assembled with weak ellipticity, 1.287 mM C2-KLVFFAE and coassemblies display minimum at 218 nm and maximum at 197 nm, consistent with β -sheet secondary structure

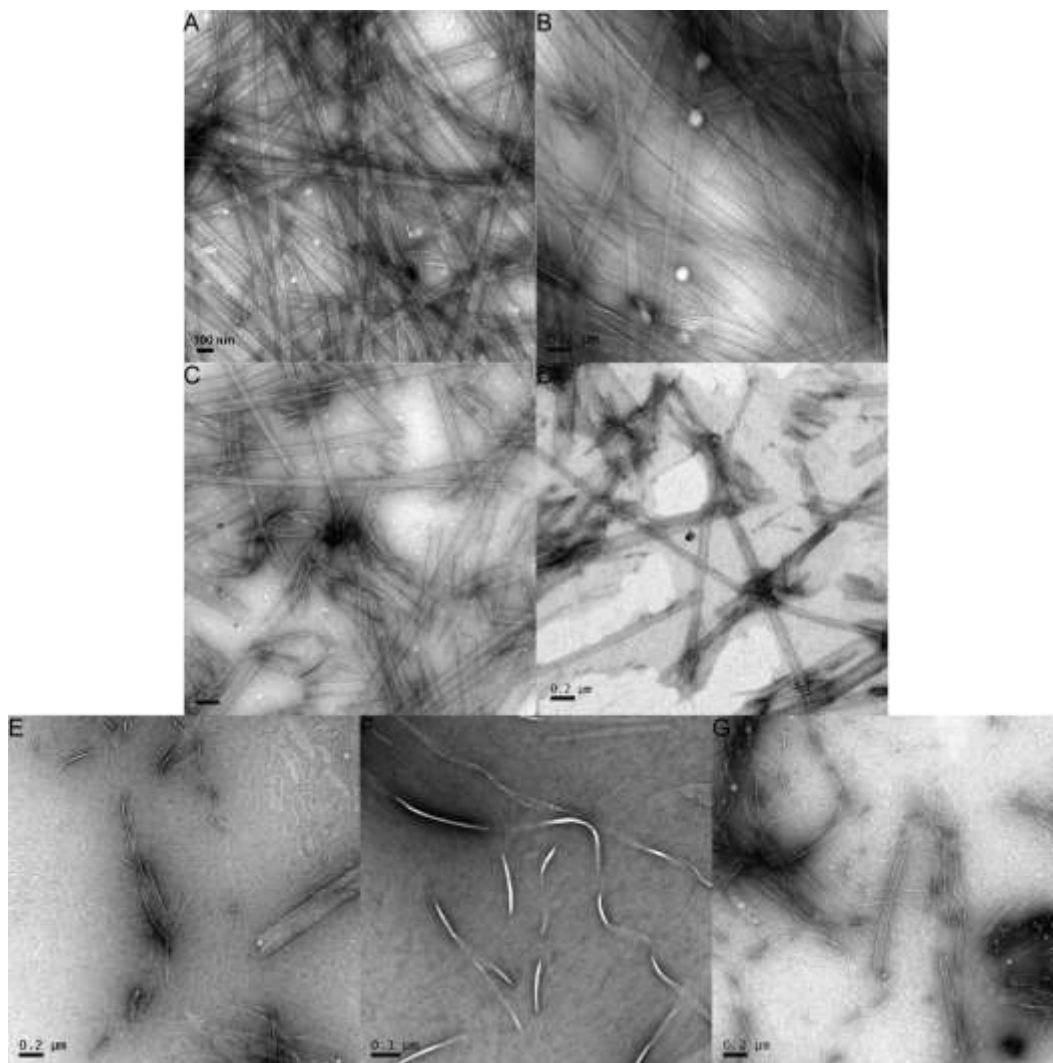


Figure 5-36 TEM micrographs of (A) C2-KLVFFAE assembled as homogeneous nanotubes; (B) C12-KLVFFAE assembled as homogeneous nanotubes; (C) nanotubes (D) nanotubes (E) ribbons (E) ribbons (G) fibrils that are observed in coassemblies of C2-KLVFFAE and C12-KLVFFAE in all 1:1, 9:1 and 99:1 coassemblies

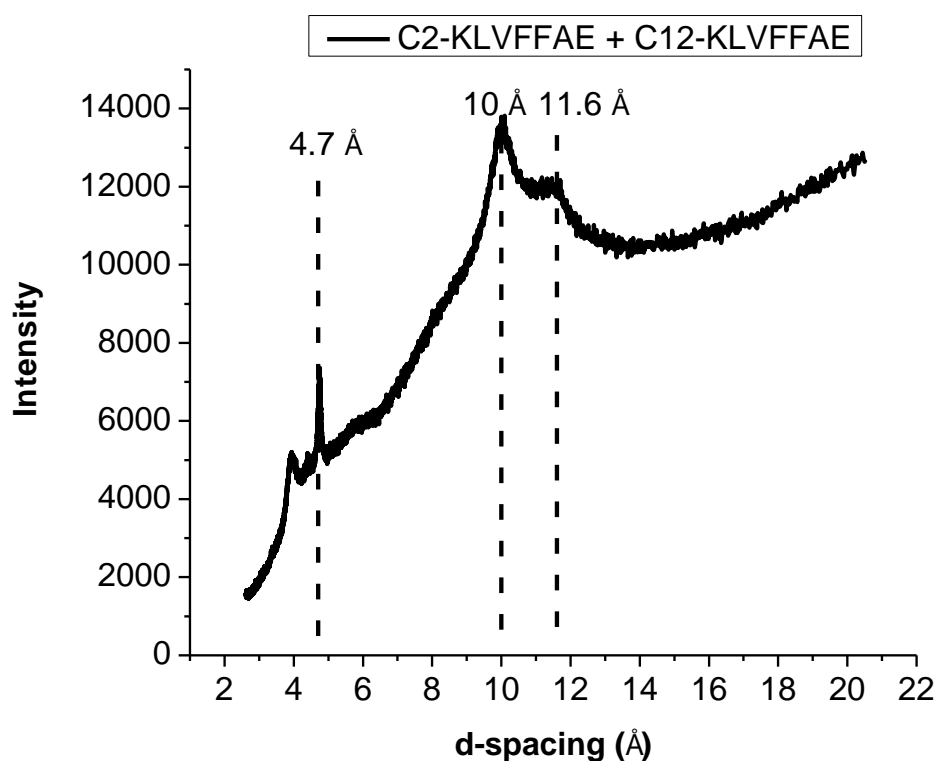


Figure 5-37 Powder X-ray diffraction of mixed C2-KLVFFAE and C12-KLVFFAE coassemblies in 1:1 ratio showing reflections at d-spacings of 4.7 Å, 10 Å and 11.6 Å

Cross-Seeding of Lipid-Peptide Chimeras

With above preliminary evaluation of peptide mixing compatibility, cross-seeding experiments were conducted to understand lipid and peptide collaborations and competitions. Peptides were allowed to assemble into matured structures and sonicated for 2-3 hours as seeds. The seeds were then added to peptide monomers treated with HFIP to prevent any preformed structures.

First, C2-KLVFFAE peptide monomers were seeded by 1% and 10% C12-KLVFFAE respectively. CD (Figure 5-38) showed that seeded assemblies exhibit higher ellipticities than unseeded peptides. Figure 5-39 contain TEM images of seeded assemblies, nanotubes of both C2-KLVFFAE and C12-KLVFFAE sizes were observed along with large amounts of ribbons. The result is comparable to that of coassembly except no amorphous aggregates were seen in seeding experiments anymore. Seeding seems to be more effective in directing new nucleation events than coassembly.

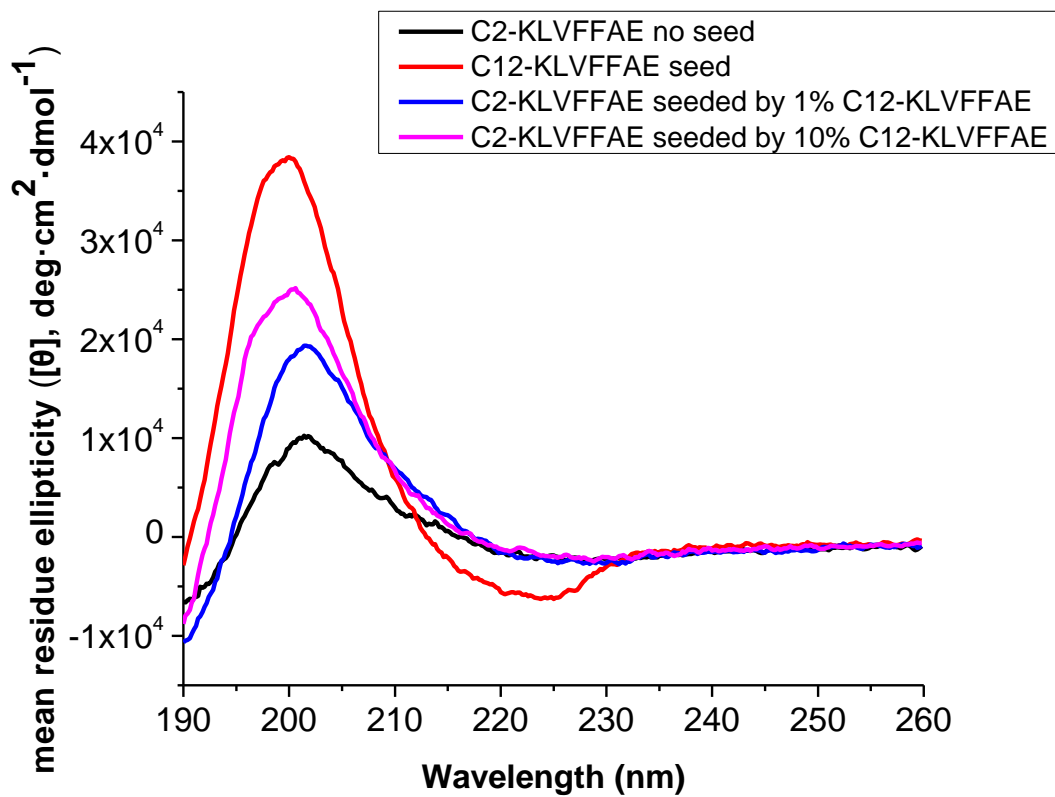


Figure 5-38 Circular Dichroism of C2-KLVFFAE alone (black), C12-KLVFFAE alone (red) C2-KLVFFAE seeded by 1% C12-KLVFFAE (blue) and 10% C12-KLVFFAE (magenta). All assemblies display minimum at 222 nm and maximum at 202 nm, consistent with β -sheet secondary structure

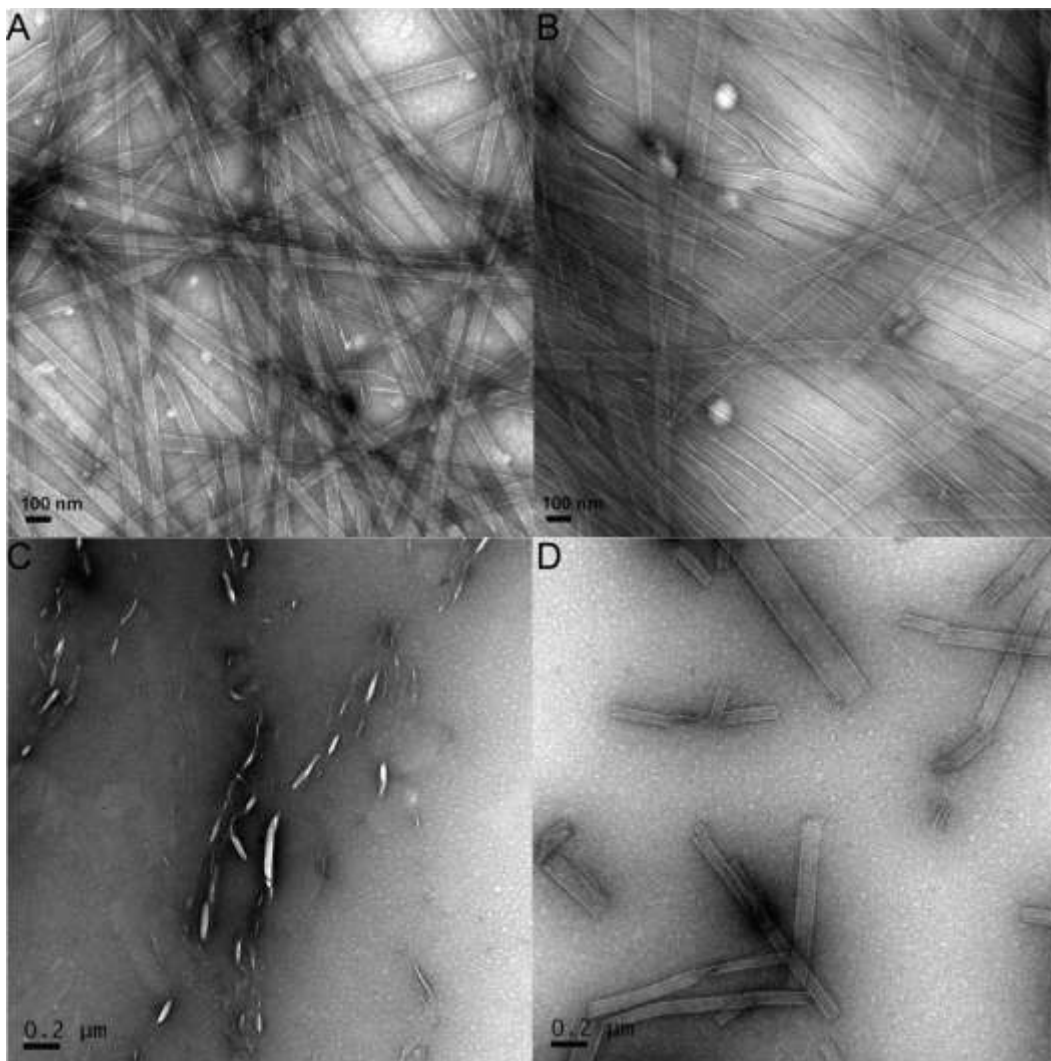


Figure 5-39 TEM micrographs of (A) unseeded C2-KLVFFAE; (B) C12-KLVFFAE seed parent; (C) ribbons and (D) nanotubes that are observed in C2-KLVFFAE seeded by 1% or 10% C12-KLVFFAE

Next, C2-KLVFFAE was seeded by all previous studied lipid-peptide chimeras including C12:1 (cis-5)-KLVFFAE, C12-KLVIIAE, C12-KLVYYAE, C12-EAFFVLK and C12-ELVFFAK. Seed parent solutions all assembled into matured nanostructures as described in previous sections in this chapter and confirmed by CD and TEM. CD (Figure 5-40) showed that when seeded by C12:1 (cis-5)-KLVFFAE, C2-KLVFFAE assemblies exhibited almost 10 times higher ellipticity than unseeded peptides. Figure 5-41 contains TEM images of seeded assemblies. Interestingly, nanotubes with C2-KLVFFAE sizes were observed with split ends or growing ends. Twisted fibrils were observed in the seeded solution, too.

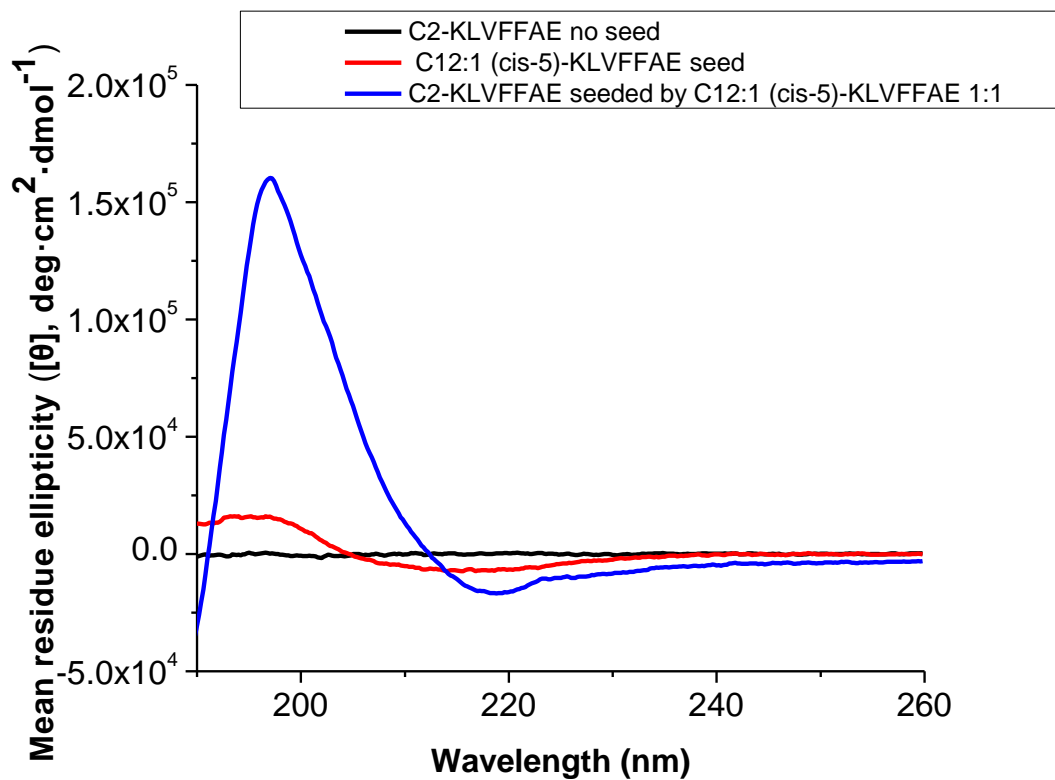


Figure 5-40 Circular Dichroism of C2-KLVFFAE 0.23mM alone (black), C12:1 (cis-5)-KLVFFAE 0.23 mM alone (red) and C2-KLVFFAE peptide monomers seeded by 50% C12:1 (cis-5)-KLVFFAE (blue), displayed ellipticity minimum at 218 nm and maximum at 197 nm

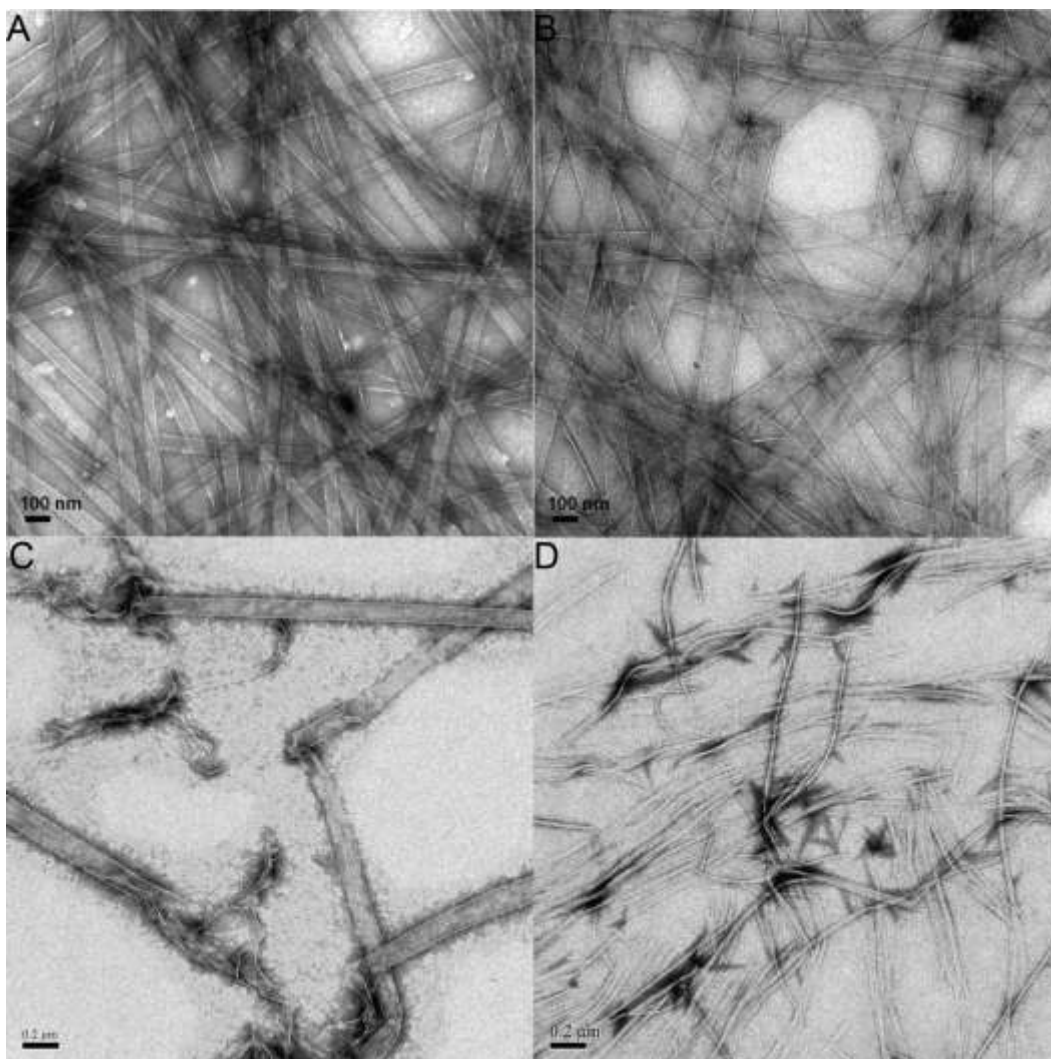


Figure 5-41 TEM micrographs of (A) unseeded C2-KLVFFAE; (B) C12:1 (cis-5)-KLVFFAE seed parent; (C) ribbons and (D) fibrils that are observed in C2-KLVFFAE seeded by 50% C12:1 (cis-5)-KLVFFAE assemble

Although almost no difference in ellipticity when C2-KLVFFAE was seeded by C12-KLVIIAE, the ellipticity maximum and minimum wavelengths were shifted (Figure 5-42). Figure 5-43 contains TEM images of seeded assemblies, nanotubes of both C2-KLVFFAE and C12-KLVIIAE sizes were observed along with large amounts of fibrils.

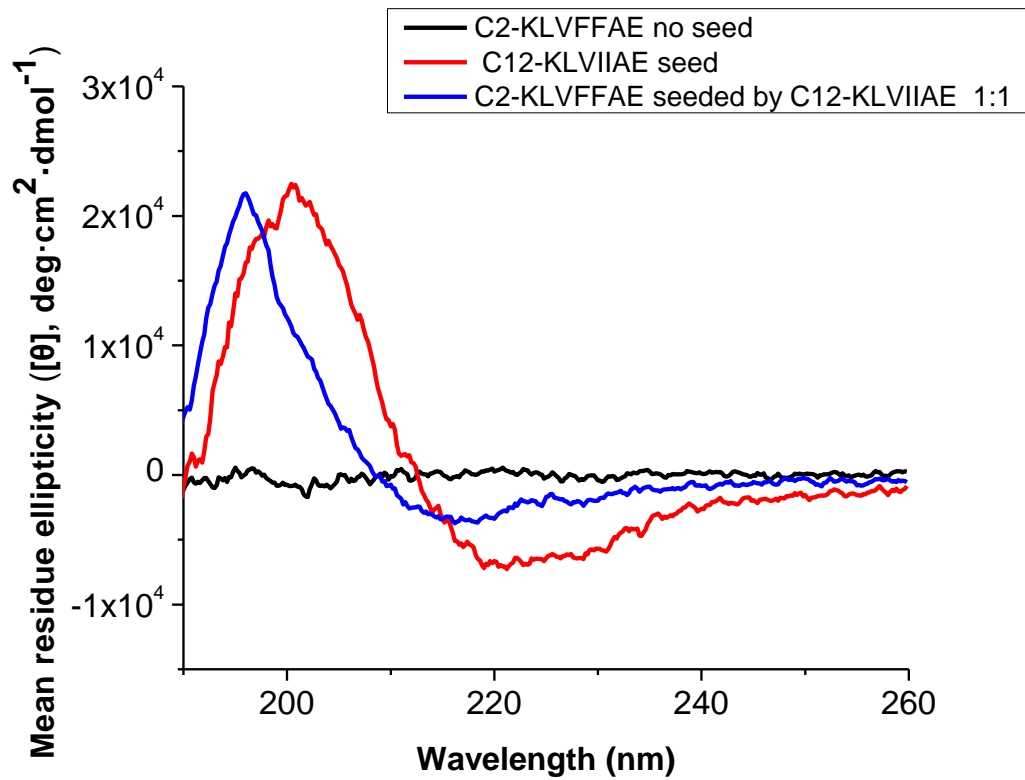


Figure 5-42 Circular Dichroism of C2-KLVFFAE 0.23mM alone (black), C12-KLVIIAE 0.23 mM alone (red) with ellipticity minimum at 218 nm and maximum at 197 nm and C2-KLVFFAE peptide monomers seeded by C12-KLVIIAE (blue) with ellipticity minimum at 220 nm and maximum at 200 nm consistent with β -sheet secondary structure

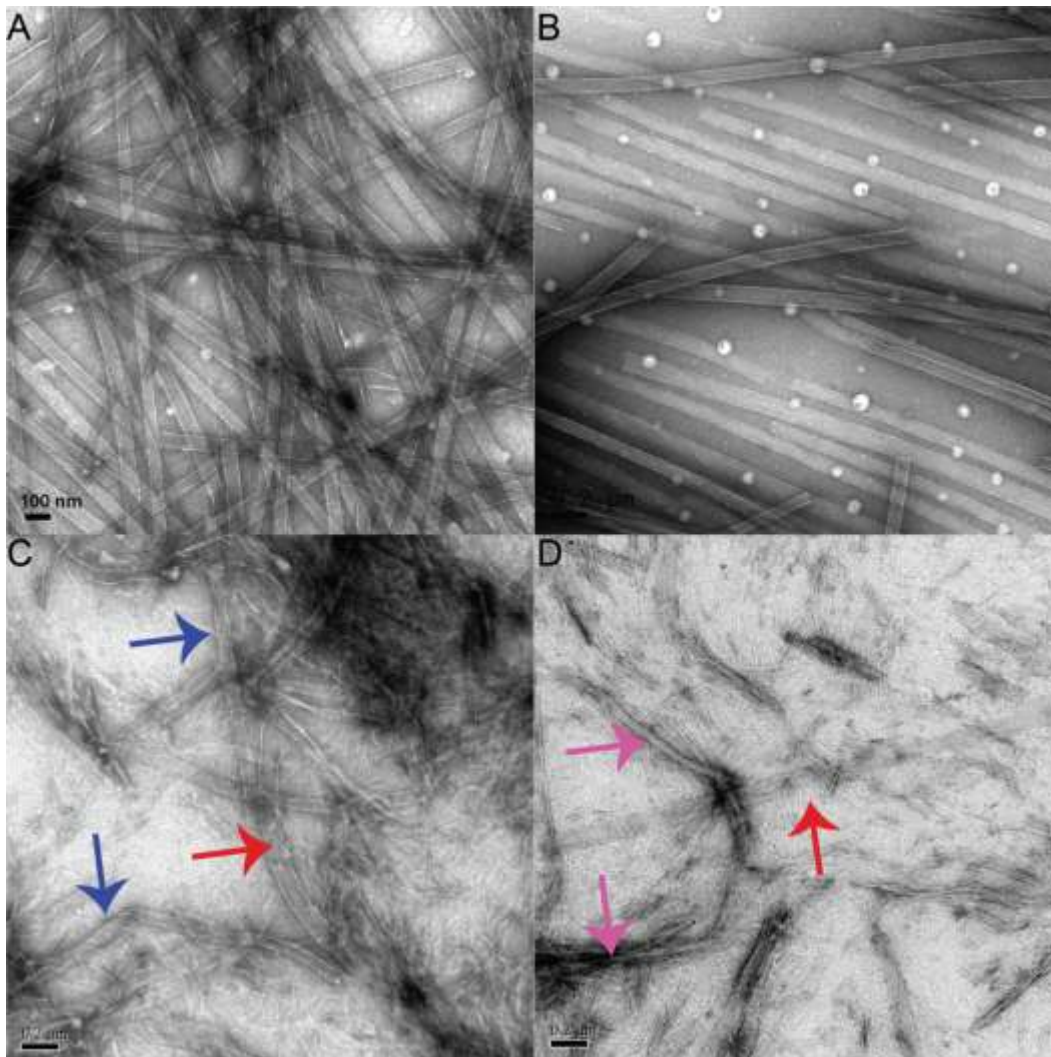


Figure 5-43 TEM micrographs of (A) unseeded C2-KLVFFAE; (B) C12-KLVIIAE seed parent; (C) and (D) C2-KLVFFAE seeded C12-KLVIIAE in 1:1 ratio. Blue arrows: tubes with same sizes as C12-KLVIIAE; Red arrow: tubes with same sizes as C12-KLVIIAE; Magenta arrow: fibrils

CD spectra (Figure 5-44) showed that when seeded by C12-KLVYYAE, C2-KLVFFAE assemblies exhibited slightly higher ellipticity than unseeded peptides. Figure 5-45 contains TEM images of seeded assemblies. Similar fibrils to the original C12-KLVYYAE were observed.

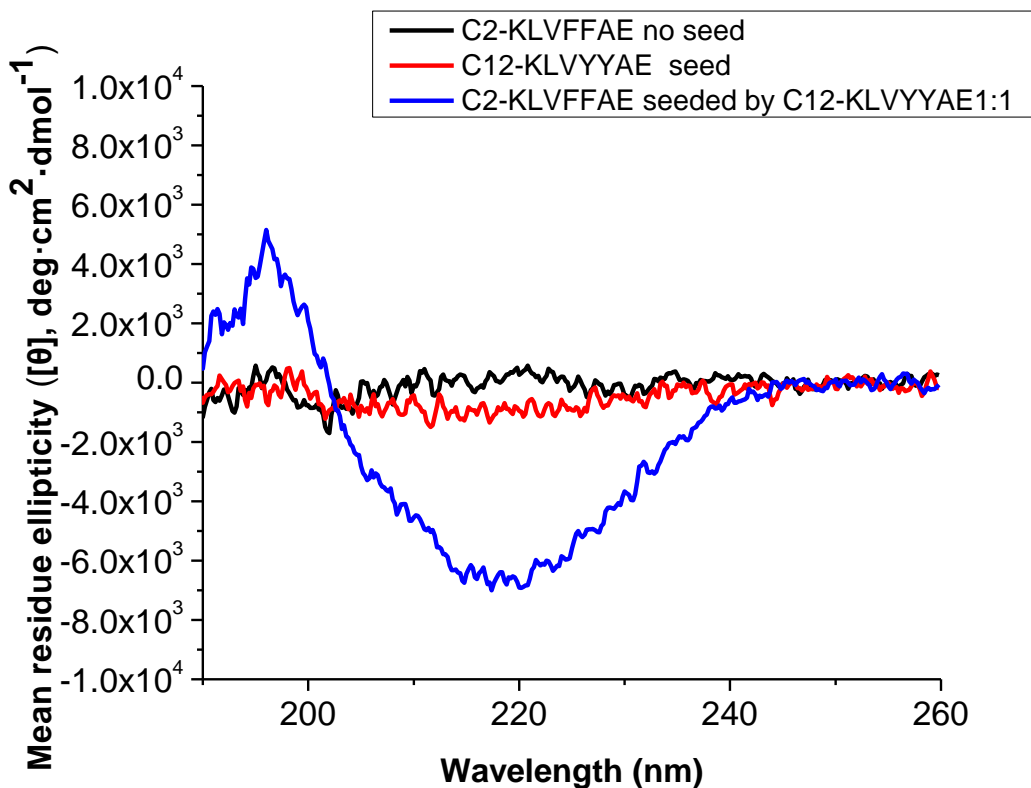


Figure 5-44 Circular Dichroism of C2-KLVFFAE 0.23mM alone (black), C12-KLVYYAE 0.23 mM alone (red) and C2-KLVFFAE peptide monomers seeded by C12-KLVYYAE (blue) with minimum at 218 nm and maximum at 197 nm consistent with β -sheet secondary structure

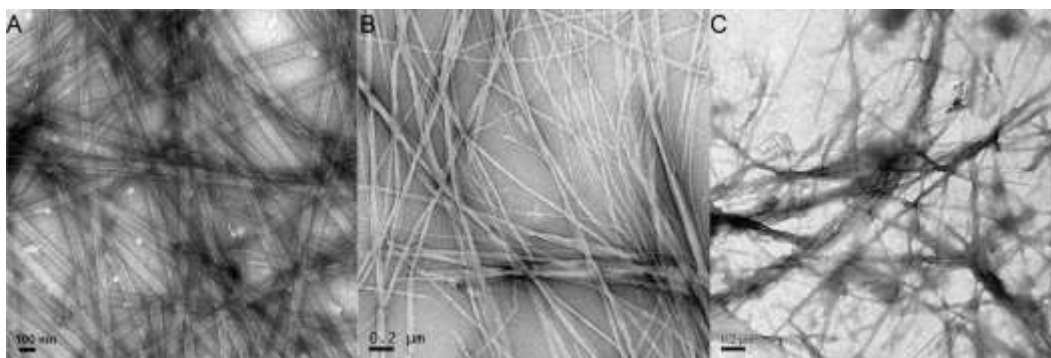


Figure 5-45 TEM micrographs of (A) unseeded C2-KLVFFAE; (B) C12-KLVYYAE seed parent; (C) C12-KLVYYAE seeded by 50% C2-KLVFFAE

CD (Figure 5-46) showed that when seeded by C12-EAFFVLK, C2-KLVFFAE assemblies exhibited higher ellipticity than unseeded peptides. Figure 5-47 contains TEM images of seeded assemblies. Similar fibrils to the original C12-EAFFVLK were observed in seeded assemblies.

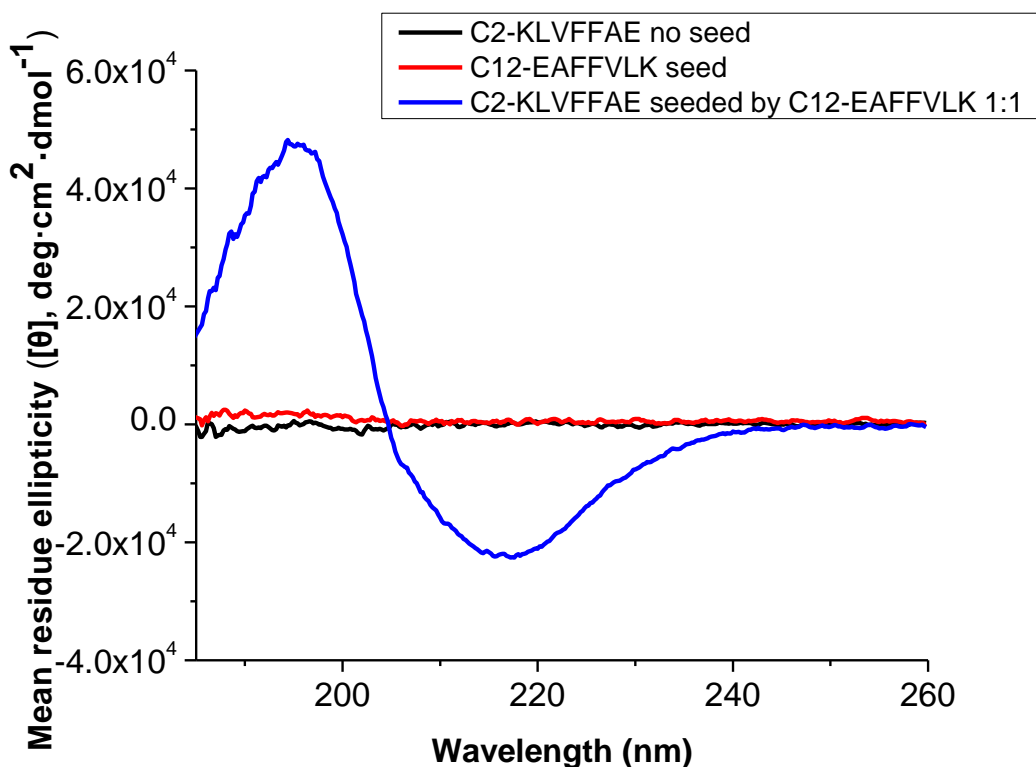


Figure 5-46 Circular Dichroism of C2-KLVFFAE 0.23mM alone (black), C12-EAFFVLK 0.23 mM alone (red) and C2-KLVFFAE peptide monomers seeded by C12- EAFFVLK (blue) with minimum at 218 nm and maximum at 197 nm consistent with β -sheet secondary structure

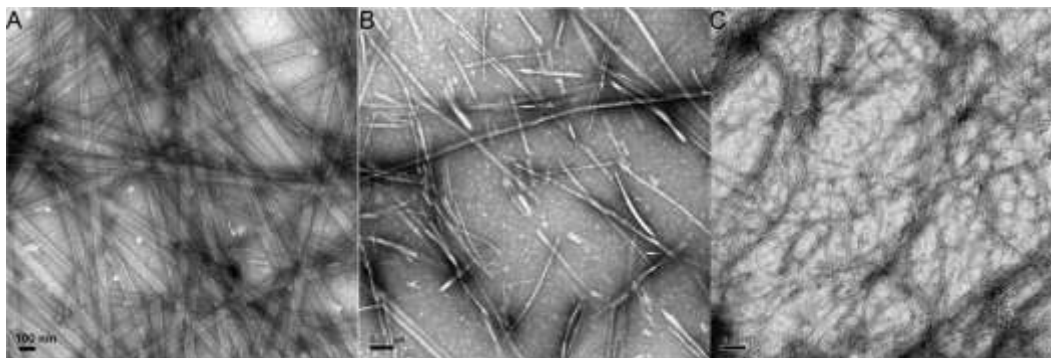


Figure 5-47 TEM micrographs of (A) C2-KLVFFAE; (B) C12-EAFFVLK; (C) C12-EAFFVLK seeded by 50% C2-KLVFFAE

CD (Figure 5-48) showed that when seeded by C12-ELVFFAK, C2-KLVFFAE assemblies exhibited higher ellipticity than unseeded peptides. Figure 5-49 contains TEM images of seeded assemblies. Fibrils were observed in seeded assemblies, however, they displayed as straight fibrils, contrast to the original C12-ELVFFAK fibrils which are more twisted.

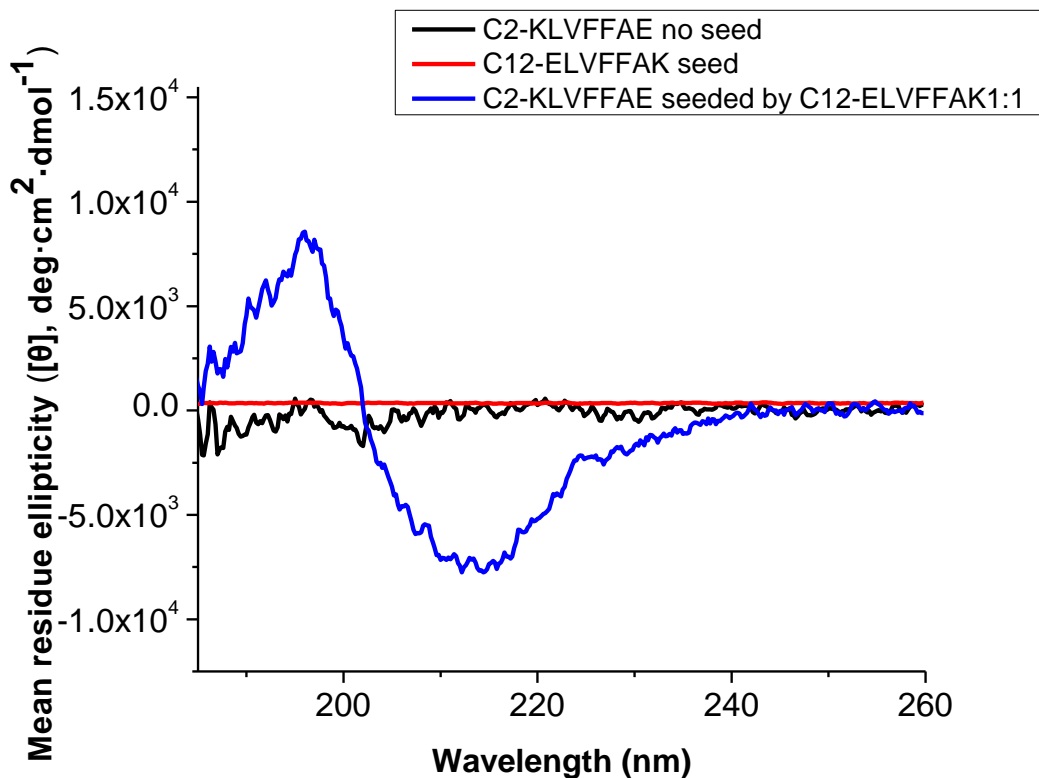


Figure 5-48 Circular Dichroism of C2-KLVFFAE 0.23mM alone (black), C12-ELVFFAK 0.23 mM alone (red) and C2-KLVFFAE peptide monomers seeded by C12-ELVFFAK (blue) with minimum at 218 nm and maximum at 197 nm, consistent with β -sheet secondary structure

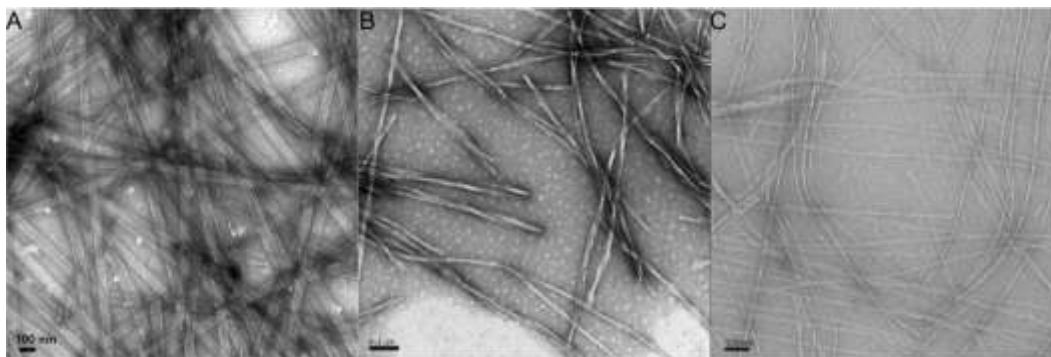


Figure 5-49 TEM micrographs of (A) unseeded C2-KLVFFAE; (B) C12-ELVFFAK seed parent; (C) C12-ELVFFAK seeded by 50% C2-KLVFFAE

All seeding results were summarized in Table 2-2. All lipid-peptide chimeras and peptides coassemblies presented different structural features compared the lipid-peptide chimeras or the peptide assemblies. The results highlighted the structural compatibility between lipid-peptide amphiphiles and peptides. Systematically control of seeding conditions and concentration ratios will push the assemblies towards homogeneous.

Table 5-1 Summary of morphologies observed by TEM in seeding experiments. All assemblies were incubated in 40% MeCN/H₂O, pH2. C2-KLVFFAE monomers were seeded by the following peptides in 1:1 concentration ratio. C2-KLVFFAE self-assembles into homogeneous nanotubes with ~48nm diameter.

Seed sequence	Seed parent morphology	Seeded assemblies morphology
C12-KLVFFAE	Nanotubes ~52nm diameter	Nanotubes ~50nm diameter and ribbons
C12:1(cis-5)-KLVFFAE	Nanotubes ~82nm diameter	Nanotubes ~50nm diameter and fibrils
C12-KLVIIAE	Nanotubes ~56nm diameter	Nanotubes ~50nm diameter and fibrils
C12-KLVYYAE	Fibrils, gel-like, 10-20 nm width	Fibrils, gel-like, 10-20 nm width
C12-KLVWWAE	Fibrils 5-10nm width and particles ~81 and 178 nm width	N/A
C12-EAFFVLK	Short, straight fibrils 5-10 nm width	Fibrils
C12-ELVFFAK	Twisted fibrils 5-10 nm width	Straight fibrils 5-10 nm width

Conclusions

This chapter highlights the remarkable plasticity of the cross- β structures. It is able to accommodate saturated (C12-KLVFFAE) as well as unsaturated acyl chains (C12:1 (cis-5)-KLVFFAE) within the interior of the β -sheet laminates. The acyl chains are positioned to fill a well-defined cavity around the side chains of the peptides and such packing is more delicate than we expected before. In fact, when the peptide sequence core F-F dyad was adjusted to residues with different geometry (II, YY and WW) or N-terminal lysine was switched to C-terminal (ELVFFAK and EAFFVLK), the lipid-peptide amphiphiles will self-assemble into drastically different morphologies. Overall, acyl chains direct cross- β assemblies and creates complementary β -sheet surfaces. The ability to systematically alter the solvent accessible surfaces, that already known to bind molecules^{22,23} and metals^{24,25} by simply incorporating lipid chains with different saturation

degrees within the cross- β folds provide new strategies for the construction of ordered mesoscale assemblies with unique functionalities.

The stabilizing effects on peptide secondary structures by the attachment of hydrophobic alkyl chains were discovered in thermal stability examination section. Use of lipidation to introduce hydrophobicity/amphiphilicity into short unstructured peptide sequences in order to control its final conformation and aggregation capability was demonstrated in this chapter, too. In fact, post-translational lipidation is widely seen in cells that could lead to the enhancement or redirection of biological function²⁶⁻³⁰. Acylated peptides and proteins with long-chain, saturated lipids have been demonstrated to extend biological action^{31,32} and induce membrane association.^{33,34} Inspired from biology, lipid-conjugation is becoming a powerful tool to engineer peptide assemblies³⁵. These studies on lipid-peptide chimeras can be utilized for studying the mechanisms of post-translational lipidation and protein-membrane interactions. They are of great importance for the lipid sequestering of amyloid proteins implicated in Alzheimer's and other neurodegenerative disease mechanism.^{36,37}

Successful cross-seeding and coassembling between peptides and peptide-lipid amphiphiles further supports the unique plasticity of the cross- β assemblies. Due to the complexity of these processes however, further investigations are still needed to be carried out to clarify the molecular mechanism for collaborative interactions between lipid-peptide chimeras. The advantages of lipid-peptide chimeras are that they are easy to be designed and synthesized, which could guarantee their quality and purity; moreover, the biocompatibility of lipid-peptide chimeras makes them perfect materials for biological and biomedical applications. The foresight of constructing tailor made self-assembling lipid-peptide chimeras, with high levels of structural and functional control has such a high potential in widespread application as immunogenic constructs, peptidomimetics, bioactive nanomaterials or antimicrobial agents^{7,38}.

Methods

Peptide synthesis and purification

Peptides were synthesized using a Liberty CEM Microwave Automated Peptide Synthesizer (NC, USA) and a Fmoc-Rink Amide MBHA Resin (AnaSpec, CA, USA). Fmoc-Rink Amide MBHA Resin was swollen using dimethylformamide for 15 minutes. Microwave assisted Fmoc deprotection was completed using 20% piperidine in dimethylformamide at 45-55°C for 180 sec, followed by 3X dimethylformamide flushes. Each Fmoc-amino acid coupling step was performed using 0.1M Fmoc protected amino acid and activated with 0.1 M 2-(1H-Benzotriazole-1-yl)-1,1,3,3-tetramethyluronium hexafluorophosphate (HBTU), and 0.2 M N,N – Diisopropylethylamine (DIEA) in DMF. Coupling temperatures using microwave were maintained between 75-82°C for 300 sec, then rinsed with three aliquots of dimethylformamide. Final acetylation of the N-terminus was achieved by addition 20% acetic anhydride in dimethylformamide. For lipid-amphiphiles synthesis, no final acetylation will be conducted leaving a free-NH₂ on the N-terminal of the peptide. Resin was filtered and washed with dichloromethane and allowed to air dry. Peptides were cleaved from the resin using trifluoroacetic acid/thioanisole/1,2-ethanedithiol/anisole (90: 5 : 3 : 2, v/v/v/v) at room temperature for 3 hrs. The cleaved peptide-TFA solution was filtered, and precipitated by drop-wise addition to cold (-20°C) diethyl ether. Precipitated product was centrifuged at 3000 rpm for 10 min, and the pellet was further washed 3 times with cold diethyl ether. Dried peptides were dissolved in minimal volume of 40% acetonitrile/H₂O + 0.1% trifluoroacetic acid and purified by RP-HPLC using a C18-reverse phase column with an acetonitrile-water gradient. Molecular weight was confirmed by MALDI-TOF using a 2,5-dihydroxybenzoic acid matrix.

Lipid-peptide coupling

Lauric acid (w261408, Aldrich) or Cis-5-Dodecenoic acid (445029 Aldrich) were purchased and used with no further purification. Peptide was prepared on a solid support resin using Fmoc microwave-assisted peptide synthesis without final acetylation leaving a free-NH₂ on the N-terminal of the peptide. The resin was washed with DCM before the coupling reaction. For coupling of alkyl chains, a 3x molar equivalent (assuming a 0.1mmol scale for peptide synthesis) of lauric acid or cis-5-dodecenoic acid was added to a minimal volume of DCM and stirred to dissolve. To this solution 6 equivalents of DIPEA was added. After 10 minutes, 6 equivalents of HBTU was added to the solution for activation. After another 10 minutes, the resin slurry was added to this solution. Reaction was stirred overnight under N₂ gas and was monitored by TLC. Following

either reaction, the resin was washed with 1:1 DMF:DMSO (2x), DMF (2x) and DCM (2x) to remove excess lauric acid or cis-5-dodecenoic acid from the resin. Resins were then dried and the peptides cleaved as previously described.

Peptide self-assembly

Peptide powders were dissolved in HFIP to make sure no pre-formed aggregates were present before assembly and dried via a centrivap concentrator. The HFIP treated peptide sample was dissolved in 40% acetonitrile/water, with 0.1% TFA, pH tested as 2. Incubation at 4°C for 1-2 weeks was generally required for the sample maturation.

Peptide seeding experiments

Seed parent solution were allowed to mature in 40% acetonitrile/60% water + 0.1% TFA solution 4C and sonicated for 2-3 hours before seeding experiments. For a monomer pool, the purified peptide was dissolved in HFIP to disrupt any preformed nuclei and then the solvent was evaporated via a centrivap concentrator. The peptide monomer was resuspended in a 40% acetonitrile/60% water solution that was then adjusted to pH 2.0 by adding 0.1% TFA. The molar percentage indicated of seed parent solution was added to the A β (16-22) monomer. The solutions were incubated at 4C for until matured as indicated by CD.

Circular Dichroism and melting

CD spectra were recorded using a JASCO J-810 spectropolarimeter fitted with a Peltier temperature controller. Samples (25 μ L) were placed into a quartz cuvette with a 0.1 mm path length (Starna Cells). Each spectrum was obtained by scanning wavelength from 260 nm to 190 nm at a scanning rate of 100 nm/min with a resolution of 0.2 nm. Three successive wavelength scans were averaged for each sample. Buffer control spectra were averaged and subtracted from the sample spectra.

An aliquot (50-70 μ L) of peptide assemblies was placed in 0.1mm path length demountable window cell with Teflon tape wrapped around the window edges to minimize evaporation. Initially, CD at 215 nm was recorded over a 15 minute period at controlled starting temperature (4C) until CD signature of solution stabilized. After temperature incubation, the ellipticity at 215 nm was recorded as a function of temperature in increments of 2 °C/min and fit to the sigmoidal form of the Boltzmann equation.

The ellipticity ($[\theta]_{\text{observed}} \text{ mdeg}$) was converted to mean residue ellipticity ($[\theta]$, $\text{deg}\cdot\text{cm}^2\cdot\text{dmol}^{-1}$) with the equation $[\theta] = [\theta]_{\text{obs}} / (10 \times n \times C \times l)$, in which, n is the number of peptide bonds, C is the concentration (mol/L) and l is the path length of the cell (cm).

Transmission Electron Microscopy Imaging

Upon addition to TEM grid (carbon/copper), the peptide assemblies were allowed to adsorb for 1 min. Excess peptide solution was wicked away with filter paper. 2-wt % uranyl acetate was added to TEM grids and incubated for 3-5 minutes. Samples were then placed in a vacuum dessicator overnight. TEM micrographs were recorded with a Hitachi 7500 TEM at magnifications ranging from 2, 000x to 200, 000x with a Tungsten filament at an accelerating voltage of 75 kV.

Powder X-ray diffraction

Assembled peptide were frozen and lyophilized to yield dry powder for X-ray diffraction. The powder spectra were obtained using a Bruker D8 Discover diffractometer, equipped with a multiposition X, Y, Z stage, a cobalt X-ray tube with Goebel mirror and a Vantec1 solid state detector. The sample was placed in a zero-background holder on the stage and the spectrum obtained using Bragg-Brentano geometry. The scan step was repeated several times to maximize the diffracted intensity and minimize noise.

References

- (1) Barbeau, K.; Rue, E. L.; Bruland, K. W.; Butler, A. *Nature* **2001**, *413*, 409.
- (2) Rainaldi, M.; Moretto, A.; Peggion, C.; Formaggio, F.; Mammi, S.; Peggion, E.; Galvez, J. A.; Díaz-de-Villegas, M. D.; Cativiela, C.; Toniolo, C. *Chemistry – A European Journal* **2003**, *9*, 3567.
- (3) Smith, A. W. *Biochimica et Biophysica Acta (BBA) - Biomembranes* **2012**, *1818*, 172.
- (4) Lee, A. G. *Biochimica et Biophysica Acta (BBA) - Biomembranes* **2003**, *1612*, 1.
- (5) Yu, Y.-C.; Tirrell, M.; Fields, G. B. *J. Am. Chem. Soc.* **1998**, *120*, 9979.
- (6) Forns, P.; Lauer-Fields, J. L.; Gao, S.; Fields, G. B. *Biopolymers* **2000**, *54*, 531.
- (7) Cui, H.; Webber, M. J.; Stupp, S. I. *Peptide Science* **2010**, *94*, 1.
- (8) Velichko, Y. S.; Stupp, S. I.; de la Cruz, M. O. *The Journal of Physical Chemistry B* **2008**, *112*, 2326.
- (9) Martin, S. E.; Peterson, B. R. *Bioconjugate Chem.* **2003**, *14*, 67.
- (10) Huo, Q.; Sui, G.; Zheng, Y.; Kele, P.; Leblanc, R. M.; Hasegawa, T.; Nishijo, J.; Umemura, J. *Chemistry – A European Journal* **2001**, *7*, 4796.
- (11) Ni, R., Emory University, 2010.
- (12) Ni, R.; Childers, W. S.; Hardcastle, K. I.; Mehta, A. K.; Lynn, D. G. *Angewandte Chemie-International Edition* **2012**, *51*, 6635.
- (13) Alberts B, J. A., Lewis J, et al. *Molecular Biology of the Cell*; 4th edition ed.; Garland Science: New York, 2002.
- (14) Mehta, A. K.; Lu, K.; Childers, W. S.; Liang, Y.; Dublin, S. N.; Dong, J.; Snyder, J. P.; Pingali, S. V.; Thiyagarajan, P.; Lynn, D. G. *J. Am. Chem. Soc.* **2008**, *130*, 9829.
- (15) Childers, S. W. T., Emory University, 2010.
- (16) Myers, D. *Surfactant Science and Technology*; Second Edition ed.; VCH Weinheim: New York.
- (17) Bull, S. R.; Guler, M. O.; Bras, R. E.; Venkatasubramanian, P. N.; Stupp, S. I.; Meade, T. J. *Bioconjugate Chem.* **2005**, *16*, 1343.
- (18) Hartgerink, J. D.; Beniash, E.; Stupp, S. I. *Proceedings of the National Academy of Sciences* **2002**, *99*, 5133.
- (19) Hartgerink, J. D.; Beniash, E.; Stupp, S. I. *Science* **2001**, *294*, 1684.
- (20) Lu, K., Emory University, 2005.
- (21) Liang, Y.; Lynn, D. G.; Berland, K. M. *J. Am. Chem. Soc.* **2010**, *132*, 6306.
- (22) Childers, W. S.; Mehta, A. K.; Lu, K.; Lynn, D. G. *J. Am. Chem. Soc.* **2009**, *131*, 10165.
- (23) Liang, Y.; Guo, P.; Pingali, S. V.; Pabit, S.; Thiyagarajan, P.; Berland, K. M.; Lynn, D. G. *Chem. Commun.* **2008**, 6522.
- (24) Dong, J.; Canfield, J. M.; Mehta, A. K.; Shokes, J. E.; Tian, B.; Childers, W. S.; Simmons, J. A.; Mao, Z.; Scott, R. A.; Warncke, K.; Lynn, D. G. *Proc. Natl. Acad. Sci. U.S.A.* **2007**, *104*, 13313.
- (25) Dong, J. J.; Shokes, J. E.; Scott, R. A.; Lynn, D. G. *J. Am. Chem. Soc.* **2006**, *128*, 3540.
- (26) Lin, D.-T.; Makino, Y.; Sharma, K.; Hayashi, T.; Neve, R.; Takamiya, K.; Huganir, R. L. *Nat Neurosci* **2009**, *12*, 879.
- (27) Moffett, S.; Adam, L.; Bonin, H.; Loisel, T. P.; Bouvier, M.; Mouillac, B. *J. Biol. Chem.* **1996**, *271*, 21490.

- (28) Johansson, J.; Nilsson, G.; Strömberg, R.; Robertson, B.; Jörnvall, H.; Curstedt, T. *Biochem. J* **1995**, *307*, 535.
- (29) Pylypenko, O.; Schönichen, A.; Ludwig, D.; Ungermann, C.; Goody, R. S.; Rak, A.; Geyer, M. *J. Mol. Biol.* **2008**, *377*, 1334.
- (30) Liu, Y.; Kahn, R. A.; Prestegard, J. H. *Nat. Struct. Mol. Biol.* **2010**, *17*, 876.
- (31) Havelund, S.; Plum, A.; Ribel, U.; Jonassen, I.; Volund, A.; Markussen, J.; Kurtzhals, P. *Pharm Res* **2004**, *21*, 1498.
- (32) Knudsen, L. B.; Nielsen, P. F.; Huusfeldt, P. O.; Johansen, N. L.; Madsen, K.; Pedersen, F. Z.; Thøgersen, H.; Wilken, M.; Agersø, H. *J. Med. Chem.* **2000**, *43*, 1664.
- (33) Kang, R.; Wan, J.; Arstikaitis, P.; Takahashi, H.; Huang, K.; Bailey, A. O.; Thompson, J. X.; Roth, A. F.; Drisdell, R. C.; Mastro, R.; Green, W. N.; Yates, J. R., 3rd; Davis, N. G.; El-Husseini, A. *Nature* **2008**, *456*, 904.
- (34) Aicart-Ramos, C.; Valero, R. A.; Rodriguez-Crespo, I. *Biochimica et Biophysica Acta (BBA) - Biomembranes* **2011**, *1808*, 2981.
- (35) López Deber, M. P.; Hickman, D. T.; Nand, D.; Baldus, M.; Pfeifer, A.; Muhs, A. *PLoS ONE* **2014**, *9*, e105641.
- (36) Gorbenko, G. P.; Kinnunen, P. K. J. *Chem. Phys. Lipids* **2006**, *141*, 72.
- (37) Domanov, Y. A.; Kinnunen, P. K. J. *J. Mol. Biol.* **2008**, *376*, 42.
- (38) Lowik, D. W. P. M.; van Hest, J. C. M. *Chem. Soc. Rev.* **2004**, *33*, 234.

Chapter 6 Engineering Asymmetric Cross- β Peptide Membranes for Emergent Functions

Surface Engineering of Peptide Membranes

Typical lipid membranes are organized in a parallel arrangement placing charged head groups at the exposed surface and hydrophobic alkyl chains at the buried interface. In contrast, amyloid peptides can spontaneously form membrane-like bilayer in a rich assortment of configurations based on rules of cross-strand and cross-sheet pairings derived from protein folding. The vast lipid surface modifications seen in nature have ensured diversified functionalities. In this dissertation, I have systematically explored biomimetic strategies to engineer the peptide membrane surfaces and demonstrated their feasibility, and in doing so, expanded the tool kit of surface engineering of peptide self-assembly for functional scaffolds. I'll review each of these strategies below.

Strategy 1: residue substitution

Under aqueous acidic conditions, A β (16-22) Ac-KLVFFAE and its congener Ac-KLVFFAL self-assemble as anti-parallel out-of-register peptide arrangements. With an extended peptide length of ~ 2 nm, the peptides form a bilayer membrane of ~ 4 nm. This arrangement places half of the charged N-terminal lysines buried within a bilayer interface and the remaining half exposed to the surface. Moreover, these positively charged lysines are passivated by counterions (TFA) in solvents. Since the N-terminal residues are not incorporated in the hydrogen-bonding networks, substitution of the N-terminal residue does not affect the cross- β structure but results in an entirely different membrane surface.

In chapter 2, I have replaced the N-terminal lysine residue (K) with glutamic acid (E), phosphotyrosine (pY) and phosphoserine (pS). Reasoning that the counterion is critical for self-assembly of the cross- β bilayer, these variants with negatively-charged surfaces were assembled with complementary counterions (TEAA). All variants successfully self-assembled into cross- β bilayer nanotube structures but with opposite surface properties. These Ac-ELVFFAL, Ac-pYL VFFAL and Ac-pSLVFFAL surfaces recruit positively-charged molecules (Thioflavin T, Methylene Blue, Acridine orange) as shown in chapter 2 and chapter 4. Furthermore, hyperphosphorylated surfaces are implicated in

neurogenerative diseases as neurofibrillary tangles and etiologically significant in AD by impacting RNA processing. Extending these patterned lysine peptide surface to the phosphorylated surfaces provides new possibilities for studying biologically significant protein and catalyst associations. As a demonstration of these possibilities, chapter 2 has established this assembly as a surrogate for neuronal tau tangles by demonstrating its high-affinity binding to histone H1, whose association with the DNA backbone ¹ is important in gene regulation,² chromatin condensation,³ and global control over chromatin remodeling activities .⁴

Strategy 2: peptide co-assembly

While significant efforts have been focused on single component peptide self-assembly, multicomponent peptide self-assembly or peptide co-assembly is less explored. The need for generating dynamic heterogeneous system has driven an increase in complexity. In chapter 3, two oppositely-charged peptides Ac-KLVFFAL and Ac-pYLVFFAL were co-assembled as homogeneous nanotubes with oppositely-charged outer and inner surfaces. Such asymmetric property is extremely difficult to obtain in single component systems which usually assemble as symmetric architectures. By selecting unique components for co-assembly, future studies on generating asymmetric surfaces in non-biological systems can vary from charge properties to surface plasticity, surface fluidity and surface affinity towards different molecules or proteins.

Strategy 3: seeding

An interesting feature of Ac-pYLVFFAL peptide nanotubes compared to the previous Ac-KLVFFAE and Ac-KLVFFAL peptide nanotubes is that they stain differently with uranyl acetate. This discovery made it possible to study cross-seeding of peptides easily by TEM. In fact, both Ac-KLVFFAL and Ac-pYLVFFAL peptides can serve as templates for each other and propagate the other peptide monomers. Such cross-seeding based on structural compatibility can result in homogeneous nanotubes with charge domain segregations on the surfaces. Domain segregations are common in biological self-assembly as different domains can perform different functions without compromising each other's specificity. The peptide nanotube membranes with charge domains can be a promising scaffold for building catalytic networks.

Strategy 4: lipid-peptide chimera

Previous studies have demonstrated remodeling of cross- β nanotube surfaces by simply incorporating a saturated alkane within the cross- β laminate core in peptide-lipid chimeras⁵. In chapter 5, I have extended lipid-peptide chimera from saturated carbon chain to unsaturated carbon chain. Such structures are different from conventional peptide amphiphile cylindrical fibrils that bury the alkane chain in assembly interiors with peptide segments splaying along their outer surface. Rather, the A β peptide dominates the assembly and dictates the surface properties, while lipid chains modulate the grooves and laminations of the surfaces. I have also found that lipid carbon chains can modulate previously non-ordered surfaces into ordered ones. By modifying the core dyad in the 7-residue peptide from F-F to I-I, Y-Y and W-W, the resulting peptide-lipid chimera assemblies can be modulated as nanotubes, fibrils and particles. The tuning capability can now be further utilized to design distinct functional materials.

Surface Characterization of Peptide Membranes

A variety of techniques have been developed for characterizing molecular structures of peptide assemblies such as Circular Dichroism, Fourier Transform Infrared, NMR, Electron Transfer, Small Angle X-ray Scattering, Atomic Force Microscopy etc. Nevertheless, few were aimed at surface properties⁶. The supramolecular assemblies surfaces, however, constitutes the important interface between the assemblies and the external environment. It is extremely important when the assemblies are designed as functional scaffolds. Hence, in order to monitor the performance of peptide assemblies, the surface properties must be well known. In chapter 2 and 3, AFM, EFM, gold nanoparticle binding and salt bundling strategies were developed to obtain surface chemical and morphological information of self-assembled cross- β peptide membranes. Especially EFM, which is utilized on dry surfaces, including mineral crystal faces, graphene layers and other solid materials, has been demonstrated as an effective tool in characterizing more complex and dynamic self-assembled engineered materials. These methods developed in this dissertation have great potential to be employed in characterizing other supramolecular self-assemblies and present a good example of extending surface characterization techniques on biomaterials in general.

Design Asymmetry and Control Defects in Multicomponent Self-Assembly

Biology usually uses templates to limit defects and uneven distribution of different components. For such a design it is important to have different regions perform different

functions. Self-assembly of traditional materials such as electronic devices⁷, block copolymers⁸ and organic hydrogen-bonded system⁹ that mimic biological asymmetry have been reported. In contrast to the extensive studies on self-assembled morphologies of peptides, very few studies so far have been devoted to their defects and asymmetry element. Gough et, al¹⁰ explored the self-assembly of structurally and functionally asymmetric wedge-shaped peptides into nanofibers or lamellar structures and identified a balance in positive and negative charges as well as cooperative amphiphilicity as necessities for self-assembly of asymmetric peptides. Horne et, al¹¹ have designed an asymmetric unit of extended peptide nanotubes by interrupting the hydrogen bonding network on one face of the cyclic peptide subunit through backbone N-alkylation. Such interruption restricts the self-assembly to antiparallel cylindrical dimers. All of these examples started with an asymmetric peptide structure but none of them have studied the final structures. In chapter 4, I have described a simple method to generate asymmetry in peptide self-assembly via the co-assembly of two oppositely-charged peptides (Ac-KLVFFAL and Ac-pYLVFFAL) that form cross- β nanotubes with distinctly-charged surfaces. Interestingly, these nanotubes were shown to colocalize positively- and negatively-charged fluorophores on their surfaces asymmetrically on the negatively-charged outer surface and the positively-charged inner surface. Moreover, such nanotubes are not homogeneous from one end to the other; they possess heterogeneous domain blocks shown by fluorescence imaging. Enrichment of 1-¹³C and 3-¹³C on the two peptides respectively made it possible to quantify homogeneous and heterogeneous interfaces by solid-state REDOR NMR. Under the assembly conditions, 75% of the assemblies hold heterogeneous interfaces, and 25% of the domains hold homogeneous domains.

Co-assembly of peptides opens a new chapter for making unique asymmetric biomimetic self-assemblies. Future directions can be systematically investigating on the microscopic mechanism of defect formation in peptide self-assembly. Also, investigation on controlling assembling environment (pH, solvents, coassembling molecules, temperature) and assembling kinetics for specific interface partitions will be of great interest.

Expand Molecular Codes for Supramolecular Self-Assembly

Understanding the self-assembly rules and deciphering molecular codes is essential for designing specific patterns and functional scaffolds from peptide self-assembly. Using

the 20 natural amino acids, a diversity of molecular recognitions ranging from salt bridge¹² to sterics¹³ to hydrogen-bonding¹⁴ impact the final assembled β -sheet registry. Using this knowledge from single component systems, the β -sheet registry of multicomponent systems can now be explored. This dissertation highlights a growing set of codes to rationally control the formation of supramolecular assemblies. 1) Cooperative electrostatic attraction between lysine (K) and phosphotyrosine (pY) at the interface made it possible to form homogeneous and heterogeneous leaflets from co-assemblies of two peptides (Ac-KLVFFAL and Ac-pYLVFFAL) (Chapter 4). 2) Hydrophobic packing between lipid hydrocarbon chains and hydrophobic residues in the peptide allows us to manipulate lipid-peptide chimeras by simply coding information in the peptide sequence of lipid chain hydrophobicity (Chapter 5). 3) Hydrogen-bonding and β -sheet formation between different types of peptides with structural compatibility is feasible provided appropriate co-assembly or seeding conditions (Chapter 4). Understanding more of the molecular codes for supramolecular assembly will aid the rational design of new architectures tailored to the needs of specific biological and non-biological applications.

Toward Dynamic Functional Self-Assembly System

Along the way of developing novel structures and investigation of their formation mechanism of peptide assemblies, the exploration of their biomedical and biomaterial application is gaining greater focus. Peptide based materials¹⁵ represent an especially promising class of compounds due to their relative ease of synthesis, biocompatibility, and the ability to be tailored for integration into current biology. In plants, sunlight is collected by porphyrin-derived pigment molecules noncovalently attached to polypeptide cages. The peptide cage determines the intermolecules distance and orientation of the pigments molecules, which are responsible for long-range energy transfer. Similar light-harvesting antenna have been constructed on peptide fiber,¹⁶ hydrogel¹⁷ and nanotube¹³ scaffolds, however, all of the peptide assemblies were used as a scaffold for fixing the molecules only. By taking advantage of charge separation of the unique asymmetric peptide membrane, pigments arrays can be constructed on outer and inner surfaces respectively to realize energy transfer across the peptide bilayer membrane with a 4 nm distance. This design takes a big step forward in mimicking biological photosynthesis which is a delicate interplay between a specific set of membrane-bound pigment–protein complexes that harvest and transport solar energy, execute charge separation, and interconvert physical and chemical energy. Switching the FRET fluorophores pair to

electron donor-acceptor pair facilitated electron transfer across the peptide bilayer membrane. The present approach not only provides a rational design for self-assembling asymmetric peptide membrane capable of charge separation, but also allows organization of functional molecules that alone do not show self-assembling properties. The future direction is to explore the capabilities of the ordered, robust peptide membrane scaffolds for complex catalytic reactions. The successful recruiting of large proteins on the peptide membrane in chapter 2 is the first step to mediate functional networks on peptide membranes.

In summary, studies within this dissertation have demonstrated simple residue replacement, co-assembly, and cross-seeding and chimera construction to be effective surface engineering strategies of peptide membranes. These highly ordered and charged surfaces present patterned binding sites for histochemical dyes, redox active molecules and even prototypical nucleic acid binding protein. More intriguingly, co-assembly of two oppositely-charged peptides with structural compatibility can induce the formation of a unique asymmetric peptide membrane with distinctly charged surfaces on inner and outer surfaces of nanotubes. Cross-seeding of oppositely-charged peptides can generate charge domain segregation on peptide nanotube surfaces. By taking advantage of the unique charge separation and domain segregation on peptide nanotube surfaces, fluorophore pairs are able to be organized on these unique peptide membranes for efficient energy and electron transfer. Deciphers of molecular recognition codes of heterogeneous self-assembly systems presented in this work are of great importance for constructing complex functional chemical systems on ordered nanomaterials. Overall, I argue that amyloid peptide membranes present robust and patterned surfaces capable of routinely controlling asymmetry, which rival extant biological membranes. Developing these systems for light-harvesting and charge separation of artificial photosynthesis is now within reach.

References

- (1) Graziano, V.; Gerchman, S. E.; Schneider, D. K.; Ramakrishnan, V. *Nature* **1994**, *368*, 351.
- (2) Dou, Y.; Mizzen, C. A.; Abrams, M.; Allis, C. D.; Gorovsky, M. A. *Mol. Cell* **1999**, *4*, 641.
- (3) Roth, S. Y.; Allis, C. D. *Trends Biochem. Sci* **1992**, *17*, 93.
- (4) Horn, P. J.; Carruthers, L. M.; Logie, C.; Hill, D. A.; Solomon, M. J.; Wade, P. A.; Imbalzano, A. N.; Hansen, J. C.; Peterson, C. L. *Nat Struct Mol Biol* **2002**, *9*, 263.
- (5) Ni, R.; Childers, W. S.; Hardcastle, K. I.; Mehta, A. K.; Lynn, D. G. *Angewandte Chemie-International Edition* **2012**, *51*, 6635.
- (6) Wang, H.; Chu, P. K. In *Characterization of Biomaterials*; Bose, A. B., Ed.; Academic Press: Oxford, 2013, p 105.
- (7) Boncheva, M.; Gracias, D. H.; Jacobs, H. O.; Whitesides, G. M. *Proc Natl Acad Sci U S A* **2002**, *99*, 4937.
- (8) Raez, J.; Manners, I.; Winnik, M. A. *J. Am. Chem. Soc.* **2002**, *124*, 10381.
- (9) Prins, L. J.; Huskens, J.; de Jong, F.; Timmerman, P.; Reinhoudt, D. N. *Nature* **1999**, *398*, 498.
- (10) Van Gough, D.; Wheeler, J. S.; Cheng, S.; Stevens, M. J.; Spoerke, E. D. *Langmuir* **2014**, *30*, 9201.
- (11) Horne, W. S.; Ashkenasy, N.; Ghadiri, M. R. *Chemistry – A European Journal* **2005**, *11*, 1137.
- (12) Mehta, A. K.; Lu, K.; Childers, W. S.; Liang, Y.; Dublin, S. N.; Dong, J.; Snyder, J. P.; Pingali, S. V.; Thiyagarajan, P.; Lynn, D. G. *J. Am. Chem. Soc.* **2008**, *130*, 9829.
- (13) Liang, Y.; Guo, P.; Pingali, S. V.; Pabit, S.; Thiyagarajan, P.; Berland, K. M.; Lynn, D. G. *Chem. Commun.* **2008**, 6522.
- (14) Liang, C.; Ni, R.; Smith, J. E.; Childers, W. S.; Mehta, A. K.; Lynn, D. G. *J. Am. Chem. Soc.* **2014**, *136*, 15146.
- (15) Matson, J. B.; Zha, R. H.; Stupp, S. I. *Current Opinion in Solid State & Materials Science* **2011**, *15*, 225.
- (16) Channon, K. J.; Devlin, G. L.; MacPhee, C. E. *J. Am. Chem. Soc.* **2009**, *131*, 12520.
- (17) Nakashima, T.; Kimizuka, N. *Adv. Mater.* **2002**, *14*, 1113.